GNS SCIENCE
TE PŪ AO

S+G
3762

1 Fairway Drive, Avalon
Lower Hutt 5010
PO Box 30368
Lower Hutt 5040
New Zealand
T +64-4-570 1444
F +64-4-570 4600
www.gns.cri.nz

Ground-motion prediction equations for subduction zones based on strong-motion records from Japan

John X. Zhao David A. Rhoades

GNS Science Consultancy Report 2014/236
January 2015

DISCLAIMER

This report has been prepared by the Institute of Geological and Nuclear Sciences Limited (GNS Science) exclusively for and under contract to the Earthquake Commission of New Zealand. Unless otherwise agreed in writing by GNS Science, GNS Science accepts no responsibility for any use of or reliance on any contents of this Report by any person other than the Earthquake Commission and shall not be liable to any person other than the Earthquake Commission, on any ground, for any loss, damage or expense arising from such use or reliance.

The data presented in this Report are available to GNS Science for other use from September 2014.

BIBLIOGRAPHIC REFERENCE

Zhao, J. X.; Rhoades, D. A. 2014. Ground-motion prediction equations for subduction zones based on strong-motion records from Japan, *GNS Science Consultancy Report* 2014/236. 162 p.

CONTENTS

EQUATIONS

FIGURES

TABLES

This page is intentionally left blank.

EXECUTIVE SUMMARY

In this report, a set of ground motion prediction equations (GMPEs) were developed for subduction zones, based on strong-motion data from Japan. GMPEs are a critical part of both probabilistic seismic hazard analyses (e.g., to determine the earthquake design loads for engineering structures, such as hydro-power stations), and earthquake loss modelling. The ground-motion parameters used in the this study are the peak ground acceleration and the 5% damped acceleration response spectrum.

A GMPE is an empirical model derived from strong-ground motion records that are obtained from earthquakes with a moment magnitude about 5.0 or larger and at stations within a distance to the hypocentre or to the fault rupture plane less than 200–300km. As for all empirical models, natural variability dictates that a large number of strong-motion records should be used. For engineering design purposes ground-motions at distances over 150km are not as important as those from shorter distances. However, the number of records for a given moderately large earthquake increases with increasing distance, and the distant records are important for deriving parameters that represent site effects and parameters that control the attenuation of the ground-motion with distance. We used records up to a maximum distance about 130km for a magnitude 5 earthquake and up to 300km for magnitude 7 or larger events.

Earthquake ground motions at a soil site can be larger than those at a nearby rock site subjected to moderate ground shaking, and this is usually referred to as site amplification. This part of the GMPE has to be modelled appropriately, and requires detailed site information, such as the site class based on measured soil material properties, site period or shear-wave velocity profiles down to bedrock. Unfortunately, these high-quality site parameters are very currently limited in many countries, such as New Zealand.

The modelling of ground motions in an area with a subduction tectonic setting, such as in New Zealand and Japan, is more complex than that in an area which has essentially shallow crustal earthquakes only, such as in the California, the United States. The material properties of the crust usually differ significantly from those of the upper mantle, the mantle wedge and the subducting plate. The material properties close to the subducting interface, either between the crust and the subducting slab, or between the mantle wedge and the subducting plate differ from those of the subducting slab down to a depth about 50km. Thus the ground motions from earthquakes in different tectonic locations often have very different characteristics and require different GMPEs.

Japan has a large database of strong-motion records, has high-quality site information for a large number of recording stations, and has a reasonably reliable geometric model of the subducting plate, all of which are essential for developing a set of reliable GMPEs. Also Japan is also the only country in the world that has a large number of strong-motion records and that has a tectonic setting similar to that of New Zealand. We have assembled nearly 15,000 strong-motion records from earthquakes with moment magnitudes of 5.0 or larger, which this study aims to develop a set of GMPEs that may be suitable for many subduction zones around the globe. The GMPEs will be optimised for New Zealand data in a future study.

The first step in developing GMPEs from records in Japan or other subduction zones is to classify the earthquakes according to their tectonic locations. We compared the earthquake information, including moment magnitude, focal mechanism and hypocentral location,

derived from three organizations, and designed four classification schemes. Next, we developed a set of statistically optimized GMPEs (without a requirement of having a broadly smoothed spectrum across the site period of 0.0–5.0s) using records from each scheme and then we compared the goodness-of-fit between the four models. We successfully derived the best possible tectonic category for 331 earthquakes.

Soil sites usually develop nonlinear response during strong ground shaking. The nonlinear response reduces the amplification of soil sites and sometime leads to deamplification, i.e., the ground motion at a soil site being less than that at a nearby rock site. For engineering applications, the effect of nonlinear soil response is important. However, the nonlinear terms cannot be derived from the existing strong-motion records from Japan, and so we used numerical modelling of soil sites based on the measured site parameters of a number of selected Kik-net stations. We derived the terms that control the nonlinear site effects by numerical modelling and we adjusted the weak-motion amplification terms from the numerical modelling by applying amplification ratios derived from the strong-motion records.

Next we divided the strong-motion records into three groups according to the earthquake categories and developed a GMPE for each group. These GMPEs share most parameters for the nonlinear soil response part. We attempted to use relatively simple functions for the attenuation effect, and we also modelled the effect of volcanic paths over which the strong-ground motion is further attenuated by the rock magma underneath the volcanoes. An important feature of the GMPEs is that the increase in the ground motion with increasing earthquake magnitude over 7.1 is much smaller than that from events with smaller magnitudes. This feature reduced the extent of over-predicting the response spectrum from large earthquakes, such as the M_W=9 2011 Tohoku earthquake in Japan. For large crustal earthquakes, we used world-wide records to constrain the extent of increase in response spectrum with increasing magnitude.

We carried out extensive statistical tests to evaluate whether the site terms and model prediction uncertainty from the three sets of models were statistically similar. We also approximately separated the uncertainty associated with site effects from that associated with attenuation. These separated uncertainties can be used in probabilistic seismic analyses for different earthquake categories and different site classes.

In our study, the measured site parameters proved to be important and the overall variability as well as the average predicted spectrum are improved by excluding the records from sites with inferred site conditions. This demonstrated that the measured site information is critically important. For Geonet, the strong-motion recording network in New Zealand, the measured site conditions are still rare outside of Christchurch city.

For developing "next generation attenuation models" for New Zealand, where there are far fewer high-quality strong-motion records than in Japan, the present study may provide some useful clues, lessons and insight on the different geometry of the subducting interface and the different relative positions of the strong-motion recording stations with respect to the subducting plate or subduction trench. Some of the features from the present study can be adopted directly while the other features can be adopted with appropriate modifications.

This report contains three sections, with each section having its own abstract, introduction etc. and conclusions. This format leads to some repetition of material, but has the advantage that each part is almost completely self-contained, and so readers who are interested in a particular section do not have to read the whole report.

TECHNICAL ABSTRACT

Establishing a set of ground-motion prediction equations (GMPEs) for Japan requires earthquake source categories in the dataset. Earthquakes are typically divided into three groups: shallow crustal events that occur in the Earth's crust, subduction interface events that occur at the interface between the crust or mantle and the subducting plate, and the subduction slab events that occur in the subducting plate. In the present study, we compared the hypocentral locations published in the catalogues of the International Seismological Centre (ISC-EHB), the Japan Meteorological Agency (JMA) and the National Earthquake Information Centre (NEIC). The hypocentral locations for the same earthquakes vary significantly from one catalogue to another. We used the subduction interface model from the US Geological Survey, Slab 1.0, to help guide the classification. We designed four classification schemes using locations from these three catalogues. We then fitted a random effects model to the strong-motion dataset from these earthquakes to assess the merits of the classification schemes. Our results showed that using ISC-EHB locations for events before 2005, and then using the preference order of catalogues as: 1) JMA locations with high precision levels, 2) ISC-EHB, and 3) NEIC (excluding the events with a fixed depth) for events since 2005, together with some conditions for subduction interface events, produced the best GMPEs in terms of the maximum log-likelihood. We also found that having a separate group for the earthquakes above the subduction interface, but with a depth over 25km, improved the goodness-of-fit of the GMPEs.

Nonlinear site models are an important part of ground-motion prediction equations (GMPEs) and can be constructed in a number of ways. If a numerous soil site strong-motion records contain the effect of strong nonlinear soil response, the parameters for the nonlinear model can be a part of the regression parameters for GMPEs. However, the number of strong-motion records from Japan that contain the effect of strong nonlinear soil response is still too small to derive nonlinear site terms. It is also possible to derive nonlinear site models by numerical simulation. We present a model of nonlinear site terms using site class as the site parameter in GMPEs based on a 1-D equivalent linear model. The 1-D model was constructed based on the shear-wave velocity profiles from the Kik-net strong-motion stations with a wide range of site periods, soil depth and impedance ratios. The rock site strong-motion records were from different earthquake categories in Japan and the PEER dataset. Those records had a wide range of earthquake magnitudes, source distances and peak ground accelerations. A random effects regression model was fitted to the calculated spectral amplification ratios accounting for the effect of site impedance ratios, earthquake magnitudes and source distances of the rock site records. We also designed a method to adjust the 1-D model so that it can be used in a GMPE accounting for the fact that a 1-D model is an overly simplistic assumption for many real strong-motion recording stations in many parts of the world.

Ground motion prediction equations (GMPEs) derived from strong-motion records in Japan are presented. We assembled a large dataset from earthquakes with a moment magnitude (M_W) over 4.9 and a reliable earthquake category, up to the end of 2012. The earthquakes were divided into four tectonic categories: shallow crustal, upper mantle, subduction interface and subduction slab events. The shallow crustal and the upper mantle (SC-UM) events were combined as one group, and a set of three GMPEs were derived for the SC-UM, subduction interface and subduction slab events, respectively.

The GMPEs were based on a set of simple geometric attenuation functions. A linear magnitude scaling was adopted for large earthquakes with $M_W \geq 7.1$, with the scaling rates for large events being much smaller than those for the smaller events. A magnitude squared term was used for subduction slab events with $M_W < 7.1$. The models included nonlinear site terms, most of which did not vary from one model to another. The site terms were site classes based on site period.

We modelled the effect of volcanic zones by using an anelastic attenuation coefficient applied to a horizontal portion of the seismic wave travel distance (along a straight line between the closest point of a fault plane and a recording station) within volcanic zones. The attenuation rates through the volcanic zone differed significantly from one GMPE model to another.

Most strong-motion records in the dataset used in the present study are from stations with a measured shear-wave profile down to bedrock. A small number of strong-motion records are from strong-motion stations with inferred site classes using H/V response spectral ratio or geological description of the surface soil layers. We tested the effect of site information quality, by examining the results from a dataset containing the strong-motion records from sites with an inferred site class and the results from a dataset without these records. The site information quality made a significant difference for nearly all spectral periods of the three models, i.e., the model fit improved significantly when the sites with inferred site classes were excluded.

The within-event residuals were separated into within-site and between-site approximately and the corresponding standard deviations were calculated using a random effects model with all model coefficients presented in this manuscript. The separation of within-event residuals into within-site and between-site components allows for a possibility of adopting different standard deviations for different types of earthquakes and for different site classes in a probabilistic seismic hazard analysis if desired.

Extensive statistical tests were performed for the linear site terms, within-event and between-event residuals, and within-site and between-site residuals to examine if these terms from the three different models differed statistically and if the standard deviations for the models differed significantly. The site terms from the three models were essentially statistically similar for many spectral periods among the three GMPEs, except that the site terms for some soft soil sites differed statistically between SC-UM and subduction slab models. Among the three models, the between-event standard deviations of the residuals did not differ statistically at any spectral period, whereas within-event standard deviations differed statistically at some spectral periods. The within-site and between-site standard deviations from the three models also differed statistically at some spectral periods.

1.0 AN EARTHQUAKE CLASSIFICATION SCHEME FOR GROUND-MOTION PREDICTION EQUATIONS IN JAPAN

1.1 ABSTRACT

Establishing a set of ground-motion prediction equations (GMPEs) for Japan requires earthquake source categories in the dataset. Earthquakes are typically divided into three groups: shallow crustal events that occur in the Earth's crust, subduction interface events that occur at the interface between the crust or mantle and the subducting plate, and the subduction slab events that occur in the subducting plate. In the present study, we compared the hypocentral locations published in the catalogues of the International Seismological Centre (ISC-EHB), the Japan Meteorological Agency (JMA) and the National Earthquake Information Centre (NEIC). The hypocentral locations for the same earthquakes vary significantly from one catalogue to another. We used the subduction interface model from the US Geological Survey, Slab 1.0, to help guide the classification. We designed four classification schemes using locations from these three catalogues. We then fitted a random effects model to the strong-motion dataset from these earthquakes to assess the merits of the classification schemes. Our results showed that using ISC-EHB locations for events before 2005, and then using the preference order of catalogues as: 1) JMA locations with high precision levels, 2) ISC-EHB, and 3) NEIC (excluding the events with a fixed depth) for events since 2005, together with some conditions for subduction interface events, produced the best GMPEs in terms of the maximum log-likelihood. We also found that having a separate group for the earthquakes above the subduction interface, but with a depth over 25km, improved the goodness-of-fit of the GMPEs.

1.2 INTRODUCTION

Ground-motion prediction equations (GMPEs) are one of the most important components of a probabilistic seismic hazard analysis. GMPEs are also used in estimating the response spectrum at the location of an engineering structure, given an earthquake magnitude, source distance and site conditions. Many models have been developed recently, such as the Next Generation Attenuation models (NGAs) by Abrahamson and Silva (2008), Campbell and Bozorgnia (2008), and Chiou and Youngs (2008). Apart from earthquake magnitude, two other important earthquake source parameters are contained in typical GMPEs for Japan and other subduction zones around the globe: focal depth and tectonic category, namely shallow crustal events (with a focal depth of 25km or less), subduction interface events with a focal depth of 50km or less, and subduction slab events that occur within the subduction slab (Zhao et al. 2006a, McVerry et al. 2006). Zhao et al. (2006a) and Youngs et al. (1997) show that the response spectra from earthquakes in different tectonic categories vary significantly, with subduction slab-events producing much higher short period spectra than the other two types of events.

Kobayashi et al. (2000) found that many earthquakes from Japan had been assigned focal depth of zero km, indicating that the depth could not be determined reliably. Kobayashi et al. (2000) reduced their model prediction standard deviation significantly by using the focal depths published in the EHB group from the International Seismological Centre (ISC) catalogue.

Earthquake classification usually requires three types of parameters: the epicentral location, the focal depth and the geometry of the subduction interface between the crust/mantle and the subducting plate. The epicentral location and focal depth are usually estimated by p-wave arrival time and the p-wave velocity structure in the region where the earthquake occurs. The Japan Meteoroidal Agency (JMA) locates earthquakes in Japan and publishes related information through CDs and the website of the National Research Institute for Earth Science and Disaster Prevention (NIED) (http://www.hinet.bosai.go.jp/REGS/JMA/). Also a number of other organizations publish earthquake locations in Japan. For example, the National Earthquake Information Centre (NEIC) of the United States Geological Survey (USGS) also estimates earthquake locations in Japan and publishes relevant information on its website (http://earthquake.usgs.gov/regional/neic/). The accuracy of the earthquake locations estimated by different agencies is known to vary significantly. For example, the ISC-EHB catalogue was considered to be more accurate than those from the other organizations (Zhao et al. 2006a). For many earthquakes, using local records may not lead to the best depth solutions, when the spacing of the local network is large. It is also difficult to determine focal depths for some offshore shallow earthquakes using regional network arrival times recorded at on-land stations, because of the inadequate distribution of seismic stations (Gamage et al. 2009). For earthquakes with a moment magnitude about 5 or larger, using the pP phase and/or sP phase from teleseismic records can significantly improve the accuracy (http://earthquake.usgs.gov/learn/topics/seismology/determining_depth.php). Recently, Gamage et al. (2009) successfully determined focal depth of offshore earthquakes in Japan by using the sP phase recorded at a distance of 150km or more.

There is a timeliness issue with the ISC-EHB catalogue. At present (March 2014), earthquake locations from this catalogue are available only to the end of 2008, while Kik-net and K-net in Japan have obtained over 9000 high quality strong-motion records that can be used for developing GMPEs since the end of 2008. In order to use these records, an alternative source of earthquake locations must be adopted. We used two other catalogues, the JMA catalogue and the NEIC catalogue.

JMA hypocentral locations are available from the NIED website (JMA Unified Hypocentre Catalogues). Hypocentre information is given together with the estimated errors and precision levels. JMA appears to have improved the depth estimates by a number of methods (constant depth interval and continuous depth parameter). The algorithm estimation errors for the earthquakes before or during 2004 appear to be much larger than those after 2004.

To classify earthquake categories, the geometry of the subducting plate, i.e., the depth, strike and dip angle at a given location must also be available. In the Zhao et al. (2006a) study, the subduction interface geometry model developed by the authors of that study was used. Recently, Hayes et al. (2012) of USGS constructed a subduction interface model, named Slab1.0, which is available on the USGS website (http://earthquake.usgs.gov/research/data/slab/map/). Slab1.0 covers most subduction zones around the Pacific Ocean. The advantage of using publicly available models is for model verification procedures. For example, a user or a group of users may wish to compare data with a number of GMPEs developed for the region and an inconsistent classification of earthquake categories based on different geometry of the subduction interface may lead to an erroneous assessment.

It is difficult to ascertain the best catalogue and the number events that can be classified correctly, without complex numerical modelling of each event and comparing the results with the corresponding strong-motion records. This type of modelling is not possible for the present study. As the purpose of the classification is for developing GMPEs, we will use the goodness-of-fit for a set of GMPEs as a performance indicator for each classification scheme. The classification scheme that leads to the best fits of the GMPEs to the data will be considered as the preferred scheme. Though this method does not guarantee every event to be classified correctly, an overall reasonable scheme can be derived for the sole purpose of developing GMPEs.

1.3 COMPARISON OF HYPOCENTRAL LOCATIONS FROM DIFFERENT CATALOGUES

We selected 573 earthquakes in Japan between 1996 and 2008 from the ISC-EHB catalogues. Many of those events do not yield strong-motion records in our dataset, mostly because the station distance from these earthquakes is larger than the maximum distance (about 130km for a moment magnitude 5.0 event or 300km for a magnitude 7.0 or larger event). Figure 1.1 shows the correlation between the depth in the NEIC catalogue and the depth in the ISC-EHB catalogue. It appears that the depth for a large number of events in the NEIC catalogue was fixed as 10km or 33km, probably because it was not possible to derive a reliable depth for these events. We define a depth shift – the focal depth difference between the ISC-EHB catalogue and the NEIC catalogue for the same earthquake, as an indicator of depth correlation. For 119 events with an NEIC depth fixed at 10km, the corresponding ISC-EHB depth varies between 2 and 52km. 73 of these events have a depth shift of 5km or less, 27 events have a depth shift of 5–10km, 8 events have a depth shift of 10–15km, and 11 events have a depth shift larger than 15km. The largest depth shift is 43km. For those 175 events with a fixed depth of 33km in the NEIC catalogue, the ISC-EHB depth for these events varies between 3 and 63.5km: 55 events have a depth shift of 5km or less, 33 events have a depth shift between 5 and 10km, 64 events have a depth shift between 10 and 20km, and 23 events have a depth shift larger than 20km. The largest depth shift is 30.5km. Clearly, the large number of events with a fixed depth in the NEIC catalogue would reduce the accuracy for event classifications, as depth is one of the critical parameters.

Figure 1.2 shows the depth correlation between ISC-EHB and NEIC catalogues for 279 events, excluding those events with a fixed depth of 10 or 33km in the NEIC catalogue. For events with a depth less than 100km the scatter is considerable. Figure 1.3 shows the distribution of events with various depth shift for those events in Figure 1.2. 212 events have a depth shift less than 10km, 29 events have a depth shift between 10 and 15km, 26 events between 15 and 25km and 12 events over 25km. There is no systematic distribution for events with a large depth shift. Figure 1.4 shows the depth correlation between the ISC-EHB and NEIC catalogues for those events from which we have strong-motion records. The scatter for events within a depth of 70km is still large.

Figure 1.5 shows the depth correlation between the JMA and ISC-EHB catalogues for events between 1997 and 2003, and clearly the scatter is large. The large scatter suggests that the hypocentre from the JMA catalogue should not be used if we assume that ISC-EHB locations are reliable. However, JMA has improved its earthquake location estimates by using more stations in Japan and more accurate algorithms than in the past. The JMA catalogue also presents the estimated errors for the initial time, latitude, longitude and depth, and these errors for events since 2005 are markedly smaller than those for the earlier events. Figure 1.6 shows the depth correlation between JMA and ISC-EHB catalogues for the events

between 2005 and 2008. The scatter for shallow earthquakes is reduced compared with those in Figure 1.5 but the scatter is larger for events between 30 and 60km in the JMA catalogue.

To correctly classify an earthquake, we need not only the hypocentral depth but also an accurate epicentral location. We define a distance shift: the distance from the epicentre in one catalogue to the epicentre in another catalogue for the same event. Figure 1.7 shows the distance shift between the JMA and the ISC-EHB catalogues for the same events as shown in Figure 1.6. Among 61 events, 16 events have a distance shift of 10km or less, 14 events have a distance shift between 10 and 15km, 8 events have a distance shift between 15 and 20km, 13 events have a distance shift between 20 and 30km and 10 events have a distance shift more than 30km. The events with a large distance shift tend to be the offshore earthquakes. However, many of these events are too far from the strong-motion stations and did not produce useful strong-motion records for developing GMPEs.

Figure 1.8 shows the depth correlation for a subset of the events presented in Figure 1.6 and Figure 1.7. We have strong-motion records from these events that will be used for developing GMPEs for Japan. The correlation is excellent compared with those presented in Figure 1.6 and the result suggests that the depth in the JMA catalogue is reasonable for those events that yield useful strong-motion records, possibly because these events also yielded good records in many JMA stations for locating earthquakes. The average depth shift is 3.7km for this set of events. Figure 1.9 shows the distance shift between the epicentres from the JMA and ISC-EHB catalogues. Among 28 earthquakes, 5 events have a distance shift less than 10km, 9 events have a distance shift of 10–15km, 4 events have a distance shift of 15–20km, 6 events have a distance shift of 20–30km and 4 events have a distance shift over 30km. The events with a large distance shift (over 20km) are offshore ones. The average distance shift is 17.3km. However, it is impossible to determine which catalogue is the best from the correlations of depth and or distance reported in these catalogues.

Figure 1.10 shows the depth correlation between the JMA and NEIC catalogues for 195 events during 2004 and 2012. These earthquakes all produce strong-motion records for developing GMPEs. The scatter is very large for depths up to 80km. Note that the large scatter means that the estimated depth from the two catalogues is not consistent but does not mean the estimated depth is incorrect.

1.4 Classification schemes

The JMA catalogue also provides flags for accuracy level of epicentral location and depth estimates. JMA level 0 depth estimates are for events before the end of 2004 and are considered to be less accurate than level 1 estimates. For level 2 depth estimates, the JMA catalogue gives a depth usually less than 1km and no error for depth estimates is reported. We assume that the depth for these events is not accurate. The JMA catalogue also provides precision levels for hypocentral locations and we will use only those events that have a high precision level (level K).

As presented in the Zhao et al. (2006a) study, the hypocentral locations from the ISC-EHB catalogue are still considered as the best available then, and therefore we use ISC-EHB locations for all events before the end of 2004. For those events since 2005 that yield strong-motion records for developing GMPEs, the comparison presented in Figure 1.8 suggests that the depth from the JMA catalogue for those events is likely to be as reliable as that from the ISC-EHB catalogue. We attempted to use JMA locations for the events since 2005.

The focal mechanism for each event was assigned by using plunge angles as defined by Boore and Atkinson (2008): for a reverse focal mechanism T-axis >40°, for a normal faulting P-axis >40° and the rest are strike-slip events. The plunge angles and moment magnitude are from Harvard CMT solutions when available and from NIED CMT solutions otherwise. In our dataset there are only 16 events without Harvard CMT solutions.

As described above, we use the subduction interface geometry model Slab1.0. We used the following classification schemes:

Scheme I:

- For those events before the end of 2004, ISC-EHB catalogue locations are adopted. For events since 2005, the catalogues used have the following preferences:
- Use JMA hypocentral locations with a depth precision level 1 and epicentral location precision level "K";
- ISC-EHB locations; and
- NIEC locations for events without a fixed depth.

Classification criteria:

- Subduction interface earthquakes must have a reverse focal mechanism, a depth within 5km of the subduction interface and a depth less than 50km. The dip angle for one of the nodal planes must be within 15 degrees of the dip angle of the subduction interface;
- Events that are above the subduction interface, not classified as interface earthquakes and have a depth of 25km or less are classified as shallow crustal earthquakes,
- Events that are 5km or more above the subduction interface but not shallow crustal events are classified as upper mantle earthquakes;
- Events that are not in any of the groups specified above are subduction slab earthquakes.
- Table 1.1 presents the numbers of events in each source category classified by using this scheme. Among the 311 events, 73 are shallow crustal events, 48 are upper mantle events, 60 are subduction interface events and 130 are subduction slab events. The depth tolerance of 5km is essentially arbitrary but is a number that is close to the average depth difference of 3.7km between the JMA depth and ISC-EHB depth presented in Figure 1.8.

Scheme II:

The classification scheme is the same as Scheme I, except that ISC-EHB hypocentre locations are used whenever they are available.

Scheme II leads to the same number of shallow crustal events as in Scheme I, 50 upper mantle events, 62 subduction interface events and 130 subduction slab events. Compared with Scheme I, 6 earthquakes changed tectonic categories.

Scheme III:

ISC-EHB locations are used if available, otherwise NEIC hypocentral locations are used. All other criteria are the same as those in Scheme I. Scheme III leads to 81 shallow crustal events, 90 upper mantle events, 46 subduction interface events and 94 subduction slab events.

Scheme IV:

This scheme uses hypocentral locations from the NEIC catalogue, and if not available, uses the hypocentral location from the JMA catalogue.

The interface events must satisfy the following conditions:

- The shortest distance from the hypocentre to the slab interface < 15 km
- Difference in dip with slab interface < 15°
- Rake between 45° and 135°
- Depth < 45 km
- Slab events: These events are characterized as events that are below the Slab1.0 interface and do not satisfy the interface event criteria.
- Crustal events: These are events that are located above the interface plane and are not classified as interface events.

Scheme IV does not have an upper mantle category. It leads to 125 crustal earthquakes, 79 subduction interface events and 107 subduction slab events as presented in Table 1.1. The largest depth for crustal events is 45km.

Table 1.1 shows that the numbers of events in each earthquake category from the four classification schemes vary significantly and the variation suggests a very large uncertainty in classifying earthquakes from subduction zones in Japan, primarily from the event location uncertainty in those catalogues. Although JMA locations since 2005 appear to be improved significantly over pre-2005 locations, it would be still difficult to assess, for example, whether NEIC locations (without a fixed depth) would be better than JMA locations or are as reliable as the ISC-EHB locations. For our purpose of developing a set of GMPEs based on records from Japan, it may be reasonable to test the classification schemes using a goodness-of-fit parameter from GMPEs derived from the same dataset but with different source categories.

1.5 GMPEs USED FOR TESTING CLASSIFICATION SCHEMES

Next we will develop a set of GMPEs to assess the merit of each classification scheme. The dataset used in this study is large enough to develop GMPEs for each source category independently. This method is a preferred for developing GMPEs for Japan, because standard deviations for each source category can be easily separated. To test classification schemes, we must account for the effects of data grouping and the change in the number of records in each source category. If we develop a GMPE for each earthquake category, when we compare the goodness-of-fits of the models for the corresponding source category in each classification scheme, we will somehow have to combine the goodness-of-fit from each set of models as an overall parameter for testing the classification schemes. Also the results would be affected too much by the changes in the number of records in each group alone. We therefore combine all earthquakes as one dataset and fit one set of models to all records.

We used separate source and path terms for different earthquake categories to account for the known source and path characteristics from different type of earthquakes. Because this study uses a GMPE specifically designed for assessing classification schemes, we will present the functional form but not the values for each term.

The following basic functional form for the GMPEs was then used,

$$\begin{aligned}\log_e(y_{i,j}) = &-\log_e(r_{i,j}) + f_{cr}(m_i, h_i, F_i) + f_{um}(m_i, h_i) + f_{int}(m_i, h_i) + f_{SL}(m_i, h_i) + \\ &g_{cr}(r_{i,j}, h_i) + g_{um}(r_{i,j}, h_i) + g_{intS}(r_{i,j}, h_i) + g_{intD}(r_{i,j}, h_i) + g_{SL}(r_{i,j}, h_i) + \\ &g_L log_e(x_{i,j} + 200.0) + e_{cr}x_{i,j} + e_{um}x_{i,j} + e_{intS}x_{i,j} + e_{intD}x_{i,j} + e_{SL}x_{i,j} + q_{SLh}x_{i,j} \\ &e^v_{cr}x^v_{i,j} + e^v_{int}x^v_{i,j} + e^v_{SL}x^v_{i,j} + S_k + S_{kNL} + \varepsilon_{i,j} + \eta_i\end{aligned} \quad \textbf{(1.1)}$$

$$q_{SLh} = e_{SLh}\begin{cases}0 & if\ h < 50km \\ 0.02h - 1.0 & if\ h \geq 50km\end{cases}$$

$$r_{i,j} = x_{i,j} + \exp(c_1 + c_2 C_m) \quad \textbf{(1.2a, b, c)}$$

$$C_m = \begin{cases}m_i & if\ m_i \leq C_{max} \\ C_{max} & if\ m_i > C_{max}\end{cases}$$

where *y* is either peak ground acceleration (PGA) or 5% damped acceleration response spectrum (the geometric mean of two horizontal components) for a spectral period *T*, *m* is moment magnitude, *h* is the depth of the fault plane top edge for those events that have a fault plane model and otherwise is focal depth, and *x* is source distance, the closest distance to the fault model plane if available and hypocentral distance otherwise. Distance $x^v_{i,j}$ is the volcanic path calculated from the straight line between the earthquake source and a site passing through volcanic zones (Zhao 2010). Symbol *e* denotes anelastic attenuation coefficient and q_{SLh} denotes the depth-dependent anelastic attenuation rate. S_k is the linear site-class term with site classes being defined in Zhao et al. (2006b) and S_{kNL} is the nonlinear site-class term for a given site class which will be described in Section 2. Function *f*( ) denotes source effect and *g*( ) stands for geometric attenuation functions. Symbol g_L denotes the geometric attenuation rate for distance over about 40km and is positive for all spectral periods. This term was used to avoid the requirement of positive anelastic coefficients. Subscript *i* denotes event number and *j* denotes record number from event *i*. Subscript *cr* denotes shallow crustal events, *up* denotes upper mantle events, *intS* denotes shallow subduction interface events, *intD* denotes deep subduction interface events, and *SL* denotes subduction slab events. Random variable $\varepsilon_{i,j}$ is the within-event error with a zero mean and a standard deviation of σ, and random variable η_i is between-event error with a zero mean and a standard deviation of τ. C_{max} is a magnitude constant and is taken as 7.1 determined by the model goodness-of-fit.

The Zhao (2010) study suggests that the anelastic attenuation rate for shallow subduction interface events with a depth range of 0–25km differs from that for the deep interface events with a depth over 25km, because the materials in the crust close to the subduction interface is expected to have a relatively small Q value, as illustrated in Figure 1.11. For the dataset used in the present study we found that the division significantly improved the model fit to the interface records.

The depth-dependent anelastic attenuation rate presented in Equation (1.2a) is attributed to the consideration that the distance portion passing through the upper mantle with a relatively low Q value, and is likely to cause increased anelastic attenuation with increasing event depth, as illustrated by Figure 1.11.

The function for source effect from the shallow crustal earthquakes is

$$f_{cr}(m_i, h_i, F_i) = b_{cr}h_i + F_R + F_N + \begin{cases} c_{cr}m_i + c_{cr2}m_i^2 & if\ m_i \le m_c \\ c_{cr}m_c + c_{cr2}m_c^2 + d_{cr}(m_i - m_c) & if\ m_i > m_c \end{cases} \quad (1.3)$$

where F_R is reverse fault factor F_N is normal fault factor, and b, c, and d are regression coefficients. The constant m_c is a specified magnitude that changes the magnitude scaling rate for events with a magnitude larger than m_c (Zhao and Lu 2011, Zhao and Xu 2012). We selected the same functional form for source effect in Equation (1.3) for subduction interface and slab events except for that focal mechanism terms were not used.

The depth-dependent geometric attenuation functions from Zhao (2010) were used for shallow crustal events,

$$g_{cr}(r,h) = \frac{h_m - h}{h_m - h_{crc}} \begin{cases} a_1 \ln(r) & for\ x \le x_1 \\ a_1 \ln(r_1) + a_2[\ln(r) - \ln(r_1)] & for\ x_1 \le x < x_2 \\ a_1 \ln(r_1) + a_2[\ln(r_2) - \ln(r_1)] + a_3[\ln(r) - \ln(r_2)] & for\ x_2 \le x < x_3 \\ a_1 \ln(r_1) + a_2[\ln(r_2) - \ln(r_1)] + a_3[\ln(r_3) - \ln(r_2)] + a_4[\ln(r) - \ln(r_3)] & for\ x \ge x_3 \end{cases} \quad (1.4)$$

$$r_n = x_n + \exp(c_1 + c_2 C_m) \qquad n = 1, 3 \quad (1.5)$$

where x is source distance, $x_1 \sim x_4$ are distance constants, h_m and h_{crc} are depth constants, Equation (1.4) was designed to capture the effect of Moho reflection for shallow crustal earthquakes (Somerville and Yoshimura 1990).

Moho reflection may also occur for shallow interface events above the Moho boundary of the crust, as illustrated in Figure 1.12. Our analyses show that using depth-scaled geometric attenuation functions similar to Equation (1.4) significantly improved the fit to records from shallow interface events and therefore we used the following geometric attenuation function for shallow interface events.

$$g_{int\,S}(r,h) = \frac{h_m - h}{h_m - h_{crc}} \begin{cases} a_5 \ln(r) & for\ x \le x_1 \\ a_5 \ln(r_1) + a_6[\ln(r) - \ln(r_1)] & for\ x_1 \le x < x_2 \\ a_5 \ln(r_1) + a_6[\ln(r_2) - \ln(r_1)] + a_7[\ln(r) - \ln(r_2)] & for\ x_2 \le x < x_3 \\ a_5 \ln(r_1) + a_6[\ln(r_2) - \ln(r_1)] + a_7[\ln(r_3) - \ln(r_2)] + a_8[\ln(r) - \ln(r_3)] & for\ x \ge x_3 \end{cases} \quad (1.6)$$

For subduction slab earthquakes we use the following depth-scaled geometric attenuation function from Zhao (2010),

$$g_{SL}(r,h) = \frac{h-h_1}{h_{Slbc}-h_1}\delta(h-h_1)$$

$$\begin{cases} a_9 \ln(r) \; for \; x \le x_9 \\ a_9 \ln(r_9) + a_{10}[\ln(r) - \ln(r_9)] \; for \; x_9 \le x < x_{10} \\ a_9 \ln(r_9) + a_{10}[\ln(r_{10}) - \ln(r_9)] + a_{11}[\ln(r) - \ln(r_{10})] \; for \; x \ge x_{10} \end{cases} \quad (1.7)$$

$$r_n = x_n + \exp(c_1 + c_2 C_m) \qquad n = 9,10 \quad (1.8)$$

$$\delta(h-h_1) = \begin{cases} 1 & h \ge h_1 \\ 0 & h < h_1 \end{cases} \quad (1.9)$$

where h_1 and h_{Slbc} are depth constants and x_4 and x_5 are distance constants. Zhao (2010) proposed Equation (1.7) to account for the possible constructive interferences between seismic waves propagating along different paths, and for deep events the seismic waves may have a long propagation path within the subduction plate, which is known to have higher Q values than in the mantle.

The material properties in the mantle wedge are expected to differ from those of the shallow crust. The geometry of the mantle wedge produces a special feature that the length of the seismic-wave propagation path in the mantle wedge from deep subduction interface earthquakes increases with increasing event depth, as illustrated in Figure 1.13. We attempted to model this feature by using the depth-scaled geometric attenuation function in Equation (1.7) for deep subduction interface events with a depth range of 25–50km and the model prediction is significantly improved. In this case, depth constants h_1 and h_{Slbc} are replaced by h_2 and h_{Intc}.

The regression coefficients in the GMPE were obtained by using the random effects method from Abrahamson and Youngs (1992) and the maximum log-likelihood was used as an indicator for the goodness-of-fit. GMPE developers usually aim to reduce the model prediction standard deviation. However, model standard deviations are not very sensitive to the selection of model parameters when they are close to the best solutions using a random effects model. Also model standard deviations change very little when a biased distribution of residuals against model parameters such as magnitude, distance and site parameters is eliminated, while the maximum log-likelihood is sensitive to the biased residual distribution, as demonstrated by Zhao (2010). Because, in the magnitude and distance ranges that are important for engineering applications, such as large magnitude and short distance, the predicted ground motion would always be some kind of extrapolation from the magnitude and distance ranges where the majority of the strong-motion records are from, it is important to eliminate any biased distribution of residuals. Zhao (2010) demonstrated that the model standard deviations were reduced only slightly even after the model prediction improved dramatically for many events. Another advantage of using log-likelihood is that the maximum log-likelihood increases little when a model parameter that is not statistically necessary is retained and this means that rigorous statistic testing on model parameters is not critical. In the present study we will use the maximum log-likelihood as a reasonable good-of-fit measure to judge the merit of each classification scheme.

1.6 STRONG-MOTION DATASET

We have assembled 16,362 strong-motion records from 397 earthquakes from Japan and a number of other regions including Alaska, California, Turkey and Iran (the middle-east group), Taiwan and the 2008 Wenchuan earthquake form China, as shown in Table 1.2 and Table 1.3. Among the 335 events from Japan, 31 have a magnitude of 6.5 or larger and occurred before 1996, including the 1995 Kobe earthquake. The reason for including these events is to provide a reliable constraint on the magnitude scaling rate for large earthquakes and to confirm the reduced magnitude scaling rates for large subduction interface events, suggested by Zhao and Xu (2012). These large events will also provide a necessary constraint on estimating the magnitude scaling for large subduction slab earthquakes. The maximum distance for large events from Alaska, Turkey and Iran, Wenchuan and Taiwan is 300km and the records provide a constraint for estimating the magnitude scaling for large crustal events as suggested by Zhao and Lu (2011). Also because the number of near-source records from Japan is small, we adopted 739 records from earthquakes in California (from the PEER strong-motion dataset). The maximum distance for the Californian events with a magnitude of 7.0 or larger is 300km if they are available. These records were used to constrain the magnitude scaling rates for large crustal events. For the Californian events with a magnitude range of 5.0–7.0, the maximum distance is 50km, to minimize the effect of different anelastic attenuation rates between Japan and California. These records were used to enhance the reliability of near-source parameters and the parameters for nonlinear site effect in the GMPEs. The site classes for non-Japanese records are obtained by replacing site period with T_{VS30} defined by Zhao and Xu (2013) as

$$T_{VS30} = \frac{120}{V_{S30}} \tag{1.10}$$

where V_{S30} is in meters per second and is the travel time-averaged shear-wave velocity of the surface soil layers to a depth of 30m. We added a correction term in Equation (1.1) for records using V_{S30} as the site parameter, to account for the different site class definition between the two groups of records.

We also added a term for anelastic attenuation to Equation (1.1) for those overseas event groups with records that have a maximum distance up to 300km, when necessary, as suggested by Zhao and Lu (2011).

Table 1.4 shows the number of strong-motion records from Japan in each source category (as classified in Scheme I) and focal mechanism group in four site classes. The site classes were defined in Zhao et al. (2006b) and Zhao (2010) studies and presented in Table 2.1 in Section 2. Site class (SC) I sites are either rock sites or a rock site with a thin layer soil that has a site period less than 0.2s, SC II sites are hard soil, SC III are intermedia soil, and SC IV are soft soil sites. SC I is equivalent to site class A+B, SC II and III correspond to site class C and SC IV corresponds to site class D in the Standard for earthquake loads in New Zealand NZS1170.5:2004 (Standards New Zealand, 2004). 6907 records are from SC I sites, 5079 records from SC II sites, 1701 records from SC III sites and 2675 records from SC IV sites.

Table 1.5 shows the number of records in each site class from different regions. The total number of non-Japanese records is 1519.

Table 1.6 shows the number of records from Japan in each focal mechanism and site each class. The total number of records from other regions is less than 10% of the total number of records. Figure 1.14 shows the magnitude and distance distribution of the strong-motion records used in this study, including the non-Japanese records.

1.7 TEST RESULTS

Figure 1.15 shows the increases in the maximum log-likelihood for Schemes I, II, and III, relative to Scheme IV, i.e., the maximum log-likelihood from each scheme minus that from scheme IV (which has about the smallest maximum log-likelihood for most spectral periods). Except for spectral periods over 3.0s, scheme I, using JMA locations when possible, has the highest maximum log-likelihood. At spectral periods over 3.0s, Schemes I and II have about the same maximum log-likelihood. We are slightly surprised to find that the use of ISC-EHB hypocentral locations, when they are available to replace JMA locations, leads to a slightly poorer model performance than the use of the JMA hypocentral locations (with high precision levels) whenever available. This result may suggest that JMA hypocentral locations are indeed better than the ISC-EHB locations after the expanded recording network and improve depth calculation algorithm after 2005. At spectral period 1s or longer, Schemes III and IV lead to a very similar level of maximum log-likelihood but have a much lower level than those from Schemes I and II. The comparatively poor performances of schemes III and IV are likely caused by the relatively poor hypocentral locations in the NEIC catalogue. Using an upper-mantle earthquake category in scheme III leads to significantly better performance than schemes IV at spectral periods less than 1.0s, suggesting that a separate category for upper mantle earthquakes is statistically necessary in this period range.

The total standard deviations σ_T can be calculated from within-event standard deviation σ and between-event standard deviation τ from

$$\sigma_T = \sqrt{\sigma^2 + \tau^2} \tag{1.11}$$

Figure 1.16 compares the within-event, between-event and the total standard deviations from the best scheme (Scheme I) with those from the worst scheme (Scheme IV). Figure 1.16(a) shows that these two schemes produce similar within-event standard deviations, with scheme I having slightly smaller standard deviations than scheme IV. The largest difference between the pairs of estimates is about 5% (at period 0.35 s). For between-event standard deviations, scheme I leads to slightly larger standard deviations than scheme IV at short periods (< 0.4s), while the standard deviations from both schemes are very similar for the other spectral periods, as shown in Figure 1.16(b). Figure 1.16(c) shows that the total standard deviations from the two schemes are similar, with scheme I having slightly smaller values than scheme IV.

Table 1.7 shows the source information for 311 earthquakes from Japan, including date and time (Japanese time), focal mechanism, moment magnitude, dip angles of the two nodal plane from NIED CMT solutions, the dip angles from the Harvard CMT solutions, focal depth, source category, and epicentral locations.

1.8 CONCLUSIONS

We compared the hypocentral locations from the JMA, ISC-EHB and NEIC catalogues. For the earthquakes since 2005, JMA locations have relatively small estimation errors for locations with high precision levels, and are very consistent with those from ISC-EHB catalogues for events that yield strong-motion records suitable for developing ground-motion prediction equations (GMPEs) for Japan. The depth correlations between JMA and NEIC and between NEIC and ISC-EHB catalogues are moderately poor as the NEIC catalogue appears to contain many events with a fixed depth of 10km or 33km. The hypocentral depth shifts, the depth differences in two catalogues for the same event, are considerable with some differences of tens of kilometres. Those events during 2005–2008 that yielded strong-motion records suitable for developing GMPEs have the smallest average depth shifts of 3.5km between JMA and ISC-EHB catalogues. The epicentral locations among different catalogues also vary considerably and the distance shift (the distance between two epicentres specified for the same event in two catalogues) can be larger than 30km. These inconsistent hypocentral locations may lead to a large uncertainty in the classification of earthquake into tectonic categories of shallow crustal, upper mantle, subduction interface and subduction slab.

Four classification schemes were designed and tested by comparing the maximum log-likelihoods from four sets of GMPEs. The following classification scheme appears to give the best results and is recommended:

- For events up to the end of 2004, ISC-EHB locations can be used. For events after 2004, the catalogue preference is: a) JMA locations with high-precision level, b) ISC-EHB locations, and c) NEIC locations if the depth is not fixed at a specified value;
- The geometry model from Slab1.0 by Hayes et al. (2012) can be used;
- Events that have a reverse faulting mechanism, a depth within ±5km from the subduction interface, a depth less than 50km, and the dip angle for one of the nodal planes within ±15° from the interface dip angle can be classified as subduction interface earthquakes;
- Events that are above the subduction interface, not classified as interface earthquakes, and have a depth of 25km or less can be classified as shallow crustal earthquakes;
- Events that are above the subduction interface but not shallow crustal events can be classified as upper mantle events;
- Events that are not in any of the groups specified above are subduction slab earthquakes.

The recommended classification scheme leads to the highest maximum log-likelihood among the tested schemes, but leads to relatively little reduction in the model standard deviations of the GMPEs.

Table 1.1 Number of events in each source category from four classification schemes.

	Scheme I	Scheme II	Scheme III	Scheme IV
Shallow Crustal	73	73	81	125
Upper Mantle	48	50	90	
Slab interface	60	62	46	79
Subduction slab	130	126	94	107

Table 1.2 Number of events in each source category and each focal mechanism group.

		Focal mechanism			Total in each type
		Reverse	Strike-slip	Normal	
Source category	Shallow crustal	65	54	19	**138**
	Upper mantle	26	5	16	**47**
	Subduction interface	75			**75**
	Subduction slab	98	13	26	**137**
Total in each focal mechanism		**264**	**72**	**61**	**397**

Table 1.3 Number of events in each region and each focal mechanism group.

		Focal mechanism			Total in each region
		Reverse	Strike-slip	Normal	
Region64	Alaska	1	2		**3**
	California	20	26		**46**
	Japan	235	39	61	**335**
	Middle east	1	4		**5**
	Taiwan	6	1		**7**
	Wenchuan, China	1			**1**
Total in each focal mechanism		**264**	**72**	**61**	**397**

Table 1.4 Number of records in each earthquake category and each focal mechanism group using the source classification Scheme I.

		Reverse	Strike-slip	Normal	Subtotal in each earthquake category
	SC I				
Source category	Shallow crustal	1139	707	482	2328
	Upper mantle	491	101	393	985
	Subduction interface	1563			1563
	Subduction slab	1618	105	308	2031
Subtotal in each FM group		4811	913	1183	6907
	SC II				
Source category	Shallow crustal	1034	817	302	2153
	Upper mantle	311	60	206	577
	Subduction interface	995			995
	Subduction slab	1103	86	165	1354
Subtotal in each FM group		3443	963	673	5079
	SC III				
Source category	Shallow crustal	380	260	115	755
	Upper mantle	77	17	49	143
	Subduction interface	360			360
	Subduction slab	365	19	59	443
Subtotal in each FM group		1182	296	223	1701
	SC IV				
Source category	Shallow crustal	436	234	182	852
	Upper mantle	182	31	70	283
	Subduction interface	656			656
	Subduction slab	693	55	136	884
Subtotal in each FM group		1967	320	388	2675
Total in each FM group		**11403**	**2492**	**2467**	**16362**

Table 1.5 Number of records in each earthquake category and each focal mechanism group.

	Site class				Subtotal in each region
Regions	SC I	SC II	SC III	SC IV	
Alaska	2	21	7		**30**
California	65	478	166	30	**739**
Japan	6679	4173	1386	2605	**14843**
Middle east	6	32	7	1	**46**
Taiwan	89	352	134	36	**611**
Wenchuan, China	66	23	1	3	**93**
Subtotal in each SC	**6907**	**5079**	**1701**	**2675**	**16362**

Table 1.6 Number of records in each site class and focal mechanism group from shallow crustal earthquakes in Japan.

Site class	Focal mechanism			Subtotal in each SC
	Reverse	Strike-slip	Normal	
SC I	4641	855	1183	**6679**
SC II	2989	511	673	**4173**
SC III	1011	152	223	**1386**
SC IV	1923	294	388	**2605**
Subtotal in each FM	**10564**	**1812**	**2467**	**14843**

Table 1.7 Source categories for the earthquakes used in developing GMPE for Japan.

EQ No.	EQ Date	Focal Mech.	Mw	NDip1	NDip2	HVDip1	HVDip2	Depth	ST	Latitude	Longitude
1	199610192344	R	6.74			17	73	18.0	1	31.911	131.574
2	199612030718	R	6.69			19	71	29.0	2	31.828	131.326
3	199704030433	SS	5.47	89	82	70	77	8.0	1	31.964	130.214
4	199705131438	SS	6.07	88	85	75	77	12.8	1	31.943	130.276
5	199706251850	SS	5.85	89	76	72	84	20.4	1	34.430	131.583
6	199802210955	R	5.09	49	41	44	47	18.6	1	37.278	138.706
7	199804222032	R	5.23	67	29	43	47	46.8	2	35.169	136.432
8	199805031109	SS	5.57	85	82	81	82	9.4	1	34.930	139.117
9	199808160331	SS	5.47	89	87	71	83	5.8	1	36.329	137.683
10	199809031658	R	5.84	52	44	49	54	6.2	1	39.786	140.742
11	199812160918	R	6.02	70	26	13	78	30.0	2	31.373	131.346
12	199901240937	N	6.39	90	23	24	78	34.0	4	30.649	131.135
13	199902010152	R	5.34	64	27	28	62	44.9	3	37.180	141.332
14	199902261418	R	5.28	66	26	32	64	19.2	1	39.187	139.894
15	199903071003	N	4.94	64	52			32.2	2	43.059	145.878
16	199904252127	R	5.32	70	20	33	63	56.5	2	36.480	140.473
17	199911151035	R	5.69	57	34	41	56	50.6	4	38.316	142.268
18	200001091302	R	5.37	71	19	21	70	43.8	3	37.331	141.532
19	200001282321	R	6.72	53	42			40.0	4	43.083	146.817
20	200006031754	R	6.14	69	22	27	66	51.4	4	35.576	140.469
21	200006070616	R	5.90	49	47	34	59	7.0	1	36.813	135.508
22	200006251534	R	6.05	60	31	17	74	37.7	3	31.125	131.266
23	200007010534	R	5.35	72	18			41.8	3	37.345	141.500

EQ No.	EQ Date	Focal Mech.	Mw	NDip1	NDip2	HVDip1	HVDip2	Depth	ST	Latitude	Longitude
24	200007011602	SS	6.14	75	41	85	88	12.5	1	34.223	139.171
25	200007030503	SS	5.66	62	52	76	84	16.7	1	34.146	139.255
26	200007151030	SS	6.06	82	78	83	83	13.6	1	34.396	139.257
27	200007210339	R	6.01	64	26	26	64	31.0	2	36.550	140.947
28	200007302125	SS	6.49	85	77	82	85	15.0	1	33.938	139.381
29	200008031430	R	5.57	76	15	20	72	36.4	3	31.094	131.344
30	200010061330	SS	6.68	85	81	83	89	9.0	1	35.375	133.175
31	200010081317	SS	5.35	86	79	67	89	15.0	1	35.084	133.116
32	200010310143	R	5.48	72	43	42	69	34.8	2	34.280	136.274
33	200011140057	R	5.93	67	28			26.0	2	42.520	144.736
34	200011141253	R	5.57	71	22			43.6	4	42.564	144.755
35	200012050147	R	5.70	83	10	20	70	39.0	3	35.800	140.910
36	200103241528	N	6.83	59	45	39	57	42.0	2	34.108	132.543
37	200103260541	N	5.20	62	31	33	61	45.1	2	34.061	132.565
38	200112022202	N	6.47	84	7	7	83	124.0	4	39.427	141.097
39	200305261824	R	7.03	69	22	19	72	68.0	4	38.868	141.507
40	200307260713	R	6.08	52	38	43	47	6.0	1	38.420	141.000
41	200309201255	R	5.65	59	55	51	63	51.0	2	35.000	140.170
42	200309260450	R	8.29	78	15	11	82	27.0	3	41.810	143.910
43	200309260608	R	7.37	71	21	18	72	47.6	3	42.429	143.987
44	200309261135	R	5.80	71	32			33.0	4	42.000	144.450
45	200309261527	R	5.89	70	32	28	63	33.0	4	42.160	144.670
46	200309270538	R	5.98	76	36	19	73	33.0	4	41.990	144.580
47	200309271706	R	5.34	66	26	31	64	52.0	4	42.740	144.250
48	200309280923	R	5.17	72	20	21	69	33.0	2	42.250	143.270

EQ No.	EQ Date	Focal Mech.	Mw	NDip1	NDip2	HVDip1	HVDip2	Depth	ST	Latitude	Longitude
49	200309291137	R	6.47	70	23	17	75	25.0	1	42.450	144.380
50	200309291650	N	5.40	67	42	48	63	33.0	2	42.390	143.940
51	200309292322	R	5.48	79	34	17	74	33.0	4	42.040	144.370
52	200310080241	R	5.15	66	28	27	64	33.0	3	42.460	144.660
53	200310081807	R	6.68	67	28	19	74	32.0	3	42.650	144.570
54	200310082232	R	5.85	74	28	21	75	33.0	4	42.230	144.720
55	200310090815	R	5.79	76	27	12	80	33.0	4	42.210	144.690
56	200310151630	SS	5.22	72	26	45	78	77.0	4	35.460	139.870
57	200310311006	R	7.00	64	26	9	81	10.0	3	37.810	142.620
58	200311242118	N	5.32	74	43	42	73	33.0	2	42.350	143.010
59	200312301635	SS	5.40	76	49	56	76	48.0	4	43.040	146.900
60	200401231801	R	5.31	67	23	25	66	64.0	4	37.260	140.990
61	200402041508	R	5.20	46	44	42	48	62.0	4	40.150	141.690
62	200406110312	R	5.78	66	25	39	54	49.0	2	42.400	142.960
63	200407171510	SS	5.59	81	60	62	83	46.0	2	34.750	140.220
64	200408101513	R	5.65	70	20	22	68	69.0	4	39.630	141.960
65	200409051907	R	7.23	52	38	38	53	15.0	1	33.085	136.704
66	200409101322	R	5.00			37	55	53.0	4	42.354	143.106
67	200410062340	R	5.75	64	27	31	60	64.0	2	35.950	139.920
68	200410080426	R	5.17	64	28	34	59	48.0	2	42.410	143.040
69	200410231756	R	6.59	47	43	34	56	16.0	1	37.230	138.780
70	200411042303	R	5.80	89	14	15	84	61.0	4	43.620	146.810
71	200411270742	R	5.64	69	24	31	62	58.0	4	42.380	142.900
72	200411290332	R	7.01	67	24	26	68	39.0	2	43.010	145.120
73	200412062315	R	6.77	64	26	24	71	35.0	3	42.900	145.230

EQ No.	EQ Date	Focal Mech.	Mw	NDip1	NDip2	HVDip1	HVDip2	Depth	ST	Latitude	Longitude
74	200501062200	R	5.38	72	18	30	61	61.4	4	41.457	142.104
75	200501182309	R	6.22	64	27	32	64	49.8	4	42.876	145.007
76	200501311839	R	5.41	60	35	27	63	47.5	4	41.764	143.818
77	200502262137	R	5.69	48	43	43	49	44.7	4	40.685	142.596
78	200503120347	R	5.44	68	27	38	64	60.9	4	43.012	144.860
79	200504110722	R	5.96	74	18	24	67	51.5	4	35.727	140.621
80	200504200611	SS	5.48	90	76	83	89	13.5	1	33.678	130.288
81	200506200115	R	5.70	72	18	28	62	50.4	4	35.661	140.516
82	200508161146	R	7.22	69	22	16	74	40.8	4	38.258	142.042
83	200510161605	R	5.06	70	21	30	62	47.1	2	36.039	139.938
84	200510222212	R	5.54	69	22	28	63	55.3	4	37.148	140.957
85	200512022213	R	6.50	71	19	20	70	40.3	4	38.073	142.354
86	200604102026	R	5.16	64	32	30	67	120.7	4	43.685	144.798
87	200604131327	R	5.32	66	26	31	59	47.0	3	41.841	142.748
88	200607060208	R	5.30	73	18	29	64	35.8	2	40.150	142.431
89	200609260703	R	5.29	58	55	57	60	76.0	4	33.515	131.635
90	200611222015	SS	5.65	85	41	43	86	97.4	4	44.153	146.777
91	200612310734	R	5.01	*38*	*56*	38	56	46.0	4	43.261	146.259
92	200703250942	R	6.71	66	48	40	52	8.0	1	37.339	136.555
93	200703301805	SS	5.58	87	34	38	87	103.3	4	44.144	146.075
94	200704190007	SS	5.54	84	60	53	80	119.2	4	42.675	141.907
95	200705190100	R	5.46			31	59	67.5	4	41.563	142.053
96	200707011312	N	5.81	80	22	25	79	131.9	4	43.544	144.909
97	200707161013	R	6.66	49	42	30	60	12.0	1	37.541	138.497
98	200710090210	R	5.70	47	44	43	47	40.0	4	43.353	146.727

EQ No.	EQ Date	Focal Mech.	Mw	NDip1	NDip2	HVDip1	HVDip2	Depth	ST	Latitude	Longitude
99	200711262251	R	5.95	71	20	25	66	44.1	4	37.304	141.757
100	200712252304	R	6.10	71	19	24	67	50.0	3	38.526	142.007
101	200802100937	N	5.06	66	24	30	66	94.7	4	34.795	140.237
102	200803080155	R	5.20	68	22	29	61	57.0	4	36.453	140.612
103	200803101044	R	5.10	76	47	31	59	28.7	4	31.764	131.920
104	200803131741	R	5.38	69	32	44	73	59.2	4	43.012	146.567
105	200803241240	R	5.22	70	21	28	62	47.8	3	37.120	141.447
106	200804291426	R	5.80	66	24	29	61	61.7	4	41.463	142.108
107	200805080103	R	6.22	64	26	22	68	35.0	4	36.230	141.770
108	200805080116	R	6.10	68	25	24	67	30.2	4	36.213	141.795
109	200805080145	R	6.88	68	24	15	75	50.6	4	36.228	141.608
110	200805090821	R	5.58	67	27	23	69	68.6	4	36.193	141.976
111	200805110324	N	5.21	64	27	28	65	87.3	4	43.550	145.781
112	200805312328	R	5.02	75	16	26	65	28.0	2	40.063	142.722
113	200806140843	R	6.91	51	41	42	48	12.1	1	39.112	140.763
114	200806162314	SS	5.10	80	48	84	85	1.6	1	39.014	140.733
115	200806260837	R	5.44	69	24	29	61	56.3	4	41.955	142.483
116	200807191139	R	6.95	72	20	16	74	27.5	3	37.559	142.284
117	200807212030	R	5.95	67	23	19	71	30.3	3	37.232	142.105
118	200807221747	R	5.39	80	10	3	88	25.4	3	37.789	142.343
119	200807240026	N	6.82	71	19	18	73	110.0	4	39.824	141.525
120	200808090053	R	5.45	70	21	32	60	51.5	4	41.143	142.285
121	200808221959	R	5.21	67	23	32	58	55.0	4	36.496	140.488
122	200809110921	R	6.80	78	36	15	76	30.0	3	41.998	143.859
123	200809120734	N	5.05	35	59	35	59	42.2	4	42.389	144.739

EQ No.	EQ Date	Focal Mech.	Mw	NDip1	NDip2	HVDip1	HVDip2	Depth	ST	Latitude	Longitude
124	200810300048	N	5.13	67	39	37	73	86.4	4	38.079	141.663
125	200811220044	R	5.19	67	23	35	57	48.4	4	43.212	145.799
126	200812040817	R	5.80	68	22	19	71	25.0	4	38.619	142.851
127	200812041211	R	5.38	66	24	19	71	25.0	3	38.627	142.911
128	200812060503	R	5.57	61	29	17	73	32.0	4	38.561	142.994
129	200812210413	R	5.39	75	18	20	72	20.2	3	36.722	142.046
130	200902010652	R	5.78	76	15	18	72	47.0	4	36.717	141.279
131	200902151824	R	5.74	72	18	26	66	36.0	2	40.250	142.424
132	200902222324	R	5.40	88	34	19	76	33.7	4	41.715	144.217
133	200902280936	SS	5.49	81	41	34	88	112.9	4	42.584	142.188
134	200903072333	R	5.36	66	29	24	66	39.1	4	41.795	143.823
135	200904051836	R	5.80	74	17	24	66	28.0	3	31.929	131.894
136	200904211858	R	5.36	73	18	25	65	45.4	3	37.341	141.588
137	200904280637	R	5.22	69	21	29	61	47.9	4	36.407	141.131
138	200904282021	N	5.28	68	40	31	69	38.1	4	42.590	145.093
139	200906051230	R	6.36	73	17	16	74	31.3	3	41.812	143.620
140	200906061452	N	5.79	63	35	40	68	42.4	4	35.542	141.264
141	200906201152	R	5.35	63	27	18	72	26.0	4	39.090	143.359
142	200906231637	R	5.61	48	47	47	50	38.6	4	38.896	142.533
143	200908011845	R	5.07	69	21	27	63	36.3	3	37.569	141.914
144	200908051251	N	4.99	*25*	*65*	25	65	33.0	4	32.519	132.119
145	200908110507	R	6.23	51	47			23.3	1	34.786	138.499
146	200908130749	R	6.62	68	23	18	76	57.3	4	32.869	140.826
147	200909032226	R	6.22	70	23	23	73	166.7	4	31.126	130.301
148	201003132146	N	5.54	55	35	35	56	77.7	4	37.614	141.472

EQ No.	EQ Date	Focal Mech.	Mw	NDip1	NDip2	HVDip1	HVDip2	Depth	ST	Latitude	Longitude
149	201003141708	R	6.56	69	21	24	66	39.8	3	37.724	141.818
150	201003301003	R	5.78	56	35	39	51	25.2	2	43.192	138.578
151	201006051422	R	5.47	83	17	23	77	62.3	4	43.270	146.868
152	201006131233	R	5.96	47	46	47	49	40.3	4	37.396	141.796
153	201007040433	R	5.09	51	40	46	51	7.1	1	39.025	140.913
154	201007270831	R	5.07	63	33	44	54	25.4	2	38.997	142.308
155	201008101450	R	5.93	73	18			22.0	3	39.410	143.150
156	201009011633	R	5.19	71	19	27	63	42.9	3	37.914	141.871
157	201009040615	R	5.16	56	39			61.3	4	42.743	145.514
158	201009131448	R	5.86	71	19	29	61	63.2	4	41.456	142.122
159	201009280113	SS	5.11	79	76	71	82	98.8	4	43.501	145.760
160	201009291700	R	5.49					7.6	1	37.285	140.026
161	201010142259	R	5.59	66	27	33	61	53.0	4	42.313	143.070
162	201102051056	SS	5.13	84	30	50	82	63.9	4	34.855	140.620
163	201102102203	R	5.46	71	19	26	64	48.3	3	37.159	141.409
164	201102270038	R	5.17	69	22	25	66	42.8	4	37.304	141.844
165	201102270538	R	5.18	53	52	35	58	4.3	1	36.156	137.455
166	201103091145	R	7.36	69	23	12	78	8.3	3	38.329	143.280
167	201103091157	R	6.05	67	23			23.0	3	38.360	142.910
168	201103091305	R	5.45	65	26			35.0	4	38.650	142.750
169	201103091337	R	5.92	66	24			11.3	3	38.607	143.249
170	201103100316	R	6.10	71	19	19	71	28.9	4	38.271	142.879
171	201103100345	R	5.92	66	24	17	73	23.0	4	38.500	143.170
172	201103100624	R	6.49	68	23	19	71	9.3	1	38.172	143.045
173	201103111446	R	9.12	63	27	10	80	23.7	3	38.104	142.861

EQ No.	EQ Date	Focal Mech.	Mw	NDip1	NDip2	HVDip1	HVDip2	Depth	ST	Latitude	Longitude
174	201103111515	R	7.92	59	31	17	73	43.2	4	36.109	141.265
175	201103112037	SS	6.61	87	33			25.0	1	39.240	142.460
176	201103120359	R	6.33	56	38	32	65	8.4	1	36.986	138.598
177	201103120447	SS	6.23	79	63	77	85	10.0	1	40.480	139.050
178	201103120542	SS	5.06	78	63			3.8	1	36.973	138.591
179	201103121953	N	5.72	71	20	24	69	20.5	1	38.998	142.538
180	201103122215	R	6.20	72	23	24	66	40.1	2	37.198	141.426
181	201103122343	R	5.81	81	10	5	85	9.3	1	39.470	142.696
182	201103130825	R	5.80	72	20	18	74	15.2	1	38.012	141.948
183	201103131026	N	6.20	66	43	22	68	11.2	1	35.828	141.972
184	201103141002	SS	5.72	72	63	67	74	31.8	2	36.458	141.125
185	201103141513	N	6.05	88	40	28	76	14.0	1	37.780	142.460
186	201103152231	SS	5.99	70	69	75	80	14.3	1	35.310	138.715
187	201103161252	N	5.86	57	39	34	56	10.0	1	35.837	140.907
188	201103161314	SS	5.39	89	78	82	89	25.3	2	37.535	141.581
189	201103171314	R	6.15	72	20	24	68	31.1	2	40.126	142.412
190	201103172155	N	5.83	52	38	42	48	47.0	4	36.738	141.309
191	201103181701	R	5.37	78	13	24	66	34.6	3	35.822	141.112
192	201103190833	R	5.62	86	5	2	88	36.7	4	39.185	142.421
193	201103190849	N	5.10	59	31	41	50	16.4	1	37.727	141.912
194	201103191856	N	5.86	48	42	44	51	5.4	1	36.784	140.572
195	201103202103	R	5.85	71	21	26	65	47.8	3	39.344	142.048
196	201103221238	R	5.71	81	37	27	79	37.0	4	35.264	141.237
197	201103221819	R	6.25	88	31	16	88	43.0	4	37.316	141.910
198	201103230712	N	5.71	64	27	32	58	7.6	1	37.085	140.788

EQ No.	EQ Date	Focal Mech.	Mw	NDip1	NDip2	HVDip1	HVDip2	Depth	ST	Latitude	Longitude
199	201103241721	R	5.96	73	22	22	71	33.7	3	39.077	142.358
200	201103252036	R	6.25	68	25	24	67	44.7	3	38.729	142.107
201	201103261918	R	5.32	68	22	26	64	49.0	3	38.567	141.892
202	201103280724	N	6.27	67	26	28	65	31.7	2	38.384	142.346
203	201103291954	N	6.23	57	46	29	69	13.4	1	37.409	142.470
204	201103302219	R	5.15	78	13	20	70	50.0	4	36.650	140.932
205	201103311615	R	6.07	70	21	26	65	47.4	3	38.872	142.084
206	201104012058	R	5.97	68	23	26	66	45.2	3	39.336	142.166
207	201104021308	N	5.21	49	42	44	46	41.7	4	38.773	142.097
208	201104072332	R	7.15	37	53	37	53	65.9	4	38.204	141.920
209	201104111716	N	6.69	50	41	39	53	6.4	1	36.946	140.673
210	201104230025	N	5.18	47	43	45	46	21.4	1	37.170	141.195
211	201104231913	R	6.00	56	42	36	54	35.2	4	39.133	143.001
212	201104281828	R	5.61	52	38	41	49	43.5	4	37.413	141.782
213	201104300719	R	5.24	69	21	29	62	44.1	3	38.839	142.114
214	201104301406	N	5.13	68	66	58	59	36.9	2	36.760	141.281
215	201105030626	R	5.12	71	20	25	66	30.7	3	40.057	142.722
216	201105080552	R	5.78	70	22	25	65	33.6	2	40.245	142.501
217	201105140836	R	6.12	68	22	24	66	40.9	3	37.328	141.628
218	201105150730	R	5.15			34	65	48.1	4	42.855	146.312
219	201105150851	R	5.06	55	35	42	49	47.7	4	37.656	141.583
220	201105200946	R	5.81	74	17	25	65	35.9	4	35.802	141.176
221	201105201628	SS	5.09	72	64	56	73	40.7	2	37.452	141.485
222	201105220706	R	5.56	75	22	30	61	48.3	3	35.730	140.644
223	201105241241	R	5.90	71	20	14	77	21.0	3	39.720	143.240

EQ No.	EQ Date	Focal Mech.	Mw	NDip1	NDip2	HVDip1	HVDip2	Depth	ST	Latitude	Longitude
224	201105242049	N	5.00			21	72	44.4	4	36.400	141.122
225	201105312128	R	5.45	69	24	25	66	48.0	3	39.342	142.062
226	201106040100	N	5.44	57	34	40	54	29.6	2	36.990	141.211
227	201106040157	SS	5.00	87	68	63	87	10.5	1	35.096	132.671
228	201106090711	N	5.03			19	71	33.6	2	39.040	142.443
229	201106091938	N	5.45	72	36	54	68	12.6	1	36.497	140.971
230	201106110736	N	5.02			43	47	36.1	4	38.363	142.223
231	201106131550	R	5.12	74	17	21	69	16.3	1	39.947	143.228
232	201106142149	R	5.03	59	50	53	70	73.1	4	43.118	145.362
233	201106142356	R	5.46	84	16	2	90	28.1	2	39.490	142.528
234	201106182031	N	5.85	79	36	23	83	27.7	2	37.618	141.821
235	201106211749	N	5.25	72	18	22	68	21.1	1	35.760	141.474
236	201106222329	R	5.69	68	25	19	72	22.8	1	40.064	142.915
237	201106230651	R	6.76	70	20	22	68	36.4	3	39.948	142.591
238	201106231935	R	5.34	69	23	26	64	57.2	4	38.467	141.608
239	201106250239	R	5.46	68	23	28	62	57.2	4	41.966	142.720
240	201107051918	R	5.05	52	48	38	55	7.3	1	33.991	135.234
241	201107070015	R	5.75	70	20	23	67	76.4	4	36.375	141.788
242	201107080335	R	5.53	47	43	45	45	55.5	4	37.097	141.130
243	201107100957	SS	7.03	84	74	74	75	23.0	4	38.030	143.260
244	201107111329	R	5.25	71	20	25	66	48.2	3	39.342	142.061
245	201107130547	N	5.08			43	49	14.2	1	37.291	141.175
246	201107141310	N	5.02	53	37	44	47	28.6	2	36.896	141.519
247	201107152101	R	5.57	66	24	31	60	66.4	4	36.164	140.083
248	201107191039	N	5.18	73	46	40	76	30.8	2	37.326	141.758

EQ No.	EQ Date	Focal Mech.	Mw	NDip1	NDip2	HVDip1	HVDip2	Depth	ST	Latitude	Longitude
249	201107231334	R	6.37	67	24	24	67	47.2	3	38.874	142.091
250	201107250007	R	5.16	70	22	28	63	44.5	3	38.844	142.118
251	201107250351	R	6.34	69	24	23	67	45.8	3	37.709	141.627
252	201107252055	R	5.63	80	31	13	82	37.0	4	35.245	141.232
253	201107292353	R	5.47	75	16	20	70	16.0	1	36.690	141.870
254	201107310354	R	6.40	58	35	40	55	57.3	4	36.903	141.221
255	201108012244	R	5.74	69	24	25	66	43.1	3	39.816	142.254
256	201108012358	R	5.98	57	47	33	57	22.8	1	34.709	138.548
257	201108112231	N	5.26	67	54	48	69	30.2	2	38.449	142.231
258	201108120322	R	5.93	68	26	26	65	52.3	4	36.969	141.161
259	201108120437	R	5.08	57	45	26	64	27.0	2	34.409	138.083
260	201108170435	R	5.46	74	20	26	66	35.2	2	40.124	142.446
261	201108191436	R	6.32	53	38	35	55	51.2	4	37.649	141.797
262	201108222023	R	5.95	72	22	18	72	12.0	1	36.080	141.690
263	201109070254	R	5.21	83	17	13	86	35.9	3	36.663	141.690
264	201109072229	R	5.09	72	20	25	66	10.2	1	42.261	142.589
265	201109082238	N	5.09	61	30	30	60	39.6	4	37.273	141.924
266	201109151700	R	6.27	77	24	20	70	50.9	4	36.255	141.483
267	201109170426	R	6.70	77	16	19	73	7.4	1	40.259	143.086
268	201109170608	R	6.07	70	20	20	70	3.7	1	40.247	143.213
269	201109170636	R	5.83	71	24	20	71	4.9	1	40.139	143.387
270	201109170741	R	5.73	71	23	22	68	14.8	3	40.276	143.395
271	201109171634	R	5.74	69	22	22	70	7.6	1	40.295	143.209
272	201109181604	R	5.67	76	16	21	69	19.3	3	39.930	143.224
273	201109181939	R	5.10	66	25	26	64	66.5	4	41.936	142.441

EQ No.	EQ Date	Focal Mech.	Mw	NDip1	NDip2	HVDip1	HVDip2	Depth	ST	Latitude	Longitude
274	201109190332	R	5.43	71	20	27	63	48.2	3	37.767	141.608
275	201109212230	N	5.18	58	32	40	53	8.6	1	36.737	140.577
276	201109232212	R	5.23	72	21	26	64	48.3	3	39.340	142.065
277	201110071151	R	5.34	73	18	29	63	67.2	4	41.565	142.058
278	201110101146	R	5.71	69	22	26	64	47.0	3	37.508	141.486
279	201110211703	N	6.19	82	35	43	76	195.5	4	43.794	142.653
280	201110260208	N	5.08			43	55	30.5	2	36.962	141.147
281	201111201023	N	5.07	52	47	44	56	9.0	1	36.711	140.588
282	201111240424	R	6.16	67	23	22	68	45.4	3	37.330	141.613
283	201111241925	R	6.19	70	22	23	67	43.2	3	41.750	142.887
284	201112030555	R	5.22	71	19	25	65	22.0	1	35.352	140.322
285	201112141301	N	5.14	62	35	35	61	48.8	2	35.356	137.244
286	201201121220	N	5.67	58	32	27	64	33.4	2	36.968	141.304
287	201201121437	N	5.45	58	34	42	56	28.1	4	38.377	142.622
288	201201232045	R	5.09	70	21	29	62	51.7	4	37.060	141.191
289	201201260543	R	5.25	66	24	28	62	50.7	4	38.176	141.693
290	201201280743	R	5.28	64	34	34	63	18.2	1	35.489	138.977
291	201201280922	R	5.61	73	23	25	66	36.1	2	40.153	142.427
292	201202082101	R	5.43	50	44	38	55	13.6	1	37.865	138.171
293	201202291800	R	5.42	67	23			43.8	4	37.288	141.677
294	201202292332	N	5.43	72	24			39.3	4	35.336	141.280
295	201203010732	R	5.43	68	23	29	61	55.7	4	36.439	140.626
296	201203100225	N	5.20	53	37	41	50	6.5	1	36.718	140.613
297	201203141809	N	6.98	64	26	45	46	64.0	4	40.775	145.228
298	201203142105	N	6.01	52	48	43	52	15.1	1	35.748	140.932

EQ No.	EQ Date	Focal Mech.	Mw	NDip1	NDip2	HVDip1	HVDip2	Depth	ST	Latitude	Longitude
299	201203160420	R	5.54	60	33	35	65	93.6	4	35.881	139.590
300	201203252222	R	5.20	53	39	41	52	49.5	4	37.676	141.769
301	201203272000	R	6.05	52	51	44	64	20.5	1	39.806	142.334
302	201203301338	R	5.23	70	20	27	63	46.4	3	37.516	141.473
303	201204012304	R	5.78	68	23	26	64	53.0	4	37.077	141.133
304	201204122351	SS	5.49	79	70	76	76	26.8	2	37.452	141.734
305	201204250522	R	5.55	69	22	29	61	43.1	3	35.723	140.679
306	201204291928	R	5.85	77	16	26	65	48.3	4	35.716	140.601
307	201204300002	N	5.44	70	20	26	68	22.7	1	39.742	142.255
308	201205201620	R	6.39	69	29	16	76	11.0	1	39.650	143.160
309	201205240002	R	6.01	71	23	27	64	59.6	4	41.344	142.124
310	201206060431	SS	6.16	85	82	70	83	37.0	4	34.993	141.371
311	201206180532	R	6.34	70	21	24	67	46.8	3	38.875	142.091

Note:

EQ Date: YYYYMMDDHHMM, i.e., year/month/day/hour/minute in Japanese time

FM – Focal mechanism, N – normal, R – reverse, SS – strike-slip

NDip1 – dip angle for the first nodal plane determined by NIED CMT solutions

NDip2 – dip angle for the second nodal plane determined by NIED CMT solutions

HDip1 – dip angle for the first nodal plane determined by Harvard CMT solutions

HDip2 – dip angle for the second nodal plane determined by Harvard CMT solutions

ST – source categories, 1 for shallow crustal, 2 for upper mantle, 3 for slab interface and 4 for slab events

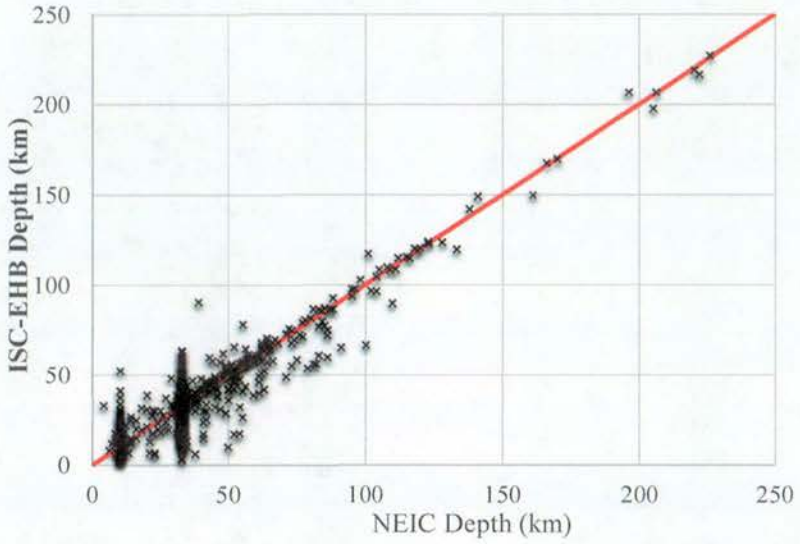

Figure 1.1 Depth correlation between the NEIC and ISC-EHB catalogues for events between 1996 and 2008.

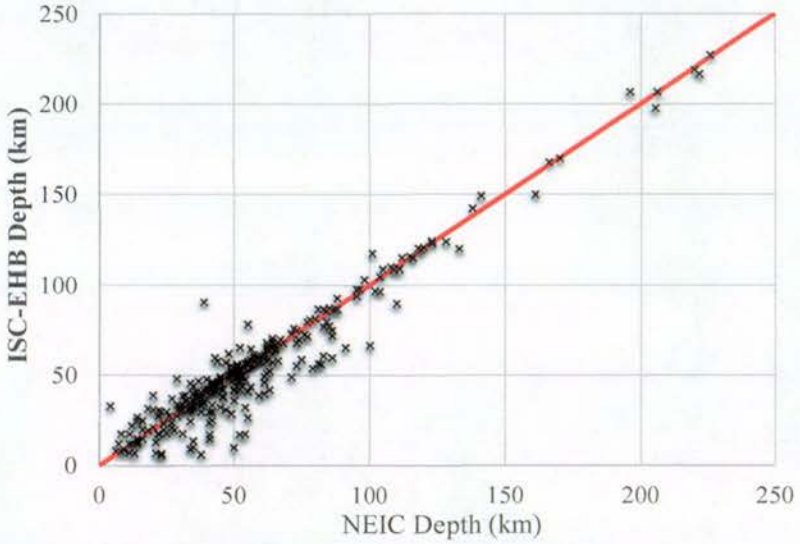

Figure 1.2 Depth correlation between the NEIC and ISC-EHB catalogues excluding the events with a depth fixed as 10 or 33km in the NEIC catalogue for events between 1996 and 2008.

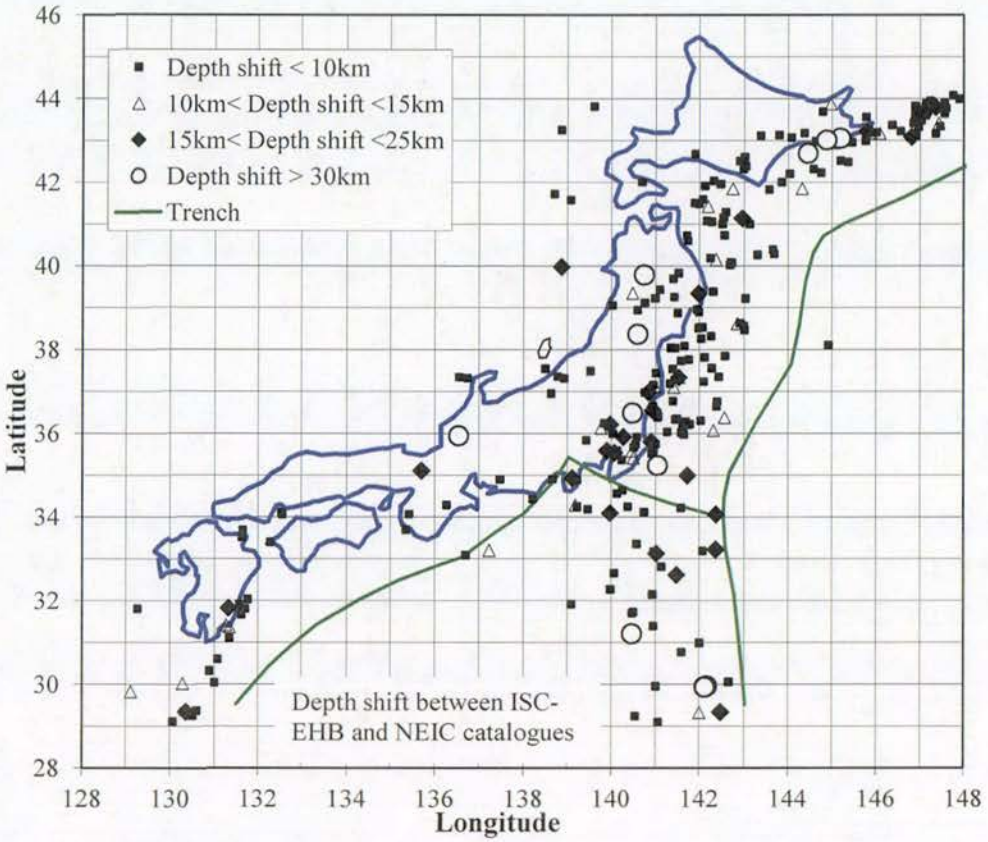

Figure 1.3 Depth shift between the ISC-EHB catalogue and the NEIC catalogue for events between 1996 and 2008.

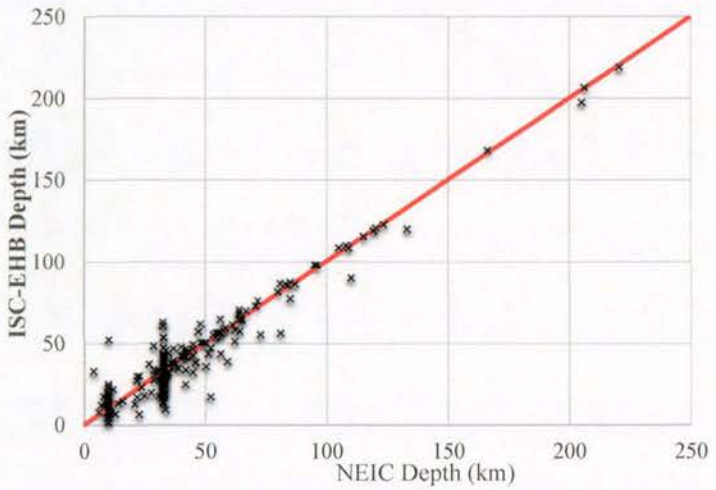

Figure 1.4 Depth correlation between NEIC and ISC-EHB catalogues for those events between 1996 and 2008 with strong-motion records suitable for developing GMPEs.

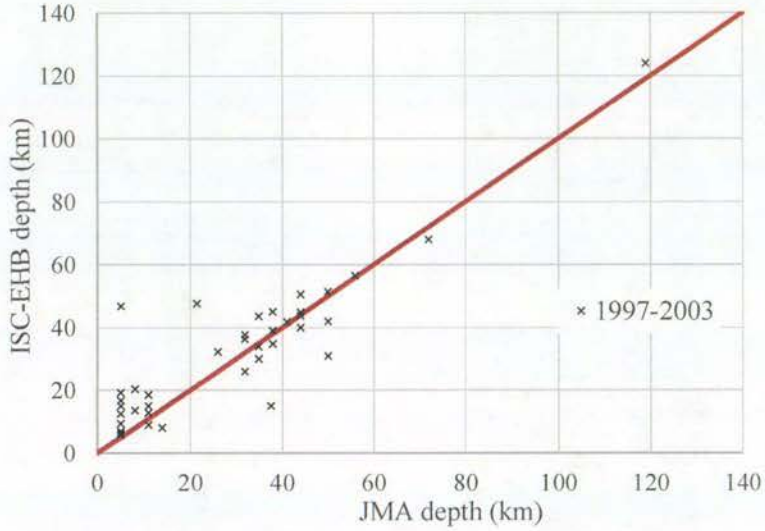

Figure 1.5 Depth correlation between JMA and ISC-EHB catalogues for earthquakes between 1997 and 2003.

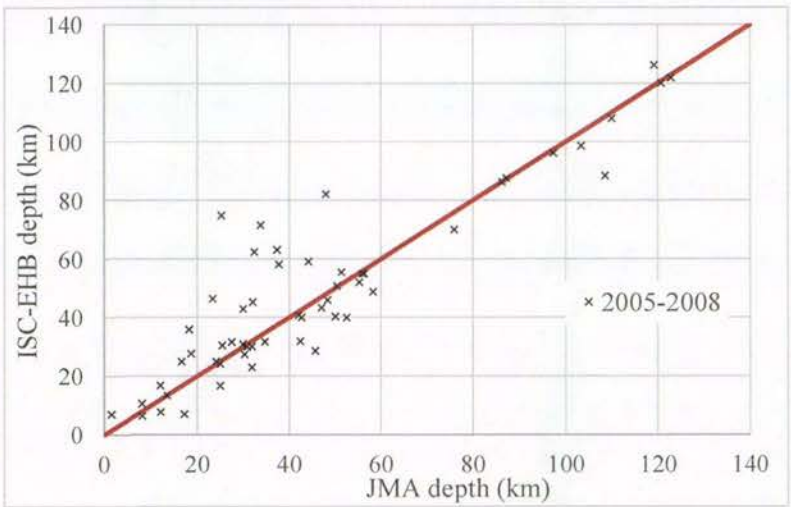

Figure 1.6 Depth correlation between JMA and ISC-EHB catalogues for earthquakes between 2005 and 2008.

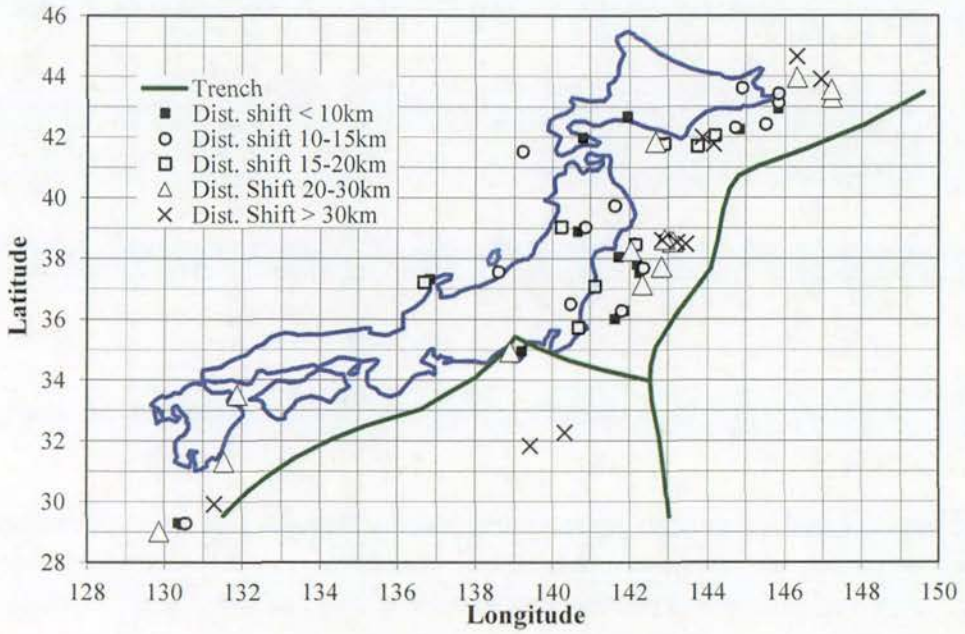

Figure 1.7 Distance shift for the epicentres from JMA and ISC-EHB catalogues for earthquakes between 2005 and 2008.

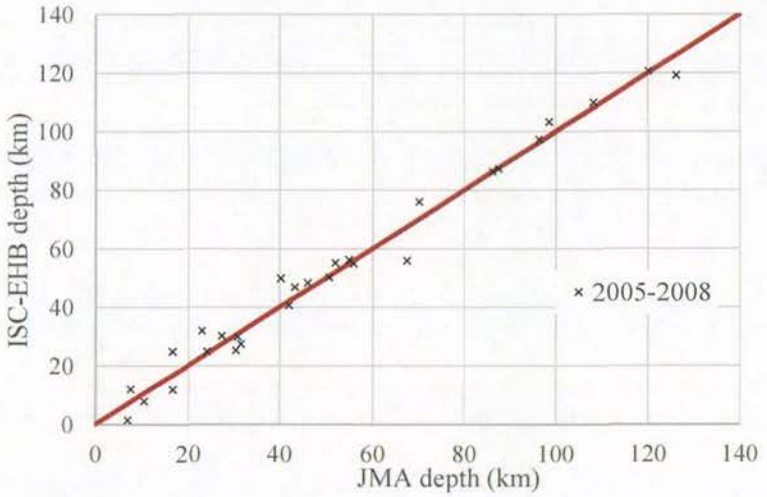

Figure 1.8 Depth correlation between JMA and ISC-EHB catalogues for earthquakes between 2005 and 2008 with strong-motion records that will be used for developing GMPEs for Japan.

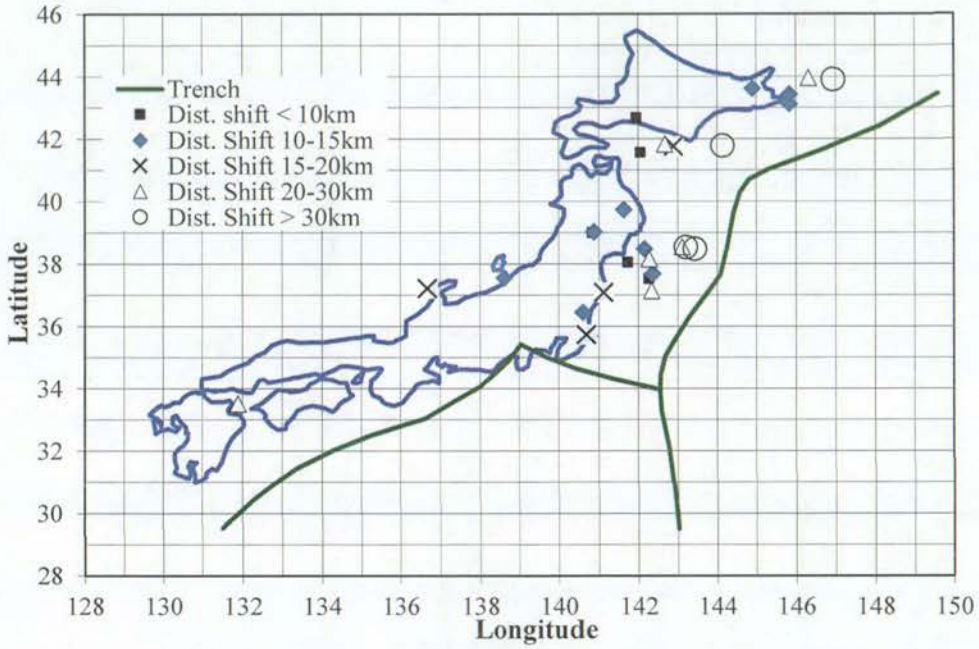

Figure 1.9 Distance shift for the epicentres from JMA and ISC-EHB catalogues for those events between 2005 and 2008 with strong-motion records that will be used to develop GMPEs for Japan.

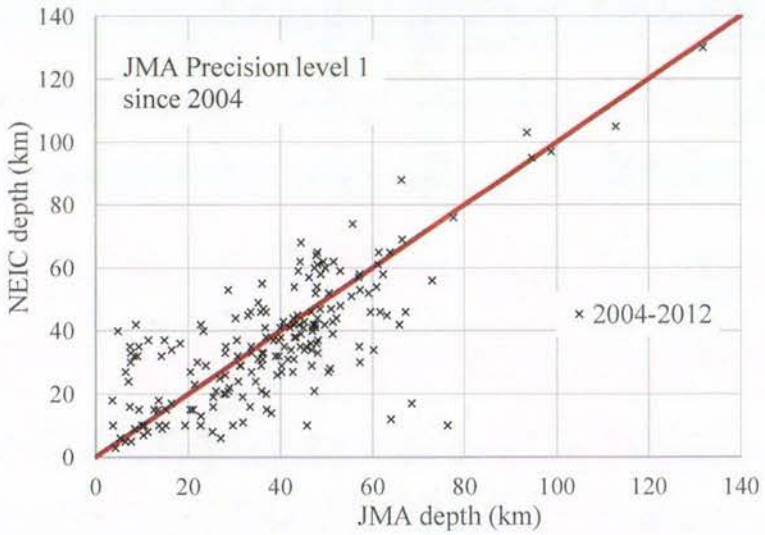

Figure 1.10 Depth correlation between JMA and NEIC catalogues for earthquakes between 2004 and 2012. The large scatter indicates the inconsistent depth estimates from the two catalogues.

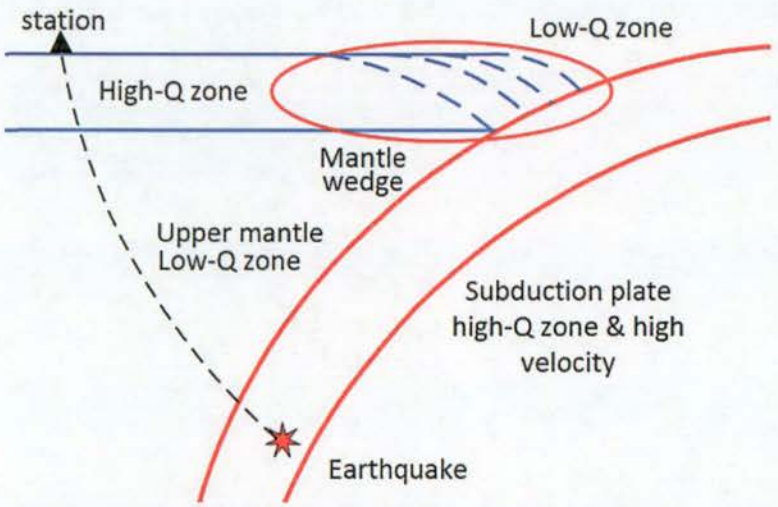

Figure 1.11 The travelling path for seismic waves from a deep subduction earthquake. Most recording stations in Japan are very far from the subduction trench.

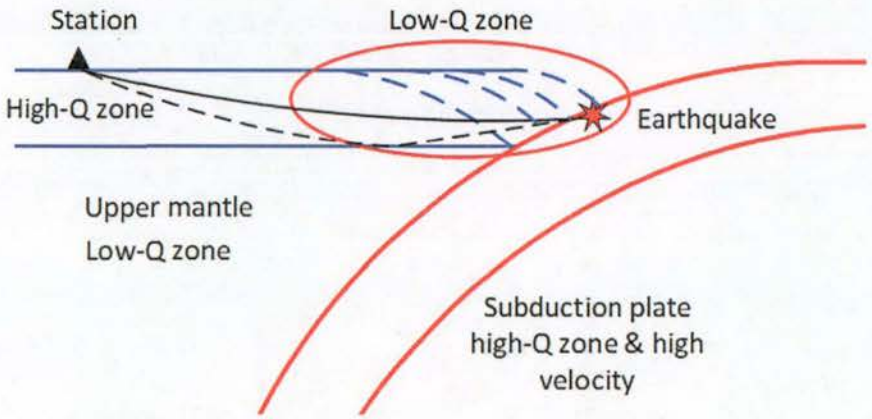

Figure 1.12 Possible Moho reflection for shallow subduction interface events.

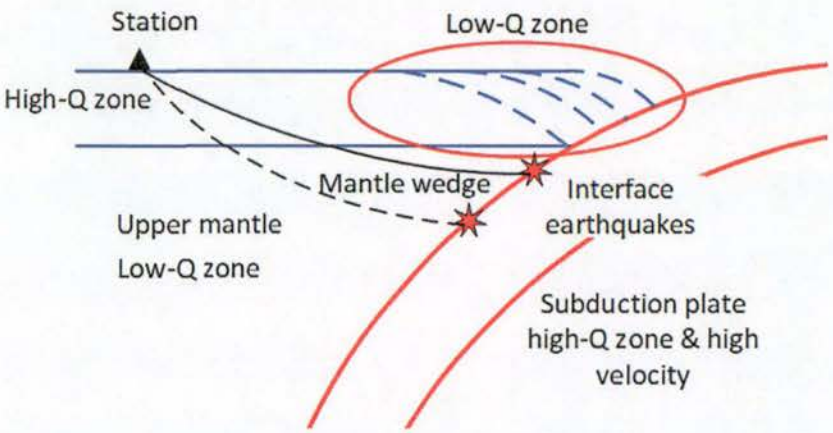

Figure 1.13 The length of the wave propagation path within the mantle wedge increase with increasing depth

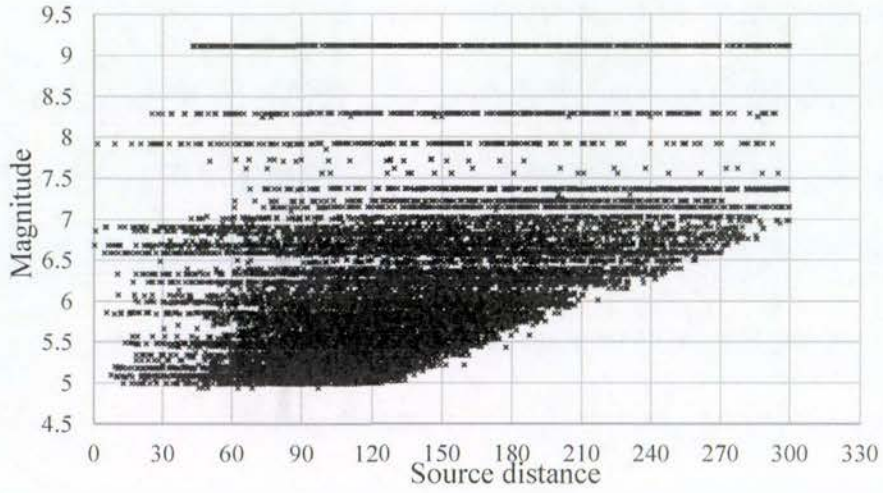

Figure 1.14 Distribution of strong-motion records used in the present study.

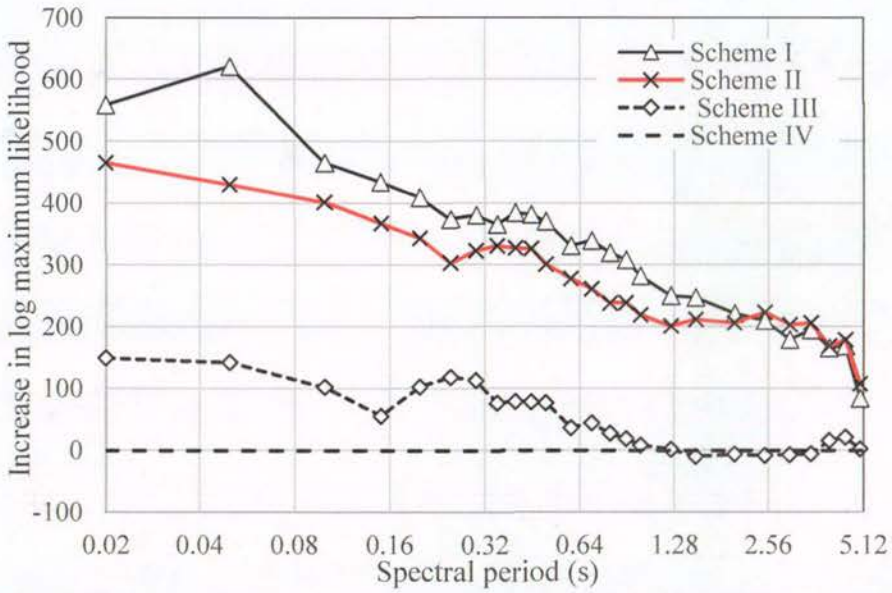

Figure 1.15 Increase in weighted log maximum likelihood relative to scheme IV.

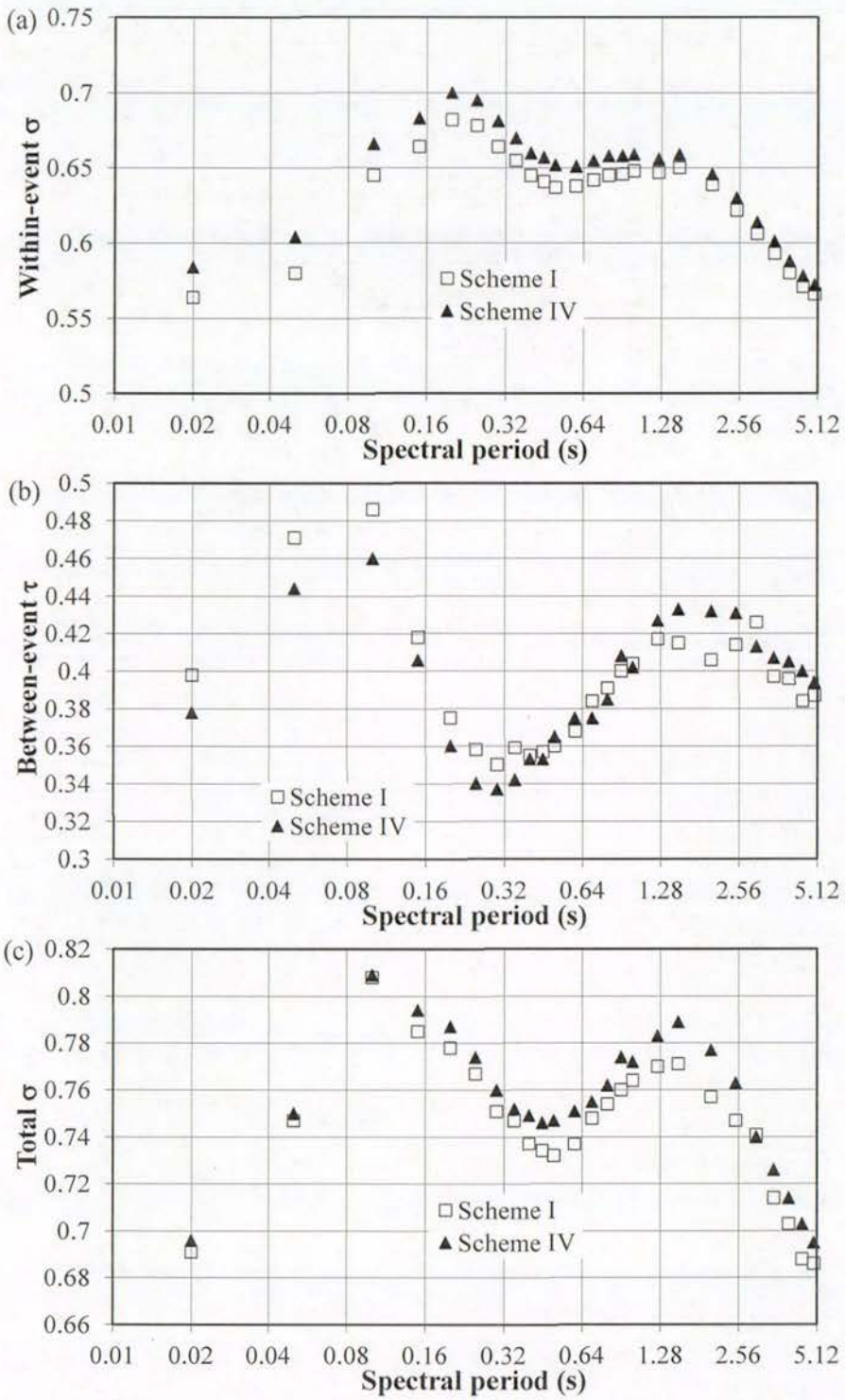

Figure 1.16 Standard deviations from schemes I and IV, (a) within-event, (b) between-event, and (c) total standard deviations.

2.0 NONLINEAR SITE MODELS DERIVED FROM 1-D ANALYSES FOR GROUND-MOTION PREDICTION EQUATIONS USING SITE CLASS AS THE SITE PARAMETER

2.1 ABSTRACT

Nonlinear site models are an important part of ground-motion prediction equations (GMPEs) and can be constructed in a number of ways. If a numerous soil site strong-motion records contain the effect of strong nonlinear soil response, the parameters for the nonlinear model can be a part of the regression parameters for GMPEs. It is also possible to derive nonlinear site models by numerical simulation. However, the number of strong-motion records from Japan that contain the effect of strong nonlinear soil response is still too small to derive nonlinear site terms. We present a model of nonlinear site terms using site class as the site parameter in GMPEs based on a 1-D equivalent linear model. The 1-D model was constructed based on the shear-wave velocity profiles from the Kik-net strong-motion stations with a wide range of site periods, soil depth and impedance ratios. The rock site strong-motion records were from different earthquake categories in Japan and the PEER dataset. Those records had a wide range of earthquake magnitudes, source distances and peak ground accelerations. A random effects regression model was fitted to the calculated spectral amplification ratios accounting for the effect of site impedance ratios, earthquake magnitudes and source distances of the rock site records. We also designed a method to adjust the 1-D model so that it can be used in a GMPE accounting for the fact that a 1-D model is an overly simplistic assumption for many real strong-motion recording stations in many parts of the world.

2.2 INTRODUCTION

Ground-motion prediction equations (GMPEs) are one of most important components of a probabilistic seismic study. Many GMPEs have been developed recently, such as the next generation of attenuation (NGA) models for shallow crustal earthquakes by Abrahamson and Silva (2008), Boore and Atkinson (2008), Campbell and Bozorgnia (2008) and Chiou and Youngs (2008). A number of models for subduction earthquakes have also been developed such as the models by Zhao et al. (2006a), Kanno et al. (2006), McVerry et al. (2006), and many others. All NGA models use the nonlinear models developed either by Choi and Stewart (2005) from strong-motion records, or Walling et al. (2008) using 1-D model analyses. Two models developed based on data from Japan, Zhao et al. (2006a) and Kanno et al. (2006), do not have nonlinear site terms. The Zhao et al. (2006a) study attempted to derive nonlinear site terms from the strong-motion records without success, because few records used in that study contained significant effects of nonlinear soil response. Also the site parameter in the NGA models, V_{S30}, a travel time averaged shear-wave velocity for the top 30m of soil, was not available for most of records used in the Zhao et al. (2006a) study. Also V_{S30} is a controversial site term as described by Zhao and Xu (2013).

During the last decade, a very large number of strong-motion records have been obtained and some of these records from soil sites in California state of US (Choi and Stewart 2005) and Japan (Bonilla et al. 2011, Régnier et al. 2013) exhibit the effects of moderate nonlinear soil response. Choi and Stewart (2005) successfully derived site nonlinear models by using the recorded spectrum divided by the predicted rock site spectrum. Sandıkkaya et al. (2013) used world-wide strong motion records, including the NGA dataset and records from K-net and Kik-net from Japan, to derive a GMPE for rock sites first. Then the site amplification

ratio, the spectrum from a soil site record divided by the rock site spectrum calculated from the rock GMPE, was used to establish a model for nonlinear site effects, in a similar manner to Choi and Stewart (2005). The total standard deviations in the natural logarithm scale from the Sandıkkaya et al. (2013) model is, however, very large, varying in the range 0.78–0.9 in the natural logarithm scale, larger than those for most GMPEs, such as the Zhao et al. (2006a) model. The large standard deviation is probably caused by the use of world-wide data that require different attenuation terms in different regions.

For Japan, the number of strong-motion records with a moderately large PGA is still relatively small, and the usually large model standard deviations, typically 0.7–0.8 in the natural logarithm scale, make it difficult to derive reliable nonlinear site terms for a GMPE from the strong-motion records alone. Also Zhao et al. (2006a) used site classes based on site periods and this site parameter limits the use of strong motion records from other countries where only V_{S30} is available. One way to overcome these problems is to use numerical modelling to derive nonlinear site amplification ratios as done by Walling et al. (2008).

In the present study, we used the soil shear-wave profiles from the Kik-net stations to establish 1-D models, and then carried out an equivalent linear analysis using SHAKE (Schnabel et al. 1972) to compute the soil site surface response. The equivalent linear analysis method is an approximate approach to calculate site response and is known to produce site amplification ratios that differ from those of a true nonlinear analysis. For our purpose, this known difference is probably much less than the within-site variability caused by different frequency contents in different rock site motions (Safak 1997) and therefore this method is reasonable. Another merit of using equivalent linear analyses is that the nonlinear model for SHAKE needs only two parameters for each type of soils: shear modulus reduction and damping ratio curves that are available for many types of soils. For the input motion, a set of rock site strong-motion records from Japan and the NGA dataset was selected. A random effects model (Abrahamson and Youngs 1992) was fitted to the computed response spectral amplification ratios.

Numerically simulated data show that many features that are unable to be quantified from the strong-motion records will have significant impact on the model derived from the simulated records. For example, one of the important parameters in a 1-D analysis is the impedance ratio. The amplification ratio usually increases with increasing impedance ratio. However, this parameter has never been used in any GMPE, probably because of its poor definition, for example, which layer we should use to define the impedance ratio for a multiple-layered soil site. The second reason for not using it is the usually large variability of a GMPE that can bury the effect of the impedance ratio. Another arguable feature of the simulated amplification ratios is that response spectral amplification ratios depend on the earthquake magnitude and source distance of the rock site records (Zhao et al. 2009 and Zhao and Zhang 2010). The physical reason for this feature is the frequency content of the rock site records (Safak 1997). The magnitude and source distance are the parameters reflecting the frequency content. These parameters can either be simply ignored, or modelled properly and then implemented in a reasonable way in a GMPE. We take the second approach. This will guarantee the best estimates for all model parameters, including the parameters that control the nonlinear effect. When we incorporate the 1-D model we can simply take the average magnitude, source distance and impedance ratio from the simulated data, if these parameters are not statistically significant in the GMPE.

A 1-D model is a highly ideal simplification of real sites. Even among over 600 Kik-net stations, the surface/borehole spectral ratios from only a small number of sites clearly have the characteristics of a 1-D model. Our evaluation suggests that the peak periods of the surface/borehole records tend to be less than the site period calculated by a 1-D assumption for the Kik-net stations; we propose that the shorter site period from surface/borehole spectral ratio than the 1-D site model is likely caused by 2-D and/or 3-D effects. Using 1-D amplification ratios in a GMPE without an appropriate modification is clearly not reasonable. We designed a model adjustment method to incorporate the 1-D amplification ratios into a GMPE to compensate for the limitations of a 1-D model.

In this study, we used site-period-based site class as the site parameter. Table 2.1 presents the site class definition and the approximately corresponding NEHRP site classes (BSSC 2000).

2.3 SOIL SITES AND NONLINEAR MODEL SELECTIONS

In the present study, we used the shear-wave velocity profiles from 293 soil sites of the strong-motion recording stations in the Kik-net. The site classes are defined in Table 2.1. Note that we have divided SC IV sites into two sub-classes: SC IV1 sites and SC IV2 sites. Among the soil sites, we used 35 SC I sites, 54 SC II sites, 40 SC III sites and 164 SC IV sites. Among the SC IV sites, 84 are SC IV1 sites with a site period range of 0.6–1.0, and 80 are SC IV2 sites with a site period larger than 1.0s. Note that many SC I sites from Japan are not rock sites and only those sites with a shear-wave velocity of 760m/s or larger at the surface are taken as the engineering bedrock sites. The site period in Table 2.1 is four times the travel time for shear waves propagating vertically through the soil layers above the engineering bedrock. A small number of the Kik-net stations have a very small shear-wave velocity, much less than 80m/s for the surface layer with a thickness of 1–2 meters. These very small shear-wave velocities may be due to measurement errors. We used 100m/s as the minimum soil shear-wave velocity for surface soil layers.

In theory, site amplification ratios strongly depend on impedance ratios between soil layers and the underlying bedrock (Schnabel et al. 1972). For a single layer overlying bedrock, an impedance ratio I_m can be defined by

$$I_m = \frac{\rho_R V_R}{\rho_S V_S} \tag{2.1}$$

where ρ denotes mass density and V denotes shear-wave velocity. The subscript R stands for bedrock and S for soil. For a site with multiple layers, it would be difficult to define a single parameter as the proxy for impedance ratio. For a GMPE, we need only a parameter that is simple and available, and therefore we used the following definition for an approximate impedance ratio,

$$I_m = \frac{V_R}{V_{Site}}$$
$$T_o = \frac{4H}{V_{Site}} \tag{2.2a, b, c}$$
$$I_m = \frac{V_R T_o}{4H}$$

where V_{Site} is the travel time averaged shear wave velocity of the soil layers above the bedrock, T_o is the site period, and H is the depth of bedrock. For a given bedrock shear-wave velocity and site period, the impedance ratio is inversely proportional to the bedrock depth. This means that for a long period site with a shallow bedrock depth the impedance ratio is likely to be large, and for a long period site with a large thickness of soil layers the impedance ratio is likely to be small. Figure 2.3(a) shows the distribution of soil site with respect to site period and impedance ratio. Figure 2.3(b) shows the soil site distribution with respect to site period and bedrock depth; the two parameters are strongly correlated. The depth range is very large. Figure 2.3(c) shows the soil site distribution with respect to impedance ratio and bedrock depth; the site with a large impedance ratio tends to have a shallow depth as indicated by the trend line. The parameter ranges selected in the present study would cover most real engineering sites.

We selected 9 sets of soil shear modulus reduction curves and damping ratio curves, a model for soft rocks , 5 clay models for PI=0, 15, 30, 50 and 100 (Vucetic and Dobry 1991), and 3 models for sands (Iwasaki et al. 1978 for 3 different values of effective mean principle stress, and Seed et al. 1986). Figure 2.4 shows the clay models and Figure 2.5 shows the sand models and soft rock model. For each soil layer, the nonlinear model was selected based on the depth and the shear-wave velocity of the layer but also based on a random selection within a given range in order to capture the variability of soil material parameters. Generally, a model with a less rapid reduction in shear modulus was selected for soil layers with a high shear-wave velocity and/or a large depth. For soil layers with a shear-wave velocity over 600m/s, the model for soft rock was selected.

For 530 soil sites subjected to 293 components, a total of 155,290 sets of amplification ratios were obtained. However, a small number of models failed to converge in the equivalent linear analysis and these amplification ratios are not used. Each rock site record has a maximum usable period within which the signal/noise ratio is reasonably large. When the maximum usable period of a rock site record is equal to or larger than the spectral period, the results are not included.

2.4 STRONG-MOTION DATASET FROM ROCK SITES

We selected 530 components (two horizontal components for each record if available) of rock site strong-motion records from 98 earthquakes. Table 2.2 presents the number of earthquakes in each category for the rock site records. Figure 2.1(a) shows the distribution of earthquakes with respect to moment magnitude and fault depth defined as the depth of the fault top edge for events with available fault rupture plane and the focal depth for other events. Table 2.3 shows the number of components from rock site records in each tectonic category and Figure 2.1(b) shows the distribution of the rock site strong-motion records with respect to moment magnitude, and source distance defined as the shortest distance to the fault plane when available and the hypocentral distance otherwise. Among 530 components of rock site records used in the present study, 294 are from shallow crustal earthquakes, of which 121 are from 24 earthquakes in Japan, and 173 are from 29 earthquakes in the PEER dataset. Among the rock site records from Japan, 54 components are from 16 subduction interface events, 120 are from 16 subduction slab earthquakes and 62 are from 13 upper mantle events with a focal depth over 25km but above the subduction interface in Japan as described in section 1. The rock site strong-motion records are from earthquakes with large magnitude, depth and source distance ranges as shown in Figure 2.1. Figure 2.2 shows the distribution of rock site records with respect to magnitude and peak ground accelerations (PGAs). The records have a wide PGA range. Most records with a PGA over 1.0g in

Figure 2.2 are from large events and were scaled up by a factor of 2.0 so as to constrain the model behaviour at extremely large soil nonlinear response, though we do not have a theoretical justification for the scaling.

Note that some rock site records have only one horizontal component.

2.5 MODEL SELECTION FOR RESPONSE SPECTRAL AMPLIFICATION RATIOS

We used the following models to describe the nonlinear site amplification ratios,

$$\log_e(A_m) = c_1 \log_e(S_R^{\alpha} + \beta) + c_2 \quad \textbf{(2.3)}$$

where A_m is the response spectral amplification ratio, and S_R is the rock site spectrum. Coefficients c_1 and c_2 are linear regression terms; α and β are nonlinear regression terms. McVerry et al. (2006) suggested that Equation (2.3) can be derived from a hyperbolic nonlinear stress and strain relationship when α = 1.0. Equation (2.3) has also been used by Sandıkkaya et al. (2013) with α = 1.0. Coefficient α is used to improve the modelling of amplification ratios for soil sites with a relatively thin soil layer where nonlinear soil response occurs only at very large rock spectrum values. We first fitted Equation (2.3) to the response spectral amplification ratios for each site class at each spectral period. We then plotted the distribution of residuals from Equation (2.3) with respect to impedance ratio, the magnitude and source distance for rock site records. Next we plotted a trend line to the residuals, for example, as a function of impedance ratio. If the linear trend line does not equal zero at the full range of the parameter and the slope is statistically significant at a significance level of 5%, this variable is included as a linear term in the empirical model. However, we fully recognize the fact that parameters such as impedance ratios are not available for most strong-motion recording stations, except for Kik-net and a small number of borehole arrays in the other countries. The strategy adopted in the present study is to model every parameter that is statistically significant, so that the parameters controlling nonlinear amplification ratios can be best estimated. When the parameters are unlikely to be available for soil sites, we can then take the average value for the parameter in our dataset. The impedance ratio is given here as an example.

We found that the effect of impedance ratio was statistically significant at many spectral periods. Physically, the impedance ratio will affect the amplification ratios in two ways:

1. the site elastic amplification ratio increases with increasing impedance ratios; and
2. at large excitation, impedance ratio would enhance the effect of soil nonlinear response and may reduce the amplification ratios at a range of spectral periods.

We used the following equation to model the effects of the impedance ratio

$$\log_e(A_m) = c_1 \log_e\left(S_{Reff}^{\alpha} + \beta\right) + c_3 ln(I_m) + c_2$$

$$I_{mf} = \frac{1}{\varphi}\begin{cases} 1.0 & if\ I_m \le I_{min} \\ 1.0 + \gamma(I_m - I_{min}) & if\ I_{min} > I_m \le I_{max} \\ 1.0 + \gamma(I_{max} - I_{min}) & if\ I_m > I_{max} \end{cases} \quad \textbf{(2.4a, b, c)}$$

$$S_{Reff} = I_{mf} S_R$$

where φ, γ, I_{min} and I_{max} are constants. The term $ln(I_m)$ is used to model the effect of the impedance ratios on all levels of rock site spectrum while I_{mf} in Equation (2.4b) is a scale factor applied to the rock spectrum to model the effect of impedance ratio on the nonlinear response (to scale up the rock spectrum when I_{mf} is larger than 1.0). We selected I_{min}=1.0, I_{max}=12.0, and Table 2.4 presents α, β, φ and γ together with the average impedance ratio I_{mav} from the Kik-net stations used in the present study. Figure 2.6 illustrates the scale factor in Equation (2.4b) and parameter γ is always positive.

Zhao et al. (2009) and Zhao and Zhang (2010) found that the numerically simulated amplification ratios of response spectra between soil and rock records depend on magnitude and source distance. We also find the same effects for the amplification ratios in the present study. We use the same residual analysis procedure as for the impedance ratio and add extra terms for magnitude and source distance when statistically necessary. Though site classes are used as the proxy for site response, we also use a term for site period T_o. This is to prevent the effect of the site period from influencing the estimates for critical parameters for modelling the nonlinear site response. Combining all the terms we have a random effects model,

$$\log_e(\mathrm{A}_{mi,j}) = c_1\log_e\left(S_{Reff}^{\alpha} + \beta\right) + c_2\log_e(\mathrm{I}_{mi}) + c_3x_{i,j} + c_4M_{wi,j} + c_5M_{wi,j}\log_e(T_{oi}) + c_6\log_e(T_{oi}) + c_7 + \varepsilon_{i,j} + \eta_i \quad \textbf{(2.5)}$$

where x is the source distance, the closest distance to the fault rupture plane when available and hypocentral distance for the others, and M_w is the moment magnitude. Subscript i denotes the i^{th} site, and j denotes the j^{th} record from the i^{th} site. The random error $\varepsilon_{i,j}$ is the within-site residual with a zero mean and a standard deviation of σ, and η_i is the between-site residual with a zero mean and a standard deviation τ. All terms were subjected to statistical tests using the AIC criterion (Akaike 1974) and the ratio between the mean value for a parameter and its standard deviation. When this ratio is less than 2 it is likely that this term is not statistically significant. We started testing the term that had the smallest mean value/standard deviation ratio. When the term is deleted from the model this term is not statistically significant if the maximum log-likelihood is reduced by less than 1.0. All terms except for the constant term c_7 were smoothed with respect to logarithm of spectral period. We derived one set of models for each site class and we then substituted the average values for impedance ratio and site period in each site class, and the average magnitude and source distance from the rock site strong-motion records in Equation (2.5). Combining all the terms of c_2-c_7 using average values for magnitude, source distance, site periods and impedance ratios of the dataset, the following model can be derived,

$$\log_e(\mathrm{A}_m) = C_1\log_e\left(S_{Reff}^{\alpha} + \beta\right) + C_B$$

$$S_{Reff} = I_{mfav}S_R$$

$$\mathrm{A}_{max} = \exp[C_1\log_e(\beta) + C_B] \quad \textbf{(2.6a, b, c, d)}$$

$$S_{ReffC} = \left[\exp\left(-\frac{C_B}{C_1}\right) - \beta\right]^{1/\alpha}$$

where the average impedance factor I_{mfav} given in Table 2.4 and coefficients C_1 and C_B are presented in Tables 2.5–2.8. A_{max} is the maximum amplification ratio when the rock site spectrum is zero, S_{ReffC} is the cross-over effective rock spectrum at which the amplification

ratio is 1.0. At spectral periods that are not included in Tables 2.5–2.8, nonlinear site terms are not required. For example, for SC II sites, nonlinear soil terms are not required for spectral periods over 0.3s.

Figure 2.7 illustrates the effect of impedance ratio. The PGA amplification ratio at low levels of rock site PGA increases with increasing impedance ratio. The cross-over point, the rock site PGA at which the amplification ratio equals 1.0 as indicated by the thick horizontal line, decreases with increasing impedance ratio because the equivalent rock site PGA is enhanced by the impedance ratio. We noted that the PGA cross-over points in Figure 2.7 are larger than the usually assumed values, for example 0.3–0.4g, for soft soil sites. For an average impedance ratio of about 3 for SC IV sites, the PGA cross-over point is nearly 0.9g and is 0.55g for an impedance ratio of 6. There are two reasons for these large cross-over values. First, the bedrock depth for many Kik-net stations in the SC IV class is usually large, which usually leads to a large average shear-wave velocity for a given site period. The large average shear-wave velocity in turn leads to a small impedance ratio and a relatively weaker soil nonlinear response. The average impedance ratio is small for SC IV Kik-net stations, between 2.5 and 3.5 and the amplification ratio is therefore moderate. Secondly, the bedrock shear-wave velocity in each Kik-net station was used instead of an assumed large value, for example, 1100m/s in the model by Walling et al. (2008). Also the engineering bedrock is assumed to have a shear-wave velocity of 760m/s or larger and the spectral amplification ratio between this type of engineering bedrock site with respect to the rock sites with a surface shear-wave velocity of 1000m/s is considerable, as large as 1.25 on average for our simulated dataset. This amplification ratio would reduce the cross-over point to 0.72 for a deep soil site with a moderate shear-wave velocity, and to 0.44 for a site with an impedance ratio of 6. Though our model captures the variability caused by impedance ratios from real sites, we recommend that the model with an impedance ratio larger than the average value for the Kik-net stations be used for shallow soft soil sites.

Figure 2.8(a) shows the within-site standard deviation and Figure 2.8 (b) shows the between-site standard deviations for four site classes. The within-site standard deviation contains the variability from the frequency content of the rock site records (Safar 1997) which is a function of earthquake magnitude and source distance (Zhao et al. 2009, Zhao and Zhang 2010). For SC I, II and III sites, the within-site standard deviation varies between 0.15 and 0.25 in a natural logarithm scale, and the standard deviation for SC IV sites are much larger than those for the other site classes. The between-site standard deviations are generally smaller than the within-site standard deviations and again SC IV sites has the largest standard deviations, probably caused by the wide site period range in this site class.

We attempted to divide SC IV sites into two sub-classes: SC IV1 for site periods between 0.6 and 1.0s and SC IV2 for site periods over 1.0s. Figure 2.9(a) compares the within-site standard deviations for SC IV and the two sub-site classes. The standard deviations for SC IV1 sites are significantly smaller than those for SC IV sites but the standard deviations for SC IV2 are similar or slightly larger than those of SC IV sites. It is the same case for between-site standard deviations as shown in Figure 2.9(b): the standard deviations for SC IV1 sites are significantly smaller than those of the SC IV sites while the standard deviations for SC IV2 sites are generally larger than those from the SC IV sites. The larger standard deviations in SC IV2 sites than those of the SC IV1 site are caused by the large site period range for SC IV2 sites (from 1.0s to 4.5s), in the present study as shown in Figure 2.3(b). We expect that using site period, instead of site classes, as the site parameter would significantly improve the nonlinear models.

2.6 ADJUSTMENT OF MAXIMUM AMPLIFICATION RATIOS BY GMPE DATA

A 1-D model is unlikely to be suitable for most of stations and the use of Equation (2.6) as a nonlinear term in a GMPE without modification may not be appropriate.

Though there is a moderately large number of strong-motion records with a PGA over 0.15g from soil sites which may have developed nonlinear response, the large variability of a GMPE, typically about 0.7–0.8 in the natural logarithm scale, would essentially bury the nonlinear site effect. We attempted to rearrange the model parameters and to separate the model parameters into two terms: the first term that is essentially controlled by the most strong-motion records without significant nonlinear response, and the second term that is essentially controlled by nonlinear soil response. Equation (2.6) can thus be rewritten as,

$$\log_e(A_m) = \log_e(A_{max}) \frac{\log_e\left(S_{ReffC}^{\alpha}+\beta\right)-\log_e(S_{Reff}^{\alpha}+\beta)}{\log_e\left(S_{ReffC}^{\alpha}+\beta\right)-\log_e(\beta)} \quad \textbf{(2.7)}$$

where A_{max} is the maximum amplification ratio when S_R is zero, S_{ReffC} is the effective crossover point that separate the amplification range from the deamplification range of the effective rock site spectrum. There are probably a number of ways to adjust the 1-D model in Equation (2.7). For example, the simplest one would be the use of the linear site amplification ratios derived in a GMPE to replace A_{max} in Equation (2.7) as shown in Figure 2.10(a) and Figure 2.10(b). However, this method will significantly shift the cross-over point.

Zhang and Zhao (2009) compared the response spectral amplification ratios between 1-D and 2-D sites. They found that a 2-D basin has much larger amplification ratios at small and weak excitations, while the amplification ratios for a 1-D model and 2-D basin are similar at strong shaking when strong nonlinear soil response develops. Also, nonlinear response in a 2-D basin tends to occur at a much smaller rock site spectrum than in a 1-D model with identical soil properties (Figure 4, Zhang and Zhao 2009). We propose the following adjustment method. First, we apply a scale factor S_F to Equation (2.7) to match the maximum amplification ratios from a GMPE, i.e., moving the 1-D model up as illustrated in Figure 2.10 (a) by using the following equation,

$$\log_e(A_{Nm}) = \log_e(A_{max}) \frac{\log_e\left(S_{ReffC}^{\alpha}+\beta\right)-\log_e\left(S_{Reff}^{\alpha}+\beta\right)}{\log_e\left(S_{ReffC}^{\alpha}+\beta\right)-\log_e(\beta)} + \log_e(S_F) \quad \textbf{(2.8a, b)}$$

$$S_F = \frac{A_{Nmax}}{A_{max}}$$

The maximum amplification ratio from Equation (2.8a) is A_{Nmax} from the GMPE, and A_{max} is the maximum amplification ratio from the 1-D model. The new cross-over point from Equation (2.8a) can be calculated by,

$$\log_e(S_{NC}^{\alpha}+\beta) = \frac{\log_e(A_{Nmax})}{\log_e(A_{max})}\left[\log_e\left(S_{ReffC}^{\alpha}+\beta\right)-\log_e(\beta)\right]+\log_e(\beta)$$

$$S_{NC} = \left\{\exp\left[\frac{\log_e(A_{Nmax})\log_e\left(S_{ReffC}^{\alpha}+\beta\right)-\log_e(S_F)\log_e(\beta)}{\log_e(A_{max})}\right]-\beta\right\}^{\frac{1}{\alpha}} \quad \textbf{(2.9a, b)}$$

Then we use a scale factor to move the new curve in Figure 2.10(b) to the left by,

$$S_{MR} = S_{Reff}\frac{S_{NC}}{S_{ReffC}} \tag{2.10}$$

Finally we obtain the following amplification ratios:

$$\log_e(A_N) = \log_e(A_{max})\frac{\log_e\left(S_{ReffC}^{\alpha}+\beta\right)-\log_e\left(S_{MR}^{\alpha}+\beta\right)}{\log_e\left(S_{ReffC}^{\alpha}+\beta\right)-\log_e(\beta)} + \log_e(S_F) \tag{2.11}$$

or

$$\log_e(A_N) = \log_e(A_{Nmax}) - \log_e(A_{max})\frac{\log_e\left(S_{MR}^{\alpha}+\beta\right)-\log_e(\beta)}{\log_e\left(S_{ReffC}^{\alpha}+\beta\right)-\log_e(\beta)} \tag{2.12}$$

where A_N is the amplification ratio described by the solid line in Figure 2.10(c). These transformations also work if the maximum amplification ratio from a GMPE are smaller than that from the 1-D models. Note that Equation (2.12) has the same cross-over point and very similar slope at large rock site spectrum as that given in Equation (2.7).

The crossover rock spectrum cannot be defined when the maximum amplification ratio is less than zero. Also when the amplification ratios is less than about 1.25, S_{Reffc} becomes too small. In this case, we defined a pseudo-crossover point can be calculated by,

$$S_{Reffc} = \frac{C_1(\alpha-1)\log_e(\theta\beta)\log_e(\beta)-C_B\log_e(\theta)}{C_1[\alpha\log_e-\log_e(\beta)]} \tag{2.13}$$

where θ is an arbitrarily large number, for example 10.0. In Equation (2.13) we used an extrapolation method from a straight line on log-log scales. The first point of the straight line has a coordinate for $S_{Reff} = \beta$ and $A_{m1}=A_{max}$. The second point is at $S_{Reff} = \theta\beta$ and the amplification ratios is given by,

$$\log_e(A_{m2}) = \alpha C_1\log_e(\theta\beta) + C_B \tag{2.14}$$

Note that the term "+ β" in Equation (2.14) has been omitted because θ is large. Equation (2.13) can be derived by an extrapolation from (β, A_{m1}) and ($\theta\,\beta$, A_{m2}) to (S_{Reffc}, A_m=1.0).

If A_{Nmax} is less than 1.25, the pseudo-crossover rock spectrum can be calculated from:

$$S_{NC} = \exp\left\{\frac{C_1\,(\alpha-1)\log_e(\beta)\log_e(\theta\beta)-\log_e(\theta)[C_B+\log_e(S_F)]}{C_1[\alpha\log_e(\theta\beta)-\log_e(\beta)]}\right\} \tag{2.15}$$

The adjusted nonlinear amplification ratio can then be calculated from Equations (2.10)–(2.12) using the pseudo-crossover rock spectrum in Equation (2.13) and (2.15). If the maximum amplification ratio for the 1-D model is less than 1.25 but the GMPE amplification ratio is larger the 1.25, S_{Reffc} can be computed from Equation (2.13) while S_{NC} can be calculated from Equation (2.9b). In fact, when the maximum amplification ratio is larger than 1.5, the pseudo-crossover rock spectrum is very similar to the crossover spectrum.

Amplification ratios for different impedance ratios

When the impedance ratios are available, the impedance ratio factor I_{mf} can be calculated from Equation (2.4b) and is presented in Table 2.9 for impedance ratios in a range of 2–8. The corresponding coefficient C_B in Equation (2.6a) is presented in Table 2.10 for SC I, SC II and SC III sites, in Table 2.11 for SC IV sites, In Table 2.12 for SC IV1 sites and in Table 2.13 for SC IV2 sites for 7 values of impedance ratios. A_{max} and S_{ReffC} for the corresponding impedance ratios can be computed from Equation (2.6), and the corresponding adjustment factors can be computed from Equations (2.6–2.12).

2.7 SUMMARY AND DISCUSSIONS

We have used the shear-wave velocity profile of 293 soil sites in the Kik-net stations to construct 1-D soil models. The sites have a large range of site periods, between 0.04s for sites with a thin soil layer and 4.4s for deep soil sites. The depth of the soil sites varies between 2m and 550m and the impedance ratio (defined as the ratio between the bedrock shear-wave velocity and the shear-wave travel time averaged shear-wave velocity of the soil sites) is in the range of 1.5–16. We have selected 530 rock site strong-motion components from 98 earthquakes, with 29 crustal events from the PEER dataset, and 24 crustal events, 16 subduction interface events, 16 subduction slab events and 13 upper mantle events (above the subduction interface but with a depth over 25km) from Japan. Among the 530 components of rock site records, 156 are from the PEER dataset and 340 are from different types of earthquakes in Japan. The peak ground accelerations are in a range between 0.03g and nearly 3.0g (scaled up from records with a PGA over 1.0g). The magnitude range for the rock records is between 5.0 and 9.0, the fault depth range is 3–124km and the source distance range is 0.6–282km. We selected 9 soil nonlinear models and assigned a model for each soil layer based on soil shear-wave velocity and depth and allowing random selection within a given range. We then used SHAKE to carry out equivalent linear analyses and calculated the site amplification ratios. Next we fitted an empirical nonlinear site amplification model to the computed amplification ratios, accounting for the effect of impedance ratios, and magnitude and source distance of the rock site records. We used a random effects regression method to derive the model coefficients, and carried out statistical tests to ensure all the coefficients were statistically significant. We used the average values for impedance ratio, magnitude and source distance to derive the 1-D model for nonlinear site amplification ratios. We also presented the nonlinear site model for 7 impedance ratios. We recommend that a larger impedance ratio than the average one from the Kik-net stations be used for shallow soft soil sites. Finally, we adjusted the model so that it had the maximum amplification ratios at small values of rock spectrum from the GMPEs, but had the same cross-over point and very similar decay slopes of the amplification ratios with respect to the rock site spectrum from the 1-D model at large values of rock spectrum. The adjusted model can be incorporated into a GMPE as nonlinear site terms.

Many Kik-net sites are deep, with soil depths over 50m, and such sites tend to have low impedance ratios and relatively high average shear-velocities for long or moderately long site periods. Such sites tend to develop less significant levels of nonlinear response at a relatively strong rock site spectrum, leading to a nonlinear model with a relatively large cross-over rock site spectrum that separates the amplification range from the deamplification range. We recommend that a model with a large impedance ratio presented in the present study be used for shallow soft soil sites.

Table 2.1 Site class definitions used in the present study and the approximately corresponding NEHRP site classes (BSSC 2000).

Site class	Description	Natural period	V_{30} calculated from site period	NEHRP site classes
SC I	Rock	$T < 0.2s$	$V_{30} > 600$	A+B+C
SC II	Hard soil	$0.2 \leq T < 0.4s$	$300 < V_{30} \leq 600$	C
SC III	Medium soil	$0.4 \leq T < 0.6s$	$200 < V_{30} \leq 300$	D
SC IV	Soft soil	$T \geq 0.6s$	$V_{30} \leq 200$	E+F
SC IV1		$0.6 \leq T < 1.0s$	$120 < V_{30} \leq 200$	E
SC IV2		$T \geq 1.0s$	$V_{30} \leq 120$	F

Table 2.2 Number of earthquakes from different regions and source categories.

EQ Category	Japan	Other countries	Total
Crustal	24	29	**53**
Subduction Interface	16		**16**
Subduction Slab	16		**16**
Upper Mantle	13		**13**
Total	**69**	**29**	**98**

Table 2.3 Number of components from different regions and source categories.

EQ Category	Japan	Overseas	Total
Crustal	121	173	**294**
Subduction Interface	54		**54**
Subduction Slab	120		**120**
Upper Mantle	62		**62**
Total	**357**	**173**	**530**

Table 2.4 Model parameters for 6 site classes.

Site Class	φ	γ	I_{mav}	I_{mfav}
SC I	3.5	0.8	3.73	0.91
SC II	3.0	1.0	3.07	1.02
SC III	2.5	0.9	2.76	1.03
SC IV	3.0	0.6	3.02	0.74
SC IV1	2.5	0.7	2.88	0.93
SC IV2	2.5	0.5	3.17	0.83
All SC	α=2.0		β=0.6	

Table 2.5 Model parameters for SC I, II and III sites.

Period No.	Spectral period T (s)	$C_B(T)$	$C_1(T)$	S_{effC}	A_{max}
	SC I				
1	PGA	0.577	-0.140	7.850	1.913
2	0.05	0.578	-0.182	4.836	1.956
3	0.1	0.677	-0.121	16.428	2.093
	SC II				
1	PGA	0.537	-0.353	1.996	2.050
2	0.05	0.507	-0.361	1.863	1.996
3	0.1	0.634	-0.222	4.099	2.112
4	0.15	0.695	-0.200	5.628	2.219
5	0.2	0.779	-0.200	6.963	2.413
6	0.25	0.823	-0.200	7.794	2.554
7	0.3	0.785	-0.164	10.919	2.384
	SC III				
1	PGA	0.364	-0.558	1.149	1.914
2	0.05	0.365	-0.492	1.224	1.852
3	0.1	0.526	-0.359	1.931	2.033
4	0.15	0.595	-0.292	2.657	2.104
5	0.2	0.588	-0.259	3.011	2.054
6	0.25	0.529	-0.247	2.810	1.925
7	0.3	0.550	-0.286	2.499	2.006
8	0.35	0.609	-0.332	2.381	2.179
9	0.4	0.643	-0.361	2.311	2.288
10	0.45	0.643	-0.364	2.291	2.291
11	0.5	0.620	-0.347	2.319	2.220
12	0.6	0.550	-0.250	2.900	1.968
13	0.7	0.495	-0.128	6.882	1.752

Table 2.6 Model parameters for SC IV sites.

Period No.	Spectral period T (s)	$C_B(T)$	$C_1(T)$	S_{effC}	A_{max}
	SC IV				
1	PGA	0.0068	-0.807	0.639	1.521
2	0.05	-0.0295	-0.671	0.597	1.368
3	0.1	0.189	-0.555	0.897	1.603
4	0.15	0.303	-0.493	1.118	1.741
5	0.2	0.357	-0.461	1.254	1.809
6	0.25	0.382	-0.449	1.320	1.832
7	0.3	0.396	-0.451	1.344	1.861
8	0.35	0.394	-0.463	1.320	1.886
9	0.4	0.402	-0.482	1.304	1.908
10	0.45	0.382	-0.507	1.235	1.928
11	0.5	0.382	-0.537	1.198	1.945
12	0.6	0.377	-0.606	1.124	1.976
13	0.7	0.352	-0.693	1.030	2.025
14	0.8	0.329	-0.754	0.973	2.043
15	0.9	0.303	-0.784	0.934	2.022
16	1	0.275	-0.788	0.905	1.970
17	1.25	0.246	-0.715	0.900	1.843
18	1.5	0.252	-0.579	0.972	1.729
19	2	0.315	-0.282	1.567	1.583
20	2.5	0.369	-0.0780	10.604	1.504

Table 2.7 Model parameters for SC IV1 sites.

Period No.	Spectral period T (s)	$C_B(T)$	$C_1(T)$	S_{effC}	A_{max}
	SC IV1				
1	PGA	0.235	-0.699	0.895	1.808
2	0.05	0.220	-0.583	0.926	1.678
3	0.10	0.433	-0.467	1.389	1.958
4	0.15	0.494	-0.408	1.661	2.019
5	0.20	0.521	-0.376	1.843	2.041
6	0.25	0.542	-0.360	1.978	2.067
7	0.30	0.525	-0.353	1.956	2.025
8	0.35	0.483	-0.353	1.825	1.941
9	0.40	0.461	-0.327	1.871	1.874
10	0.45	0.455	-0.366	1.693	1.901
11	0.50	0.460	-0.441	1.496	1.984
12	0.60	0.462	-0.597	1.253	2.153
13	0.70	0.451	-0.660	1.175	2.200
14	0.80	0.441	-0.632	1.187	2.146
15	0.90	0.422	-0.550	1.248	2.020
16	1.00	0.403	-0.457	1.346	1.889
17	1.25	0.415	-0.158	3.643	1.641

Table 2.8 Model parameters for SC IV2 sites.

Period No.	Spectral period T (s)	$C_B(T)$	$C_1(T)$	S_{effC}	A_{max}
	SC IV2				
1	PGA	-0.398	-1.170	0.335	1.221
2	0.05	-0.416	-0.936	0.203	1.064
3	0.10	-0.181	-0.748	0.430	1.222
4	0.15	-0.0023	-0.680	0.630	1.412
5	0.20	0.0899	-0.665	0.738	1.537
6	0.25	0.115	-0.678	0.765	1.587
7	0.30	0.157	-0.707	0.805	1.679
8	0.35	0.190	-0.747	0.831	1.771
9	0.40	0.199	-0.792	0.828	1.829
10	0.45	0.180	-0.843	0.799	1.842
11	0.50	0.151	-0.895	0.764	1.837
12	0.60	0.0882	-1.006	0.701	1.826
13	0.70	0.0405	-1.120	0.661	1.845
14	0.80	0.0157	-1.234	0.643	1.908
15	0.90	-0.0083	-1.348	0.628	1.974
16	1.00	-0.0501	-1.461	0.605	2.006
17	1.25	-0.170	-1.734	0.554	2.045
18	1.50	-0.326	-1.994	0.499	1.998
19	2.00	-0.635	-2.478	0.417	1.879
20	2.50	-0.552	-2.201	0.422	1.772
21	3.00	-0.372	-1.740	0.455	1.676
22	3.50	-0.145	-1.186	0.534	1.586
23	4.00	0.0955	-0.635	0.750	1.522

Table 2.9 Factors for impedance ratios.

Site class	Impedance ratio						
	2.0	3.0	4.0	5.0	6.0	7.0	8.0
SC I	0.514	0.743	0.971	1.200	1.429	1.657	1.886
SC II	0.667	1.000	1.333	1.667	2.000	2.333	2.667
SC III	0.760	1.120	1.480	1.840	2.200	2.560	2.920
SC IV	0.533	0.733	0.933	1.133	1.333	1.533	1.733
SC IV1	0.680	0.960	1.240	1.520	1.800	2.080	2.360
SC IV2	0.600	0.800	1.000	1.200	1.400	1.600	1.800

Table 2.10 $C_B(T)$ for various impedance ratios in SC I, SC II and SC III sites.

Spectral period (s) T	Impedance ratio						
	2.0	3.0	4.0	5.0	6.0	7.0	8.0
SC I							
PGA	0.431	0.526	0.594	0.646	0.689	0.726	0.757
0.05	0.444	0.531	0.593	0.641	0.680	0.713	0.742
0.10	0.536	0.628	0.693	0.743	0.785	0.819	0.850
SC II							
PGA	0.418	0.531	0.611	0.674	0.725	0.768	0.805
0.05	0.418	0.502	0.562	0.608	0.646	0.678	0.706
0.10	0.521	0.628	0.704	0.763	0.812	0.852	0.888
0.15	0.554	0.687	0.782	0.855	0.915	0.966	1.010
0.20	0.612	0.770	0.882	0.969	1.040	1.100	1.152
0.25	0.632	0.813	0.941	1.041	1.122	1.191	1.250
0.30	0.572	0.773	0.917	1.028	1.119	1.195	1.262
SC III							
PGA	0.317	0.376	0.418	0.451	0.477	0.500	0.519
0.05	0.348	0.369	0.384	0.396	0.405	0.413	0.420
0.10	0.477	0.539	0.583	0.617	0.644	0.668	0.688
0.15	0.522	0.613	0.678	0.729	0.770	0.804	0.835
0.20	0.528	0.603	0.656	0.698	0.732	0.760	0.785
0.25	0.465	0.545	0.601	0.645	0.681	0.711	0.737
0.30	0.459	0.574	0.655	0.717	0.769	0.812	0.850
0.35	0.471	0.645	0.769	0.865	0.944	1.010	1.067
0.40	0.469	0.688	0.844	0.965	1.063	1.147	1.219
0.45	0.451	0.693	0.865	0.998	1.107	1.199	1.279
0.50	0.429	0.670	0.841	0.973	1.081	1.173	1.252
0.60	0.407	0.586	0.714	0.812	0.893	0.961	1.020
0.70	0.365	0.529	0.645	0.735	0.809	0.871	0.925

Table 2.11 $C_B(T)$ for various impedance ratios of SC IV sites.

Spectral period T (s)	Impedance ratio						
	2.0	3.0	4.0	5.0	6.0	7.0	8.0
PGA	-0.0379	0.0061	0.0372	0.0614	0.0811	0.0978	0.112
0.05	-0.0750	-0.0302	0.0015	0.0261	0.0462	0.0632	0.0780
0.10	0.160	0.188	0.208	0.223	0.235	0.246	0.255
0.15	0.270	0.302	0.325	0.343	0.358	0.370	0.381
0.20	0.306	0.356	0.392	0.420	0.443	0.462	0.479
0.25	0.316	0.381	0.427	0.463	0.492	0.517	0.538
0.30	0.320	0.395	0.448	0.490	0.523	0.552	0.577
0.35	0.308	0.392	0.452	0.499	0.537	0.569	0.596
0.40	0.300	0.406	0.481	0.540	0.588	0.628	0.663
0.45	0.282	0.381	0.451	0.505	0.549	0.587	0.619
0.50	0.276	0.380	0.454	0.511	0.557	0.597	0.631
0.60	0.264	0.375	0.454	0.516	0.566	0.608	0.645
0.70	0.234	0.350	0.432	0.496	0.548	0.593	0.631
0.80	0.209	0.327	0.411	0.477	0.530	0.575	0.614
0.90	0.182	0.301	0.386	0.451	0.505	0.550	0.590
1.00	0.155	0.274	0.358	0.423	0.476	0.521	0.560
1.25	0.132	0.244	0.323	0.385	0.435	0.478	0.515
1.50	0.157	0.250	0.316	0.368	0.410	0.445	0.476
2.00	0.240	0.314	0.367	0.407	0.441	0.469	0.493
2.50	0.302	0.368	0.414	0.450	0.479	0.504	0.525

Table 2.12 $C_B(T)$ for various impedance ratios of SC IV1 sites.

Spectral period T (s)	Impedance ratio						
	2.0	3.0	4.0	5.0	6.0	7.0	8.0
PGA	0.135	0.247	0.326	0.387	0.437	0.480	0.516
0.05	0.121	0.231	0.309	0.370	0.419	0.461	0.498
0.10	0.346	0.443	0.512	0.566	0.609	0.646	0.678
0.15	0.394	0.505	0.584	0.645	0.695	0.737	0.773
0.20	0.410	0.534	0.622	0.690	0.745	0.792	0.833
0.25	0.421	0.556	0.652	0.726	0.787	0.839	0.883
0.30	0.394	0.540	0.644	0.724	0.790	0.845	0.893
0.35	0.343	0.498	0.609	0.695	0.765	0.824	0.875
0.40	0.313	0.478	0.595	0.685	0.759	0.822	0.876
0.45	0.299	0.473	0.595	0.691	0.769	0.835	0.892
0.50	0.297	0.478	0.607	0.706	0.788	0.856	0.916
0.60	0.286	0.482	0.621	0.728	0.816	0.890	0.955
0.70	0.263	0.472	0.621	0.736	0.830	0.910	0.978
0.80	0.257	0.462	0.607	0.719	0.811	0.889	0.956
0.90	0.259	0.441	0.569	0.669	0.750	0.819	0.879
1.00	0.261	0.418	0.530	0.616	0.687	0.747	0.798
1.25	0.312	0.426	0.507	0.570	0.621	0.664	0.702

Table 2.13 $C_B(T)$ for various impedance ratios of SC IV2 sites.

Spectral period T (s)	Impedance ratio						
	2.0	3.0	4.0	5.0	6.0	7.0	8.0
PGA	-0.344	-0.391	-0.425	-0.451	-0.472	-0.490	-0.506
0.05	-0.362	-0.409	-0.443	-0.470	-0.491	-0.509	-0.525
0.10	-0.104	-0.172	-0.220	-0.257	-0.288	-0.313	-0.336
0.15	0.0449	0.0033	-0.0261	-0.0490	-0.0677	-0.0835	-0.0971
0.20	0.117	0.0932	0.0760	0.0627	0.0518	0.0426	0.0346
0.25	0.127	0.117	0.110	0.104	0.100	0.0963	0.0931
0.30	0.154	0.156	0.158	0.159	0.160	0.161	0.162
0.35	0.176	0.188	0.197	0.204	0.210	0.214	0.219
0.40	0.175	0.196	0.211	0.223	0.233	0.241	0.248
0.45	0.148	0.177	0.197	0.213	0.226	0.237	0.246
0.50	0.111	0.146	0.171	0.190	0.206	0.219	0.231
0.60	0.0362	0.0820	0.115	0.140	0.160	0.178	0.193
0.70	-0.0209	0.0331	0.0715	0.101	0.125	0.146	0.164
0.80	-0.0529	0.0075	0.0504	0.0836	0.111	0.134	0.154
0.90	-0.0858	-0.0176	0.0308	0.0683	0.0990	0.125	0.147
1.00	-0.141	-0.0610	-0.0045	0.0394	0.0752	0.105	0.132
1.25	-0.282	-0.184	-0.114	-0.0595	-0.0152	0.0223	0.0548
1.50	-0.438	-0.340	-0.270	-0.216	-0.171	-0.134	-0.101
2.00	-0.733	-0.647	-0.586	-0.538	-0.499	-0.466	-0.438
2.50	-0.638	-0.562	-0.509	-0.467	-0.433	-0.404	-0.380
3.00	-0.440	-0.381	-0.338	-0.306	-0.279	-0.257	-0.237
3.50	-0.198	-0.151	-0.118	-0.0922	-0.071	-0.0535	-0.0381
4.00	0.0523	0.0903	0.117	0.138	0.155	0.170	0.182

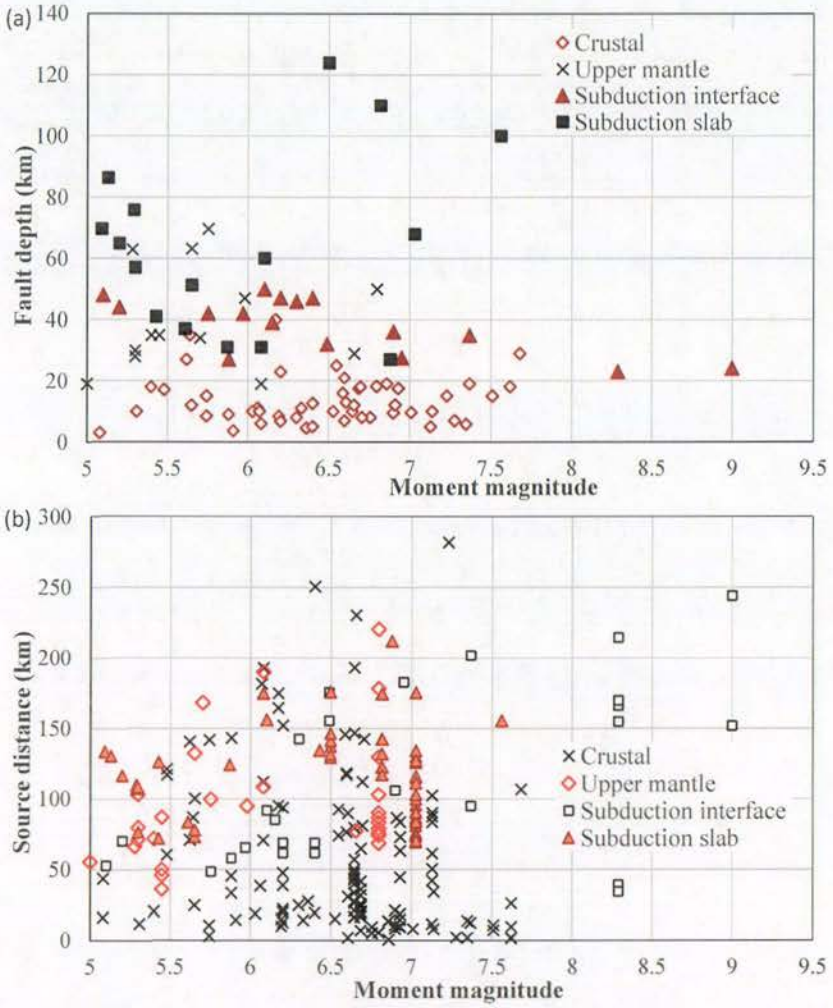

Figure 2.1 The distribution of earthquakes used in the present study with respect to moment magnitude and fault depth in (a) and the distribution of strong-motion records with respect magnitude and source distance in (b).

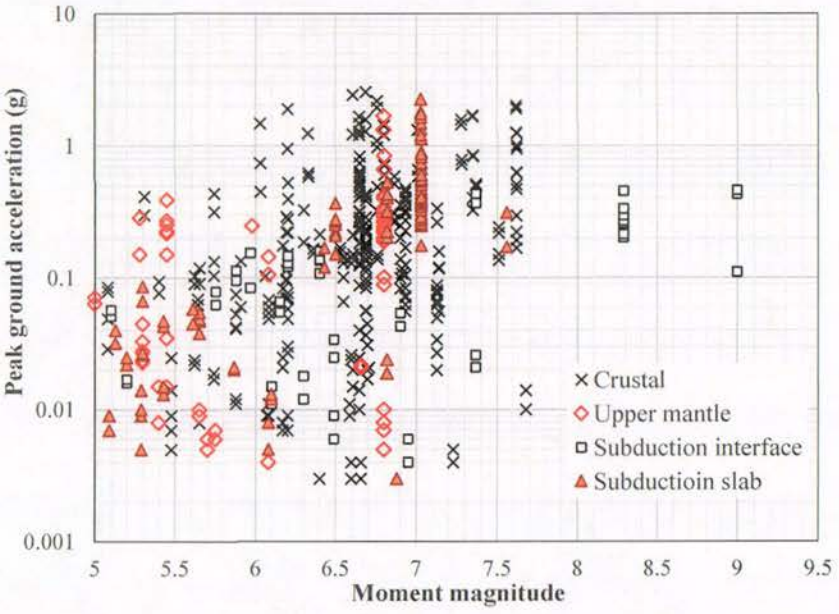

Figure 2.2 The distribution of strong-motion records with respect magnitude and PGA.

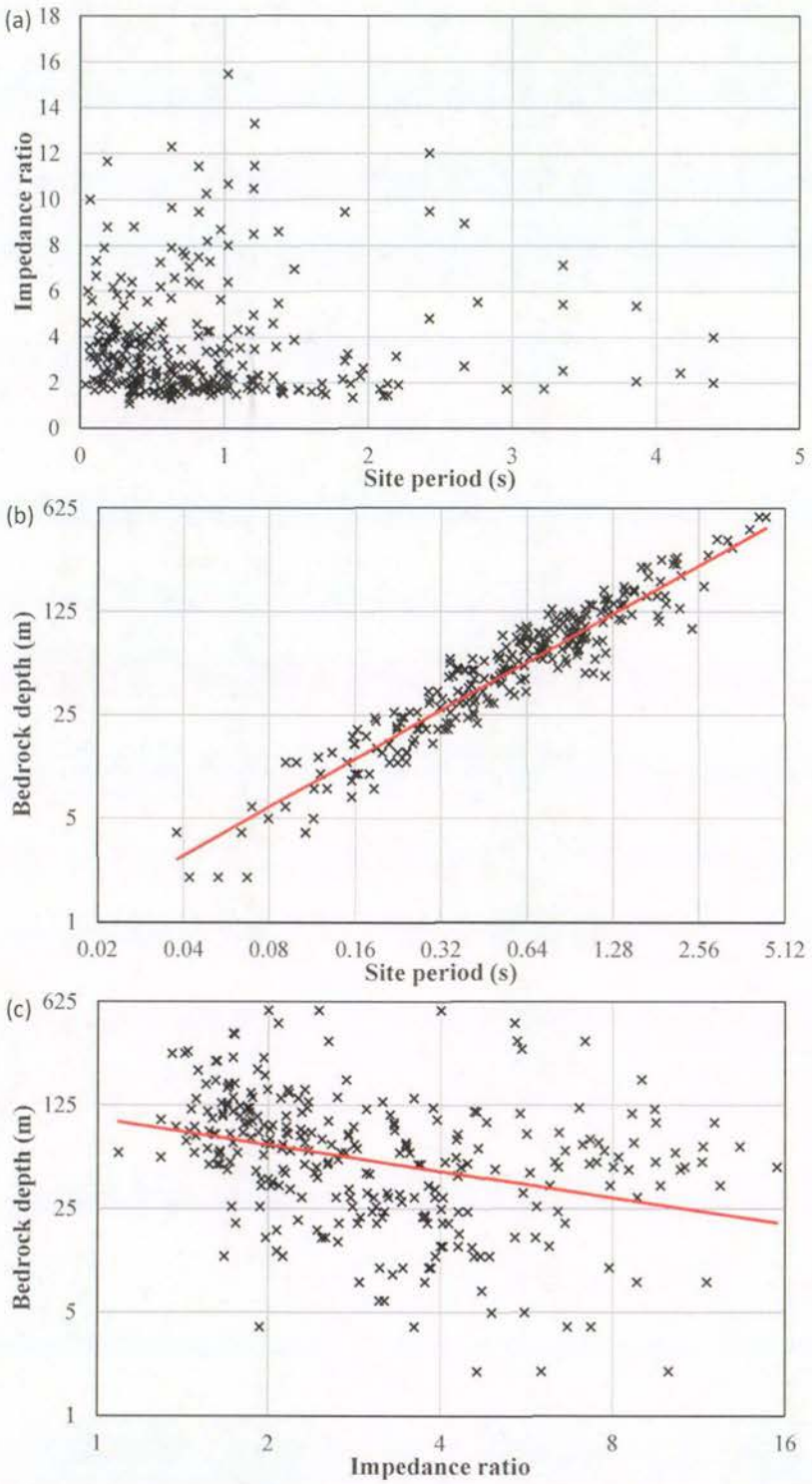

Figure 2.3 The distribution of sites with respect to site period and impedance ratio in (a), with respect to site period and bedrock depth in (b) and with respect to impedance ratio and bedrock depth in (c).

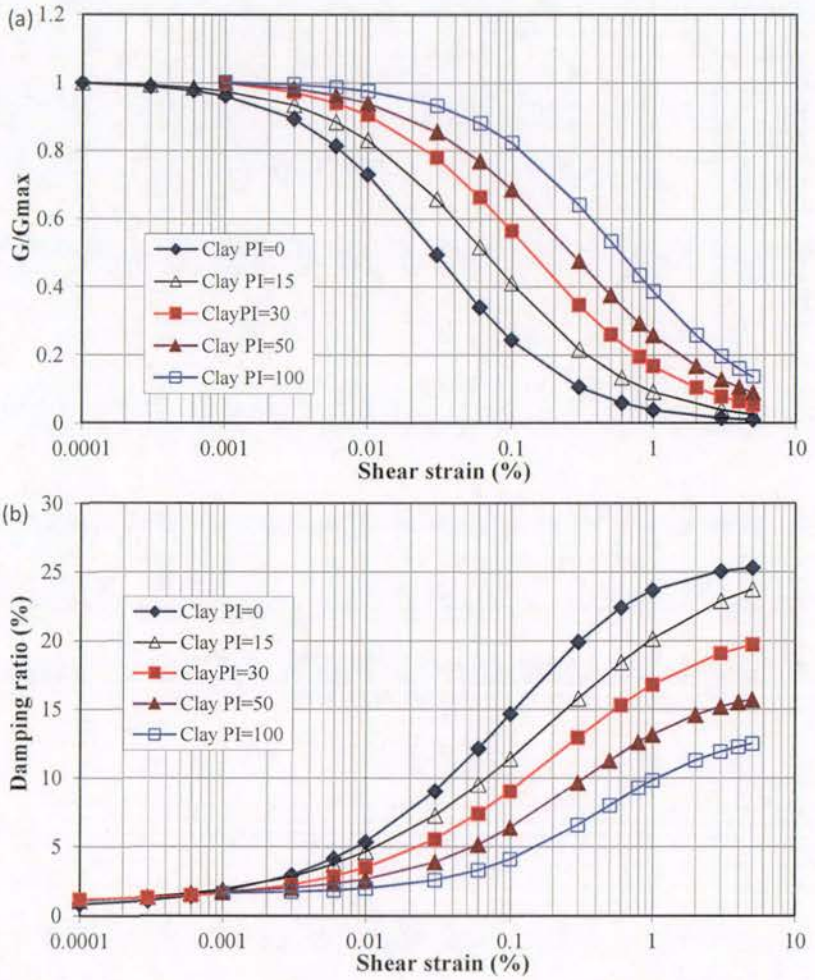

Figure 2.4 Shear modulus reduction curves in (a) and damping ratio curves in (b) for 5 clay models.

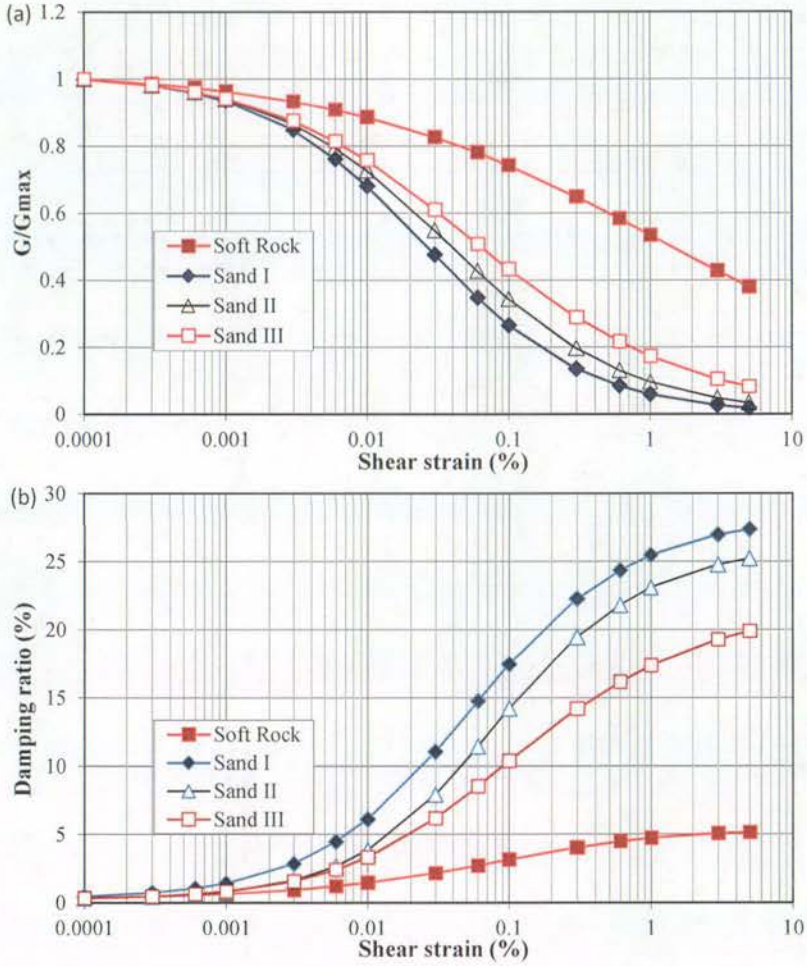

Figure 2.5 Shear modulus reduction curves in (a) and damping ratio curves in (b) for 3 sand models and 1 soft rock model.

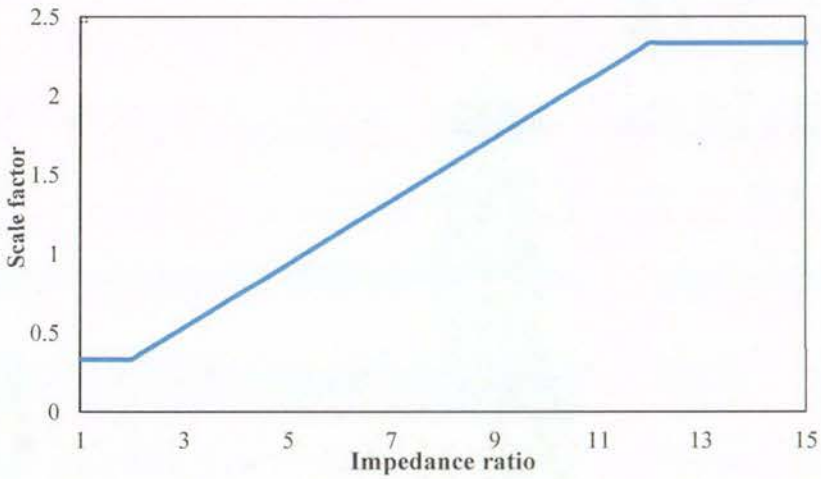

Figure 2.6 Scale factor accounting for site impedance ratio.

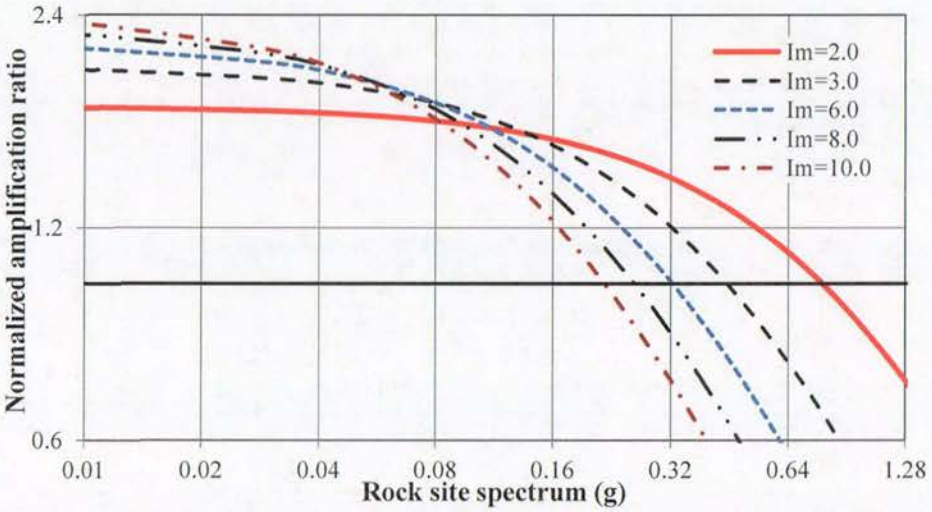

Figure 2.7 Illustration of PGA amplification ratios computed for SC IV sites with different impedance ratios for 1-D models. The thick horizontal line indicates a normalized amplification ratio of 1.0.

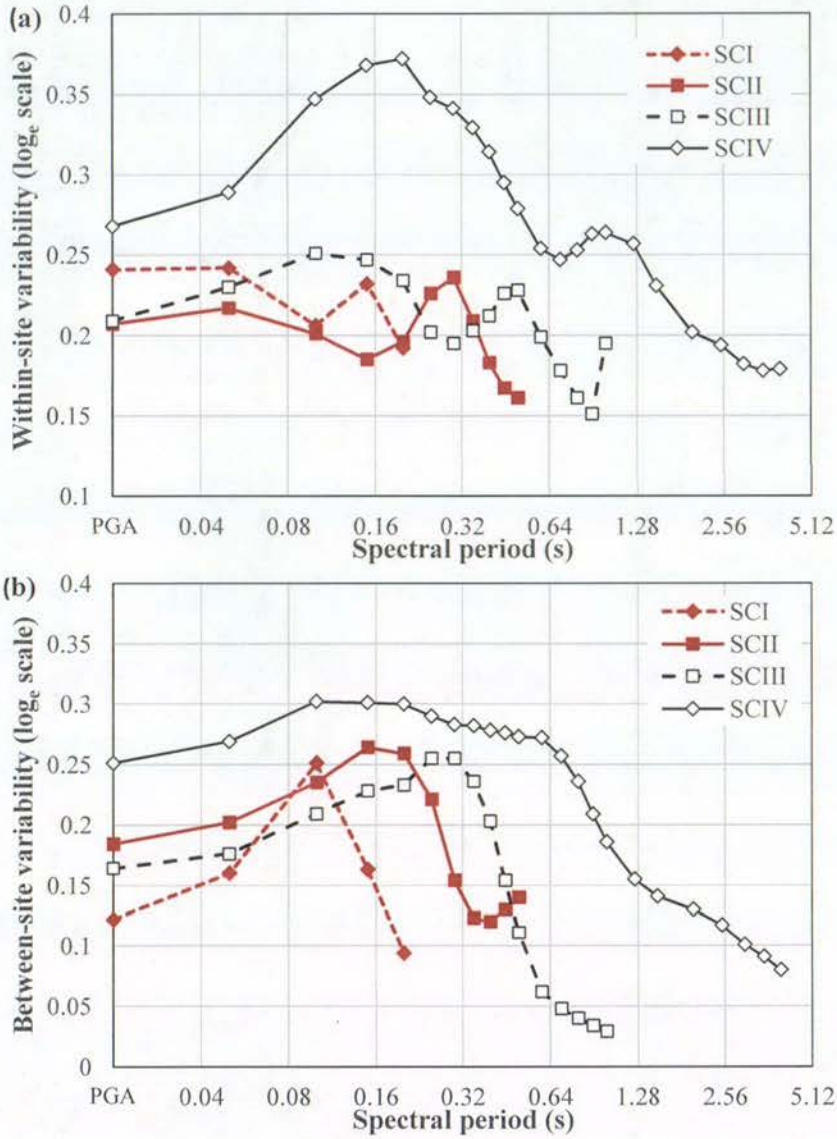

Figure 2.8 Standard deviations for the computed 1-D amplification ratios using a random effects model, (a) within-site standard deviations and (b) between-site standard deviations for four site classes.

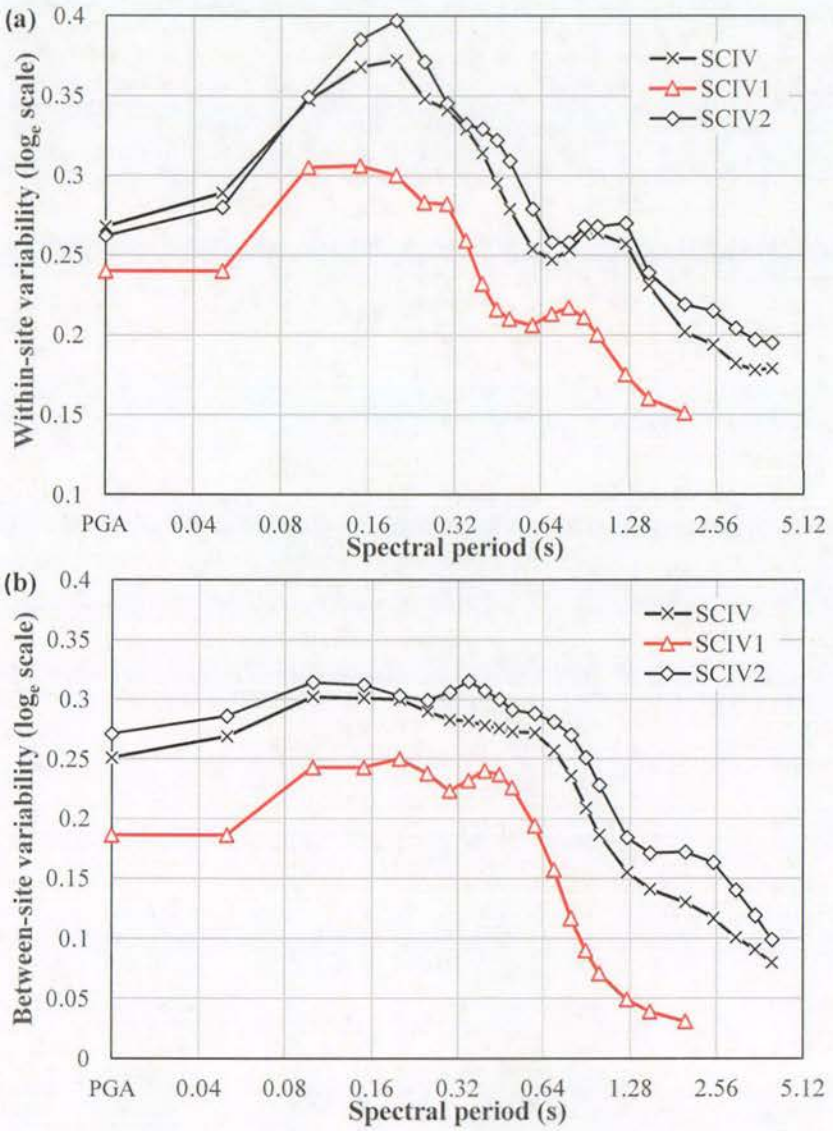

Figure 2.9 Standard deviations for the computed 1-D amplification ratios using a random effects model, (a) within-site standard deviations and (b) between-site standard deviations for SC IV, SC IV1 and SC IV2 site classes.

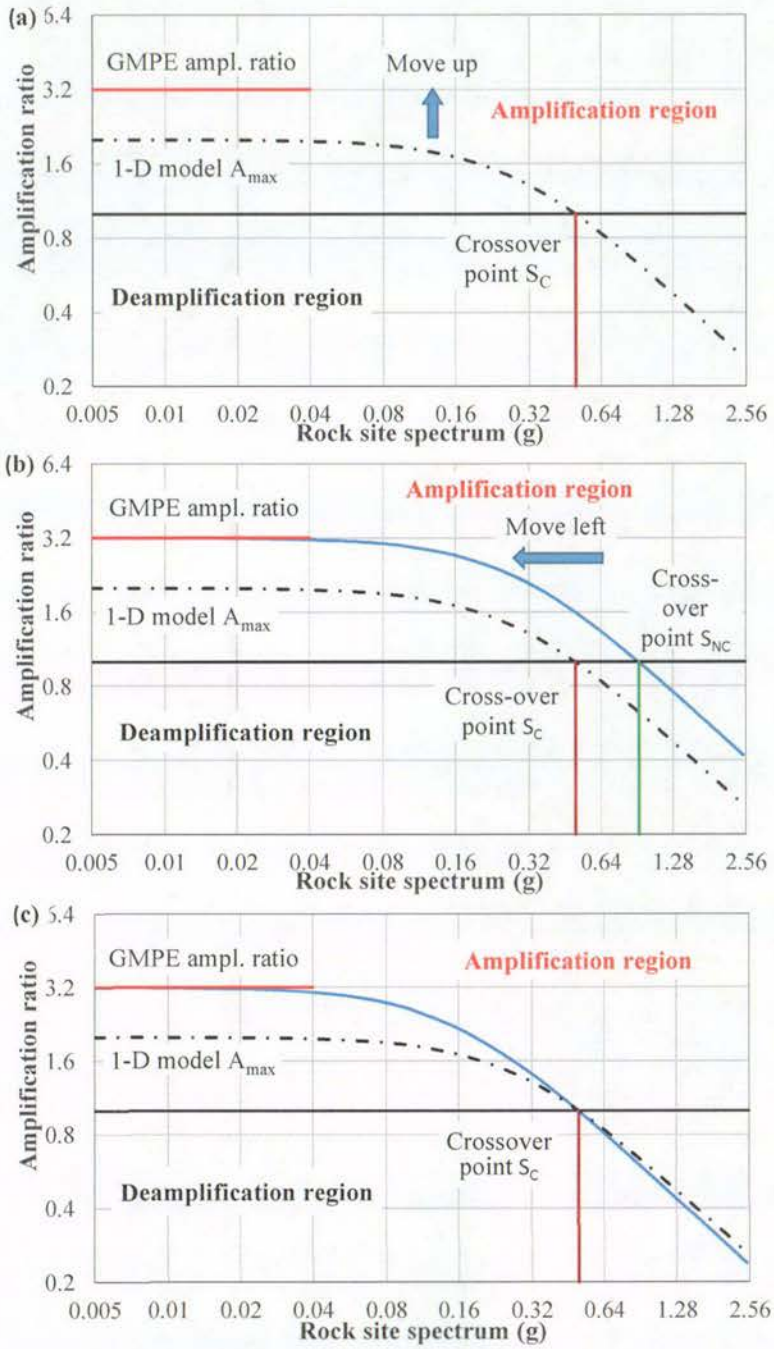

Figure 2.10 Illustration of adjusting 1-D amplification ratios by matching the amplification ratios from a GMPE, (a) move the amplification ratio curve upward to match the GMPE amplification ratio at weak motion; (b) move the amplification ratio curve to the left; and (c) adjusted amplification ratio curve that can be used in a GMPE.

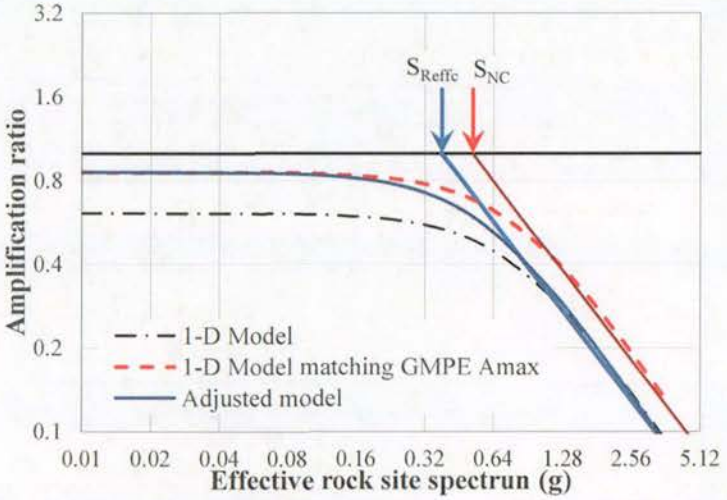

Figure 2.11 Illustration of adjusting 1-D amplification ratios by matching the maximum amplification ratios from a GMPE, when the maximum amplification ratio is less than 1.25.

3.0 GROUND-MOTION PREDICTION EQUATIONS FOR JAPAN USING SITE CLASS AND SIMPLE GEOMETRIC ATTENUATION FUNCTIONS

3.1 ABSTRACT

Ground motion prediction equations (GMPEs) derived from strong-motion records in Japan are presented. We assembled a large dataset from earthquakes with a moment magnitude (M_W) over 4.9 and a reliable earthquake category, up to the end of 2012. The earthquakes were divided into four tectonic categories: shallow crustal, upper mantle, subduction interface and subduction slab events. The shallow crustal and the upper mantle (SC-UM) events were combined as one group, and a set of three GMPEs were derived for the SC-UM, subduction interface and subduction slab events, respectively.

The GMPEs were based on a set of simple geometric attenuation functions. A linear magnitude scaling was adopted for large earthquakes with $M_W \geq 7.1$, with the scaling rates for large events being much smaller than those for the smaller events. A magnitude squared term was used for subduction slab events with $M_W < 7.1$. The models included nonlinear site terms, most of which did not vary from one model to another. The site terms were site classes based on site period.

We modelled the effect of volcanic zones by using an anelastic attenuation coefficient applied to a horizontal portion of the seismic wave travel distance (along a straight line between the closest point of a fault place and a recording station) within volcanic zones. The attenuation rates through the volcanic zone differed significantly from one GMPE model to another.

Most strong-motion records in the dataset used in the present study are from stations with a measured shear-wave profile down to bedrock. A small number of strong-motion records are from strong-motion stations with inferred site classes using H/V response spectral ratio or geological description of the surface soil layers. We tested the effect of site information quality, by examining the results from a dataset containing the strong-motion records from sites with an inferred site class and the results from a dataset without these records. The site information quality made a significant difference for nearly all spectral periods of the three models, i.e., the model fit improved significantly when the sites with inferred site classes were excluded.

The within-event residuals were separated into within-site and between-site residuals approximately and the corresponding standard deviations were calculated using a random effects model with all standard deviations presented in this report. The separation of within-event residuals into within-site and between-site components allows for a possibility of adopting different standard deviations for different types of earthquakes and for different site classes in a probabilistic seismic hazard analysis if desired.

Extensive statistical tests were performed for the linear site terms, within-event and between-event residuals, and within-site and between-site residuals to examine if these terms from the three different models differed statistically and if the standard deviations for the models differed significantly. The site terms from the three models were essentially statistically similar for many spectral periods among the three GMPEs, except that the site terms for SCIV sites differed statistically between SC-UM and subduction slab models. Among the three models, the between-event standard deviations of the residuals did not differ

statistically at any spectral period, whereas within-event standard deviations differed statistically at some spectral periods. The within-site and between-site standard deviations from the three models also differed statistically at some spectral periods.

3.2 INTRODUCTION

Ground-motion prediction equations (GMPEs) have an important role to play in earthquake engineering and probabilistic seismic hazard analyses. Even though numerical simulations estimating strong-ground motions from a particular fault at a particular site have been used (Graves and Pitarka, 2010), empirical models are still used almost universally. In the last decade or so, many modern GMPEs have been published, namely the much discussed and used Next Generation Attenuation (NGA) models mainly based on strong-motion records from California and supplemented by shallow crustal records from Taiwan, Japan, Turkey and China. The NGA models by Abrahamson and Silva (2008), Boore and Atkinson (2008), Campbell and Bozorgnia (2008) and Chiou and Youngs (2008) fit the strong-motion records from the 2008 Wenchuan earthquake in China reasonably well (Lu et al. 2010). These models all use V_{S30} as the site parameter and all have nonlinear site terms to account for reduction in site amplification ratios when the ground shaking is strong.

For subduction zones, the tectonic settings are complex and a only relatively small number of GMPEs have been developed (e.g., Atkinson and Boore (2003), Zhao et al. (2006a), McVerry et al. (2006),Kanno et al. (2006), and Ghofrani and Atkinson (2014)). The models by Zhao et al. (2006a) and Kanno et al. (2006) were based on strong-motion records from Japan, and nonlinear site terms were not used. The Zhao et al. (2006a) model used site class based on site period as the site term because many strong-motion recording stations had no site information. Based on a small number of K-net stations where the borehole depth of 20m was considered to be reaching engineering bedrock, Zhao et al. (2006b) classified the recording stations by using H/V response spectral ratios. The site classes are defined in Table 3.1 together with the approximate NEHRP site classes (BSSC 2000). The use of site classes by Zhao et al. (2006b) produced consistent site amplification ratios for three soil site classes (SC II, III, and IV) with respect to SC I sites, i.e., the peak amplification ratios occurred at the average site periods for SC II and SC III sites and the peak period for SC IV sites was 0.8s (Figure 6a in the Zhao et al. 2006a). However, terms for nonlinear soil response were not used because only a very small number of the records used in the modelling appeared to contain significant nonlinear soil response. Also the strong-motion records used in the Zhao et al. (2006a) model were obtained before the end of 2003, and since then many more strong-motion records have been obtained by the K-net and Kik-net strong-motion networks.

Zhao and Lu (2011) and Zhao and Xu (2012) investigated the magnitude scaling rates for large earthquakes with a moment magnitude over 7.0 using strong-motion data from world-wide crustal earthquakes, and from large subduction interface earthquakes in Japan. Their studies showed that the magnitude scaling rates were very small, varying in a range of 0.0–0.3, for large crustal earthquakes, and for large subduction interface earthquakes (with a moment magnitude over 7.0) were much smaller than those for smaller events. Zhao (2014) and Zhao et al. (2014) investigated the magnitude scaling rates for large earthquakes using strong-motion records from Japan and from the large crustal earthquakes in the PEER strong-motion dataset. Their study suggest that the magnitude scaling rates for three types of earthquakes with $M_W \geq 7.1$ are much smaller than those for smaller events. In the present study we used the magnitude scaling rates for large earthquakes from the Zhao (2014) and Zhao et al. (2014) study.

To develop GMPEs for Japan, earthquake tectonic categories need to be identified. Section 1 examined the earthquake locations reported in the catalogues of the Japan Meteorological Agency (JMA), an EHB group in the catalogues from the International Seismological Centre (ISC-EHB), and the National Earthquake Information Centre (NEIC) of United States Geological Survey (USGS). We used ISC-EHB locations for all events before 2005. For events since the end of 2004, we used the order of preferred locations as: JMA high-precision level locations, ISC-EHB locations and NEIC locations excluding the events with a fixed depth. We divided the events in Japan into four categories: shallow crustal, upper mantle, subduction interface and subduction slab events. We used the goodness-of-fit of a GMPE model to determine the preferred order of catalogues and we showed that a separate upper mantle category improved the goodness-of-fit for the GMPE models at short periods in Section 1 of this report.

In this study we will use site classes as defined in Table 3.1. The site parameters and the GMPEs presented in this report upgrade the Zhao et al. (2006a) model. Even though site classes do not provide a continuous predicted response spectrum across all sites, they are still useful for some design codes, such as the New Zealand design code NZS1170.5:2004 (Standards New Zealand, 2004), and for some engineering sites that may have a site class but not an accurate site period or V_{S30}.

Shear-wave velocity profiles for most Kik-net stations are available to bedrock, and so the site classes for these sites can be accurately calculated. However, many K-net sites have a bedrock depth larger than 20m while the measured shear-wave velocity extends to a maximum depth of 20m only. Their site classes were inferred by using response spectral ratios between the horizontal and the vertical components (H/V) as described by Zhao et al. (2006b). The other K-net sites have a borehole depth less than 20m. We assumed that engineering bedrock was reached for all of those sites, and so considered the site classes for these K-net sites to be accurate. We will investigate the effect of using the inferred site classes by comparing the goodness-of-fit of the GMPEs from the dataset with or without the records from the sites with inferred site classes.

In the this study we use the maximum log-likelihood, rather than the model standard deviation, as the indicator of goodness-of-fit for a GMPE. Model standard deviation has often been used to represent the goodness-of-fit, but suffers from some deficiencies. When the model parameters are close to but still significantly different from the optimal values, the standard deviation becomes nearly constant for different parameter values. Also, when a significantly biased distribution of residuals with respect to a particular parameter is corrected by adding a further term, the model standard deviation hardly changes, while the maximum log-likelihood is sensitive to the correction. We also found that the maximum log-likelihood was a good indicator to identify an apparently biased distribution of residuals with a parameter that is strongly influenced by an outlier in the dataset. In this case when an additional term is used to correct this type of biased residual distribution, the maximum log-likelihood does not change, meaning the correction is not statistically necessary.

We also adopted site terms accounting for soil nonlinear response. The number of strong-motion records from Japan that contain significantly large nonlinear soil response is still small. We adopted the nonlinear site model from Section 2 that were derived from 1-D models based on the shear-wave velocity profiles from a number of selected Kik-net stations. The model parameters that were controlled by weak motions were separated from the cross-over rock spectrum that separated amplification from deamplification ranges of rock spectrum, as described in Section 2. The parameters controlled by weak motions will be

determined from GMPE amplification ratios, while the parameters controlled by strong motions, such as the cross-over rock spectrum and the slope of attenuation in amplification ratios at a very large rock site spectrum will be determined from the 1-D model analyses. The model presented in Section 2 appears to overcome the over-simplification of the 1-D model for real sites where 2- or 3-D effects may be significant.

3.3 STRONG-MOTION DATASET

Table 3.2 lists the number of earthquakes used in this study. We used records from 335 earthquakes in Japan since 1968, including the large earthquakes from the dataset used by Zhao et al. (2006a). Figure 3.1 shows the distribution of earthquakes with respect to the depth at the top of the fault and moment magnitude. Thirteen subduction interface earthquakes and seven subduction slab earthquakes have an $M_W \geq 7.0$ while the largest magnitude from the upper mantle category is 7.0. There are 413 records from the M_W=9.12 2011 Tohoku earthquake in Japan. These records provide invaluable constraint on the magnitude scaling rate for large subduction interface earthquakes. The maximum hypocentral depth is 167 km. Seven earthquakes have a hypocentral depth over 100km, providing good constraint on the depth term for the subduction slab events. Among the shallow crustal earthquakes, 19 have a normal focal mechanism, 18 of which occurred after the 2011 Tohoku earthquake. The records from these normal faulting earthquakes provide an opportunity to investigate the strong-motion characteristics of this type of event.

Table 3.3 presents the number of records among each source category and focal mechanism group in each site class. SC I sites have 6679 records, the largest number of strong-motion records among the four site classes, and 2100 records are from shallow crustal events, with 969 records being from reverse faulting mechanism events. SC II sites have 4173 records, the second largest group, with 1247 records from shallow crustal earthquakes. In this site class, 580 records are from crustal reverse faulting events and 302 records are from normal fault events. SC III sites have 1386 records, the smallest number of records among the four site classes and SC IV sites have 2605 records.

Among the records from earthquakes before 1996 and records from some K-net stations, the site class for these stations was inferred from geological description (all records from the 1995 Kobe earthquake) or H/V response spectral ratios, while almost all Kik-net and some K-net recording stations have a measured shear-wave velocity profile down to engineering bedrock. The inferred site classes are likely much less reliable than those from the measured shear-wave velocity profiles. The number of earthquakes with records from sites with reliable site classes is presented in Table 3.4 in each source category and each focal mechanism group, and the number of records in each site class and earthquake category is presented in Table 3.5. A total of 33 events were excluded: six from shallow crustal, 16 from subduction interface, and 11 events from subduction slab earthquake categories. A total of 1208 records – 232 from shallow crustal, 467 from upper mantle, 480 from subduction interface and 331 from subduction slab events – were excluded. Figure 3.2 shows the distribution of records with respect to source distance and magnitude for the records used to derive the GMPEs presented in this report. Magnitude-dependent distance truncation was used for all records to avoid possible effects from untriggered stations.

We had fault rupture models for a number of earthquakes and the references for these models are presented in the Section 6, References for fault rupture models.

3.4 MODEL FUNCTION FORMS

In the present study, we employed the following functions to model the source effect, i.e., the magnitude, fault/focal depth and focal mechanism, for shallow crustal events,

$$f_{mcr}(m_i, h_i, F_i) = b_{cr}h_i + F_N + \begin{cases} c_{cr}m_i & if\ m_i \le m_c \\ c_{cr}m_c + d_{cr}(m_i - m_c) & if\ m_i > m_c \end{cases} \quad (3.1)$$

where f_{mcr} represents source terms, h_i is the fault-top depth when a fault model is available and otherwise focal depth. Subscript *cr* indicates that the term is associated with shallow crustal events. F_N is a constant for normal faulting earthquakes. We found that the reverse faulting events in the shallow crustal dataset do not produce statistically significantly different response spectrum compared with strike-slip events. The normal faulting events, however, have statistically larger spectrum than the strike-slip and reverse faulting events among the shallow crustal earthquakes. McBeen et al. (2014) also found that the PGAs from a small group of normal events that occurred after the M_W=9.0 2011 Tohoku earthquake in Japan needed a positive event terms to fit the NGA models, consistent with our findings. The bilinear magnitude scaling in Equation (3.1) was found to be appropriate, and a magnitude squared term was not statistically necessary. The use of bilinear magnitude scaling reduces the constraint on magnitude scaling rate at large magnitude from a relatively much larger number of small events. Coefficient d_{cr} was determined by the records from Japan and the larger crustal earthquakes used in the Zhao and Lu (2011) study.

The model for the upper mantle earthquakes is given by

$$f_{mum}(m_i, h_i, F_i) = \begin{cases} c_{cr}m_i & if\ m_i \le m_c \\ c_{cr}m_c + d_{cr}(m_i - m_c) & if\ m_i > m_c \end{cases} \quad (3.2)$$

Subscript *um* means that the term is associated to the upper mantle events. For this event category we used the same magnitude scaling as for the shallow crustal events and the fault-top depth does not appear to have a significant effect on the response spectrum. The upper mantle group does not have events with a magnitude over 7.0 and we adopted the scaling rate d_{cr} derived from large shallow crustal events, as well as the magnitude scaling rate c_{cr} for shallow crustal events.

For subduction interface events, Zhao (2010) suggested that the events occurred at the interface between crust and the subduction plate behaved differently from those events at the interface between the mantle wedge and the subducting plate. Zhao (2010) found that the shallow interface events (0–25km) required a larger anelastic attenuation rate than for the records from deep interface events with a depth over 25km. In the present study we also tested whether the two groups of events may need different source terms because of the different materials at the shallow and deep interfaces. For interface events with a focal depth of 25km or less, the following function was used for the source effects:

$$f_{mintS}(m_i, h_i) = b_{int}h_i + \gamma_{intS} + \begin{cases} c_{intS}m_i & if\ m_i \le m_c \\ c_{intS}m_c + d_{int}(m_i - m_c) & if\ m_i > m_c \end{cases} \quad (3.3)$$

where γ_{intS} is the constant term for shallow interface events, b_{intS}, c_{intS} and d_{int} are regression coefficients for depth and magnitude terms respectively. Subscript *intS* means shallow interface events and subscript *int* means for all subduction interface earthquakes. However the number of shallow interface events is very small.

For interface events with a focal depth over 25km, the following function was used for the source effects:

$$f_{mintD}(m_i, h_i) = b_{int}h_i + \begin{cases} c_{intD}m_i & if\ m_i \leq m_c \\ c_{intD}m_c + d_{int}(m_i - m_c) & if\ m_i > m_c \end{cases} \quad (3.4)$$

Subscript *intD* means that the term is associated with the deep subduction interface events. Coefficient c_{intD} is the magnitude scaling rate for deep subduction interface events. For subduction slab events:

$$f_{mSL}(m_i, h_i) = b_{SL}h_i + \begin{cases} c_{SL1}m_i + c_{SL2}(m_i - m_{sc})^2 & if\ m_i \leq m_c \\ c_{SL1}m_c + c_{SL2}(m_c - m_{sc})^2 + d_{SL}(m_i - m_c) & if\ m_i > m_c \end{cases} \quad (3.5)$$

where b_{SL} is the coefficient for the depth term, c_{SL1} and c_{SL2} are the coefficients for the linear magnitude and the magnitude squared terms respectively for events with a magnitude less than or equal to m_c. The magnitude squared term with a positive value was found to be statistically significant. In the Zhao et al. (2006a) model, a positive magnitude squared term was used, and this term led to an unrealistically large short-period spectrum for large subduction slab events. In this study we found that the magnitude-squared term is only necessary for events with an $M_W \leq 7.1$ and the positive value for c_{SL2} essentially reduces the magnitude scaling rate for small events. Coefficient d_{SL} is the magnitude term for large events. In the present study we selected m_c=7.1 based on the results of Zhao and Lu (2011), Zhao and Xu (2012), Zhao (2014) and Zhao et al. (2014).

The GMPE for shallow crustal earthquakes is,

$$log_e(y_{i,j}) = f_{mcr} + g_{cr}log_e(r_{i,j}) + g_{crL}log_e(x_{i,j} + 200.0) + g_N(x_{i,j}) + e_{cr}x_{i.j} + e^v_{cr}x^v_{i,j} + \gamma_{cr} + \log_e(A^{cr}) + \xi^{cr}_{i,j} + \eta^{cr}_i \quad (3.6)$$

Variable *y* is for peak ground acceleration (PGA) or 5% damped response spectrum in units of acceleration as a percentage of gravity. Variable *e* denotes anelastic attenuation rate, *x* denotes the shortest distance from a recording station to the fault plane if a fault model is available and otherwise the hypocentral distance, γ is a constant and *g* denotes whole path geometric attenuation rates. Term g_{crL} is the large distance geometric attenuation rate and g_N is the near-field geometric attenuation rate. Subscript or superscript *cr* indicates that the term is associated with shallow crustal earthquakes. Superscript *v* indicates the association with the volcanic path. Anelastic attenuation rate e^v is applied to the horizontal distance passing through volcanic zones denoted by x^v. Subscript *i* indicates the i^{th} event in the dataset and *j* indicates the j^{th} record in the i^{th} event. Parameter A^{cr} is the amplification ratios for this event group and it contains both linear and nonlinear site terms that will be described later. The random variable ξ is the within-event residual with an average value of 0.0 and a standard deviation of σ referred to as the within-event standard deviation. Random variable η is the between-event residuals with an average value of 0.0 and a standard deviation τ referred to as between-event standard deviation. The distance used for geometric spreading is defined by

$$r_{i,j} = x_{cro} + x_{i,j} + \exp(c_1 + c_2C_m) \quad (3.7)$$

$$C_m = \begin{cases} m_i & if\ m_i \leq C_{max} \\ C_{max} & if\ m_i > C_{max} \end{cases} \quad (3.8)$$

We introduced a distance constant x_{cro} to avoid magnitude-distance oversaturation, for which the ground motion at the source decreases with increasing magnitude. Without x_{cro} term, the sum $c_{cr}+g_{cr}c_2$ must be positive. Because g_{cr} is negative and much less than -1 for nearly all spectral periods, to maintain $c_{cr} \geq g_{cr}c_2$ is impossible if a reasonable value for c_2 is used. We interpreted that the term $\exp(c_1 + c_2 m_i)$ is related to the fault length for an earthquake with a moment magnitude of m_i. Typically, fault length is proportional to $10^{0.5m}$ (Dowrick and Rhoades 2004; Somerville et al. 1998) and this leads to c_2=1.151 when a natural logarithm scale is used. Our regression analyses show that c_2 is very close to 1.151 for nearly all spectral periods for all types of earthquakes, and therefore it is not reasonable for c_2 to take a value much less than 1.151 in order to avoid the magnitude-distance oversaturation. The introduction of variable x_{cro}=2.0 solves the problem neatly for almost all spectral periods. We also used a maximum magnitude C_{max} in Equations (3.7) and (3.8) to account for oversaturation, for a very large earthquake with a very long fault rupture, only a part of fault contributes to the ground motion spectrum at a near-field station because both geometric and anelastic attenuation would diminish the ground motions produced by the fault rupture at a large distance. Also the finite rupture speed leads to that the energy released from different part of the fault distributed at different time, not a simple amplitude addition. In the present study, we selected $C_{max} = m_c$ as both terms are based on the same assumption.

Figure 3.3(a) illustrates the distance x^v in four different cases with earthquake and the recording-station locations inside or outside of an example volcanic zone and Figure 3.3(b) shows the slant distance within the volcanic zone where h is focal depth and R is the epicentral distance. When a fault plane model is available, the location of the earthquake is at a point in the fault plane that is closest to the recording station.

We introduced a term $g_{crL}\log_e(x_{i,j}+200)$ with g_{crL} having a positive value to avoid a positive anelastic attenuation rate.

For the shallow crustal earthquakes, after we determined near-source parameters c_1, c_2, and d_{cr}, we excluded the strong-motion records from the PEER dataset and used the data from Japan to determine the other terms. We found that the model for shallow crustal events systematically underestimates the short-period spectrum and over-estimates the long-period spectrum for about 170 records from Japan within a source distance of 30km. We investigated the residuals for the near-field records from Japan in the model we used to determine the near-source terms and we found that the average residuals for these records is close to zero. A plausible reason is that the near-source records from the large earthquakes in PEER dataset do not only put constraint on the near-source terms and the magnitude scaling rate for large events, but also affect the estimates of all other parameters, especially the geometric attenuation rate. When these near-source terms are fixed and those near-source records are excluded, the changes in the geometric attenuation rate lead to a model that have a biased distribution of residues for the near-source records from Japan. We added the following term to eliminate the bias,

$$g_N(x_{i,j}) = g_{crN}\begin{cases} log_e[x_{i,j} + \exp(c_1 + 6.5c_2)] & if\ x_{i,j} \leq 30 \\ log_e[30.0 + \exp(c_1 + 6.5c_2)] & if\ x_{i,j} > 30 \end{cases} \quad (3.9)$$

We used C_m=6.5 in Equation (3.9) instead of magnitude to avoid the magnitude-distance oversaturation problem and this term improved the model prediction considerably.

The GMPE for the upper mantle earthquakes is,

$$log_e(y_{i,j}) = f_{mum} + g_{um}log_e(r_{i,j}) + g_{crL}log_e(x_{i,j} + 200.0) + g_N(x_{i,j}) + e_{um}x_{i.j} + e^v_{cr}x^v_{i,j} + \gamma_{cr} + \log_e(A^{cr}) + \xi^{cr}_{i,j} + \eta^{cr}_i \quad (3.10)$$

Subscript um indicates that the variable is associated with the upper mantle earthquake group. For upper mantle events, there is no record within a source distance of 30km and the term g_N is essentially a constant. However, retaining this term for the upper mantle events leads to an easy smoothing for all parameters in Equations (3.6) and (3.10) with respect to logarithm of spectral periods.

As discussed earlier, Zhao (2010) found that the attenuation rate for shallow interface earthquakes (with a depth of 25km or less) is larger than for deep subduction interface events with a depth over 25km because the materials in the shallow crust close to the interface and the mantle wedge may have different properties. For shallow subduction interface earthquakes, the following model is used,

$$log_e(y_{i,j}) = f_{mintS} + g_{int}log_e(r_{i,j}) + g_{intL}log_e(x_{i,j} + 200.0) + e_{intS}x_{i.j} + e^v_{int}x^v_{i,j} + \gamma_{int} + \log_e(A^{int}) + \xi^{int}_{i,j} + \eta^{int}_i \quad (3.11)$$

where A^{int} is the site amplification ratios for interface event group. Subscript or superscript *int* means the variable is associated with interface earthquakes, and subscript *ints* means that the variable is associated with shallow interface events. For deep subduction interface earthquakes, the following model is used,

$$log_e(y_{i,j}) = f_{mintD} + g_{int}log_e(r_{i,j}) + 0.5g_{intL}log_e(x_{i,j} + 200.0) + e^v_{int}x^v_{i,j} + \gamma_{int} + \log_e(A^{int}) + \xi^{int}_{i,j} + \eta^{int}_i \quad (3.12)$$

$$r_{i,j} = x_{into} + x_{i,j} + \exp(c_1 + c_2C_m) \quad (3.13)$$

A^{int} is the site amplification ratio that contains both linear and nonlinear parts. We found that anelastic attenuation term is not necessary for deep interface earthquakes. Coefficient g_{intL} is the large distance geometric attenuation rate for subduction interface events. We used $0.5g_{intL}$ for deep interface events to achieve an improved model fitting and x_{into} =10 was used to avoid magnitude-distance oversaturation. For Japan, the closest distance to an subduction interface events is about over 30km and oversaturation would occur only when the distance is less than about 10km if x_{into} is not used. This term is only necessary if the model presented here is used for the subduction interface earthquakes in the other parts of the world where the closest distance is within 20km.

For subduction slab earthquakes,

$$log_e(y_{i,j}) = f_{mSL} + g_{SL}log_e(r_{i,j}) + g_{SLL}log_e(x_{i,j} + 200.0) + e_{SL}x_{i.j} + q_{SLH}x_{i.j} + e^v_{SL}x^v_{i,j} + \gamma_{SL} + \log_e(A^{SL}) + \xi^{SL}_{i,j} + \eta^{SL}_i \quad (3.14)$$

where A^{SL} is the amplification ratios for slab events. Subscript or superscript *SL* indicates that the term is associated with subduction slab earthquakes. Coefficient g_{SLL} is the large distance geometric attenuation rate for subduction slab events. The anelastic attenuation term q_{SLH} is defined by,

$$q_{SLH} = e_{SLH} \begin{cases} 0 & if\ h < 50 \\ 0.02h - 1.0 & if\ h \geq 50 \end{cases} \quad \textbf{(3.15)}$$

The fault-top depth is denoted by h in Equation (3.15) for the depth-dependent anelastic attenuation rate. The depth-dependent anelastic attenuation rate in Equation (3.15) for slab events does not appear to be reasonable because we would expect that the seismic waves from a deep slab event would have a long travel path within the subducting slab that has high Q values. From this simple reasoning the anelastic attenuation rate for deep slab events should be inversely proportional to the fault depth, as shown by Eberhart-Phillips and McVerry (2003). We attempted to use an anelastic attenuation rate inversely proportional to the fault depth. However, this term is not statistically significant, while the term q_{SLH} in Equation (3.15) leads to sizable increase in the maximum log-likelihood. The physical reason for Equation (3.15) is probably the geometry of the subduction interface and location of the strong-motion recording stations relative to the subduction trench as shown in Figure 3.4. For the North Island of New Zealand, the onshore depth of the interface is relatively small (starting from about 20km) and the trench formed by the subducting slab is also relatively close to the shorelines. For many slab earthquakes, a large portion of the travel path for the seismic waves recorded by New Zealand onshore stations has a large part within the subduction slab, as illustrated by the seismic wave travel path to the recording station at right side of Figure 3.4. Therefore the length of the travel path within the high-Q slab increases with increasing earthquake depth and this travel path leads to an anelastic attenuation coefficient inversely proportional to the fault depth, assuming that the Q values for the slab increases with increasing depth. For Japan, the subduction trench is usually very far from land and the seismic wave reaching the recording stations travels in the slab and also through upper mantle and crust that have smaller Q values than the subducting slab. We expect that the Q values in the upper mantle is likely to be smaller than the Q values within the subducting slab. The travel path within the mantle would increase with increasing depth and therefore an apparent anelastic attenuation rate may increase with increasing depth as shown in Equation (3.15). Zhao (2010) showed that if the constructive interference between the seismic waves traveling along the direct path and the waves traveling along a detoured path through the slab are modelled by depth-scaled geometric attenuation functions, the apparent anelastic attenuation rate for the slab events decreases. The anelastic attenuation rate from Zhao et al. (2014) study, using the depth-dependent geometric attenuation functions from Zhao (2010) for the subduction events, is the same as in Equation (3.15).

For subduction slab event, the distance term is given by,

$$r_{i,j} = x_{i,j} + \exp(c_1 + c_2 C_m) \quad \textbf{(3.16)}$$

In the regression analyses, we divided the models into three groups: the shallow crustal and upper mantle events (SC-UM) in one group, the shallow and deep subduction interface events in the second group, and the subduction slab events in the third group. All groups have most common nonlinear site terms. Regressions for each group were carried out separately. During the model regression analyses we used the maximum log-likelihood and

AIC criterion (Akaike 1974) to test each parameter and those not supported by the AIC criterion were removed from the model.

Random variable ξ can be divided into a within-site component ξ^S and a between-site component η^S. We fit the following random effects model to the within-event residuals,

$$\xi_{k,n} = \xi^S_{k,n} + \eta^S_k \quad (3.17)$$

where the subscript k stands for the site number and n denotes the n^{th} record from the k^{th} site. The within-site component $\xi^S_{k,n}$ has a zero mean and a within-site standard deviation of σ_S. The between-site component η^S_k has a zero mean and a between-site standard deviation of τ_S. When the dataset is large, it is quite difficult to find a stable algorithm to decompose the within- and between-site residuals as well as the within- and between-event residuals using the random effects methodology. We took an approximate method by fitting a random effects model to the within-event residuals using the same algorithm by Abrahamson and Youngs (1992). The between-site residuals are an indicator of how well the site effects are modelled. The within-event residuals contain the random errors associated with path effects as well as any other effects that are not modelled. For a particular engineering site where the site effect can be modelled with confidence, the between-site standard deviation may be set as zero in the probabilistic seismic hazard study and the within-site standard deviation may substitute the single-station σ suggested by Atkinson (2006).

The separation of between- and within-site residuals leads to a possibility that different total standard deviations for each site class and each earthquake group can be used in a probabilistic seismic hazard analysis. For a given site class and earthquake group, the total standard deviation can be calculated by,

$$\sigma^k_{i,T} = \sqrt{\sigma^2_{sk} + \tau^2_i + \tau^2_{sk}} \quad (3.18)$$

where $\sigma^k_{i,T}$ is the total standard deviation for the i^{th} earthquake group and for the k^{th} site class; σ_{sk} and τ_{sk} are, respectively, the within-site and between-site standard deviation for the k^{th} site class. However, when the different spectra from the probabilistic seismic hazard analysis are achieved using different values for the standard deviations but the standard deviations selected are statistically similar, the difference in the hazard spectra is statistically meaningless. We will present the results of statistical tests for different site terms and standard deviations in the following section.

The horizontal portion of the distance that passes through volcanic zones (along a straight line between a station and the fault plane), x^v, instead of the slant distance within the volcanic zones (close to the actual wave propagation distance), is used to model the effect of volcanoes. The calculation of an accurate slant distance requires detailed volcanic (low Q) zone boundary models down to considerable depth, which is currently unavailable, and the horizontal distance serves as a good approximation of the volcanic path untailed a detailed 3-D Q structure becomes available. However, using the horizontal distance has a problem: the slant distance within a volcanic zone can become significantly larger than the horizontal distance for deep earthquakes. If accurate 3-D Q structures are available, this problem can be avoided by using slant distances. Even though x^v does not represent the accurate seismic wave-propagation distance, it would still be a better one than the binary parameter for fore-arc and back-arc stations (Boore et al. 2009 and Ghofrani and Atkinson 2014), at least in theory. We found that the residuals distributions at small x^v and large x^v for the records affected by volcanic path attenuation were biased, thus we adopted the minimum and the

maximum values for x^v as 12km and 80km respectively, e.g., when $0.0<x^v\leq 12.0$km, $x^v=12.0$km, and when $x^v\geq 80.0$km, $x^v=80.0$km. We do not have any plausible explanation for these limits. Also there is a self-correction for the volcanic path effect, i.e., if x^v is systemically and uniformly overestimated, the anelastic attenuation rate e^v will reduce, leading to similar effect of the volcanic path.

SC I sites are neither rock site nor engineering bedrock. Many SC I sites have a layer of soil with a thickness up to 24m and a shear wave-velocity as small as 200m/s. The average impedance ratio is 3.7 and many sites have an impedance ratio between 4 and 8. The sites with a thin soil layer usually have a small average shear-wave velocity and a large impedance ratio. The sites with a thick soil layer usually have a large average shear-wave velocity and a relatively small impedance ratio for a given site period. These characters of the SC I site lead to small nonlinear soil response even when subjected to large rock motions because the shear stress from inertial force in the thin layer soil can be smaller than the soil yielding stress even at a strong ground shaking. Also the definition for rock sites, with a shear-wave velocity of 760m/s or larger at the ground surface, means that the V_{S30} for these sites could be over 1000m/s and the site could be classified as A in the NEHRP site classification (BSSC 2003). Because the amplification ratios of the nonlinear site mode is the spectral ratio between soil site and rock sites, not between soil sites and SC I sites, we needs to estimate the amplification ratio for SC I sites relative to the rock sites.

We used the following method to determine the amplification ratios for SC I sites or deamplification ratios. We examined the within-event residuals of the SC I sites and fitted a linear function of site periods to the SC I within-event residuals from all three GMPEs. Figure 3.5–Figure 3.7 shows the distribution of within event-residuals with respect to site period and the distributions are clearly biased. The solid trend lines represent the average within-event residuals and the negative value of the average residuals at zero site period is then defined as S_{1N}, the negative intercept of the linear trend line. Note that S_{1N} is also the absolute value of the intercept. We used linear functions for all spectral periods. Figure 3.8(a) shows the smoothed deamplification ratios for rock sites with respect to SC I sites. At short spectral periods, between PGA and 0.5s, the deamplification ratios range from 1.05 to 1.38. The deamplification ratios then increase to 2.05 at 0.3s, then decrease with increasing spectral periods down to 1.27 at 5.0s. These deamplification ratios are surprisingly large and may be caused by large impedance ratios. We referred to the logarithm of these amplification ratios as the 'hard rock site' term. Figure 3.8(b) shows an example SC I spectrum and the rock site spectrum derived from dividing the SCI site spectrum by the deamplification ratio presented in Figure 3.8(a). The spectral period at the peak spectrum for rock sites is close to 0.05s, shifted slightly from that of the SCI spectrum. This method does not require iterations because very few records from SC I sites contains the effect of significant soil nonlinear response. Table 3.6 presents the deamplification ratios $A_{mSCI}=\exp(S_{1N})$.

We adopt the following functions to model both linear and nonlinear site effect as described in Section 2,

$$\ln(A) = S_k + S_{1N} + \ln(A_N) \qquad \textbf{(3.19)}$$

where S_k is the linear site term, S_{1N} is the hard rock site term. The nonlinear amplification ratios derived from 1-D analyses is given by,

$$\log_e(\mathrm{A}_N) = C_A \log_e\left(S_{Reff}^{\alpha} + \beta\right) + C_B$$

$$S_{Reff} = I_{mfav} S_R$$

$$\mathrm{A}_{max} = \exp[C_A \log_e(\beta) + C_B] \qquad \textbf{(3.20a, b, c, d)}$$

$$S_{ReffC} = \left[\exp\left(-\frac{C_B}{C_A}\right) - \beta\right]^{1/\alpha}$$

$$I_{mfav} = \frac{1}{\varphi}\begin{cases} 1.0 & if\ I_{mav} \le I_{min} \\ 1.0 + \gamma(I_{mav} - I_{min}) & if\ I_{min} > I_{mav} \le I_{max} \\ 1.0 + \gamma(I_{max} - I_{min}) & if\ I_{mav} > I_{max} \end{cases} \qquad \textbf{(3.21a, b, c)}$$

$$S_{Reffc} = I_{mfav} S_{Rc}$$

$$S_{Rc} = \frac{S_{Reffc}}{I_{mfav}}$$

where C_A, C_B, α and β are regression coefficients, I_{mfav} is the average impedance ratio factor, S_R is the rock site spectrum, A_{max} is the response spectral amplification ratio when the rock site spectrum is 0.0 and S_{Reffc} is the effective cross-over rock spectrum that separates the amplification range from the deamplification range of rock site spectrum. S_{Rc} is the cross-over rock spectrum. Parameters α=2.0 and β=0.6 were selected and presented in Table 3.7. The amplification ratio is 1.0 when the effective rock site spectrum equals S_{Reffc}. Tables 3.7–3.10 present the values for all parameters in Equations (3.20) and (3.21).

The nonlinear amplification term is given by,

$$\log_e(A_N) = \log_e(A_{Nmax}) - \log_e(A_{max}) \frac{\log_e\left(S_{MR}^{\alpha}+\beta\right) - \log_e(\beta)}{\log_e\left(S_{ReffC}^{\alpha}+\beta\right) - \log_e(\beta)} \qquad \textbf{(3.22a, b)}$$

$$S_F = \frac{A_{Nmax}}{A_{max}}$$

$$S_{NC} = \left\{\exp\left[\frac{\log_e(A_{Nmax}) \log_e\left(S_{ReffC}^{\alpha}+\beta\right) - \log_e(S_F)\ln(\beta)}{\log_e(A_{max})}\right] - \beta\right\}^{\frac{1}{\alpha}} \qquad \textbf{(3.23)}$$

$$S_{MR} = S_{Reff} \frac{S_{NC}}{S_{ReffC}} f_{SR} \qquad \textbf{(3.24)}$$

where A_N is the amplification ratio, A_{Nmax} is the maximum amplification ratio of A_N when the rock spectrum is zero. Parameter f_{SR} is an adjustment factor so that a broadly smoothed nonlinear soil site spectrum can be obtained and this parameter has a value in a range of 0–1.2, as shown in Table 3.11. The values for this parameter were determined by achieving visually smoothed nonlinear spectrum at most distance and magnitude ranges. When this parameter equals zero, only linear amplification ratios are necessary. Note that A_{Nmax} is determined by strong-motion records for the GMPE, and for the k^{th} site class it is calculated from the site class term S_k as

$$A_{Nkmax} = \exp(S_{1N}) \qquad for\ SC\ I\ sites\ (k = 1)$$

$$A_{Nkmax} = \exp(S_k + S_{1N}) \quad for\ SC\ II, III, IV\ sites\ (k = 2,3,4) \qquad \textbf{(3.25a, b)}$$

In a case when A_{max} or A_{Nmax} is less than 1.25, the pseudo-crossover rock site spectrum should be calculated as described in Section 2.

3.5 MODEL COEFFICIENTS AND STANDARD DEVIATIONS

We established two sets of GMPEs for each earthquake group with identical functional forms. The first set used all strong-motion records presented in Table 3.2 and Table 3.3, and the second set used the records presented in Table 3.4 and Table 3.5, excluding those records from the sites with inferred site class. We used maximum log-likelihoods (MLL) from the two models to identify the effect of excluding the records from sites with an inferred site class. However, MLL usually increases when the number of records is reduced when all data have the same statistical properties. To account for the reduction in the number of data, we calculated a weighted MLL, i.e., the MLL values multiplied by the number of records in the data group and then divided by the number of records from the first dataset. The differences between the weighted MLL from the second dataset and those from the first dataset are presented in Figure 3.9. We refer to the differences as the site information quality effect, a positive value suggesting that a better model can be derived when records from sites with an inferred site class are excluded, and a negative value suggesting that the exclusion leads to a worse model. For the subduction interface model the improvement is significant at all spectral periods, with the increase in the weighted MLL being over 25 at all spectral periods except 5.0s. For the subduction slab models, the increase varies between 18 and 75, suggesting a better model without those records from sites with inferred site class. For SC-UM events, the model from the 2nd dataset has a much larger weighted MLL than that from the first dataset at spectral periods over 0.8s, while model from the first dataset has a larger weighted MLL than that from the second dataset at PGAs and other spectral periods up to 0.8s. Overall, the exclusion of the records from sites with an inferred site class improves the model fit and we present the model parameters from the 2nd set of GMPEs.

We adopted the magnitude scaling rates d_{cr}, d_{int} and d_{SL} for large SC-UM events, subduction interface events and subduction slab events with a magnitude of 7.1 or larger from the Zhao (2014) and Zhao et al. (2014) studies. Figure 3.10 shows the values for d_{cr} for each spectral period and the solid line is used in this study. Figure 3.11(a) shows the values of d_{int} and the ratio of d_{int}/c_{int} for subduction interface events and Figure 3.11(b) shows the values of d_{SL} and the ratio of d_{SL}/c_{SL} for subduction slab earthquakes. The magnitude scaling rates for events with an M_W over 7.0 are much smaller than those for the smaller events.

The strategy of determining model parameters is presented next. The first step is to include all terms as presented in Equations (3.1–3.15) as well as others not presented in this report, including magnitude squared term, geometric attenuation rate with and without magnitude dependence, separate depth terms, geometric and anelastic attenuation rates for each type of earthquakes, but without nonlinear site terms in each set of models. For example, for the SC-UM group, an anelastic term is used for both types of events and an additional anelastic term was used for the upper mantle events. We then used the AIC criterion to test if the term for the upper mantle events was statistically significant. If the term is not statistically significant, this term can be eliminated and the two types of event have the same anelastic

attenuation rates. If the term for the upper mantle event is statistically significant but has an opposite sign to the coefficient of the shallow crustal events, we then use two separate anelastic attenuation rates for the two types of events and a statistical test is performed for both of them. This process was carried out for all spectral periods and all regression coefficients. For each term, we calculate the ratio between the mean value and the standard deviation of the term and statistical tests started from the term that has the smallest mean/standard deviation ratio. For practical use, we need not only a set of models that have the best statistical properties but also a model that would produce a moderately smooth spectrum over the spectral period range. If a term is statistically significant at only a very small number of spectral periods, then it is set to zero. Usually the elimination of such terms does not lead to significant reduction in MLL. For a term that is statistically significant at a number of consecutive spectral periods we smooth the values of this term using a polynomial function of $\log_e(T)$, with T denoting the spectral period. The smoothing is carried out for most terms. However, this smoothing of the model terms does not guarantee a smoothed spectrum over all spectral periods, especially at the limits of any magnitude, distance and depth range. We did not attempt to modify the model coefficients further to produce smooth spectra at all parameter ranges.

Table 3.12 presents the coefficients in the model for SC-UM events described in Equations (3.1), (3.2), (3.6) and (3.10). These coefficients have been smoothed with respect to $\log_e(T)$. For PGA, T=0.02s was used in the smoothing function. Figure 3.12 compares the depth term from the Chiou and Youngs (2008) model with those in the present study. The negative values for the depth are retained in this study, as we interpreted the term as a depth effect relative to the depth of the upper mantle events, i.e., the depth term for shallow crustal events with a depth close to 25km is reduced by the depth term relative to the upper mantle events that does not have a depth term. The values for the depth term from the Chiou and Youngs (2008) is much larger than those from the present study. One reason for the small depth term in this study is that a part of the surface rupture effect in the Chiou and Youngs (2008) model is accounted for by the reduced magnitude scaling for large events, because most large earthquakes in our dataset has surface rupture. It is difficult to be certain which modelling is better than the other.

Figure 3.13–Figure 3.20 present the distribution of the between-event residuals with respect to magnitude and depth to the top of the fault, and within-event residuals with respect to magnitude and source distance for the SC-UM model. Ideally the trend line fitted to the residuals should have a zero value over the full parameter range; a non-zero slope in the trend line indicates a biased residual distribution. If the trend line has a non-zero slope, a term should be introduced to correct the bias only when the slope is statistically significant. None of the residuals is apparently biased; the slopes of the trend lines are not statistically significant, including for those spectral periods not presented in this report. Also, the smoothing of coefficients with respect to spectral periods leads to an apparent biased distribution of between-event residuals with respect to magnitude and depth as shown in Figure 3.19 but the slopes are not statistically significant.

Table 3.13 presents the smoothed coefficients in the model for subduction interface events described in Equations (3.3), (3.4), (3.11) and (3.12). Note that the anelastic attenuation coefficient for the deep subduction interface events is zero. Also the coefficients for the $log_e(r_{i,j}+200)$ term are the same as those for the SC-UM records. Figure 3.21–Figure 3.28 present the residual distributions for the subduction interface model. Nearly all distributions are unbiased, even though many coefficients were smoothed with respect to the logarithm of spectral periods.

Table 3.14 presents the smoothed coefficients in the model for subduction slab events described in Equations (3.5), (3.14) and (3.15). Figure 3.29–Figure 3.36 show the residual distribution for the subduction slab model. All trend lines have nearly zero slope even though all coefficients have been smoothed with respect to spectral periods.

However, if the residual distributions, especially the within-event residuals with respect to source distance, are grouped together for a number of depth ranges, the distribution within each depth group is biased. Zhao (2010) shows that these biased distributions can be corrected by using depth-dependent geometric attenuation functions and Zhao (2010) presented a number of possible physical reasons. The models using depth-dependent geometric attenuation functions are presented elsewhere (Zhao et al. 2014).

The coefficient c_2=1.151 was used for all models except for PGA and short periods up to 0.25s for SC-UM model. The modification was used to avoid the magnitude-distance oversaturation. For shallow crustal events, we found that the spectrum from reverse faulting events is similar to that from strike-slip events. However, we found that the spectrum from normal faulting events is larger than that from reverse or strike-slip faulting events. Figure 3.37 shows the event term F_N for the records from shallow crustal events with a normal faulting mechanism, varying between 0.349 (at a spectral period of 0.15s) and 0.0835 (at spectral period of 5.0s). This is a surprising result, because normal faulting events in the NGA models, for example, the Abrahamson and Silva (2008) model, have a negative value of -0.06 while the coefficient for this term is positive in the present study. Among 70 shallow crustal events in the dataset presented in Table 3.4 and Table 3.5, 18 are normal faulting events with a magnitude range of 5.0–6.6 that occurred in a time period between 12 March 2011 and the end of April in 2012, after the M_W=9.0 2011 Tohoku earthquake. Figure 3.38 shows the location of these earthquakes and they are all above the fault plane of the 2011 Tohoku earthquake. Because of their concentration in a relatively small region, it is not possible to be certain whether the event terms for normal events presented in Figure 3.37 are applicable to normal events in other regions in Japan. There were four shallow crustal events with a normal focal mechanism presented in the dataset used by Zhao et al. (2006a). Their locations are also presented in Figure 3.38. They are not in the same region as the normal events in the present study. Zhao et al. (2006a) reported that the term for normal events was positive and this term was set to zero in their model.

Figure 3.39(a) shows the coefficients for the linear magnitude terms, c_{cr}, c_{intS}, c_{intD} and c_{SL1} for SC-UM events, shallow and deep interface events and slab events with M_W<7.1 respectively. The values of c_{cr}, and c_{intD} are quite similar while the slab events have a much higher magnitude scaling rates than the other types of events at all spectral periods. The magnitude squared term c_{SL2} will enhance the overall magnitude scaling rate for the slab events with a magnitude less than about 6.3. Figure 3.39(b) shows the magnitude-squared term c_{SL2}. This coefficient is positive, varying between 0.0741 at spectral periods of 5.0s and 0.4364 at 0.10s. The subduction slab model by Zhao et al. (2006a) has a magnitude-squared term for the slab events and this term is also positive, leading to a rapid increase in the predicted spectrum with increasing magnitude. In fact, the positive magnitude-squared term in their model should be used only for small events. When the magnitude-squared term is used over the full magnitude range, it leads to an unrealistically large spectrum for large events. In the present study we used linear magnitude scaling for large events to ensure a realistic predicted spectrum for these events. The magnitude-squared term for small events will lead to a similar magnitude scaling rate for these events as in the Zhao et al. (2006a) model.

Figure 3.40(a) compares the anelastic attenuation rates (the absolute values of coefficients in percentage) for shallow crustal, upper mantle and shallow interface events. For spectral periods over 0.3s, shallow crustal events have the smallest anelastic attenuation rate, and the shallow interface events have the largest anelastic attenuation rate. At short periods less than 0.3s, upper mantle events have the largest anelastic attenuation rate. Because each event group has a different geometric attenuation coefficient, the differences in the anelastic attenuation rates between groups do not necessarily reflect the differences in the Q values between different tectonic locations. Generally, we would expect that the Q value in the upper mantle would be smaller than the Q value in the crust and the Q value in the crust close to the subduction trench would be smaller than the Q value in the other parts of the crust (Zhao 2010). Figure 3.40(b) compares the anelastic attenuation rates for shallow crustal and slab events and the depth dependent attenuation rate for slab events at a depth of 150km. At short periods up to 0.3s, the anelastic attenuation rate for shallow crustal events is considerably larger than that for slab events; at longer periods these two rates are similar. Figure 3.41(a) shows the near-field geometric attenuation coefficient g_N presented in Equations (3.6), (3.9) and (3.10) and in Table 3.12. The near-field attenuation coefficient has a negative value for spectral periods up to 2.5s and becomes positive at longer spectral periods. Figure 3.41(b) shows the far-field geometric attenuation coefficient g_{crL} in Equations (3.6), and in Tables 3.12.

Figure 3.42 shows the anelastic attenuation rates for travel paths within volcanic zones as shown in Figure 3.43. It is particularly interesting that the attenuation rate for the SC-UM events is the smallest in absolute value, that the slab events have the largest rates at spectral periods less than about 1.3s, and that the values for all three types of earthquake are similar at longer spectral periods, where they tend to zero. It is possible that the horizontal distance is shorter than the actual volcanic distance for deep events and that the difference increases within increasing fault depth. Using slant distance in the volcanic zones may lead to similar anelastic attenuation rates for all three earthquake categories. It is also possible that the lateral dimensions of the low-Q volcanic materials may increase with increasing depth. Because of the simple and to some extent arbitrary volcanic zones assigned by Zhao (2010), we cannot be certain on this aspect. A systematic 3-D Q-value inversion may be necessary to explain this feature.

Figure 3.44 presents the coefficients for the linear site terms from 3 models for SC II, SC III and SC IV sites. All linear site terms have a trough at 0.05–0.1s. The linear site terms for SC II sites have maximum values at around 0.3s which is the middle period for SC II sites. The linear site terms for SC III site have maximum values at about 0.5s which is also the middle period for SC III sites, while SC IV sites have peak values at periods over 1.0s. These results are very similar to those of Zhao et al. (2006a and 2006b). For SC II sites, the site terms for subduction interface records are generally larger than those from the other two types of events at most spectral periods. The values for the slab events are smaller than those for the other two types of events at short spectral periods up to 0.3s. At spectral periods over 1.25s the values for crustal and upper mantle records are smaller than those for the other two types of events as shown in Figure 3.44(a). For SC III sites, the site terms are nearly identical at spectral periods up to 0.3s, and the values for slab events are larger than the others as shown in Figure 3.44(b). For SC IV sites, the site terms from the three types of events are very similar for spectral periods up to 0.3s. At longer spectral periods, the terms for crustal and upper mantle have the largest values and the terms for subduction slab events have the smallest values. Table 3.15 presents the results of the *t*-test using the number of sites and the between-site standard deviations for three event-group pairs. In this table, a zero value indicates that the site terms for the event pairs do not differ at the 5%

significance level. The SC IV site terms for crustal and upper mantle events within a spectral period range of 0.35s–0.6s differ significantly from those of interface events. The SC IV site terms from SC-UM events within a spectral period range of 0.3s–1.5s differ significantly from those of the slab events, with the largest difference being about 20%. For all other event pairs most of the site terms are statistically similar and hence the same site terms can be used for these event pairs. For those site terms that are statistically different, the differences may be due to different frequency contents as suggested by the study of Zhao et al. (2009) and Zhao and Zhang (2010) or by coincidence.

Tables 3.16–3.18 present the within-site and between-site standard deviations derived from the within-event residuals by using a random effects model described in Equation (3.17), for SC-UM event group, subduction interface and subduction slab event groups. The between-site standard deviation is an indicator of how well the site terms in the GMPEs model the site effects, at least in theory. In this study site class is used as the site parameter. It is possible that the between-site standard deviation may be reduced if a better site parameter, such as site period, is adopted. The within-site residuals contain the random errors from path effects, and other random errors cannot be reduced by an improved model for site effect in theory. The ratio of σ_S/τ_S varies in a range of 0.65–1.58, but the average values in each site class and the overall average values are very close to 1.0.

For each site class, we define the total site standard deviation as

$$\sigma_{ST,k} = \sqrt{\sigma_{S,k}^2 + \tau_{S,k}^2} \tag{3.26}$$

where the subscript *k* denotes the site class number.

Figure 3.45 compares the total site standard deviations from four site classes with the within-event standard deviations for each earthquake. Figure 3.45(a) shows that the total site standard deviations for different site classes are similar to the within-event standard deviations, but the differences among different site classes are considerable at some spectral periods. For the SC-UM event group at spectral periods up to 0.6s, the total site standard deviations for SC IV sites are smaller than most of those of the other site classes and less than the within-event standard deviations. The SC IV total site standard deviations are the largest ones for spectral periods over about 0.8s. At very short periods, the total site standard deviations from all site classes are very similar. Figure 3.45(b) shows that SC III sites have the smallest standard deviations at short periods, and SC IV sites have the largest standard deviations at long periods. For slab events, Figure 3.45(c) shows that the standard deviations for all site classes are very similar at spectral periods over 0.5s. At short periods, SC I sites have the largest total-site standard deviation; the largest difference among the four site classes is close to 20%. These results show that the total site standard deviations tend to be large at spectral periods similar to the average site periods of each site class, presumably caused by resonate response of the soil sites, except for the slab events at long spectral periods. We do not have a plausible explanation for the similar standard deviations for slab event at spectral periods over 0.6s for all four site classes.

For both within- and between-site standard deviations, the differences among the four site classes are considerable at many spectral periods. Table 3.19 shows the *F*-test probabilities for the hypothesis that the within-site residuals from each pair of earthquake groups have statistically similar standard deviations. Table 3.20 shows the probabilities for the hypothesis that the between-site residuals from each pair of the earthquake groups have statistically similar standard deviations in each site class. The cells that have probabilities less 5% are

presented in bold font, meaning that the standard deviations of the two event groups differ at the 5% significance level. For within-site standard deviations about 28% of the pairs have statistically different values and only 23% of the pairs with statistically different between-site standard deviations. Statistically different within-site standard deviations mean that the path effects among different event groups are not modelled equally well. Statistically different between-site standard deviations suggest that the scatter due to site effect differs from one type of event to another, a possible result of interaction between site effect and earthquake categories as described by Zhao and Zhang (2010).

Figure 3.46–Figure 3.49 show the within-site and between-site standard deviations of SC II, SC III and SC IV sites for the three groups of events. Together with Table 3.19, Figure 3.46(a) shows that the within-site standard deviation of the SC I sites from the SR-UM group is statistically larger than from the subduction interface group in a spectral period range of 0.1–1.25s. The within-site standard deviation of the SC-UM group in a spectral period range of 0.4-0.6s is statistically larger than that of the subduction slab events. The within-site standard deviation of slab events is statistically larger than those of the interface events in a spectral period range of 0.1–1.0s, as shown in Table 3.19. The differences are practically significant too, with the largest difference about being 15%. Figure 3.46(b) shows that between-site standard deviations are very similar at spectral periods greater than 0.3s. However, the slab events have the largest values at short periods, while the SC-UM events have the smallest values for spectral periods less than 0.3s. These differences are statistically significant as shown in Table 3.20.

Figure 3.47 shows the within- and between-site standard deviations for SC II sites. The within-event standard deviations from each pair of earthquake groups are statistically different at only a smaller number of periods. Similar to SC I sites, the values for τ_S among the three models are statistically different at short periods up to 0.25s while they are very similar for the other spectral periods. The difference between the SC-UM and slab groups is statistically significant for PGA and spectral periods up to 0.25s, as shown in Table 3.20.

Figure 3.48 and Figure 3.49 show the within-site and between-site standard deviations for SC III and SC IV sites respectively. The differences among the three models are considerable and statistically significant at some spectral periods. For SC III sites, the between-site standard deviations at long periods are still similar but for SC IV sites they differ significantly. For all site classes for PGA and at short periods, the between-site standard deviation of the slab events is the largest and that of the SC-UM event group is the smallest, among the three event groups, as shown in Figure 3.49b.

Figure 3.50 shows the model standard deviations from the three GMPEs, and Table 3.21 presents the *F*-test probabilities among the three models. For the within-event standard deviations, the *F*-test probabilities are larger than 5% for all spectral periods. All three models have similar within-event standard deviations at many spectral periods. The differences between SC-UM and the two subduction groups in a period range of 0.4 and 1.25s and at a few other long spectral periods are statistically significant, with the *F*-test probabilities presented in Table 3.21 being less than 5%. The total standard deviations from the subduction slab events at PGA and in a spectral period range between 0.05s and 0.2s are much larger than those for the other two earthquake groups as shown in Figure 3.50(c). One possible interpretation for the statistically similar between-event standard deviation is that the source effects for the three event groups (four event source categories) are modelled uniformly well, with each event group having different magnitude scaling functions and depth terms. The statistically different within-event standard deviation among the three event

groups may suggest that the path and site effects are not modelled uniformly well. Zhao (2010) showed that the depth-scaled geometric attenuation functions with multiple-linear segments improved the model fitting significantly. The simple functions for the geometric attenuation used in the present study for the three event groups may mean that not all groups are modelled equally well. Of course, it is possible that one type of earthquake may have a larger inherent scatter than the others no matter how well the models perform.

Table 3.22 shows the coordinates for the volcanic zones used to compute the distance x^v, the portion of the straight line distance (the closest distance between a fault and a station) that passes through the volcanic zones.

3.6 PREDICTED RESPONSE SPECTRA

Though each model parameter has been smoothed with respect to the logarithm of spectral periods, the model does not provide smoothed spectra at all magnitude and distance ranges. The adjustment of the nonlinear soil site spectra leads to a broadly smoothed nonlinear spectrum. Next, we present the predicted spectra for various magnitude, depth and distance ranges.

Figure 3.51–Figure 3.54 show the predicted spectra for shallow crustal events with magnitudes of 5.0, 6.0, 7.0 and 8.0, a fault depth of 1km, and at a source distance of 1km for four site classes plus the rock sites. Note that the rock site spectrum and the SC I site spectrum are also presented in the figures for the four site classes, for easy comparisons between the soil spectra and the rock/SCI spectra. For a magnitude 5.0 event, the PGA is 0.54g for a SC I site, and 0.39g for a rock site. Among the spectral periods modelled, the largest SCI spectrum is 1.23g at 0.15s and the largest rock spectrum is 0.88g at 0.1s. The nonlinear soil spectrum is practically identical to the SC I spectrum. For SC II sites, the PGA for the nonlinear soil spectrum is 0.68g, reduced from 0.72g for the elastic soil spectrum. For SC III and SC IV sites, the nonlinear soil spectrum at short periods is about 15–20% less than the elastic soil spectrum. Figure 3.52(a) shows that for an M_W=6 event the SC I PGA is 0.84g, the rock site PGA is 0.61g and the nonlinear spectrum has a PGA of 0.80g, nearly identical to the SC I PGA. The PGA for the nonlinear soil spectrum is 0.80g for SC II sites, 0.80g for SC III sites and 0.77g for SC IV sites, as shown in Figure 3.52(b)–3.52(d). The nonlinear soil spectrum for both SC III and SC IV sites is much smaller than the elastic soil site spectrum in a spectral period range of 0.1–0.6s.

Figure 3.53 shows the predicted spectra for an M_W=7 event. The SC I PGA is 1.04g, the rock site PGA is 0.75 and the nonlinear soil site PGA is 1.03g. The nonlinear soil site PGA is 1.15g for SC II sites, 0.92g for SC III sites and 0.84g for SC IV sites, much smaller than those for the corresponding elastic soil PGAs. The nonlinear soil spectra for SC II, III and IV sites are much smaller than the elastic soil spectra in a spectral period range around the period of the peak spectra.

Figure 3.54 show the spectra from an M_W=8.0 event. The SC I PGA is 1.26g, the rock site PGA is 0.92g and the PGA for a SC IV nonlinear soil site spectrum is 0.88g. The increase from the PGA of a magnitude 7 event is small at short periods and zero at periods over 3s. The nonlinear site spectra for SC II, SC III and SC IV sites are markedly smaller than the corresponding elastic soil spectra in a considerable period range around the period of the peak SCI spectrum.

Figure 3.55 shows the attenuation of SC I spectrum with source distance for four shallow crustal events with a depth of 1km over a distance range of 1km to 300km. The term of $g_L(x_{i,j}+200)$ leads to a reduced geometric attenuation rate for distances over about 30km for all spectral periods. The change of the geometric attenuation rate is more obvious at long spectral periods than for short spectral periods, because of the reduced anelastic attenuation rates at long periods. The term g_N, a geometric attenuation coefficient for records within a source distance of 30km, is negative for spectral periods up to 2.5s as shown in Figure 3.41(a), leading to an increased geometric attenuation rate within a source distance of 30km. At spectral periods over 3s, g_N is positive, leading to a reduced geometric attenuation rate at short distances as shown in Figure 3.55(d). The magnitude scaling is not fully saturated at zero distance. Our shallow crustal model has a zero average residual for all records within a source distance of 30km. Even though the predicted values at a source distance of 1km are still a significant extrapolation from the data magnitude range, we believe that model predictions are reasonably well supported by the large near-source PGAs from the large earthquakes such as the 2008 Wenchuan in China (Lu et al. 2008a, 2008b), and the 2010 Darfield earthquake in New Zealand (Cousins and McVerry, 2010).

Figure 3.56–Figure 3.59 show the spectra from shallow subduction interface events with a magnitude of 5, 6, 7, and 8 at a source distance of 20km and a top-of-fault depth of 20km. For an M_W=5 event in Figure 3.56, the SC I site PGA is 0.086g and the rock site PGA is 0.062g. Among the periods that have been modelled, the peak SC I spectrum is 0.28g at a spectral period of 0.15s and the nonlinear soil spectra for all site classes are practically identical to the elastic soil spectra.

Figure 3.57 shows that, for an M_W=6 event, the SC I site PGA is 0.27g, the rock site PGA is 0.20g and the nonlinear site PGAs are close to the elastic soil PGA of 0.27g. The nonlinear soil site spectrum is nearly identical to the corresponding elastic soil spectrum for all site classes.

Figure 3.58 shows that, for an M_W=7 event, the SC I site PGA is 0.61g and the rock site PGA is 0.44g. The nonlinear soil site PGA is 0.61g for SC I sites, 0.78g for SC II sites, 0.62g for SC III sites and 0.64g for SC IV site. The nonlinear soil site spectrum is smaller than the corresponding elastic spectrum for SC II, III and IV sites in a narrow period range around the spectral period of the peak elastic soil site spectrum.

Figure 3.59 shows that the PGA from an M_W=8 events at SC I sites is 1.05g, and the rock site PGA is 0.76g. The nonlinear soil site PGA is 1.05g for SC I sites, 1.19g for SC II sites, 0.92g for SC III sites and 0.84g for SC IV sites. At short periods up to 0.15s at SC IV sites, the nonlinear soil spectra are less than the rock site spectra. The nonlinear soil site spectrum is much smaller than the elastic soil site spectrum in spectral periods up to 0.6s.

Figure 3.60 shows the spectra from an M_W=9.0 event with a top-of-fault depth of 14km at a source distance of 30km. The SC I PGA is 1.08g, and the rock PGA is 0.78g. The nonlinear soil site PGA is 1.08g for SC I sites, 1.21g for SC II sites, 0.94g for SC III sites and 0.85g for SC IV sites. The spectra from large subduction interface events as shown in Figure 3.59 and Figure 3.60 have a gentle "trench" centred at about 0.6s spectral periods. We attempted to eliminate this trench by adjusting the magnitude scaling rates at these spectral periods but the correction led to a significant reduction in the maximum log-likelihood. We believe that the "trench" is likely a result of very small number of large events in the dataset and no correction is adopted.

Figure 3.61 shows the attenuation of PGA, and spectra at 0.5s, 1.0s and 3.0s spectral periods from events with a magnitude of 5, 6, 7, 8 and 9 within a source distance range of 20–320km at a fault depth of 20km for the M_W=5-8 events, and a fault depth of 14km for the M_W=9 event. These figures clearly show the reduced magnitude scaling for events with M_W >7.0. The PGAs in Figure 3.61(a) are similar to the spectra at a spectral period of 0.5s as shown in Figure 3.61(b).

The between-event residuals for the subduction interface events in Figure 3.22(a), Figure 3.24(a), Figure 3.26(a) and Figure 3.28(a) shows that the overall modelling for the M_W=9.0 2011 Tohoku earthquake and the M_W=8.3 2003 Off Tokachi earthquake were reasonable; these results validate the selected bi-linear magnitude scaling for the subduction interface events. Figure 3.62 shows the residual factor of the between-event residuals, $\exp(-\eta_i)$ for each spectral period together with the factor for mean ±1 between-event standard deviation τ, i.e., $\exp(\pm\tau)$, for these two great subduction interface earthquakes. On average across all spectral periods, the response spectra from the 2003 M_W=8.3 Tokachi-Oki earthquake were underestimated by a factor of 0.92 and the long-period spectra over 2.0s were overestimated significantly, exceeding mean minus one between-event standard deviation. For the 2011 M_W=9.0 Tohoku earthquake, the spectra on average were overestimated by about 15% for all spectral periods and this is a fraction of the mean $\pm\ \tau$ factor.

Figure 3.63(a) shows the within-event residuals for all records from the Tohoku event and the trend line suggests predicted PGAs within a distance of 100km are larger than those for the records at large distances. The trend line fitted to the residuals is a second order polynomial of source distance and the trend line can be approximated by the following conventional attenuation function,

$$log_e(y_j) = glog_e(r_j) + ex_j + c \quad \textbf{(3.27)}$$

where g is the geometric attenuation coefficient, e is the anelastic attenuation coefficient, and c is a constant term. The biased residuals distribution within a distance range of 130km can be corrected by Equation (3.27) with g=-0.25, e=0.0 and c=1.24. This means that the anelastic attenuation for the shallow interface events is adequate for this earthquake if Equation 3.27 is used. In fact, because one earthquake does not produce median ground motions, the biased distribution in Figure 3.63(a) is tolerable. Figure 3.63(b) shows the residuals that is presented in Figure 3.63(a) but the trend line is a third order polynomial of source distance and clearly that the distribution is biased at a distance within about 70km and at a large distance over about 200km. The trend line is very similar to those fitted to the shallow crustal events in the Zhao (2010) study and the biased distribution was attributed to the Moho reflection effect. The ground motion from a shallow subduction interface event (within 25km) is likely to be affected by Moho reflection, at least in theory. The trend lines in Figure 3.63(b) cannot be described by Equation (3.27) adequately and the multi-segmented linear geometric attenuation functions similar to that used by Zhao (2010) in Equation (1.4) in section 1 should be used to eliminate the bias.

Figure 3.64–Figure 3.67 show the predicted spectra from subduction slab earthquakes with a depth of 30km, at a distance of 30km and with M_W = 5, 6, 7, and 8 respectively. Figure 3.65 shows that a magnitude 5 event has a PGA of 0.10g at SC I sites and 0.072g at rock sites. For the other three site classes, the elastic and nonlinear soil site PGAs are nearly identical at about 0.12g.

Figure 3.65 shows that the PGA for a slab event with M_W=6 is 0.18g at a SC I site and 0.13g at a rock site. Again, the elastic and nonlinear soil site PGAs are nearly identical and varies between 0.18–0.21g, suggesting that the nonlinear soil response is not significant at this level of ground shaking.

Figure 3.66 shows the spectra from an M_W=7 subduction slab event at a source distance of 30km. The SCI site PGA is 0.53g, the rock site PGA is 0.38g and the nonlinear site PGA varies between 0.53g at a SC I site and 0.64g at a SC II site while the soil site PGA for SC III and IV sites is smaller than that of the SC II sites. The nonlinear soil site spectra for SC II, III and IV sites are generally very similar to the corresponding elastic soil site spectra and are marginally smaller than the elastic soil spectra in a spectral period range of 0.1–0.4s.

Figure 3.67 shows that the SC I PGA is 0.92g for slab events with a moment magnitude of 8.0. The rock site PGA is 0.67g and the nonlinear soil site PGA is 0.92g, 1.02g, 0.86g and 0.78g for SC I, SC II, SC III and SC IV sites respectively. The effect of nonlinear soil response is evident in Figure 3.67(b), (c) and (d) in a period range around the period of the peak elastic soil spectrum.

Figure 3.68 presents the attenuation of PGA and spectra at periods of 0.5s, 1.0s and 3.0s with source distance. Because of the positive values of the magnitude-squared term at short periods, the increase in the spectrum with magnitude increasing from 5.0 to 6.0 is much smaller than that from 6.0 to 7.0, as shown in Figure 3.68(a) for PGA and (b) for 0.5s spectra. The increase in the spectrum from magnitude 7.0 to magnitude 8.0 event is smaller than from 5.0 to 6.0 and from 6.0 to 7.0 at all spectral periods.

Figure 3.69 shows the effect of volcanic path on the predicted response spectra for a shallow crustal, a shallow subduction interface and a slab event with a magnitude of 7.0 and at a distance of 60km. The top-of-fault depth is 1km for the crustal event, 20km for the subduction interface event and 40km for the slab event. The distance within volcanic zones is 0, 20, 40, and 60km. The attenuation within the volcanic zone is evident. The SC I PGA from the crustal event is reduced from 0.088g for a zero volcanic distance to 0.078, 0.069 and 0.060g at volcanic distances of 20, 40, and 60km respectively, as shown in Figure 3.69(a). For the interface event, the SC I PGA is 0.15, 0.12, 0.10 and 0.080g at a volcanic zone distance of 0, 20, 40 and 60km, respectively, as shown in Figure 3.69(b). The volcanic path effect for the subduction interface event is larger than that for the shallow crustal event. Figure 3.69(c) shows that the volcanic path effect for slab events is much greater than those for shallow crustal and subduction interface events. The SC I PGA is 0.25g, 0.18g, 0.098g and 0.073g at a volcanic distance of 0, 20, 40 and 60km. For all events, the volcanic path effect diminishes to a negligible level at long spectral periods over about 1.0s.

Discussion and conclusions

We have presented a set of ground-motion prediction equations (GMPEs) based on the strong-motion records from four categories of earthquakes in Japan – shallow crustal events with a focal depth of 25km or less, upper mantle events that are above the subduction interface but with a depth over 25km, subduction interface, and subduction slab events. We combined the shallow crustal and upper mantle (SC-UM) events as one group, because of the relatively small number of records in the upper mantle category, and developed a GMPE for this group plus two separate GMPEs for the subduction interface and slab events. The models used simple geometric attenuation functions, with the coefficients differing among different earthquake categories. The model adopted a linear magnitude term for events with an $M_W \geq 7.1$ and the coefficient for this magnitude term was much smaller than that for the

events with M_W<7.1. The magnitude scaling rate for the large events was taken from a study by Zhao (2014) and Zhao et al. (2014), using depth-dependent geometric attenuation functions both from the Zhao (2010) study and those presented in Section 1. Site classes based on site period were used as the site term. The effect of volcanoes on the attenuation of seismic waves was modelled by applying an anelastic attenuation rate to the horizontal portion of a straight line distance (closest distance), between the fault plane and the recording station that passes through the assumed low-Q zones around the active volcanoes.

We have tested the effect of site information quality. We found that the overall goodness-of-fit of the attenuation models improved significantly after records from sites for which the site classes were inferred from H/V response spectral ratios or geological descriptions, were excluded. The model coefficients presented in the present study are from records obtained from stations that had a measured shear-wave velocity profile down to engineering bedrock. We also separated the within-event residuals into within-site and between-site residuals using an approximate random effects model. The separation enabled us to investigate if the differences among the separately estimated site terms from the three earthquake groups were statistically significant at a given significance level, such as 5%.

The GMPEs of the three earthquake groups – shallow crustal and upper mantle (SC-UM) events, subduction interface, and subduction slab events – were found to have three differing sets of linear site terms, but all had common nonlinear site terms apart from a factor used to obtain a smoothed nonlinear soil spectrum. Because the number of records with strong nonlinear soil response was still small, the nonlinear site terms could not be assessed by the model's goodness-of-fit. Using the linear site terms and the between-site residuals we compared the linear site terms from the three models. The *t*-test results suggested that for many spectral periods the site terms were not statistically different. However, the terms for SC IV sites derived from the SC-UM group differ statistically from those of the subduction slab group in a period range of 0.3–2.0s. In a period range of 0.35–0.6s, the terms for SC IV sites from the SC-UM events differed from those of the subduction interface events. For nearly all other spectral periods the linear site terms from the three models were statistically similar. This means that the average of the three site terms could be used for all three models, if so desired.

We found that the amplification ratios for the SC I sites (rock), with respect to hard-rock sites (i.e., sites with a shear-wave velocity of 760m/s or more at ground surface), was large. Some SC I sites had V_{S30} values (the travel time averaged shear-wave velocity to a depth of 30m) well over 1000m/s. We fitted a linear function of site period to the within-event residuals from the SC I sites and used the intercept of the fitted model as the logarithm of the deamplification ratio. The rock spectrum can be obtained by, dividing the SC I spectrum by the deamplification ratios. We refer the logarithm of the deamplification ratio as the hard-rock site term. The smoothed deamplification ratios varied from 1.054 (at 0.05s spectral period) to 2.05 (at 0.3s). The peak ground acceleration (PGA) deamplification ratio was 1.38. Some of the large deamplification ratios may have been caused by the presence of thin layers of soft soil and large impedance ratios. Because the soil layers were thin, very little nonlinear response would be expected to develop under moderately strong ground shaking.

We found that the models for SC-UM and subduction interface records had a magnitude-distance oversaturation, i.e., the response spectrum at source (zero distance) decreased with increasing magnitude. This effect cannot be justified physically, and so to eliminate it we adopted a distance constant term. Another way of removing the effect was to reduce one of

the near-source terms. However, this method was rejected because the near-source term was based on the relationship of earthquake magnitude and fault length, and we felt that a significant reduction of either was not physically plausible.

We also presented the within-site and between-site standard deviations derived from the within-event residuals. If the site model is improved, the between-site standard deviations can be reduced, while the within-site standard deviations can be reduced if the model for path effect is improved, in theory. On average, the within-site and between-site standard deviations from different earthquake groups were very similar but some differed significantly. It is possible to use different standard deviations for different site classes and for different earthquake categories, but is only necessary if the standard deviations are statistically different. We tested the between-site and within-site residuals from three models to check whether they had statistically similar standard deviations. Our results suggested that only 20% of the combinations in three earthquake-group pairs (at 25 spectral periods) had statistically different between-site standard deviations, and that only 30% of the within-event standard deviations were statistically different. When the different spectra from a probabilistic seismic hazard analysis using different standard deviation values are obtained but the standard deviations selected are statistically similar, the differences in the calculated hazard spectra are not meaningful. The results from the statistical tests among different standard deviations presented in this manuscript are therefore important.

Three sets of within-event and between-event standard deviations have been presented. The smallest ratio of within-event standard deviations from each pair of earthquake groups was 0.91 and the largest ratio was 1.08. Also the between-event standard deviations from the three models did not differ statistically. The within-event standard deviations among the three models varied moderately; with the smallest ratio of within-event standard deviations from each model pair being 0.88 and the largest ratio being 1.25. The total standard deviation ratios between each model pair varied between 0.93 and 1.11 among the three models.

We found that the magnitude scaling rates for subduction slab events were considerably larger than those for the other types of earthquakes, and that a magnitude-squared term was necessary for the slab events. We also found that the normal shallow crustal events produced larger response spectra than the reverse and strike-slip events. The spectra from the reverse and strike-slip events were similar. However, the normal shallow crustal events were all located above the fault plane of the M_W=9.0 2011 Tohoku earthquake, and occurred after this great event. It is possible, therefore, that the event term from these normal events may not be applicable to normal shallow crustal earthquakes in other regions of Japan or in the other parts of the world.

A set of anelastic attenuation rates for the portion of the straight line distance (the shortest distance between the fault plane and a station) that passes through volcanic zones was derived for the three groups of earthquakes. The absolute values of the anelastic attenuation rates from different tectonic categories of earthquakes differed significantly, with the values for subduction slab events being the largest and the values for the SC-UM events being the smallest among the three models. It is possible that these differences are caused by the use of horizontal volcanic distance in our model, as the difference between the horizontal volcanic distance and the slant distance within the volcanic zones increases with increasing depth, leading to large attenuation rates for deep earthquakes. It is also possible that the lateral dimensions of the low-Q materials in the volcanic zones increase with increasing depth. That increase could lead to large anelastic volcanic-zone attenuation rates for subduction slab events, because the subduction slab events are generally deeper than the

events in the other tectonic categories. Our approach to the modelling of volcanic zones appears to be more plausible than using a factor for fore-arc and back-arc stations (Boore et al. 2009 and Ghofrani and Atkinson 2014). Also our modelling approach has a self-correction effect for Japan, i.e., if the length of the volcanic path is larger than the actual values, the anelastic attenuation rate for the volcanic effect will be smaller. Our purpose in modelling the volcanic path is not only to model the volcanic effect accurately, but also to improve the models for other subduction zones without the presence of volcanoes. If the volcanic effect is not modelled, the effect will be buried in the increased standard deviations.

If our model is used for other subduction zones where there are no volcanic zones, the effect of the volcanoes in Japan will be essentially removed when we assign a zero value to the corresponding terms for the volcanic effect.

The nonlinear soil site terms were derived from equivalent linear 1-D analyses on site models based on the shear-wave velocity profiles of the Kik-net stations as described in Section 2. However, for SC III and SC IV sites, the Kik-net stations tended to have thick soil layers. For a given site period, the average shear-wave velocity of the soil is proportional to the layer thickness. Therefore, the impedance ratio as defined in Section 2 would be smaller for a deeper soil site (given the same rock site shear-wave velocity). As we did not model the effect of impedance ratios in the present study, the nonlinear soil site terms were calculated from the average impedance ratios of the selected Kik-net stations, though we believe that the GMPE presented in this report is probably more suitable for soil sites with low impedance ratios (i.e., less than 3.5), than for soil sites with high impedance ratios.

Another undesirable feature of the present models is the discontinuity at the boundaries between various earthquake groups. For example, the predicted spectra from an earthquake with a depth smaller than 25km (shallow crustal events) would differ from those from an upper mantle earthquake with a depth of 26km. The subduction interface events have the same depth boundary problem. We did not attempt to put all events in one tectonic category and then use continuous variables to model all the observed differences. Although it can be done in theory, it would be impossible to do in practice until we understand the characteristics of different earthquake categories and have a sizeable and a similar number of records from each category so that data in the most numeral group would not affect the estimates for the coefficients from the least numeral group. Another problem is the uncertainty associated with earthquake classification, especially the poorly constrained assumption of a depth tolerance of 5km above or below the subduction interface for defining subduction interface events. We would recommend that for an event located at one or other of the boundaries, to account for the error range associated with the event classification, the users can take the average ground motion from the two competing models, at least until the creation of a model that does not have an abrupt change in parameters between the event categories.

Table 3.1 Site class definitions used in the present study and the approximately corresponding NEHRP site classes (BSSC 2000).

Site class	Description	Natural period	V_{30} calculated from site period	NEHRP site classes
SC I	Rock	$T < 0.2s$	$V_{30} > 600$	A+B+C
SC II	Hard soil	$0.2 \leq T < 0.4s$	$300 < V_{30} \leq 600$	C
SC III	Medium soil	$0.4 \leq T < 0.6s$	$200 < V_{30} \leq 300$	D
SC IV	Soft soil	$T \geq 0.6s$	$V_{30} \leq 200$	E+F

Table 3.2 Number of events in each region and each focal mechanism group for all events from Japan.

Earthquake category	Focal mechanism			Total in each EQ category
	Reverse	Strike-slip	Normal	
Crustal	36	21	19	76
Upper mantle	26	5	16	47
Interface	75		1	76
Slab	98	13	25	136
Total in each FM group	**235**	**39**	**61**	**335**

Table 3.3 Number of records in each tectonic category and each focal mechanism group, for all records from Japan.

Tectonic category	Focal mechanism			Subtotal in each EQ category
	Reverse	Strike-slip	Normal	
	SC I			
Crustal	969	649	482	2100
Upper mantle	491	101	393	985
Interface	1563			1563
Slab	1618	105	308	2031
Subtotal in each FM group	**4641**	**855**	**1183**	**6679**
	SC II			
Crustal	580	365	302	1247
Upper mantle	311	60	206	577
Interface	995			995
Slab	1103	86	165	1354
Subtotal in each FM group	**2989**	**511**	**673**	**4173**
	SC III			
Crustal	209	116	115	440
Upper mantle	77	17	49	143
Interface	360			360
Slab	365	19	59	443
Subtotal in each FM group	**1011**	**152**	**223**	**1386**
	SC IV			
Crustal	392	208	182	782
Upper mantle	182	31	70	283
Interface	656		2	658
Slab	693	55	134	882
Subtotal in each FM group	**1923**	**294**	**388**	**2605**
Total in each FM group	**10564**	**1812**	**2467**	**14843**

Table 3.4 Number of selected events in each earthquake category and each focal mechanism group from Japan.

Earthquake category	Focal mechanism			Total in each EQ category
	Reverse	Strike-slip	Normal	
Crustal	35	17	18	**70**
Upper mantle	26	5	16	**47**
Interface	60			**60**
Slab	95	10	20	**125**
Total in each FM group	**216**	**32**	**54**	**302**

Table 3.5 Number of selected records in each earthquake category and each focal mechanism group.

Earthquake category	Focal mechanism			Subtotal in each EQ category
	Reverse	Strike-slip	Normal	
	SC I			
Crustal	959	535	474	1968
Upper mantle	485	101	393	979
Interface	1497			1497
Slab	1609	91	303	2003
Subtotal in each FM group	**4550**	**727**	**1170**	**6447**
	SC II			
Crustal	560	266	238	1064
Upper mantle	296	60	206	562
Interface	787			787
Slab	1057	79	157	1293
Subtotal in each FM group	**2700**	**405**	**601**	**3706**
	SC III			
Crustal	203	80	88	371
Upper mantle	71	17	49	137
Interface	285			285
Slab	344	13	58	415
Subtotal in each FM group	**903**	**110**	**195**	**1208**
	SC IV			
Crustal	374	92	146	612
Upper mantle	169	31	64	264
Interface	547			547
Slab	672	52	127	851
Subtotal in each FM group	**1762**	**175**	**337**	**2274**
Total in each FM group	**9915**	**1417**	**2303**	**13635**

Table 3.6 Average deamplification ratios with respect to SC I sites, exp(-S_{1N}), for engineering bedrock with a surface shear-wave velocity over 760m/s.

No.	Period (s)	A_{mSCI}	No.	Period (s)	A_{mSCI}	No.	Period (s)	A_{mSCI}	No.	Period (s)	A_{mSCI}
1	0.02	1.380	8	0.35	2.052	15	0.8	1.822	22	3.5	1.387
2	0.05	1.054	9	0.4	2.025	16	1	1.791	23	4	1.341
3	0.1	1.196	10	0.45	1.999	17	1.25	1.724	24	4.5	1.301
4	0.15	1.568	11	0.5	1.975	18	1.5	1.667	25	5	1.265
5	0.2	1.916	12	0.5	1.931	19	2	1.574			
6	0.25	2.014	13	0.6	1.891	20	2.5	1.500			
7	0.3	2.054	14	0.7	1.855	21	3	1.439			

Table 3.7 Parameters for nonlinear site terms for all sites.

	SC I	SC II	SC III	SC IV
φ	3.5	3.0	2.5	3.0
γ_N	0.8	1.0	0.9	0.6
I_{mfav}	0.910	1.023	1.034	0.737
I_{mav}	3.73	3.07	2.76	3.02
α	2.0			
β	0.6			

Table 3.8 Parameters for nonlinear site terms for SC I and SC II sites.

No.	Period (s)	A_{max1D}	S_{c1D}
		SC I	
1	0.02	1.913	8.629
2	0.05	1.956	5.316
3	0.1	2.093	18.06
		SC II	
1	0.02	2.050	1.95
2	0.05	1.996	1.82
3	0.1	2.112	4.01
4	0.15	2.219	5.50
5	0.2	2.413	6.80
6	0.25	2.554	8.50
7	0.3	2.586	10.67

Table 3.9 Maximum amplification ratios and cross-over rock spectrum from 1-D analyses for SC III sites.

No.	Period (s)	A_{max1D}	S_{c1D}	No.	Period (s)	A_{max1D}	S_{c1D}
1	0.02	1.914	1.112	8	0.35	2.179	2.304
2	0.05	1.852	1.184	9	0.4	2.288	2.236
3	0.1	2.033	1.869	10	0.45	2.402	2.217
4	0.15	2.104	2.571	11	0.5	2.522	2.243
5	0.2	2.054	2.913	12	0.6	2.648	2.805
6	0.25	1.925	2.719	13	0.7	2.780	6.658
7	0.3	2.006	2.418				

Table 3.10 Maximum amplification ratios and cross-over rock spectrum from 1-D analyses for SCIV sites.

No.	Period (s)	A_{max1D}	S_{c1D}	No.	Period (s)	A_{max1D}	S_{c1D}
1	0.02	1.521	0.867	11	0.5	1.945	1.625
2	0.05	1.368	0.810	12	0.6	1.976	1.525
3	0.1	1.603	1.217	13	0.7	2.025	1.397
4	0.15	1.741	1.516	14	0.8	2.043	1.320
5	0.2	1.809	1.700	15	0.9	2.022	1.266
6	0.25	1.832	1.790	16	1	1.970	1.227
7	0.3	1.861	1.823	17	1.25	1.843	1.221
8	0.35	1.886	1.790	18	1.5	1.729	1.318
9	0.4	1.908	1.768	19	2	1.729	2.125
10	0.45	1.928	1.675	20	2.5	1.729	2.932

Table 3.11 Adjustment factors for cross-over rock site spectrum.

T (s)	Shallow crustal				Upper mantle				Subduction interface				Subduction slab			
	I	II	III	IV	I	II	III	IV	I	II	III	IV	I	II	III	IV
0.02	1.0	1.0	1.0	1.0	1.0	1.0	1.0	1.0	1.0	1.0	1.0	1.0	1.0	1.0	1.0	1.0
0.05	1.0	1.0	1.0	1.0	1.0	1.0	1.0	1.0	1.0	1.0	1.0	1.0	1.0	1.0	1.0	1.0
0.1	1.0	1.0	1.2	1.120	1.0	1.0	1.20	1.0	1.0	1.1	1.25	1.25	1.0	1.2	1.30	1.0
0.15	1.0	1.0	1.2	1.140	1.0	0.85	1.10	1.0	0.0	1.0	1.20	1.0	0.0	0.950	1.19	1.0
0.2	0.0	0.920	0.800	1.030	0.0	0.85	0.88	1.0	0.0	1.0	0.900	0.930	0.0	0.850	0.928	1.0
0.25	0.0	0.921	0.550	0.943	0.0	0.85	0.65	1.0	0.0	1.0	0.700	0.930	0.0	0.850	0.645	1.0
0.3	0.0	0.761	0.470	0.867	0.0	0.80	0.54	0.90	0.0	1.0	0.675	0.950	0.0	0.825	0.625	1.0
0.35	0.0	1.0	0.486	0.823	0.0	1.0	0.55	0.95	0.0	1.0	0.737	0.950	0.0	1.0	0.655	1.0
0.4	0.0	1.0	0.490	0.804	0.0	1.0	0.55	0.95	0.0	1.0	0.797	1.0	0.0	1.0	0.685	1.0
0.45	0.0	1.0	0.512	0.787	0.0	1.0	0.57	1.0	0.0	1.0	0.850	1.0	0.0	1.0	0.715	1.0
0.5	0.0	1.0	0.538	0.792	0.0	1.0	0.60	1.0	0.0	1.0	0.900	1.0	0.0	1.0	0.745	1.0
0.6	0.0	1.0	0.605	0.827	0.0	0.0	0.65	1.0	0.0	1.0	0.950	1.0	0.0	1.0	0.775	1.0
0.7	0.0	0.0	0.730	0.882	0.0	0.0	0.85	1.0	0.0	0.0	1.0	1.0	0.0	1.0	0.805	1.0
0.8	0.0	0.0	0.920	0.949	0.0	0.0	0.90	1.0	0.0	0.0	1.0	1.0	0.0	0.0	0.835	1.0
0.9	0.0	0.0	1.0	1.0	0.0	0.0	1.0	1.0	0.0	0.0	1.0	1.0	0.0	0.0	1.0	1.0
1	0.0	0.0	1.0	1.0	0.0	0.0	1.0	1.0	0.0	0.0	0.0	1.0	0.0	0.0	1.0	1.0
1.25	0.0	0.0	0.0	1.0	0.0	0.0	0.0	1.0	0.0	0.0	0.0	1.0	0.0	0.0	1.0	1.0
1.5	0.0	0.0	0.0	1.0	0.0	0.0	0.0	1.0	0.0	0.0	0.0	1.0	0.0	0.0	1.0	1.0
2	0.0	0.0	0.0	1.0	0.0	0.0	0.0	1.0	0.0	0.0	0.0	1.0	0.0	0.0	0.0	1.0
2.5	0.0	0.0	0.0	1.0	0.0	0.0	0.0	1.0	0.0	0.0	0.0	0.80	0.0	0.0	0.0	1.0
3	0.0	0.0	0.0	0.0	0.0	0.0	0.0	0.0	0.0	0.0	0.0	0.0	0.0	0.0	0.0	0.0

Table 3.12 Model parameters for shallow crustal and upper mantle (SC-UM) earthquakes.

T (s)	c_1	c_2	c_{cr}	d_{cr}	F_N	b_{cr}	g_{cr}	g_{UM}	g_{crN}	g_L
PGA	-3.519	0.9	1.0896	0.200	0.3196	0.00908	-1.2570	-1.0930	-0.4953	1.2408
0.05	-3.852	0.95	1.0259	0.200	0.3141	0.00302	-1.1929	-1.0420	-0.4052	1.1735
0.10	-4.189	1	1.0030	0.200	0.3816	0.00224	-0.8730	-0.7660	-0.6068	1.2002
0.15	-4.882	1.1	1.1046	0.200	0.3616	0.00388	-0.9916	-0.8316	-0.7650	1.5518
0.20	-5.233	1.151	1.1752	0.200	0.3298	0.01064	-1.1050	-0.9094	-0.8408	1.7568
0.25	-5.229	1.151	1.2736	0.200	0.2977	0.01465	-1.2051	-0.9985	-0.8863	1.9067
0.30	-5.226	1.151	1.3325	0.200	0.2683	0.01712	-1.2792	-1.0712	-0.9177	2.0251
0.35	-5.223	1.151	1.3823	0.200	0.2423	0.01866	-1.3427	-1.1375	-0.9342	2.1184
0.40	-5.221	1.151	1.4255	0.200	0.2196	0.01957	-1.3980	-1.1972	-0.9391	2.1929
0.45	-5.218	1.151	1.4635	0.200	0.2000	0.02005	-1.4467	-1.2511	-0.9354	2.2533
0.50	-5.216	1.151	1.4976	0.190	0.1830	0.02023	-1.4899	-1.2996	-0.9280	2.3045
0.60	-5.213	1.151	1.5565	0.178	0.1555	0.01996	-1.5634	-1.3834	-0.8965	2.3803
0.70	-5.21	1.151	1.6063	0.162	0.1350	0.01918	-1.6233	-1.4529	-0.8546	2.4337
0.80	-5.208	1.151	1.6494	0.148	0.1196	0.01809	-1.6728	-1.5112	-0.8056	2.4708
0.90	-5.206	1.151	1.6874	0.136	0.1081	0.01680	-1.7142	-1.5607	-0.7531	2.4968
1.00	-5.204	1.151	1.7215	0.125	0.0996	0.01540	-1.7490	-1.6030	-0.6994	2.5150
1.25	-5.200	1.151	1.7936	0.101	0.0873	0.01163	-1.8140	-1.6856	-0.5675	2.5388
1.50	-5.196	1.151	1.8525	0.083	0.0829	0.00775	-1.8563	-1.7446	-0.4447	2.5451
2.00	-5.191	1.151	1.9454	0.053	0.0842	0.00017	-1.8975	-1.8196	-0.2345	2.5356
2.50	-5.187	1.151	2.0175	0.030	0.0842	-0.00695	-1.9027	-1.8607	-0.0518	2.5057
3.00	-5.183	1.151	2.0764	0.011	0.0842	-0.01356	-1.8857	-1.8822	0.0959	2.4747
3.50	-5.181	1.151	2.1262	0.000	0.0842	-0.01971	-1.8543	-1.8915	0.2157	2.4453
4.00	-5.178	1.151	2.1368	0.000	0.0842	-0.02546	-1.8129	-1.8929	0.3131	2.4187
4.50	-5.176	1.151	2.1368	0.000	0.0842	-0.03085	-1.7645	-1.8889	0.3942	2.3936
5.00	-5.174	1.151	2.1368	0.000	0.0842	-0.03593	-1.7108	-1.8812	0.4730	2.3627

Table 3.12 Model parameters for shallow crustal and upper mantle earthquakes (*continued*).

T (s)	e_{cr}	e_{um}	e_{cr}^{V}	γ_{cr}	S_2	S_3	S_4	σ	τ	σ_T
PGA	-0.00757	-0.01058	-0.00628	-9.177	0.2775	0.1341	0.2212	0.555	0.416	0.694
0.05	-0.00954	-0.01219	-0.00706	-8.460	0.1320	-0.0617	0.0020	0.564	0.498	0.752
0.10	-0.01246	-0.01373	-0.00741	-8.312	0.1515	-0.0804	-0.0013	0.641	0.492	0.808
0.15	-0.01110	-0.01353	-0.00743	-10.028	0.3648	0.1153	0.2102	0.665	0.426	0.790
0.20	-0.00966	-0.01298	-0.00725	-11.173	0.5240	0.3200	0.4128	0.691	0.382	0.790
0.25	-0.00833	-0.01224	-0.00697	-12.330	0.5907	0.4959	0.5892	0.695	0.368	0.786
0.30	-0.00749	-0.01150	-0.00664	-13.249	0.5779	0.5895	0.6895	0.688	0.373	0.782
0.35	-0.00674	-0.01080	-0.00627	-13.975	0.5337	0.6384	0.7382	0.674	0.376	0.772
0.40	-0.00614	-0.01016	-0.00589	-14.607	0.4991	0.6776	0.7861	0.667	0.384	0.769
0.45	-0.00563	-0.00958	-0.00551	-15.165	0.4735	0.7028	0.8322	0.665	0.379	0.765
0.50	-0.00515	-0.00905	-0.00514	-15.669	0.4485	0.7184	0.8693	0.664	0.379	0.765
0.60	-0.00437	-0.00814	-0.00442	-16.543	0.4025	0.7304	0.9237	0.669	0.380	0.769
0.70	-0.00375	-0.00738	-0.00376	-17.285	0.3631	0.7152	0.9598	0.670	0.388	0.774
0.80	-0.00325	-0.00675	-0.00316	-17.931	0.3300	0.6803	0.9835	0.673	0.399	0.782
0.90	-0.00285	-0.00621	-0.00262	-18.504	0.3022	0.6526	0.9985	0.672	0.404	0.784
1.00	-0.00252	-0.00574	-0.00214	-19.018	0.2790	0.6301	1.0074	0.669	0.407	0.784
1.25	-0.00194	-0.00484	-0.00118	-20.120	0.2362	0.5889	1.0123	0.660	0.413	0.779
1.50	-0.00159	-0.00419	-0.00052	-21.034	0.2085	0.5610	1.0030	0.655	0.411	0.774
2.00	-0.00130	-0.00333	0.0	-22.515	0.1788	0.5256	0.9666	0.629	0.392	0.742
2.50	-0.00129	-0.00279	0.0	-23.685	0.1666	0.5038	0.9231	0.604	0.390	0.719
3.00	-0.00145	-0.00243	0.0	-24.668	0.1619	0.4886	0.8803	0.590	0.377	0.701
3.50	-0.00171	-0.00217	0.0	-25.522	0.1601	0.4770	0.8407	0.577	0.377	0.689
4.00	-0.00204	-0.00197	0.0	-26.050	0.1591	0.4675	0.8051	0.555	0.386	0.676
4.50	-0.00239	-0.00181	0.0	-26.463	0.1576	0.4593	0.7736	0.542	0.391	0.668
5.00	-0.00275	-0.00165	0.0	-26.830	0.1550	0.4519	0.7459	0.536	0.422	0.683

Table 3.13 Model parameters for subduction interface earthquakes.

T (s)	c_1	c_2	c_{int}	c_{intS}	d_{int}	γ_{intS}	b_{int}	g_{intS}	g_{intL}
PGA	-5.276	1.151	1.0689	1.3695	0.553	-3.9575	0.01918	-2.0762	1.0638
0.05	-5.259	1.151	1.0346	1.3338	0.553	-3.9575	0.02307	-2.3560	1.0471
0.10	-5.246	1.151	0.9846	1.3045	0.553	-3.9575	0.02423	-2.1479	1.1050
0.15	-5.239	1.151	1.0398	1.2715	0.553	-3.9575	0.01478	-2.0100	1.3443
0.20	-5.233	1.151	1.0857	1.2079	0.553	-3.8800	0.00844	-1.9590	1.5843
0.25	-5.229	1.151	1.1454	1.1865	0.553	-3.8665	0.00424	-1.9356	1.7607
0.30	-5.226	1.151	1.2055	1.1929	0.553	-3.9618	0.00124	-1.9192	1.9161
0.35	-5.223	1.151	1.2624	1.2034	0.553	-4.0089	0.0	-1.9112	2.0322
0.40	-5.221	1.151	1.3152	1.2012	0.553	-3.9430	0.0	-1.9063	2.1275
0.45	-5.218	1.151	1.3639	1.2117	0.553	-3.9395	0.0	-1.9023	2.2021
0.50	-5.216	1.151	1.4088	1.2246	0.553	-3.9420	0.0	-1.8995	2.2632
0.60	-5.213	1.151	1.4889	1.2538	0.553	-3.9540	0.0	-1.8937	2.3549
0.70	-5.210	1.151	1.5580	1.2893	0.560	-4.0035	0.0	-1.8876	2.4204
0.80	-5.208	1.151	1.6184	1.3328	0.580	-4.0067	0.0	-1.8815	2.4447
0.90	-5.206	1.151	1.6716	1.3669	0.602	-3.9763	0.0	-1.8754	2.4631
1.00	-5.204	1.151	1.7190	1.3939	0.622	-3.9215	0.0	-1.8695	2.4773
1.25	-5.200	1.151	1.8172	1.4718	0.667	-3.9393	0.0	-1.8561	2.4967
1.50	-5.196	1.151	1.8937	1.5343	0.705	-3.9421	0.0	-1.8449	2.5011
2.00	-5.191	1.151	2.0027	1.6293	0.768	-3.9837	0.0	-1.8299	2.5010
2.50	-5.187	1.151	2.0720	1.6969	0.820	-4.0556	0.0	-1.8237	2.4919
3.00	-5.183	1.151	2.1145	1.7415	0.863	-4.1628	0.0	-1.8248	2.4912
3.50	-5.181	1.151	2.1374	1.7636	0.902	-4.2520	0.0	-1.8321	2.4958
4.00	-5.178	1.151	2.1452	1.7724	0.935	-4.3548	0.0	-1.8441	2.5007
4.50	-5.176	1.151	2.1452	1.7719	0.966	-4.4802	0.0	-1.8604	2.5193
5.00	-5.174	1.151	2.1452	1.7758	0.994	-4.5702	0.0	-1.8876	2.5130

Table 3.13 Model parameters for subduction interface earthquakes (*continued*).

T (s)	e_{intS}	e_{int}^{V}	γ	S_2	S_3	S_4	σ	τ	σ_T
PGA	-0.00619	-0.01100	-4.1714	0.3326	0.1144	0.2338	0.568	0.373	0.680
0.05	-0.00552	-0.01216	-2.2640	0.1818	-0.0493	0.0369	0.586	0.445	0.736
0.10	-0.00760	-0.01446	-2.7290	0.1884	-0.0374	0.1016	0.651	0.465	0.800
0.15	-0.00920	-0.01312	-4.0841	0.4463	0.0648	0.1852	0.670	0.396	0.779
0.20	-0.01000	-0.01188	-5.2198	0.5901	0.2379	0.3106	0.689	0.383	0.789
0.25	-0.01033	-0.01074	-6.2471	0.6453	0.3875	0.4329	0.670	0.364	0.762
0.30	-0.01044	-0.00971	-7.2525	0.6443	0.5131	0.5462	0.651	0.345	0.736
0.35	-0.01040	-0.00878	-8.1104	0.5978	0.5996	0.6304	0.644	0.353	0.735
0.40	-0.01024	-0.00795	-8.8822	0.5596	0.6615	0.6969	0.637	0.348	0.726
0.45	-0.01010	-0.00720	-9.5643	0.5276	0.7060	0.7503	0.630	0.357	0.724
0.50	-0.00982	-0.00653	-10.1559	0.5003	0.7341	0.7903	0.621	0.360	0.718
0.60	-0.00928	-0.00540	-11.1739	0.4559	0.7679	0.8527	0.622	0.375	0.726
0.70	-0.00876	-0.00447	-12.0259	0.4213	0.7617	0.8779	0.634	0.387	0.743
0.80	-0.00850	-0.00372	-12.6729	0.3934	0.7389	0.8990	0.636	0.392	0.747
0.90	-0.00825	-0.00309	-13.2450	0.3705	0.6962	0.8990	0.636	0.396	0.749
1.00	-0.00799	-0.00258	-13.7596	0.3513	0.6711	0.8990	0.640	0.400	0.755
1.25	-0.00742	-0.00163	-14.8462	0.3147	0.6291	0.8990	0.641	0.401	0.756
1.50	-0.00686	-0.00103	-15.6822	0.2889	0.5839	0.8990	0.649	0.389	0.756
2.00	-0.00600	-0.00039	-16.9045	0.2558	0.5268	0.8990	0.638	0.382	0.744
2.50	-0.00538	-0.00014	-17.6955	0.2364	0.4742	0.8990	0.624	0.390	0.736
3.00	-0.00482	0.0	-18.2492	0.2247	0.4463	0.8697	0.605	0.382	0.715
3.50	-0.00442	0.0	-18.6283	0.2176	0.4309	0.8329	0.586	0.374	0.696
4.00	-0.00408	0.0	-18.8419	0.2137	0.4102	0.7932	0.575	0.375	0.686
4.50	-0.00379	0.0	-19.0197	0.2118	0.4004	0.7517	0.559	0.372	0.671
5.00	-0.00375	0.0	-19.0197	0.2115	0.3906	0.7091	0.574	0.378	0.687

Table 3.14 Model parameters for subduction slab earthquakes.

T (s)	c_1	c_2	c_{SL1}	c_{SL2}	d_{SL}	b_{SL}	g_{SL}	g_{SLL}	$e_{SL}{}^{V}$
PGA	-5.276	1.151	1.4510	0.3935	0.476	0.0196	-2.0128	1.1023	-0.01491
0.05	-5.259	1.151	1.5127	0.4201	0.300	0.0201	-1.8799	1.0747	-0.01685
0.10	-5.246	1.151	1.4893	0.4364	0.370	0.0211	-1.5879	1.1620	-0.01778
0.15	-5.239	1.151	1.4321	0.3878	0.450	0.0205	-1.6726	1.4165	-0.01675
0.20	-5.233	1.151	1.4456	0.3224	0.509	0.0194	-1.8204	1.6359	-0.01512
0.25	-5.229	1.151	1.4826	0.2842	0.555	0.0188	-1.9564	1.8129	-0.01386
0.30	-5.226	1.151	1.5207	0.2533	0.593	0.0184	-2.0707	1.9556	-0.01251
0.35	-5.223	1.151	1.5525	0.2221	0.625	0.0181	-2.1640	2.0720	-0.01128
0.40	-5.221	1.151	1.5828	0.1959	0.652	0.0180	-2.2408	2.1680	-0.01018
0.45	-5.218	1.151	1.6116	0.1738	0.675	0.0179	-2.3037	2.2482	-0.00920
0.50	-5.216	1.151	1.6388	0.1551	0.695	0.0178	-2.3556	2.3158	-0.00832
0.60	-5.213	1.151	1.6889	0.1255	0.729	0.0178	-2.4336	2.4224	-0.00682
0.70	-5.210	1.151	1.7339	0.1036	0.756	0.0179	-2.4861	2.5016	-0.00561
0.80	-5.208	1.151	1.7746	0.0872	0.778	0.0180	-2.5208	2.5616	-0.00462
0.90	-5.206	1.151	1.8116	0.0749	0.796	0.0182	-2.5426	2.6078	-0.00381
1.00	-5.204	1.151	1.8456	0.0656	0.812	0.0183	-2.5547	2.6438	-0.00314
1.25	-5.200	1.151	1.9195	0.0513	0.841	0.0186	-2.5577	2.7038	-0.00192
1.50	-5.196	1.151	1.9815	0.0449	0.861	0.0188	-2.5373	2.7376	-0.00114
2.00	-5.191	1.151	2.0810	0.0434	0.884	0.0188	-2.4670	2.7675	-0.00033
2.50	-5.187	1.151	2.1583	0.0481	0.900	0.0184	-2.3844	2.7763	0.0
3.00	-5.183	1.151	2.2210	0.0546	0.900	0.0177	-2.3185	2.7898	0.0
3.50	-5.181	1.151	2.2732	0.0610	0.900	0.0168	-2.2453	2.7931	0.0
4.00	-5.178	1.151	2.3177	0.0665	0.900	0.0156	-2.1756	2.7957	0.0
4.50	-5.176	1.151	2.3560	0.0709	0.900	0.0144	-2.1143	2.8016	0.0
5.00	-5.174	1.151	2.3896	0.0741	0.900	0.0130	-2.0046	2.7709	0.0

Table 3.14 Model parameters for subduction slab earthquakes (*continued*).

T (s)	e_{SL}	e_{SLH}	γ	S_2	S_3	S_4	σ	τ	σ_T
PGA	-0.00306	-0.00070	-9.7609	0.2346	0.1522	0.1475	0.587	0.458	0.745
0.05	-0.00495	-0.00070	-10.0206	0.0701	-0.0810	-0.0666	0.607	0.557	0.824
0.10	-0.00685	-0.00070	-11.1535	0.0928	-0.0261	0.0083	0.673	0.573	0.884
0.15	-0.00660	-0.00070	-11.8432	0.3154	0.1798	0.1945	0.696	0.489	0.850
0.20	-0.00584	-0.00070	-12.6583	0.4808	0.3452	0.3379	0.712	0.412	0.823
0.25	-0.00508	-0.00072	-13.4916	0.5711	0.4679	0.4436	0.710	0.389	0.810
0.30	-0.00440	-0.00077	-14.2359	0.5816	0.5597	0.5240	0.682	0.367	0.775
0.35	-0.00382	-0.00083	-14.8680	0.5299	0.6309	0.5868	0.665	0.374	0.763
0.40	-0.00332	-0.00090	-15.4389	0.4893	0.6913	0.6364	0.657	0.383	0.761
0.45	-0.00288	-0.00099	-15.9591	0.4566	0.7322	0.6760	0.647	0.390	0.756
0.50	-0.00251	-0.00107	-16.4368	0.4297	0.7596	0.7082	0.640	0.402	0.756
0.60	-0.00190	-0.00123	-17.2882	0.3880	0.7885	0.7558	0.633	0.410	0.754
0.70	-0.00144	-0.00139	-18.0299	0.3573	0.7965	0.7881	0.632	0.431	0.765
0.80	-0.00108	-0.00153	-18.6866	0.3338	0.7930	0.8102	0.635	0.435	0.770
0.90	-0.00081	-0.00166	-19.2754	0.3154	0.7828	0.8252	0.636	0.437	0.772
1.00	-0.00061	-0.00178	-19.8087	0.3006	0.7689	0.8350	0.637	0.438	0.772
1.25	-0.00032	-0.00201	-20.9549	0.2741	0.7272	0.8457	0.635	0.446	0.776
1.50	-0.00025	-0.00217	-21.9039	0.2567	0.6841	0.8450	0.645	0.446	0.784
2.00	-0.00048	-0.00235	-23.4133	0.2360	0.6080	0.8298	0.632	0.424	0.761
2.50	-0.00100	-0.00237	-24.5851	0.2245	0.5491	0.8094	0.607	0.412	0.734
3.00	-0.00162	-0.00230	-25.5372	0.2174	0.5055	0.7896	0.582	0.406	0.710
3.50	-0.00240	-0.00216	-26.3351	0.2127	0.4745	0.7721	0.562	0.394	0.687
4.00	-0.00326	-0.00196	-27.0189	0.2092	0.4535	0.7578	0.540	0.382	0.661
4.50	-0.00416	-0.00173	-27.6151	0.2065	0.4406	0.7463	0.526	0.365	0.640
5.00	-0.00500	-0.00164	-28.1418	0.2042	0.4342	0.7348	0.523	0.375	0.643

Table 3.15 *T-test* on linear site terms for 3 pairs of earthquake groups.

Periods	Crustal & Upper mantle			Interface			Crustal & Upper mantle		
	Interface			Slab			Slab		
	SC II	SC III	SC IV	SC II	SC III	SC IV	SC II	SC III	SC IV
PGA	0	0	0	0	0	0	0	0	0
0.05	0	0	0	1	0	0	0	0	0
0.1	0	0	0	0	0	0	0	0	0
0.15	0	0	0	0	0	0	0	0	0
0.2	0	0	0	0	0	0	0	0	0
0.25	0	0	1	0	0	0	0	0	1
0.3	0	0	1	0	0	0	0	0	1
0.35	0	0	1	0	0	0	0	0	1
0.4	0	0	0	0	0	0	0	0	1
0.45	0	0	0	0	0	0	0	0	1
0.5	0	0	0	0	0	0	0	0	1
0.6	0	0	0	0	0	0	0	0	1
0.7	0	0	0	0	0	0	0	0	1
0.8	0	0	0	0	0	0	0	0	1
0.9	0	0	0	0	0	0	0	0	1
1	0	0	0	0	0	0	0	0	1
1.25	0	0	0	0	0	0	0	0	1
1.5	0	0	0	0	0	0	0	0	1
2	0	0	0	0	0	0	0	0	1
2.5	0	0	0	0	0	0	0	0	0
3	0	0	0	0	0	0	0	0	0
3.5	0	0	0	0	0	0	0	0	0
4	0	0	0	0	0	0	0	0	0
4.5	0	0	0	0	0	0	0	0	0
5	0	0	0	0	0	0	0	0	0

Table 3.16 Within-site and between-site standard deviations for shallow crustal and upper mantle earthquakes.

T (s)	SCI			SCII			SCIII			SCIV		
	σ_S	τ_S	σ_{ST}	σ_S	τ_S	σ_{ST}	σ_S	τ_S	σ_{ST}	σ_S	τ_S	σ_{ST}
PGA	0.414	0.358	0.547	0.436	0.360	0.565	0.423	0.351	0.549	0.442	0.280	0.523
0.05	0.405	0.403	0.571	0.429	0.381	0.574	0.417	0.350	0.545	0.443	0.295	0.533
0.10	0.438	0.494	0.661	0.448	0.449	0.634	0.425	0.423	0.600	0.441	0.417	0.607
0.15	0.459	0.482	0.666	0.455	0.480	0.661	0.438	0.452	0.629	0.470	0.385	0.607
0.20	0.473	0.470	0.666	0.481	0.494	0.690	0.449	0.445	0.632	0.482	0.399	0.626
0.25	0.478	0.465	0.667	0.489	0.547	0.734	0.463	0.419	0.624	0.485	0.395	0.625
0.30	0.490	0.459	0.671	0.498	0.527	0.725	0.484	0.435	0.651	0.493	0.375	0.619
0.35	0.491	0.445	0.663	0.503	0.488	0.701	0.478	0.469	0.670	0.491	0.343	0.599
0.40	0.494	0.430	0.655	0.506	0.472	0.692	0.472	0.482	0.674	0.478	0.347	0.590
0.45	0.492	0.432	0.654	0.504	0.466	0.687	0.494	0.463	0.677	0.478	0.360	0.599
0.50	0.488	0.434	0.653	0.512	0.450	0.682	0.494	0.433	0.657	0.476	0.401	0.622
0.60	0.478	0.441	0.651	0.515	0.450	0.684	0.484	0.459	0.667	0.485	0.446	0.659
0.70	0.465	0.443	0.642	0.502	0.453	0.676	0.481	0.470	0.672	0.470	0.498	0.685
0.80	0.459	0.450	0.643	0.493	0.452	0.669	0.474	0.458	0.660	0.483	0.518	0.709
0.90	0.454	0.459	0.645	0.482	0.456	0.664	0.455	0.471	0.655	0.472	0.536	0.714
1.00	0.447	0.468	0.647	0.471	0.461	0.659	0.442	0.464	0.641	0.471	0.524	0.704
1.25	0.441	0.464	0.639	0.459	0.461	0.650	0.438	0.448	0.626	0.463	0.494	0.677
1.50	0.428	0.455	0.624	0.449	0.470	0.650	0.421	0.464	0.627	0.457	0.496	0.674
2.00	0.414	0.419	0.589	0.437	0.454	0.631	0.416	0.476	0.632	0.432	0.521	0.677
2.50	0.400	0.408	0.572	0.434	0.431	0.612	0.395	0.457	0.604	0.413	0.507	0.654
3.00	0.403	0.405	0.571	0.432	0.417	0.600	0.399	0.405	0.569	0.416	0.486	0.640
3.50	0.402	0.388	0.558	0.421	0.396	0.578	0.413	0.382	0.562	0.426	0.492	0.651
4.00	0.382	0.378	0.537	0.427	0.369	0.564	0.405	0.323	0.518	0.425	0.448	0.617
4.50	0.376	0.368	0.526	0.431	0.361	0.562	0.391	0.306	0.497	0.426	0.436	0.609
5.00	0.382	0.363	0.527	0.440	0.330	0.550	0.376	0.309	0.486	0.420	0.377	0.564

Table 3.17 Within-site and between-site standard deviations for subduction interface earthquakes.

T (s)	SCI			SCII			SCIII			SCIV		
	σ_S	τ_S	σ_{ST}	σ_S	τ_S	σ_{ST}	σ_S	τ_S	σ_{ST}	σ_S	τ_S	σ_{ST}
PGA	0.394	0.414	0.572	0.453	0.416	0.615	0.419	0.369	0.558	0.458	0.346	0.574
0.05	0.395	0.468	0.613	0.457	0.434	0.630	0.432	0.371	0.569	0.469	0.363	0.593
0.10	0.416	0.564	0.701	0.461	0.503	0.682	0.431	0.417	0.599	0.473	0.442	0.647
0.15	0.422	0.555	0.697	0.467	0.558	0.728	0.439	0.428	0.613	0.473	0.475	0.670
0.20	0.431	0.530	0.683	0.493	0.530	0.724	0.436	0.426	0.610	0.494	0.465	0.678
0.25	0.428	0.494	0.653	0.491	0.552	0.739	0.432	0.392	0.583	0.488	0.434	0.653
0.30	0.425	0.471	0.634	0.495	0.506	0.707	0.417	0.416	0.589	0.474	0.432	0.641
0.35	0.416	0.475	0.632	0.506	0.467	0.689	0.417	0.451	0.614	0.465	0.439	0.640
0.40	0.417	0.451	0.614	0.487	0.483	0.686	0.412	0.452	0.611	0.458	0.429	0.628
0.45	0.423	0.425	0.600	0.481	0.483	0.682	0.409	0.440	0.601	0.453	0.421	0.619
0.50	0.414	0.416	0.587	0.473	0.464	0.662	0.401	0.432	0.590	0.453	0.435	0.628
0.60	0.401	0.416	0.578	0.468	0.443	0.644	0.402	0.435	0.592	0.435	0.443	0.621
0.70	0.401	0.424	0.583	0.462	0.450	0.645	0.401	0.454	0.606	0.441	0.456	0.634
0.80	0.398	0.428	0.585	0.462	0.447	0.642	0.409	0.444	0.604	0.442	0.471	0.646
0.90	0.402	0.429	0.588	0.450	0.445	0.633	0.409	0.443	0.603	0.431	0.485	0.649
1.00	0.408	0.452	0.609	0.445	0.444	0.629	0.408	0.422	0.587	0.428	0.499	0.657
1.25	0.412	0.455	0.614	0.438	0.456	0.632	0.412	0.425	0.592	0.435	0.506	0.667
1.50	0.414	0.462	0.620	0.451	0.447	0.635	0.430	0.429	0.608	0.431	0.499	0.660
2.00	0.419	0.465	0.626	0.446	0.458	0.639	0.418	0.466	0.625	0.429	0.518	0.673
2.50	0.410	0.442	0.603	0.446	0.446	0.630	0.422	0.450	0.617	0.442	0.522	0.684
3.00	0.399	0.410	0.572	0.448	0.445	0.631	0.404	0.407	0.573	0.437	0.522	0.681
3.50	0.391	0.393	0.554	0.442	0.427	0.615	0.406	0.354	0.538	0.431	0.531	0.684
4.00	0.392	0.376	0.544	0.451	0.408	0.608	0.402	0.367	0.544	0.421	0.537	0.682
4.50	0.386	0.364	0.531	0.451	0.398	0.601	0.388	0.350	0.522	0.404	0.527	0.664
5.00	0.399	0.350	0.530	0.473	0.416	0.630	0.376	0.308	0.486	0.393	0.514	0.647

Table 3.18 Within-site and between-site standard deviations for subduction slab earthquakes.

T (s)	SCI			SCII			SCIII			SCIV		
	σ_S	τ_S	σ_{ST}	σ_S	τ_S	σ_{ST}	σ_S	τ_S	σ_{ST}	σ_S	τ_S	σ_{ST}
PGA	0.398	0.510	0.647	0.418	0.450	0.614	0.410	0.431	0.594	0.417	0.423	0.594
0.05	0.387	0.586	0.703	0.423	0.480	0.640	0.410	0.426	0.591	0.424	0.442	0.613
0.10	0.429	0.622	0.756	0.418	0.564	0.702	0.394	0.514	0.648	0.429	0.565	0.709
0.15	0.449	0.604	0.752	0.440	0.594	0.739	0.420	0.497	0.650	0.441	0.555	0.709
0.20	0.462	0.587	0.747	0.450	0.596	0.747	0.443	0.493	0.663	0.434	0.560	0.708
0.25	0.474	0.550	0.725	0.470	0.609	0.770	0.461	0.447	0.642	0.431	0.506	0.664
0.30	0.471	0.524	0.705	0.475	0.567	0.739	0.439	0.495	0.661	0.432	0.486	0.650
0.35	0.468	0.496	0.682	0.477	0.518	0.704	0.444	0.533	0.694	0.433	0.464	0.635
0.40	0.457	0.477	0.661	0.483	0.488	0.687	0.454	0.545	0.709	0.417	0.468	0.627
0.45	0.450	0.459	0.643	0.477	0.476	0.674	0.477	0.529	0.713	0.408	0.464	0.618
0.50	0.446	0.449	0.633	0.469	0.467	0.662	0.472	0.494	0.683	0.409	0.468	0.622
0.60	0.448	0.434	0.624	0.461	0.464	0.654	0.460	0.473	0.659	0.407	0.434	0.595
0.70	0.439	0.429	0.614	0.460	0.463	0.653	0.462	0.475	0.662	0.404	0.431	0.590
0.80	0.442	0.426	0.614	0.459	0.457	0.648	0.458	0.459	0.648	0.407	0.456	0.611
0.90	0.435	0.431	0.612	0.456	0.466	0.652	0.450	0.443	0.631	0.409	0.454	0.611
1.00	0.427	0.440	0.613	0.448	0.471	0.650	0.442	0.445	0.628	0.409	0.463	0.618
1.25	0.412	0.440	0.603	0.442	0.475	0.649	0.428	0.436	0.611	0.411	0.447	0.608
1.50	0.416	0.449	0.612	0.448	0.472	0.651	0.419	0.464	0.625	0.417	0.445	0.610
2.00	0.409	0.441	0.602	0.437	0.461	0.635	0.407	0.472	0.623	0.413	0.439	0.603
2.50	0.398	0.425	0.582	0.430	0.426	0.605	0.388	0.483	0.620	0.415	0.426	0.594
3.00	0.390	0.396	0.556	0.423	0.402	0.584	0.371	0.444	0.579	0.413	0.429	0.595
3.50	0.386	0.386	0.545	0.410	0.401	0.574	0.378	0.431	0.573	0.402	0.411	0.575
4.00	0.377	0.373	0.530	0.412	0.384	0.563	0.364	0.402	0.542	0.394	0.393	0.556
4.50	0.361	0.364	0.512	0.412	0.374	0.556	0.368	0.382	0.530	0.386	0.369	0.534
5.00	0.360	0.358	0.507	0.446	0.326	0.552	0.378	0.320	0.495	0.379	0.331	0.503

Table 3.19 Probabilities (unit: percentage) from *F-test* for within-site residuals for 3 pairs of earthquake groups.

Period (s)	Crustal & Upper mantle / interface				Crustal & Upper mantle / Slab				Interface / Slab			
	SCI	SCII	SCIII	SCIV	SCI	SCII	SCIII	SCIV	SCI	SCII	SCIII	SCIV
0.02	**1.9**	28.7	77.5	61.3	10.6	37.7	58.4	8.6	41.1	7.9	84.6	**4.3**
0.05	18.2	**4.7**	51.7	29.4	10.5	86.9	80.1	23.0	89.4	7.7	40.1	**3.5**
0.1	**1.4**	47.8	85.4	14.3	86.3	8.2	17.0	63.5	**3.3**	**3.3**	17.2	6.1
0.15	**0.0**	59.3	97.0	67.9	73.0	67.8	52.0	10.4	**0.1**	39.1	55.4	30.9
0.2	**0.0**	61.2	51.7	87.2	69.1	8.6	93.8	**0.3**	**0.0**	5.6	57.7	**0.5**
0.25	**0.0**	92.9	15.3	81.9	79.5	53.8	91.9	**0.2**	**0.0**	67.3	14.3	**1.0**
0.3	**0.0**	72.8	**0.3**	14.6	26.3	35.5	5.0	**0.0**	**0.0**	66.8	23.8	7.8
0.35	**0.0**	90.3	**0.7**	**5.0**	10.3	25.5	17.0	**0.0**	**0.0**	28.9	14.5	22.3
0.4	**0.0**	15.1	**0.7**	9.8	**0.2**	41.6	55.4	**0.0**	**0.0**	47.6	**3.5**	7.6
0.45	**0.0**	6.8	**0.0**	6.1	**0.0**	21.7	59.9	**0.0**	**0.1**	45.7	**0.2**	**4.3**
0.5	**0.0**	**0.4**	**0.0**	8.0	**0.0**	**1.1**	43.2	**0.0**	**0.0**	49.0	**0.1**	5.7
0.6	**0.0**	**0.1**	**0.0**	**0.1**	**2.0**	**0.1**	38.9	**0.0**	**0.0**	69.2	**0.6**	33.6
0.7	**0.0**	**0.4**	**0.0**	**4.1**	6.7	**1.3**	55.6	**0.0**	**0.0**	46.6	**0.3**	13.6
0.8	**0.0**	**2.3**	**0.3**	**0.7**	35.7	6.7	61.7	**0.0**	**0.0**	49.5	**1.4**	16.8
0.9	**0.0**	**1.8**	**3.7**	**0.6**	28.9	22.1	92.3	**0.0**	**0.0**	20.3	**3.6**	59.2
1	**0.0**	5.5	11.2	**0.3**	22.9	33.1	74.4	**0.0**	**0.8**	29.1	7.0	77.6
1.25	**0.4**	8.3	21.8	**3.7**	**2.8**	62.1	84.7	**0.3**	41.5	20.6	30.7	59.9
1.5	14.0	98.1	71.2	5.2	68.5	40.6	87.6	**3.0**	30.2	50.9	82.6	97.1
2	61.2	64.3	97.9	51.4	77.8	34.4	87.0	38.8	81.6	73.8	90.8	91.3
2.5	23.4	45.3	23.1	19.8	42.1	48.7	96.5	43.0	67.1	88.1	22.9	55.5
3	95.2	32.2	88.4	43.3	74.3	74.9	24.3	65.3	82.2	48.4	23.9	69.2
3.5	35.4	14.1	84.3	99.8	44.1	83.4	20.2	51.7	83.3	20.3	34.2	55.1
4	17.2	13.1	83.3	51.3	49.4	91.2	9.8	25.2	48.1	10.9	19.5	70.6
4.5	20.3	21.0	83.6	11.9	51.1	66.7	42.2	8.9	7.5	10.5	60.1	95.7
5	20.7	29.3	88.2	11.0	39.8	24.1	53.9	29.4	**4.7**	98.9	65.8	49.4

Table 3.20 Probabilities (unit: percentage) from *F-test* for between-site residuals for 3 pairs of earthquake groups.

T (s)	Crustal & Upper mantle/Interface				Crustal & Upper mantle/Slab				Interface/Slab			
	SCI	SCII	SCIII	SCIV	SCI	SCII	SCIII	SCIV	SCI	SCII	SCIII	SCIV
0.02	**2.7**	8.1	77.7	**1.1**	**0.0**	**0.0**	**4.7**	**0.0**	**0.0**	**3.2**	13.0	**0.2**
0.05	5.6	15.5	82.6	**1.7**	**0.0**	**0.0**	6.3	**0.0**	**0.0**	**1.6**	14.5	**0.3**
0.1	**3.2**	20.6	74.6	73.0	**0.0**	**0.0**	8.3	**0.0**	**3.0**	**1.5**	6.6	**0.1**
0.15	**1.5**	9.1	49.6	**1.1**	**0.0**	**0.0**	46.4	**0.0**	**5.8**	6.6	20.0	**2.6**
0.2	5.2	75.6	60.1	7.8	**0.0**	**0.1**	38.5	**0.0**	**3.2**	**0.8**	20.8	**0.8**
0.25	55.0	56.2	49.7	30.4	**0.1**	5.4	60.1	**0.0**	**2.0**	**2.8**	27.5	**1.7**
0.3	91.2	11.5	71.2	8.3	**0.8**	23.3	17.3	**0.0**	**2.7**	**1.5**	12.0	**4.0**
0.35	25.8	9.5	78.5	**0.2**	**2.0**	28.1	17.4	**0.0**	28.4	**1.6**	14.4	17.2
0.4	42.9	69.1	64.5	**0.9**	**2.4**	46.1	20.3	**0.0**	19.7	31.8	11.9	7.2
0.45	48.7	94.9	75.7	7.7	16.8	50.9	18.4	**0.0**	7.1	59.6	14.2	**4.6**
0.5	24.2	93.9	90.5	45.0	41.0	26.1	20.0	**1.2**	8.3	35.3	29.9	9.0
0.6	13.4	53.5	62.6	81.0	84.9	27.5	75.4	71.6	26.0	13.3	46.6	57.0
0.7	20.3	57.5	72.5	18.6	63.3	36.0	89.4	25.9	50.0	19.5	65.8	89.6
0.8	13.2	49.6	67.7	17.5	27.7	51.3	99.9	33.3	73.9	24.2	70.3	74.9
0.9	5.9	37.7	52.9	18.5	23.0	46.4	47.9	16.6	56.9	15.7	94.6	90.9
1	17.6	28.6	34.2	49.0	24.6	49.4	56.2	33.5	89.3	12.5	72.8	77.0
1.25	33.1	44.8	51.6	81.8	39.9	47.2	66.8	57.8	93.0	19.5	83.7	45.8
1.5	71.9	14.2	36.8	91.5	87.9	76.6	84.7	47.7	86.1	12.3	51.4	43.7
2	14.9	59.0	73.3	87.8	16.2	66.7	92.5	14.8	99.6	39.6	82.1	21.1
2.5	40.6	88.5	74.8	85.3	28.2	89.3	57.4	12.5	81.9	80.6	42.2	10.1
3	62.9	65.6	99.3	41.3	83.9	97.4	29.2	38.9	81.2	67.9	34.1	11.5
3.5	73.0	54.6	52.9	33.7	82.6	47.1	14.4	13.6	62.1	90.4	5.6	**2.1**
4	40.3	23.0	16.4	**2.3**	95.4	13.4	**0.7**	38.1	43.5	75.9	23.8	**0.3**
4.5	33.8	23.2	13.6	**1.1**	72.0	15.2	**0.8**	25.2	24.8	80.1	28.5	**0.1**
5	18.5	**0.0**	88.0	**0.0**	33.2	26.2	34.6	58.3	3.9	1.9	45.5	**0.0**

Table 3.21 Probabilities (unit: percentage) from *F-test* for between- and within-event residuals for 3 pairs of earthquake groups.

T (s)	Between-event residuals			Within-event residuals		
	Cru.&UM/ Interface	Cru.&UM/ Slab	Interface/ Slab	Cru.&UM/ Interface	Cru.&UM/ Slab	Interface/ Slab
0.02	26.7	31.9	5.8	12.6	**0.0**	8.6
0.05	27.6	23.8	**4.3**	**1.1**	**0.0**	5.4
0.1	52.5	12.9	6.6	35.3	**0.1**	5.9
0.15	43.2	17.5	6.3	60.6	**0.3**	**4.3**
0.2	85.7	58.0	53.0	90.5	**4.3**	6.9
0.25	83.8	77.3	66.0	**2.5**	14.6	**0.1**
0.3	43.3	65.5	66.4	**0.1**	46.1	**0.8**
0.35	51.2	74.4	68.8	**0.5**	23.9	9.4
0.4	34.9	83.9	43.3	**0.4**	22.8	8.3
0.45	54.5	83.1	43.4	**0.1**	**2.7**	14.9
0.5	58.6	55.0	30.4	**0.0**	**0.3**	11.9
0.6	88.8	41.6	42.4	**0.0**	**0.0**	39.1
0.7	95.6	28.5	35.9	**0.0**	**0.0**	73.3
0.8	88.5	32.3	34.7	**0.0**	**0.0**	75.3
0.9	83.3	39.6	37.0	**0.0**	**0.0**	79.3
1	84.2	45.8	42.4	**0.4**	**0.0**	56.8
1.25	75.4	44.4	35.3	6.0	**0.2**	42.2
1.5	54.7	40.0	20.2	54.2	19.6	60.6
2	74.1	41.6	32.5	34.1	92.2	41.1
2.5	93.9	57.9	59.8	**3.8**	90.1	5.9
3	96.0	44.6	57.1	12.0	25.5	**1.3**
3.5	91.3	64.2	62.6	31.1	5.4	**0.7**
4	78.5	84.9	90.2	**3.7**	6.9	**0.0**
4.5	60.0	32.1	78.4	6.9	5.1	**0.0**
5	26.0	18.6	93.5	**0.2**	18.6	**0.0**

Table 3.22 The latitudes and longitudes at the corners of each approximate volcanic zone.

Zone number	Latitude					Longitude				
	1	2	3	4	5	1	2	3	4	5
1	45.64	43.89	43.70	44.15	46.00	149.42	145.81	145.20	144.90	149.02
2	43.80	43.55	43.20	43.40		144.47	144.80	143.90	143.72	
3	43.00	43.45	43.80	43.80	43.50	143.17	142.40	142.60	143.10	143.30
4	42.52	42.27	42.90	43.10		141.76	141.00	140.40	141.00	
5	42.20	42.25	42.00	41.70	41.70	140.10	140.70	141.20	141.29	141.00
6	41.55	41.53	39.60	39.60		140.87	141.29	141.10	140.60	
7	39.05	38.55	38.00	38.00	39.05	140.90	140.85	140.63	140.02	139.96
8	37.76	37.00	37.04	37.88		140.40	140.15	139.68	140.02	
9	36.30	36.60	37.00	36.50	36.30	138.13	137.40	138.05	139.00	139.00
10	36.90	36.35	36.50	37.00	37.00	139.90	139.21	139.00	139.20	139.68
11	35.89	35.70	36.18	36.30	36.30	138.00	137.26	136.40	136.68	137.40
12	35.50	33.30	33.30	35.30		139.10	140.15	139.45	138.40	
13	33.30	31.79	31.79	33.30		140.15	140.56	139.80	139.45	
14	33.51	32.72	32.90	33.60		131.88	131.53	131.10	131.45	
15	32.72	32.62	32.96	33.00		131.20	130.40	130.40	131.00	
16	32.10	31.22	29.50	29.50	32.10	131.20	130.91	130.00	129.40	130.85
17	41.60	41.60	41.40	41.40		139.20	139.50	139.50	139.20	
18	40.75	40.55	40.55	40.75		140.40	140.40	140.15	140.15	

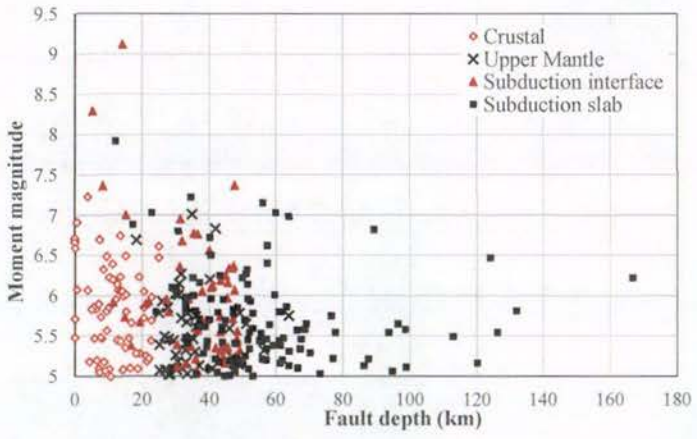

Figure 3.1 The distribution of strong-motion records used in the present study with respect to fault depth and moment magnitude.

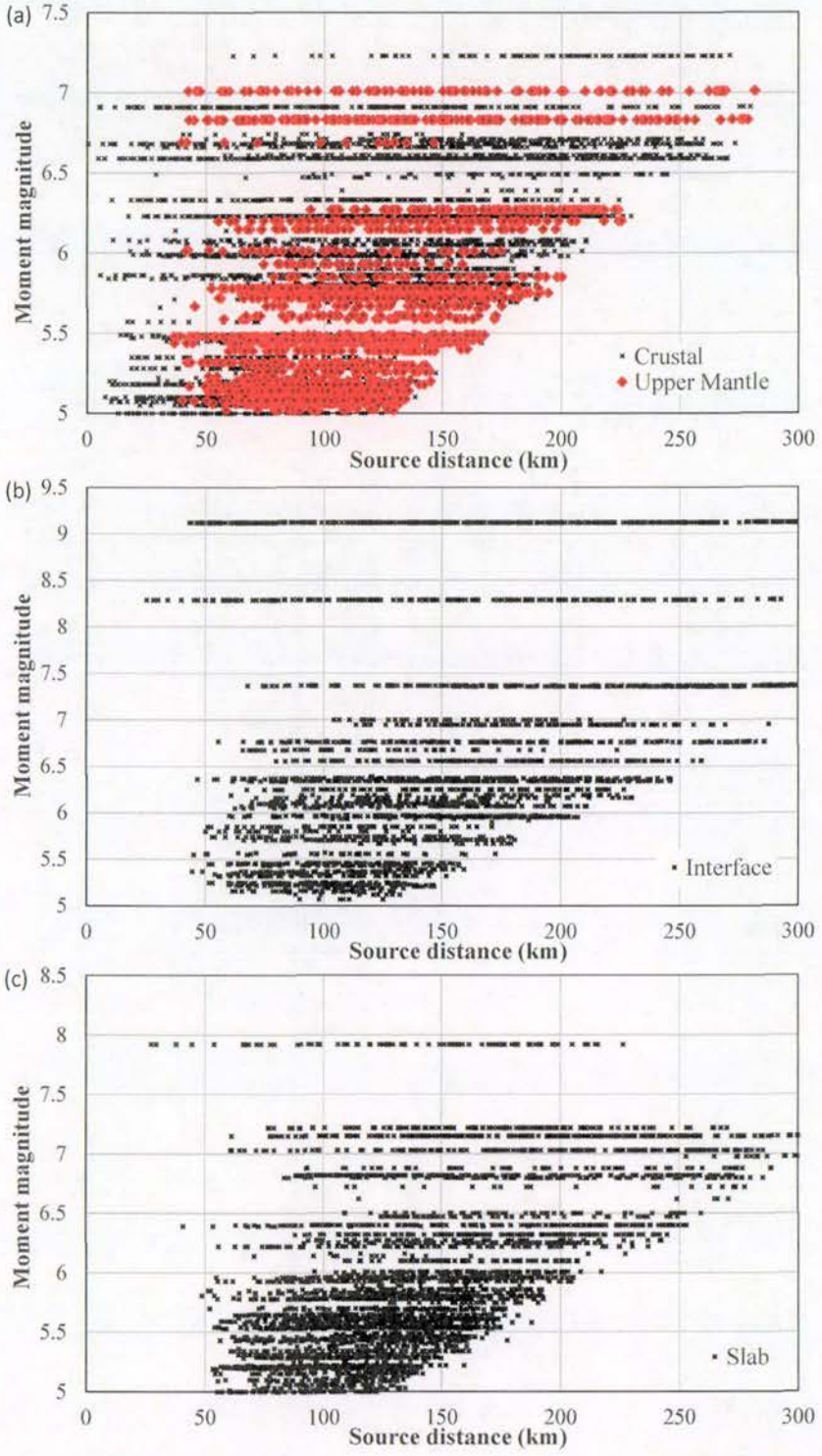

Figure 3.2 The distribution of strong-motion records used in the present study with respect to source distance and magnitude for (a) shallow crustal and upper mantle records, (b) subduction interface records, and (c), subduction slab events.

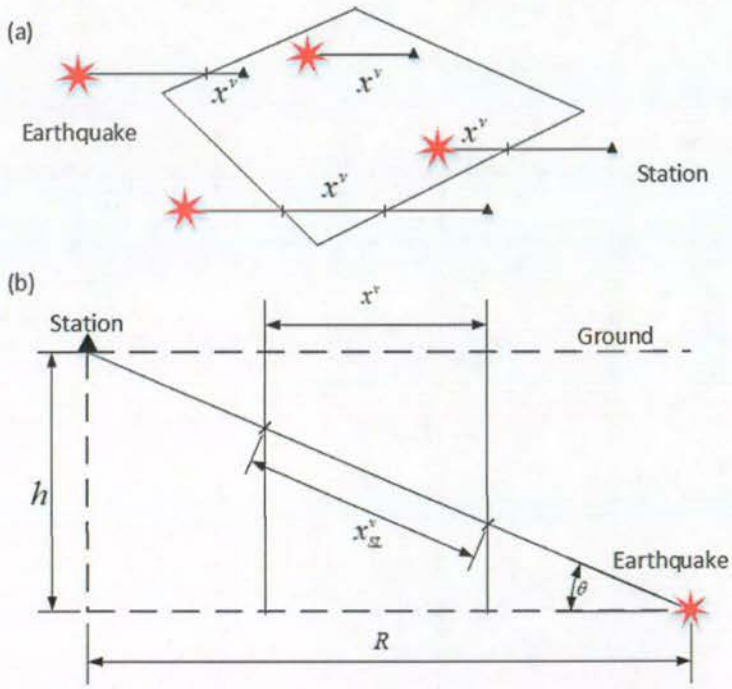

Figure 3.3 The definition of volcanic path for four cases in (a) and the horizontal and slant volcanic distance in (b).

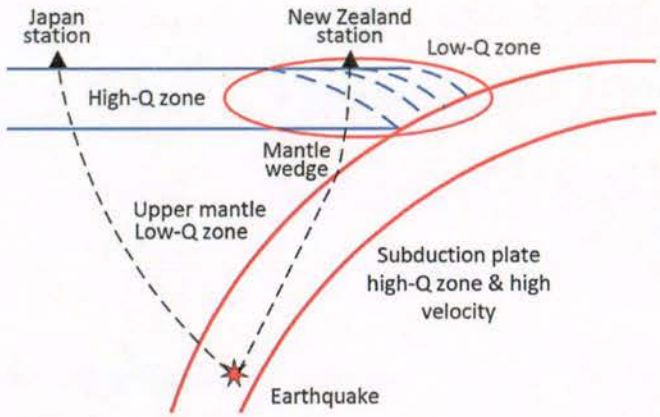

Figure 3.4 Illustration different seismic-wave propagation paths from a deep subduction slab events to a recording station in Japan in the left and a recording station in New Zealand in the right. Japan islands are much further from the subduction trench than the North Island of New Zealand is from the Hikurangi trench.

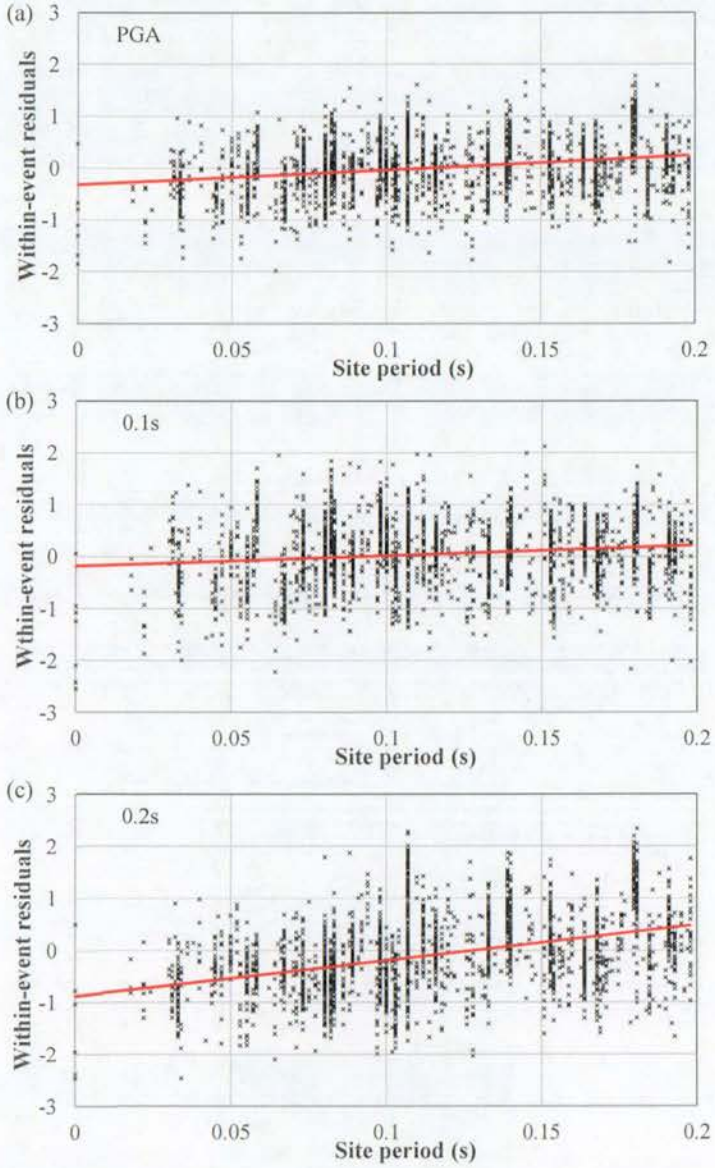

Figure 3.5 Distribution of within-event residuals for SC I sites with respect to site period for (a) PGA, (b) 0.1s and (c) 0.2s spectral periods.

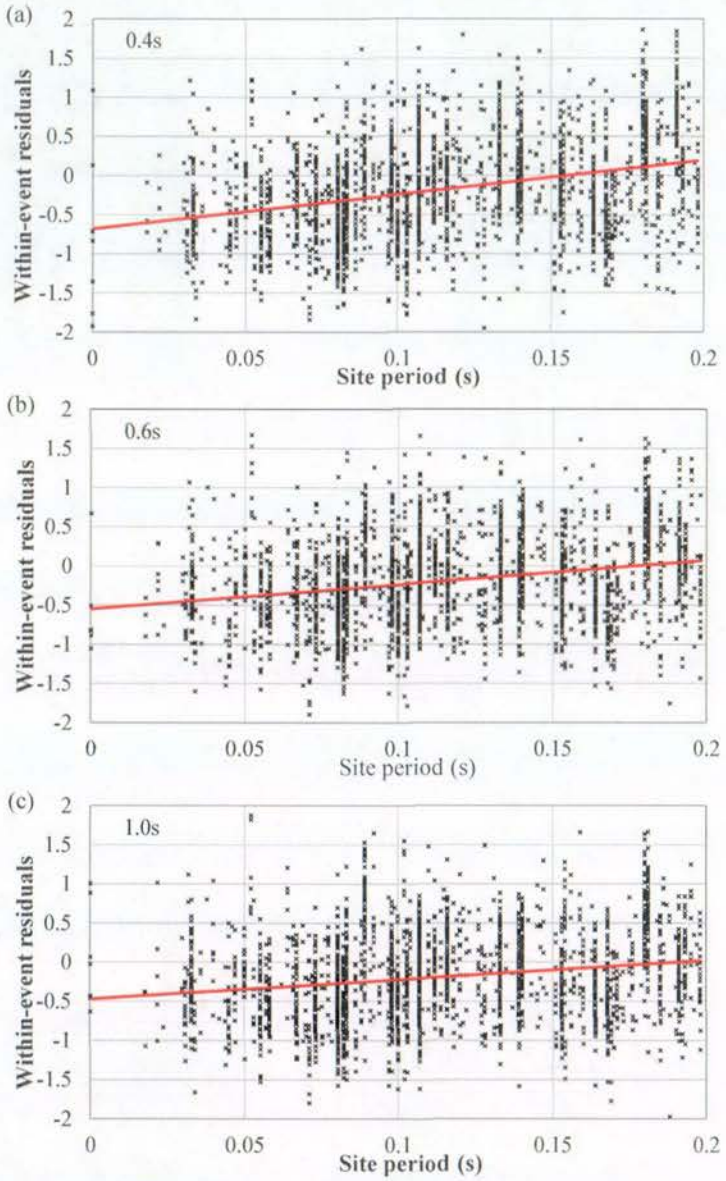

Figure 3.6 Distribution of within-event residuals for SC I sites with respect to site period for (a) 0.4, (b) 0.6s and (c) 1.0s spectral periods.

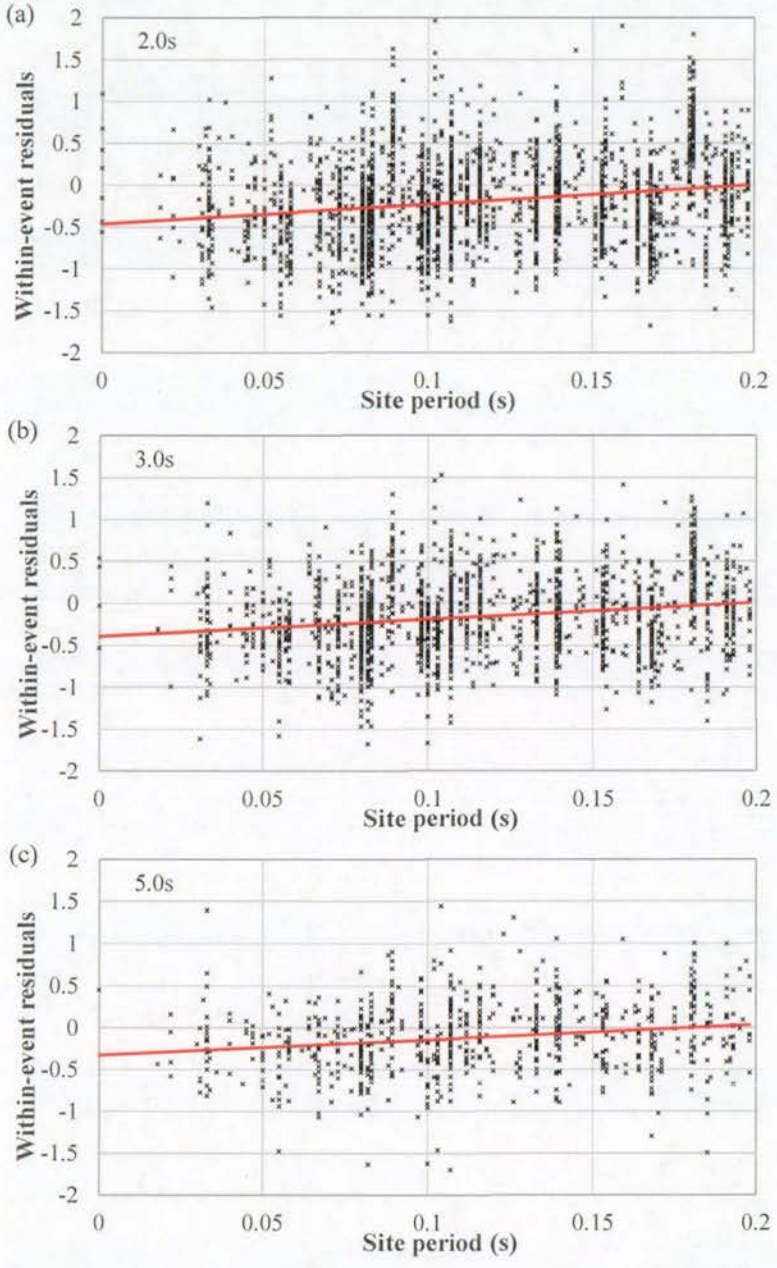

Figure 3.7 Distribution of within-event residuals for SC I sites with respect to site period for (a) 2.0s, (b) 3.0s and (c) 5.0s spectral periods.

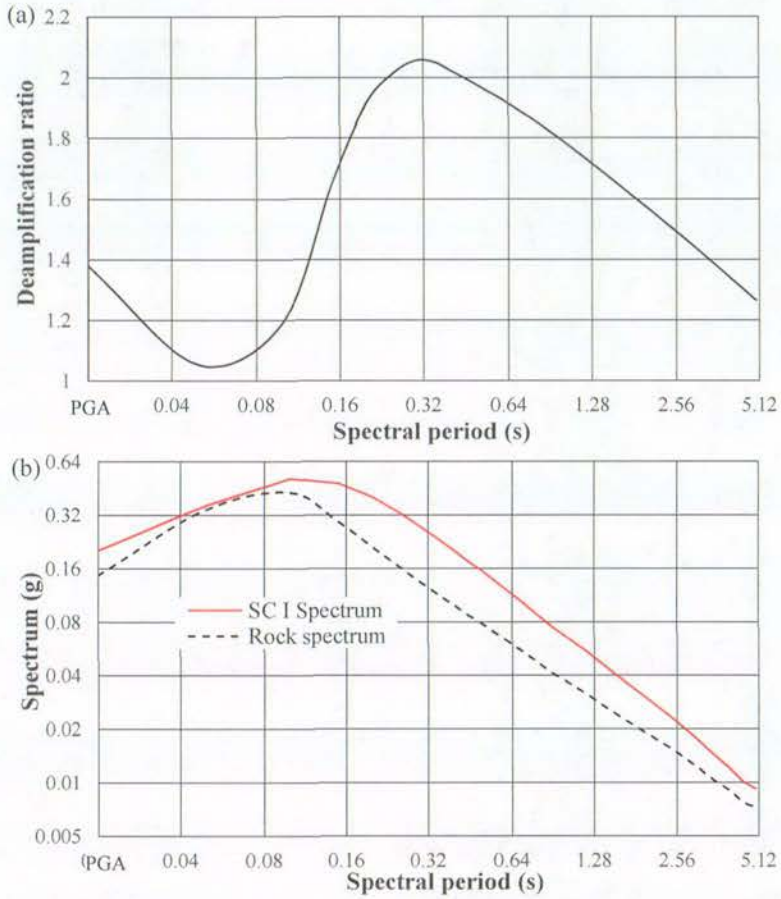

Figure 3.8 Smoothed deamplification ratio for a rock site spectrum with respect to SCI sites in (a) and an example SC I and rock spectrum in (b). The rock site spectrum equals the SC I spectrum divided by the deamplification ratio presented in (a). Rock site with a surface shear-wave velocity of 760m/s or larger.

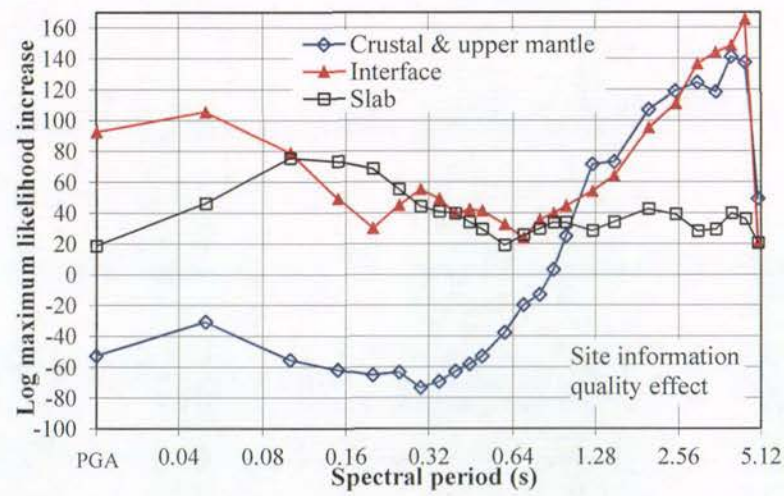

Figure 3.9 The effect of site information quality – the increase in maximum log likelihood for using strong-motion records from stations with measured shear-wave velocity profile down to engineering bedrock, relative to records from stations with inferred site class using H/V response spectral ratios.

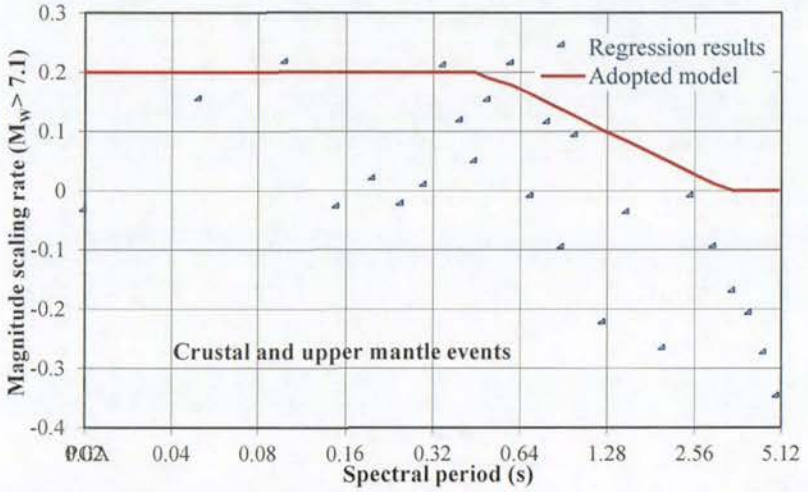

Figure 3.10 Magnitude scaling coefficient d_{cr} for shallow crustal events from Japan and large earthquakes selected from the PEER dataset.

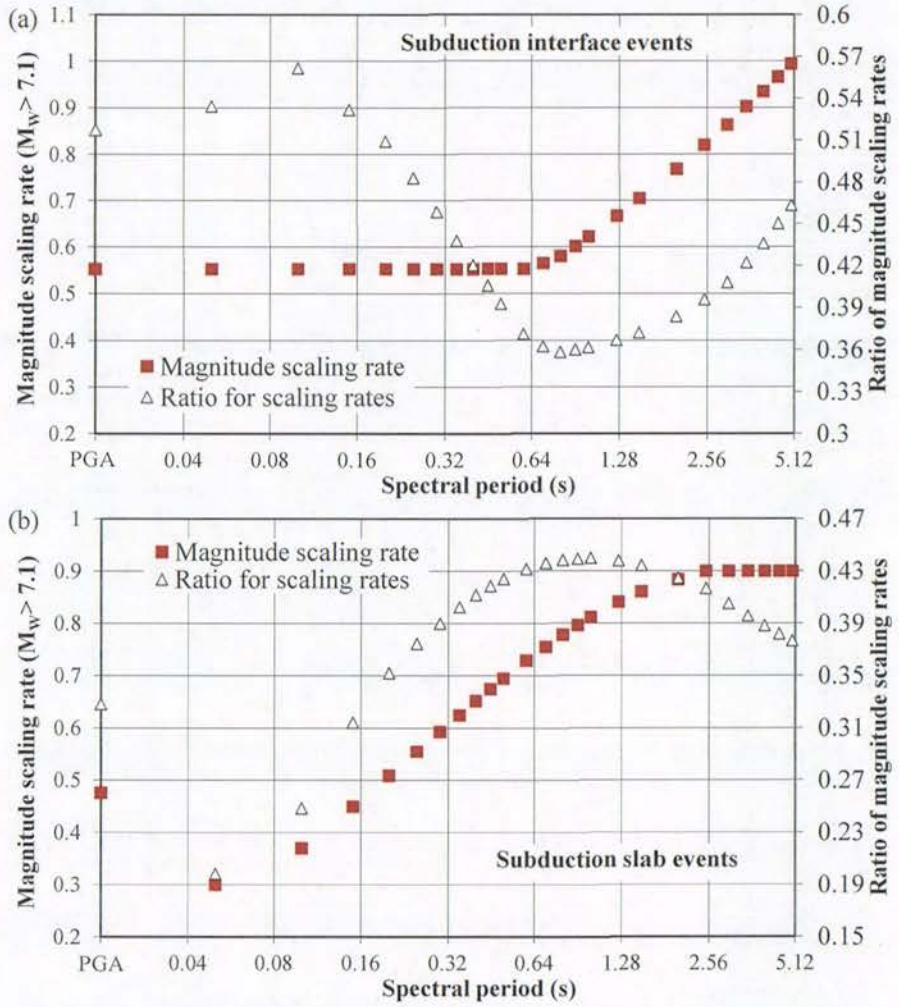

Figure 3.11 Magnitude scaling coefficient d_{int} for large subduction interface events and the ratio d_{int}/c_{int} events in (a) and d_{SL} for large subduction slab events and the ratio d_{SL}/c_{SL} in (b).

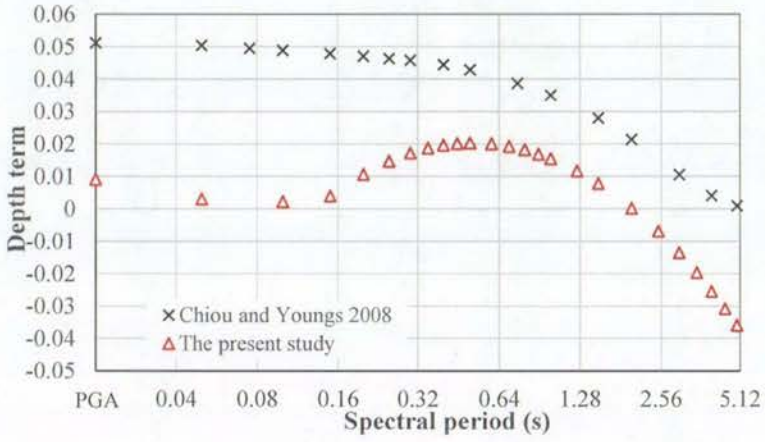

Figure 3.12 Comparison of the depth terms in the Chiou and Youngs (2008) study with that of the present study.

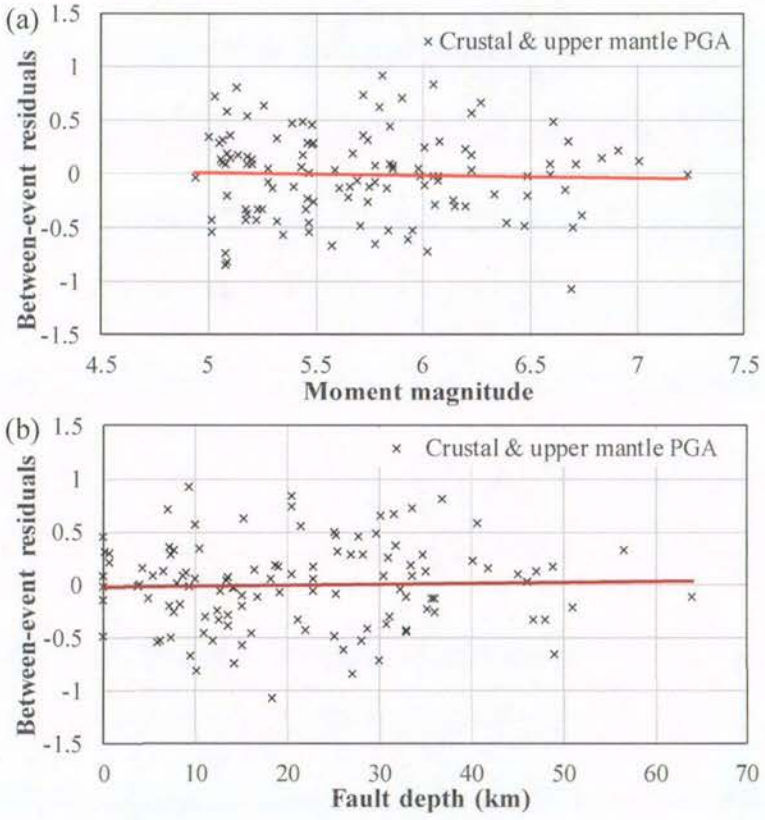

Figure 3.13 Distribution of between-event residuals for PGA from crustal and upper mantle earthquakes, with respect to (a) magnitude and (b) fault depth.

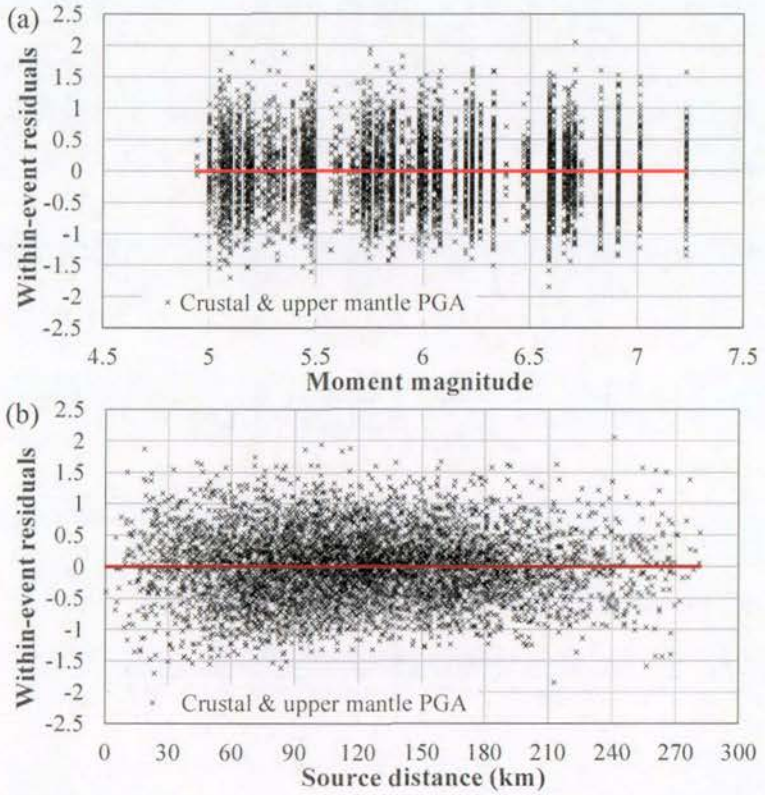

Figure 3.14 Distribution of within-event residuals for PGA from crustal and upper mantle earthquakes, with respect to (a) magnitude and (b) source distance.

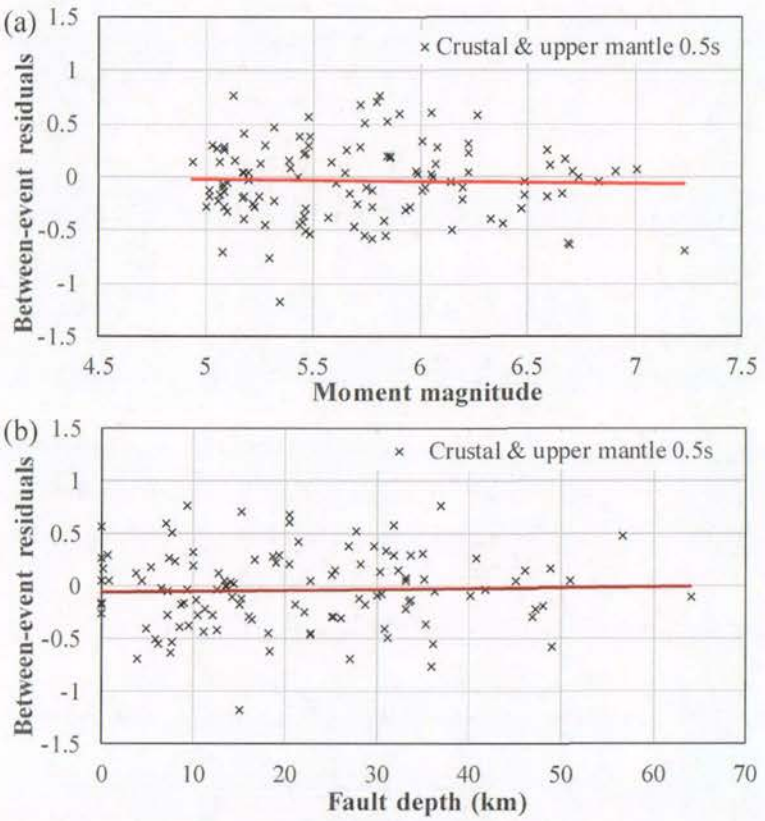

Figure 3.15 Distribution of between-event residuals for 0.5s spectral acceleration from crustal and upper mantle earthquakes, with respect to (a) magnitude and (b) fault depth.

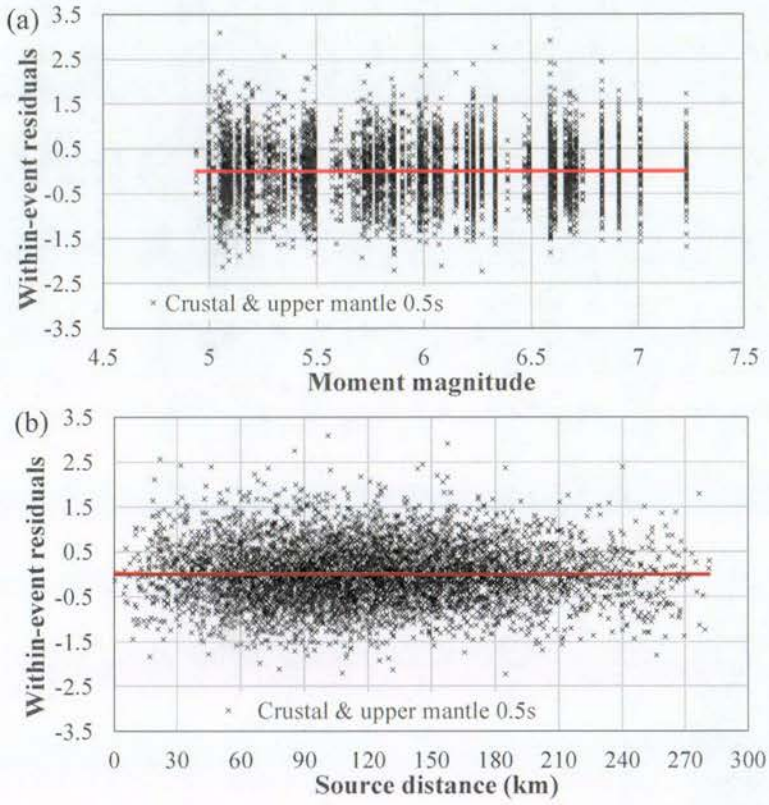

Figure 3.16 Distribution of within-event residuals for 0.5s spectral acceleration from crustal and upper mantle earthquakes, with respect to (a) magnitude and (b) source distance.

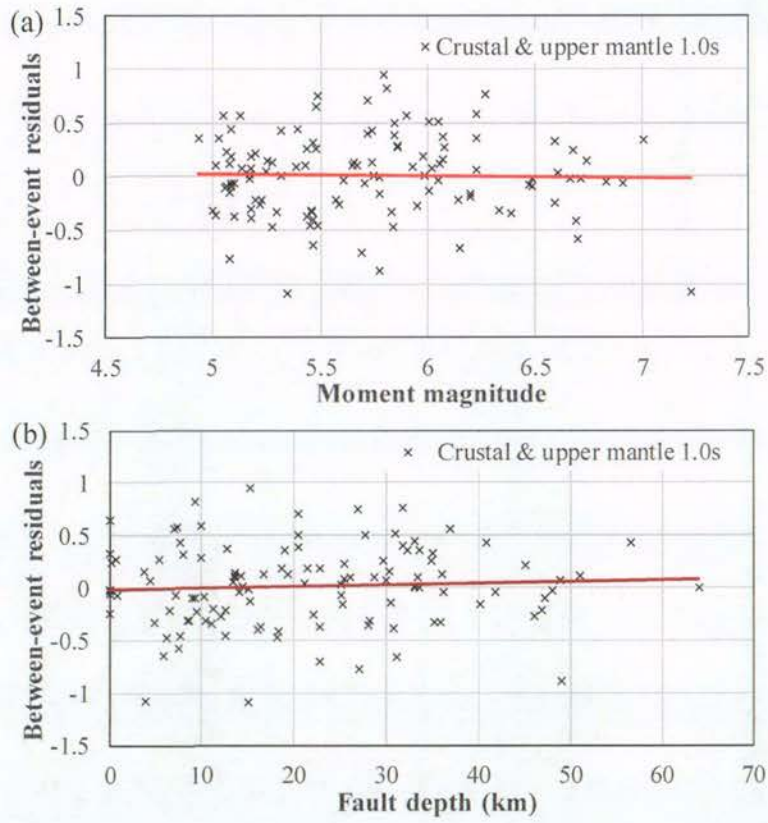

Figure 3.17 Distribution of between-event residuals for 1.0s spectral acceleration from crustal and upper mantle earthquakes, with respect to (a) magnitude and (b) fault depth.

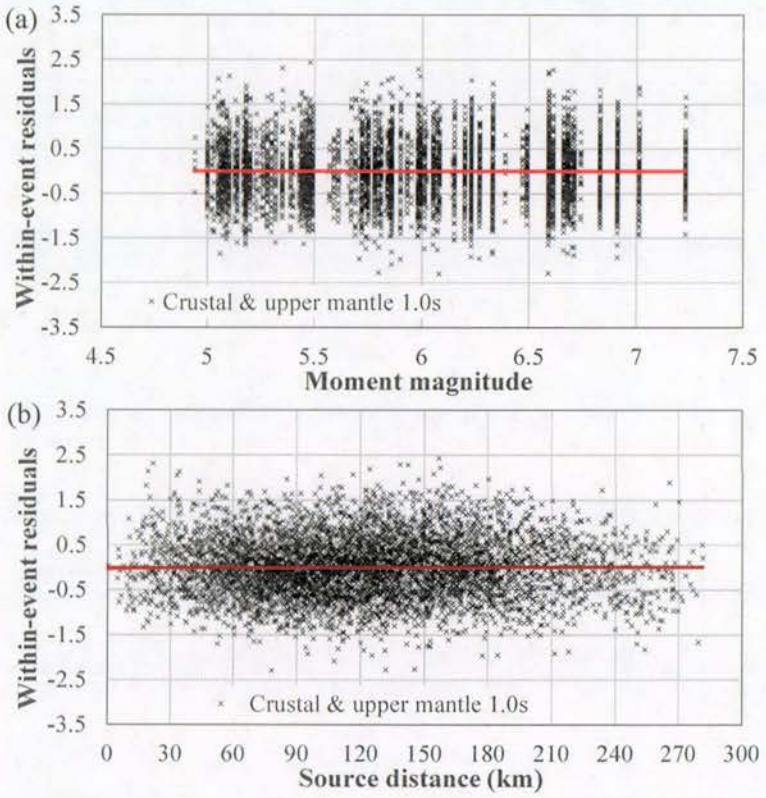

Figure 3.18 Distribution of within-event residuals for 1.0s spectral acceleration from crustal and upper mantle earthquakes, with respect to (a) magnitude and (b) source distance.

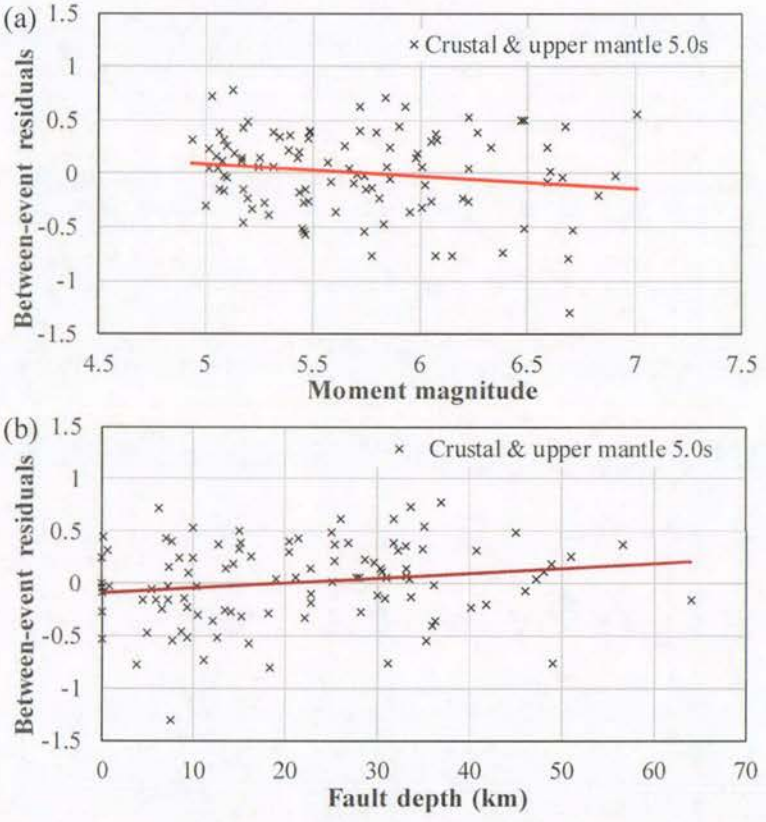

Figure 3.19 Distribution of between-event residuals for 5.0s spectral acceleration from crustal and upper mantle earthquakes, with respect to (a) magnitude and (b) fault depth.

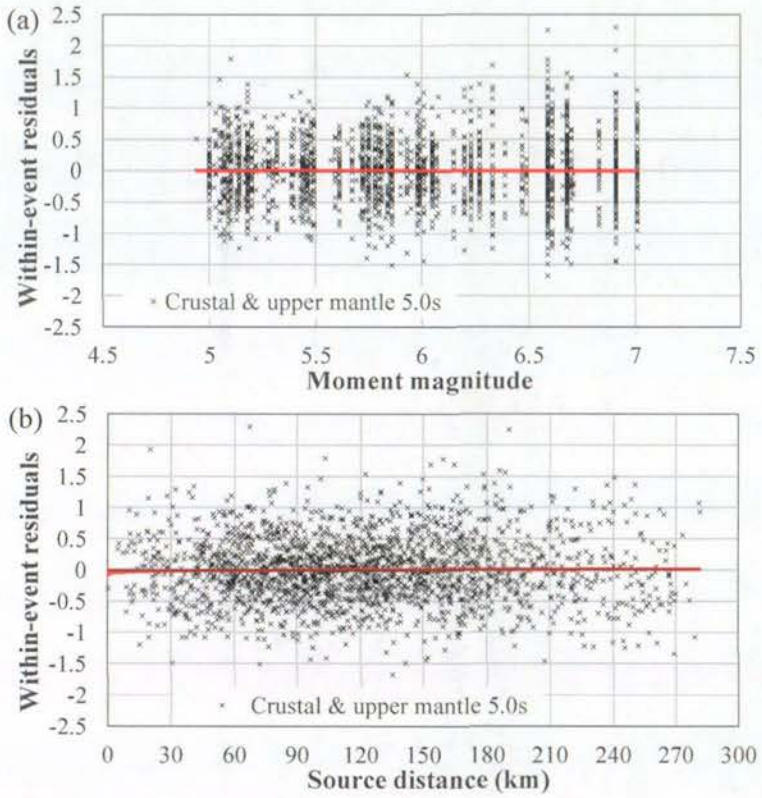

Figure 3.20 Distribution of within-event residuals for 5.0s from crustal and upper mantle earthquakes, with respect to (a) magnitude and (b) source distance.

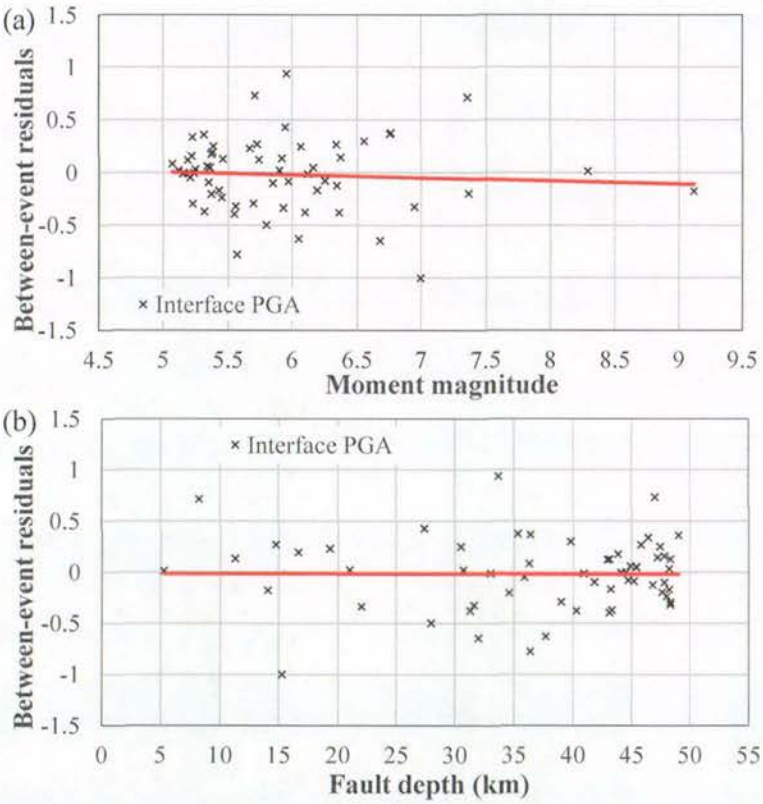

Figure 3.21 Distribution of between-event residuals for PGA from subduction interface earthquakes, with respect to (a) magnitude and (b) fault depth.

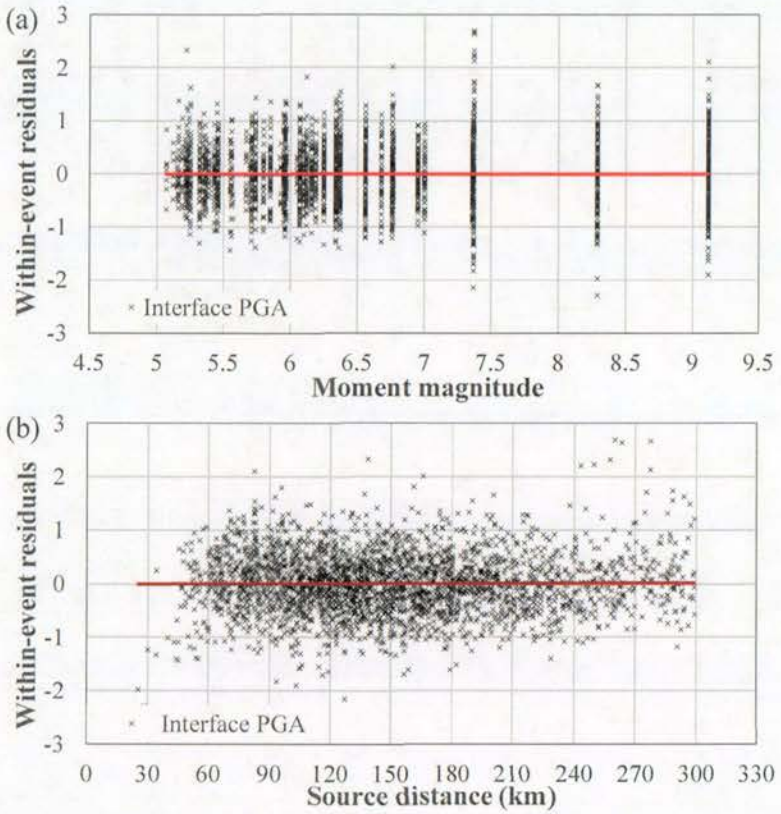

Figure 3.22 Distribution of within-event residuals for PGA from subduction interface earthquakes, with respect to (a) magnitude and (b) source distance.

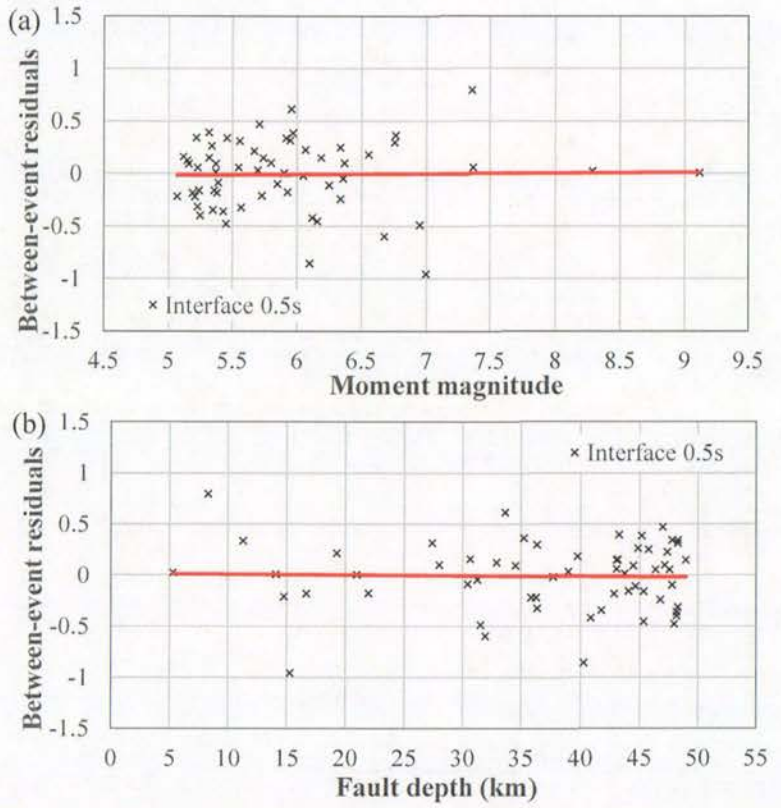

Figure 3.23 Distribution of between-event residuals for 0.5s spectral acceleration from subduction interface earthquakes, with respect to (a) magnitude and (b) fault depth.

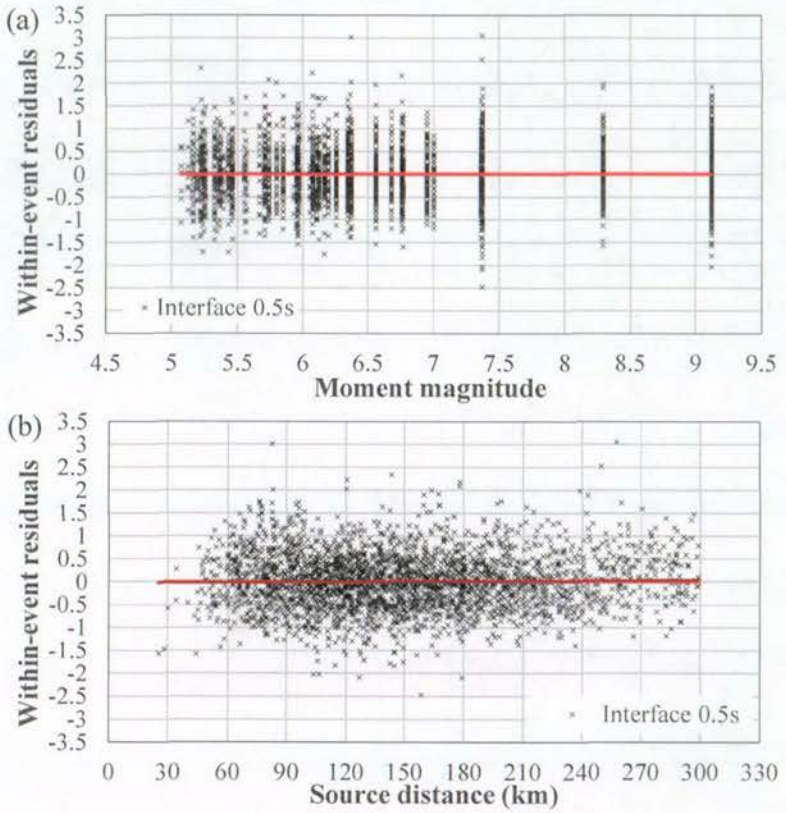

Figure 3.24 Distribution of within-event residuals for 0.5s spectral acceleration from subduction interface earthquakes, with respect to (a) magnitude and (b) source distance.

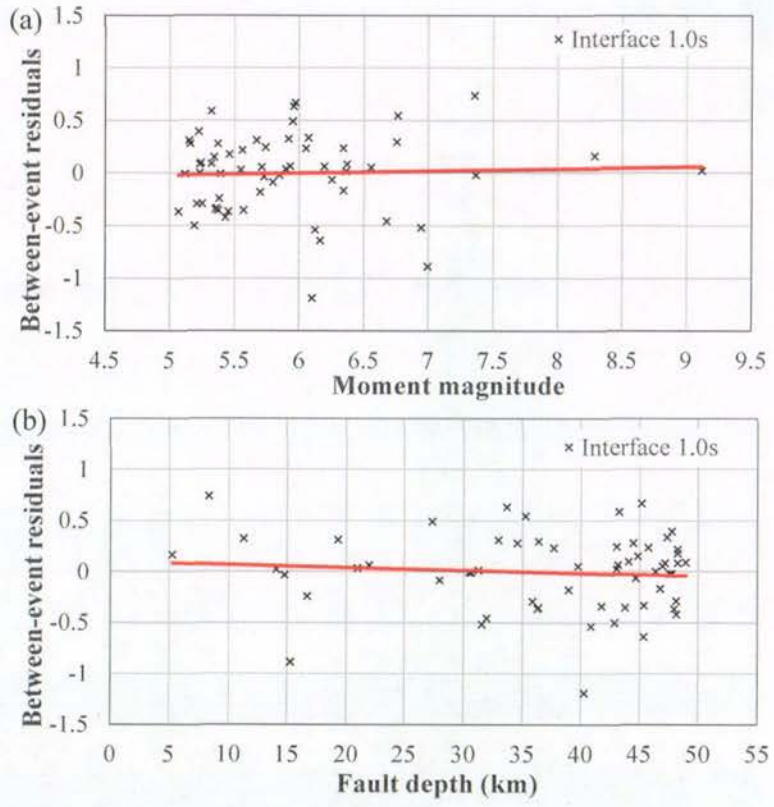

Figure 3.25 Distribution of between-event residuals for 1.0s spectral acceleration from subduction interface earthquakes, with respect to (a) magnitude and (b) fault depth.

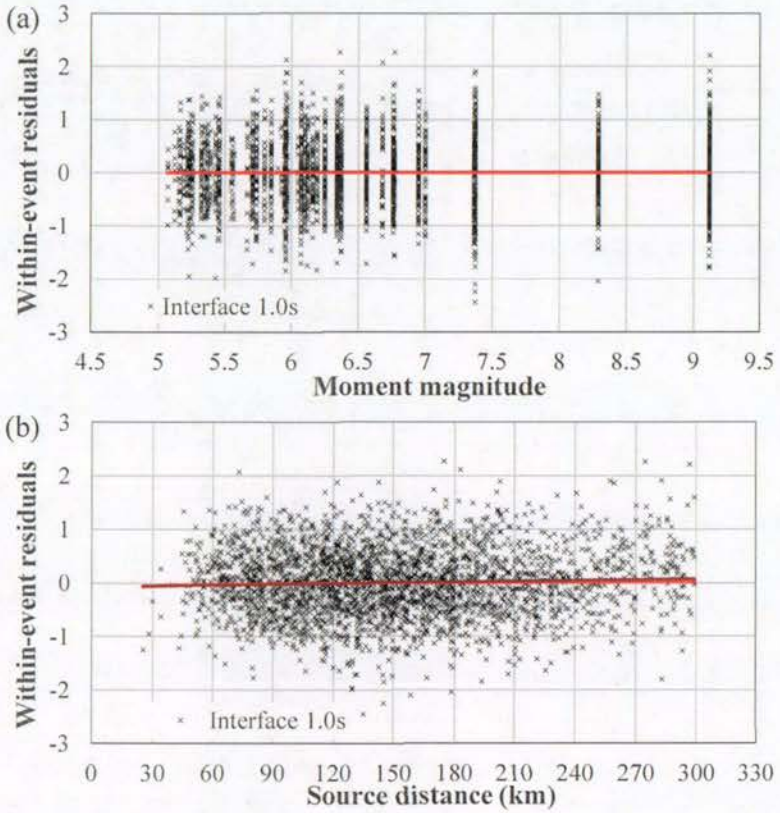

Figure 3.26 Distribution of within-event residuals for 1.0s spectral acceleration from subduction interface earthquakes, with respect to (a) magnitude and (b) source distance.

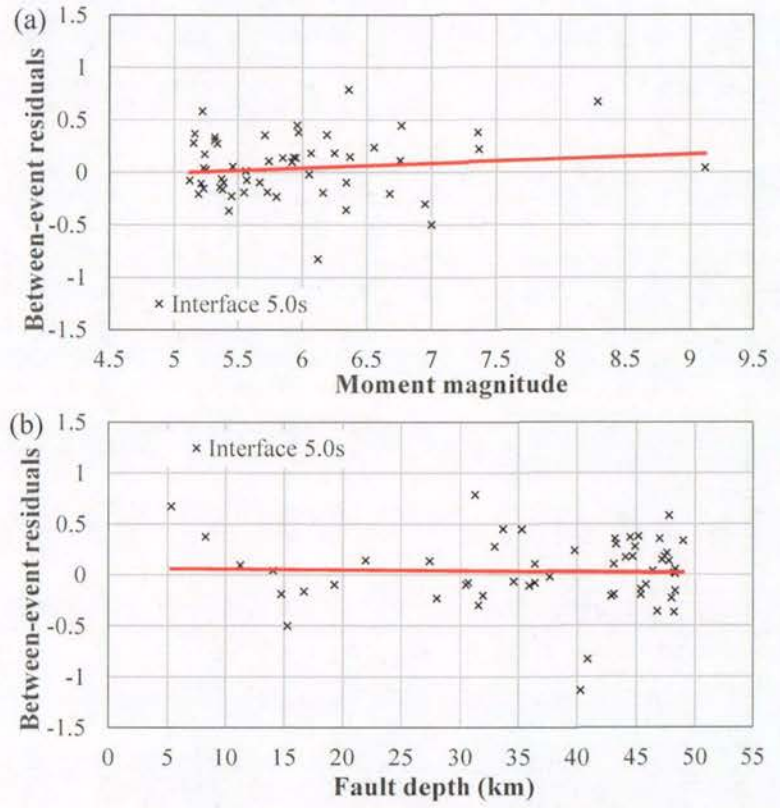

Figure 3.27 Distribution of between-event residuals for 5.0s spectral acceleration from subduction interface earthquakes, with respect to (a) magnitude and (b) fault depth.

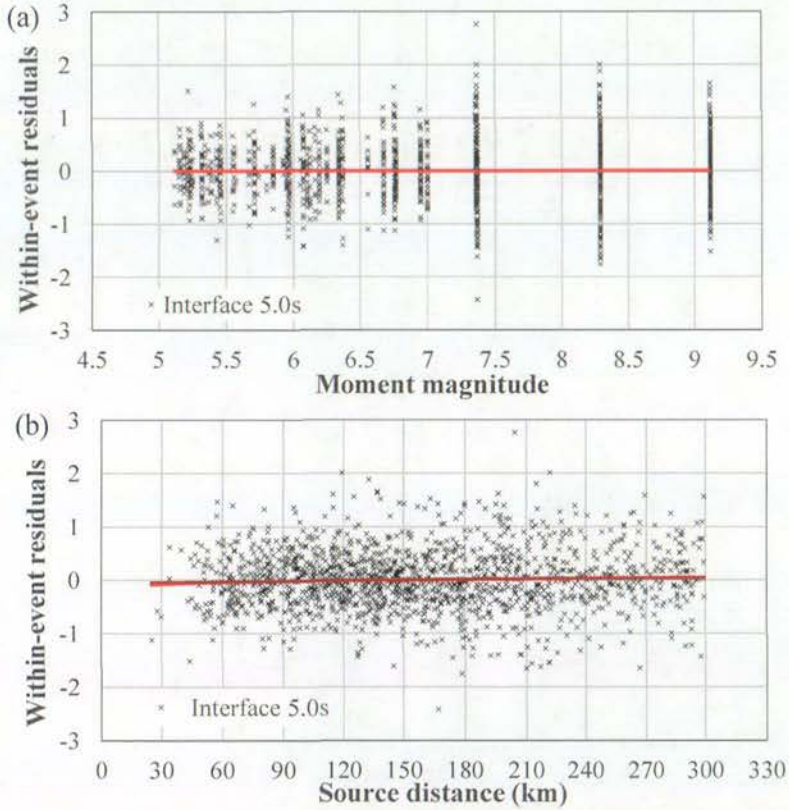

Figure 3.28 Distribution of within-event residuals for 5.0s spectral acceleration from subduction interface earthquakes, with respect to (a) magnitude and (b) source distance.

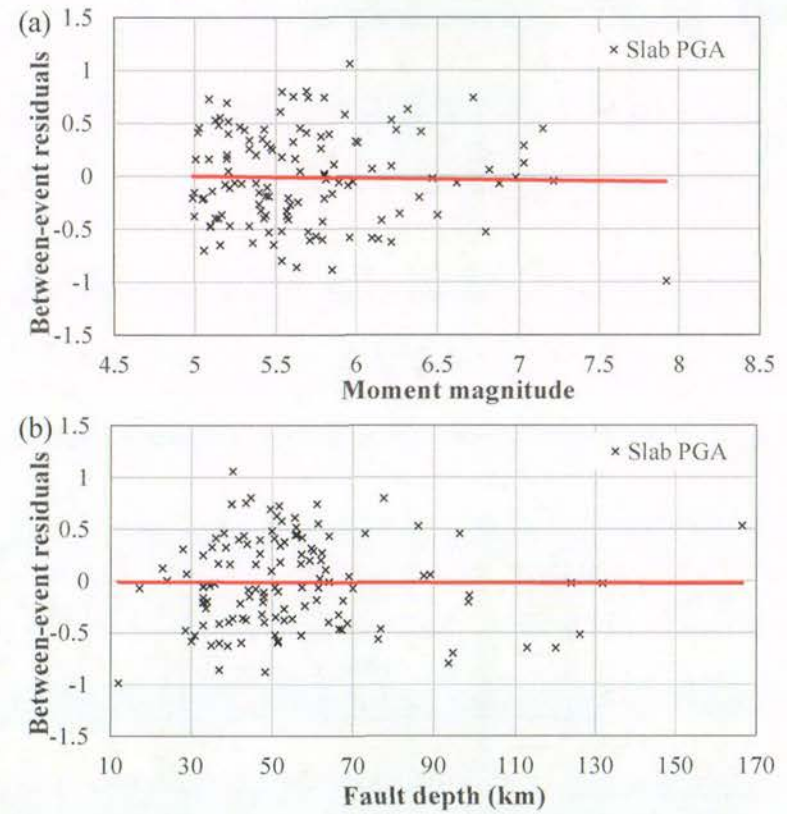

Figure 3.29 Distribution of between-event residuals for PGA from subduction slab earthquakes, with respect to (a) magnitude and (b) source distance.

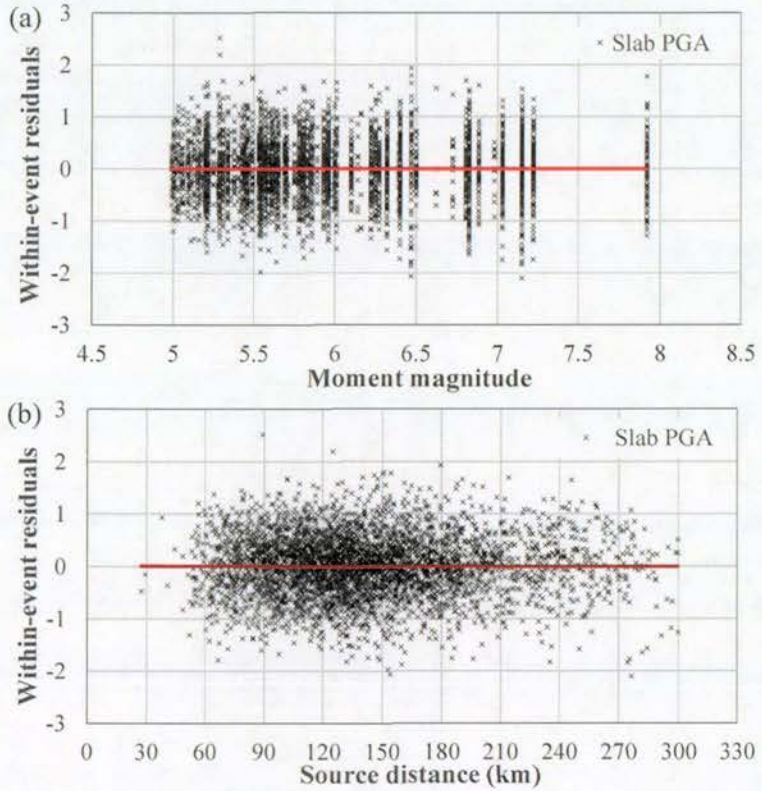

Figure 3.30 Distribution of within-event residuals for PGA from subduction slab earthquakes, with respect to (a) magnitude and (b) source distance.

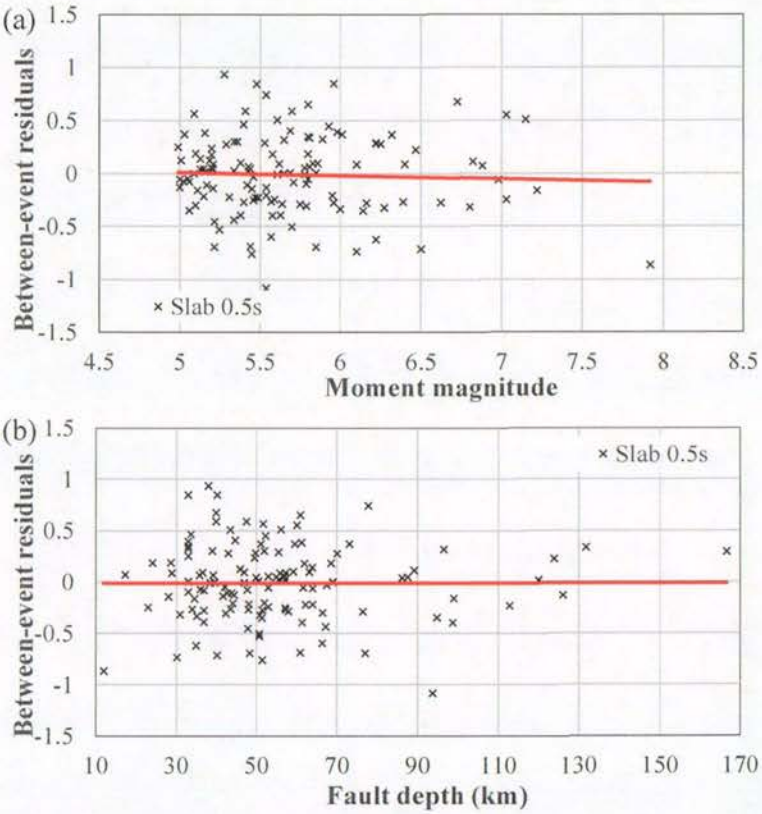

Figure 3.31 Distribution of between-event residuals for 0.5s spectral acceleration from subduction slab earthquakes, with respect to (a) magnitude and (b) fault depth.

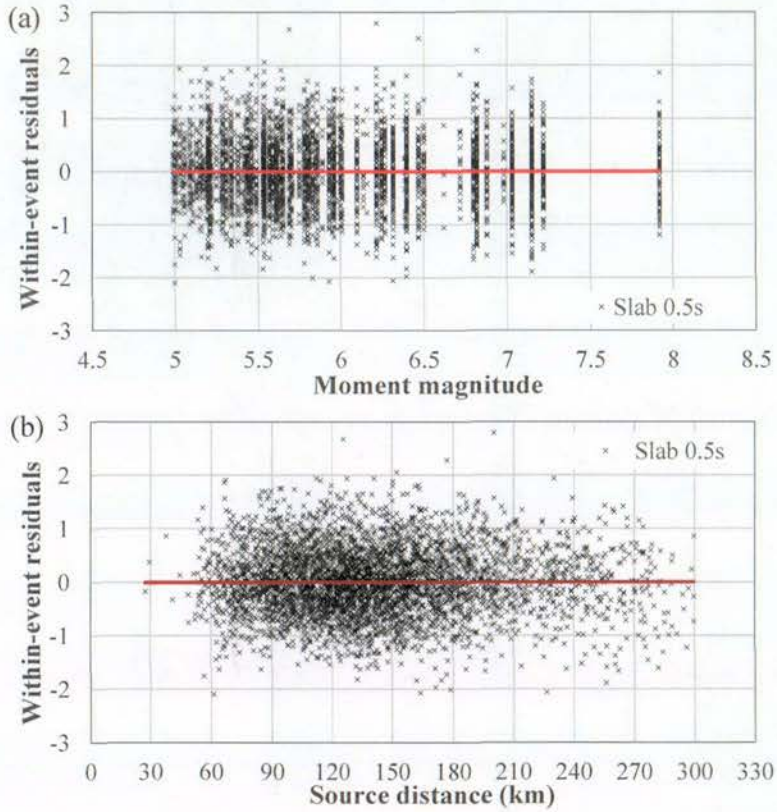

Figure 3.32 Distribution of within-event residuals for 0.5s spectral acceleration from subduction slab earthquakes, with respect to (a) magnitude and (b) source distance.

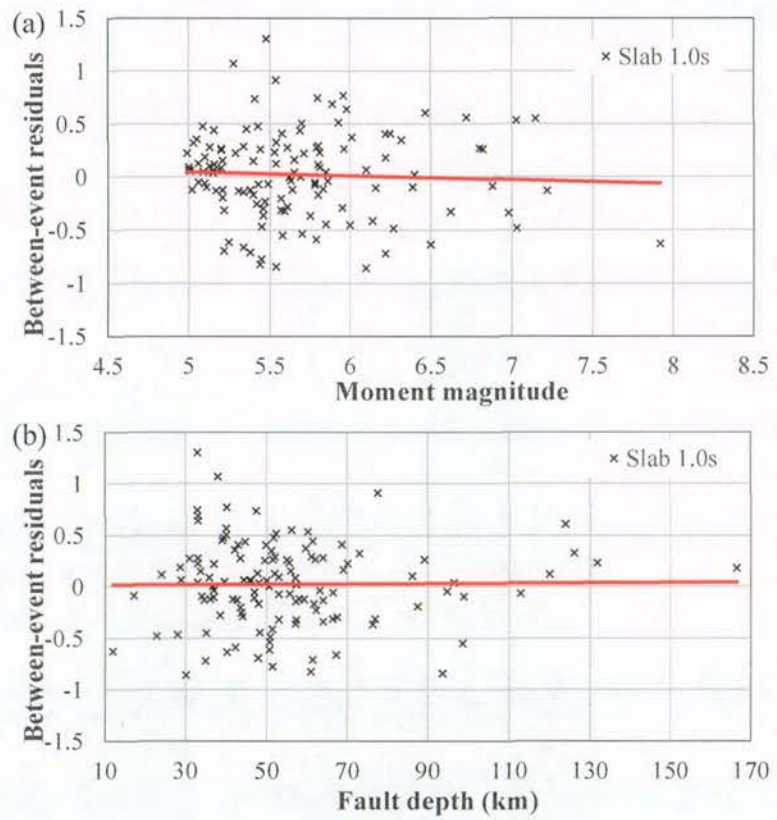

Figure 3.33 Distribution of between-event residuals for 1.0s spectral acceleration from subduction slab earthquakes with respect to (a) magnitude and (b) fault depth.

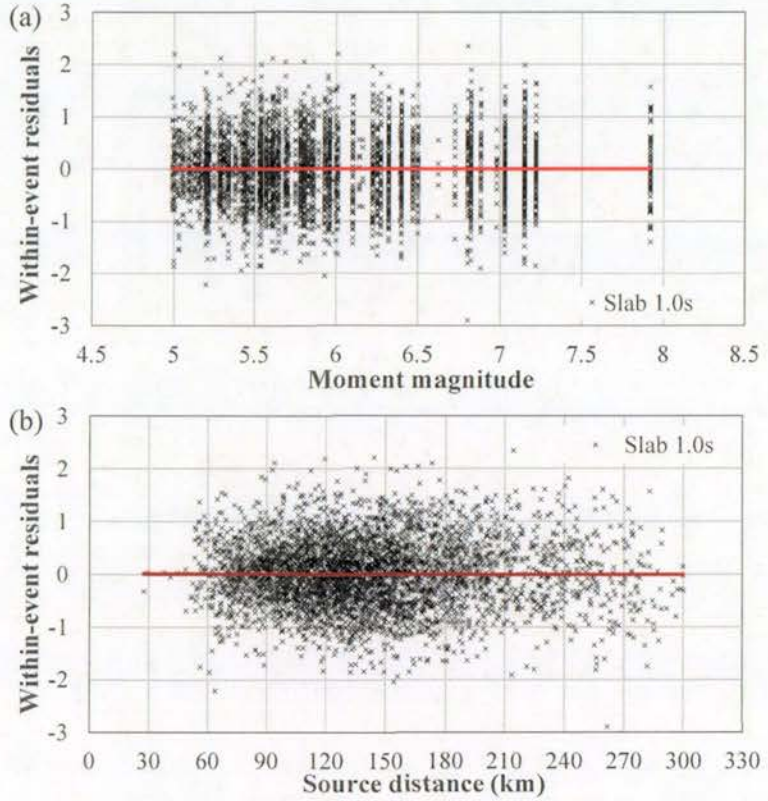

Figure 3.34 Distribution of within-event residuals for 1.0s spectral acceleration from subduction slab earthquakes, with respect to (a) magnitude and (b) source distance.

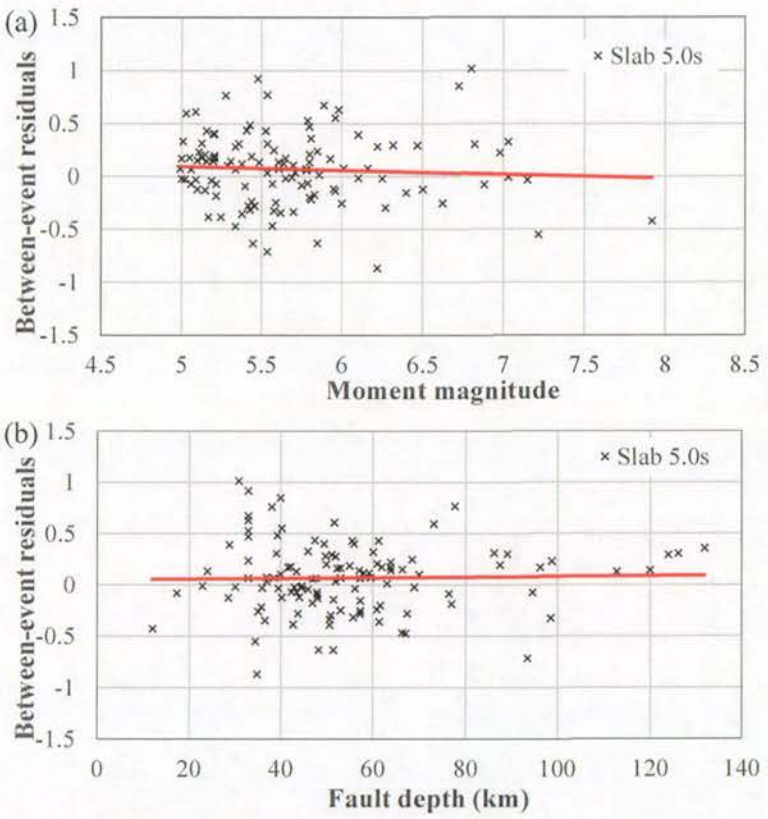

Figure 3.35 Distribution of between-event residuals for 5.0s spectral acceleration from subduction slab earthquakes, with respect to (a) magnitude and (b) fault depth.

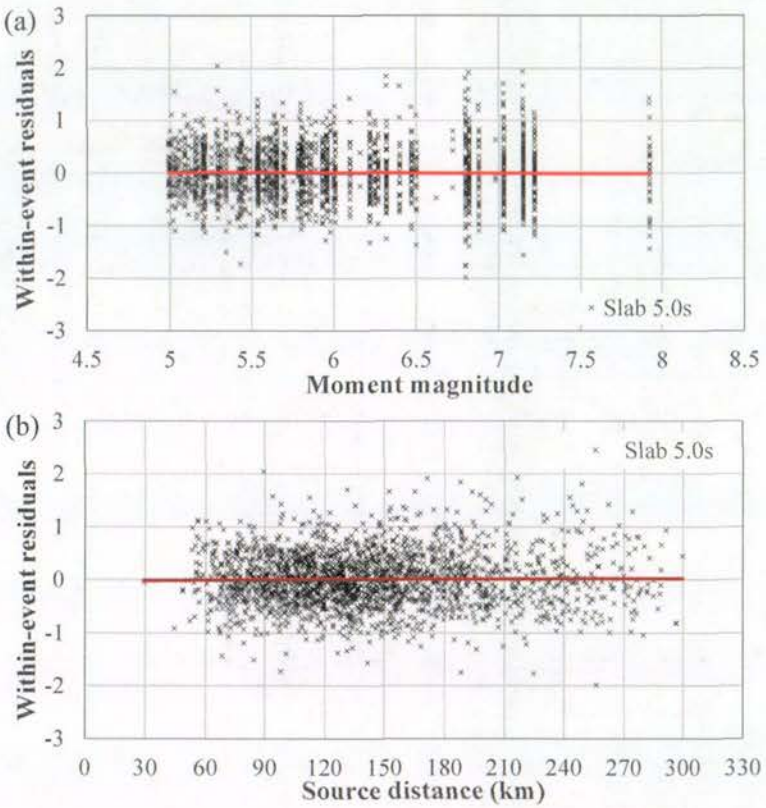

Figure 3.36 Distribution of within-event residuals for 5.0s spectral acceleration from subduction slab earthquakes, with respect to (a) magnitude and (b) source distance.

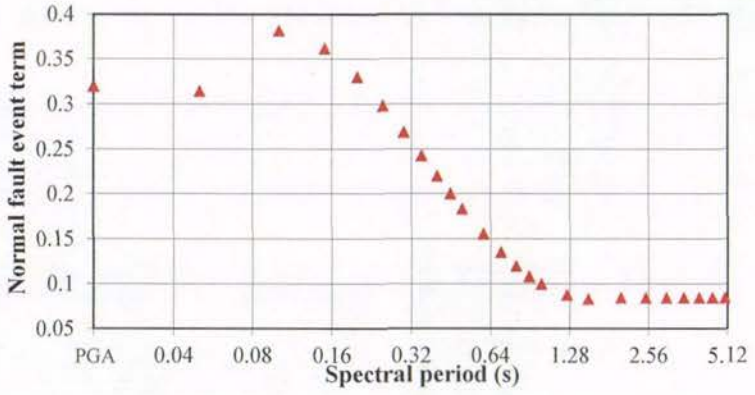

Figure 3.37 Event term for shallow crustal normal faulting events.

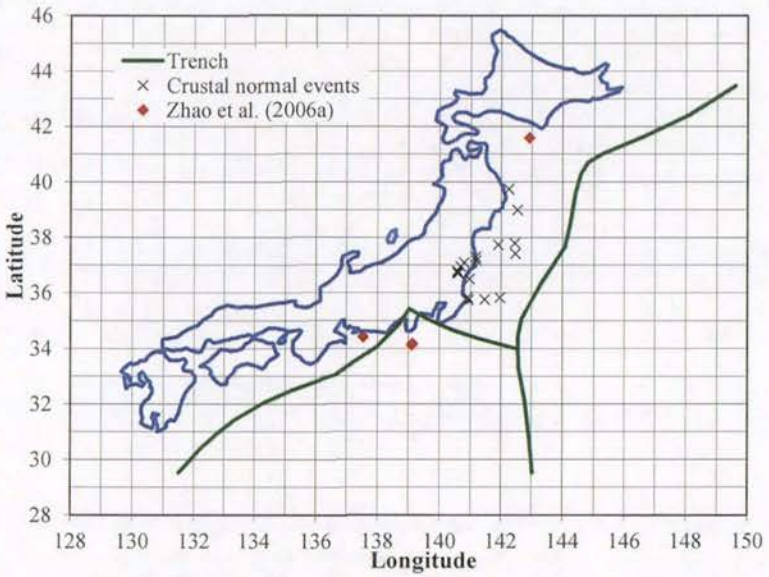

Figure 3.38 Locations of the shallow crustal earthquakes with a normal faulting mechanism.

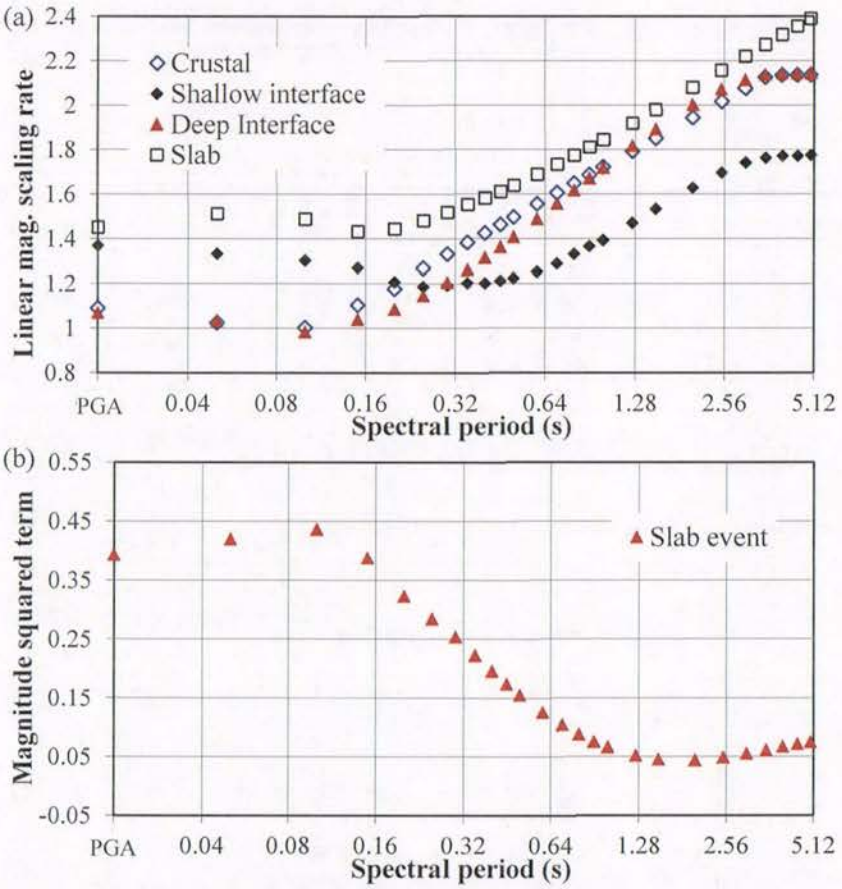

Figure 3.39 Comparison of linear magnitude coefficients for shallow crustal, upper mantle, subduction interface and subduction slab events in (a), and the magnitude squared term for slab events with a magnitude less than 7.1 in (b).

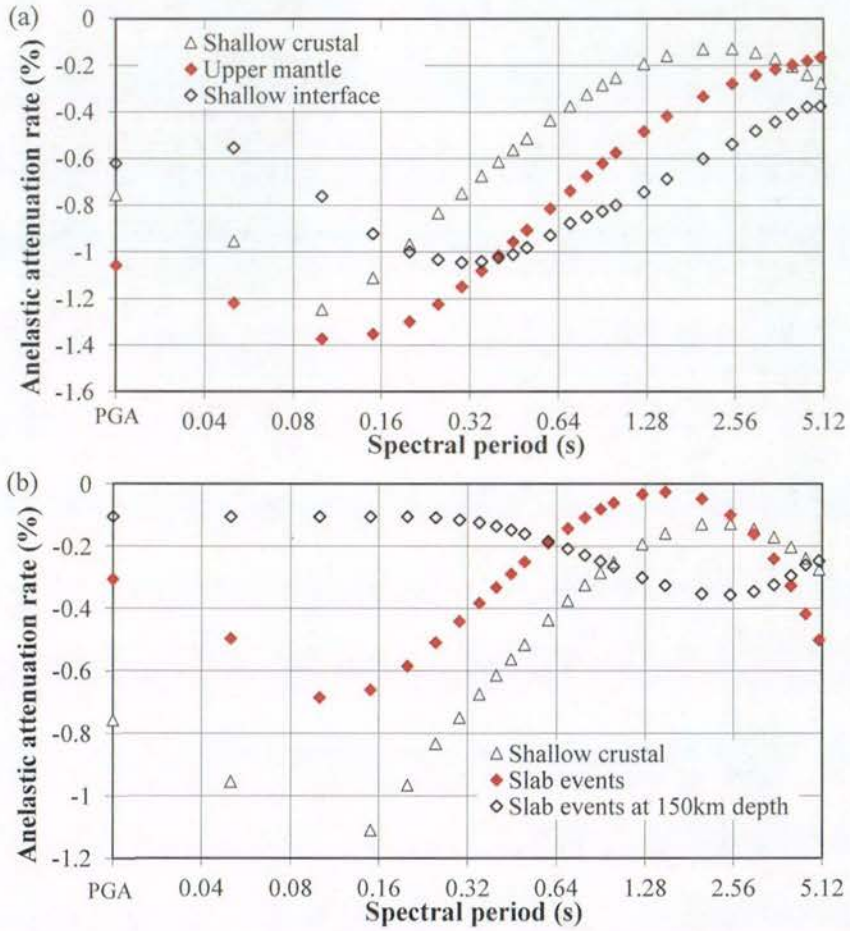

Figure 3.40 Comparison of anelastic attenuation rates for shallow crustal, upper mantle and shallow interface events in (a) and shallow crustal, slab events and the anelastic attenuation rate for a slab event at a 150km depth in (b).

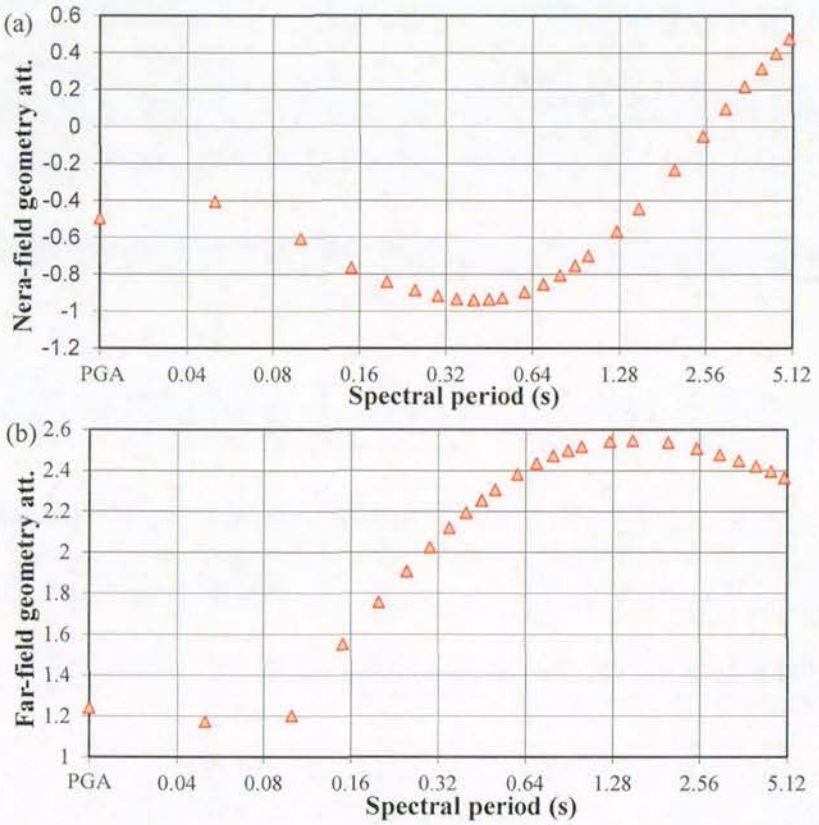

Figure 3.41 The near-field geometric attenuation coefficient of g_N for SC-UM events in (a) and the far-field attenuation coefficient g_{crL} for SC-UM events and subduction interface events.

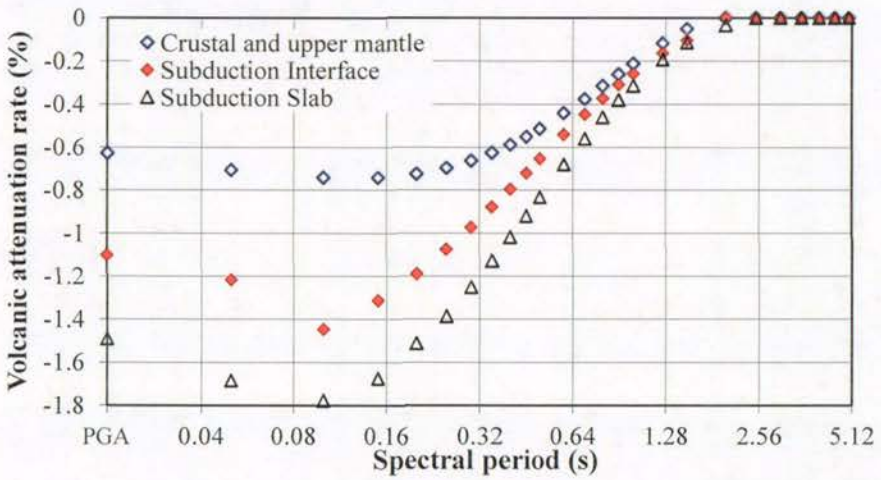

Figure 3.42 Comparison of anelastic attenuation coefficients associated with volcanic path for crustal and upper mantle events, subduction interface and subduction slab events.

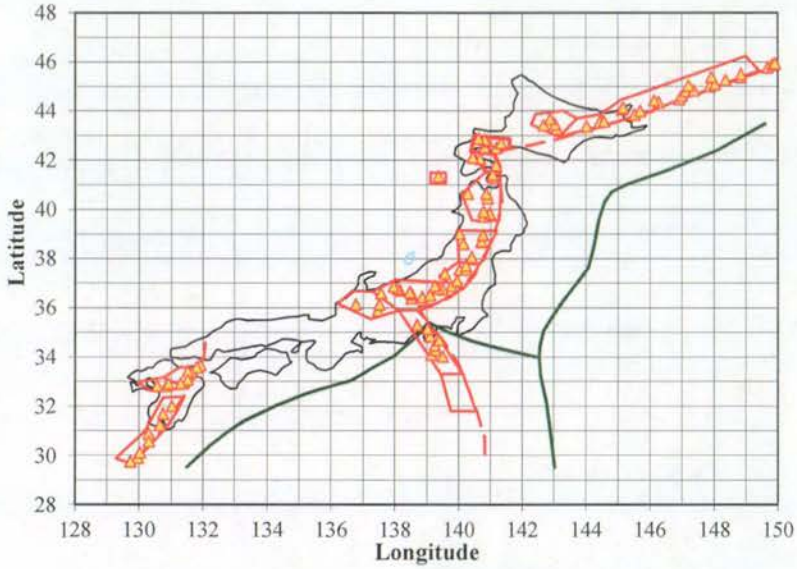

Figure 3.43 The distribution of active volcanoes in Japan. Volcanoes are marked by triangles, and the areas enclosed by the solid lines are the volcanic zones.

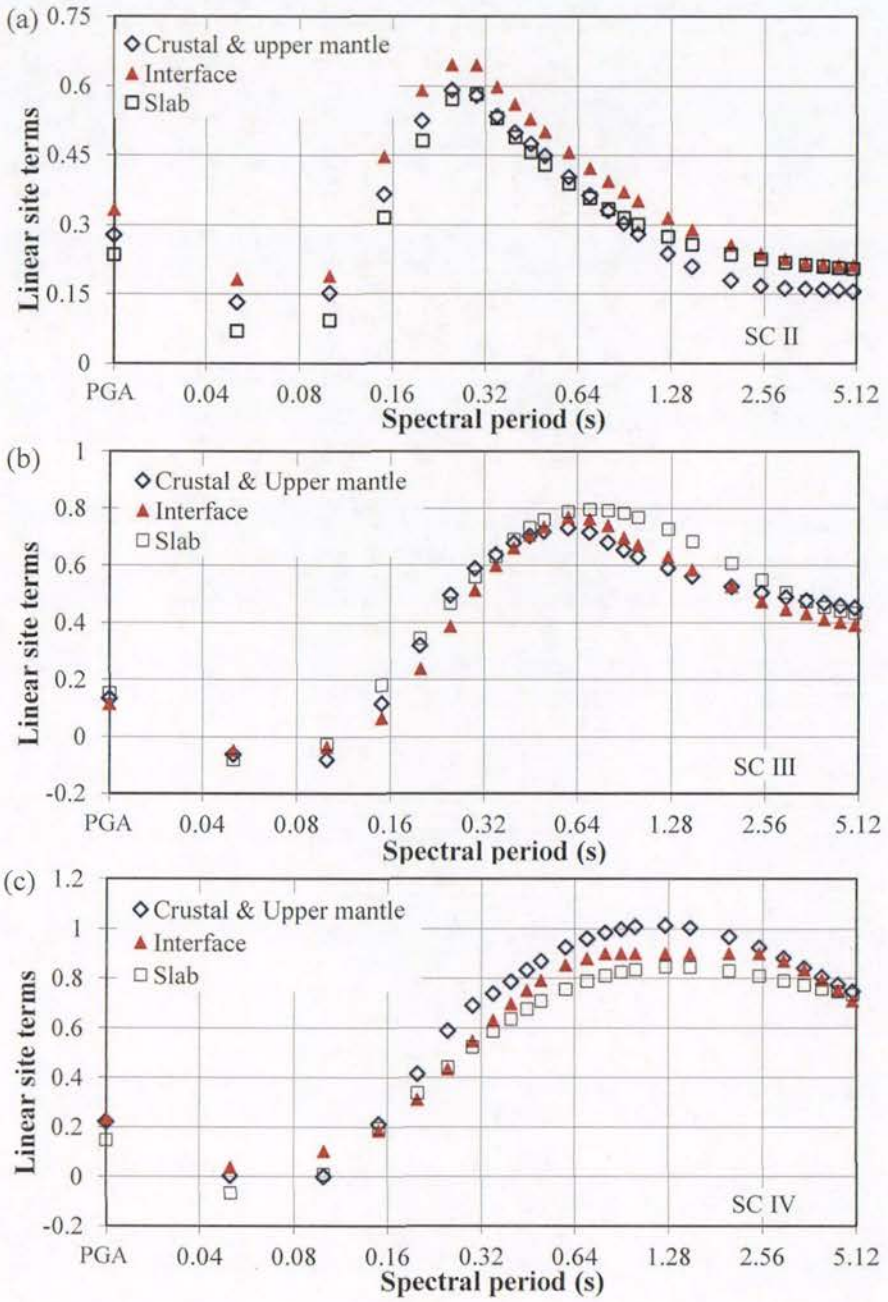

Figure 3.44 Comparison of linear-site terms for (a) SC II sites, (b) SC III sites and (c) SCIV sites from the models for shallow crustal and upper mantle earthquakes, subduction interface events and subduction slab events.

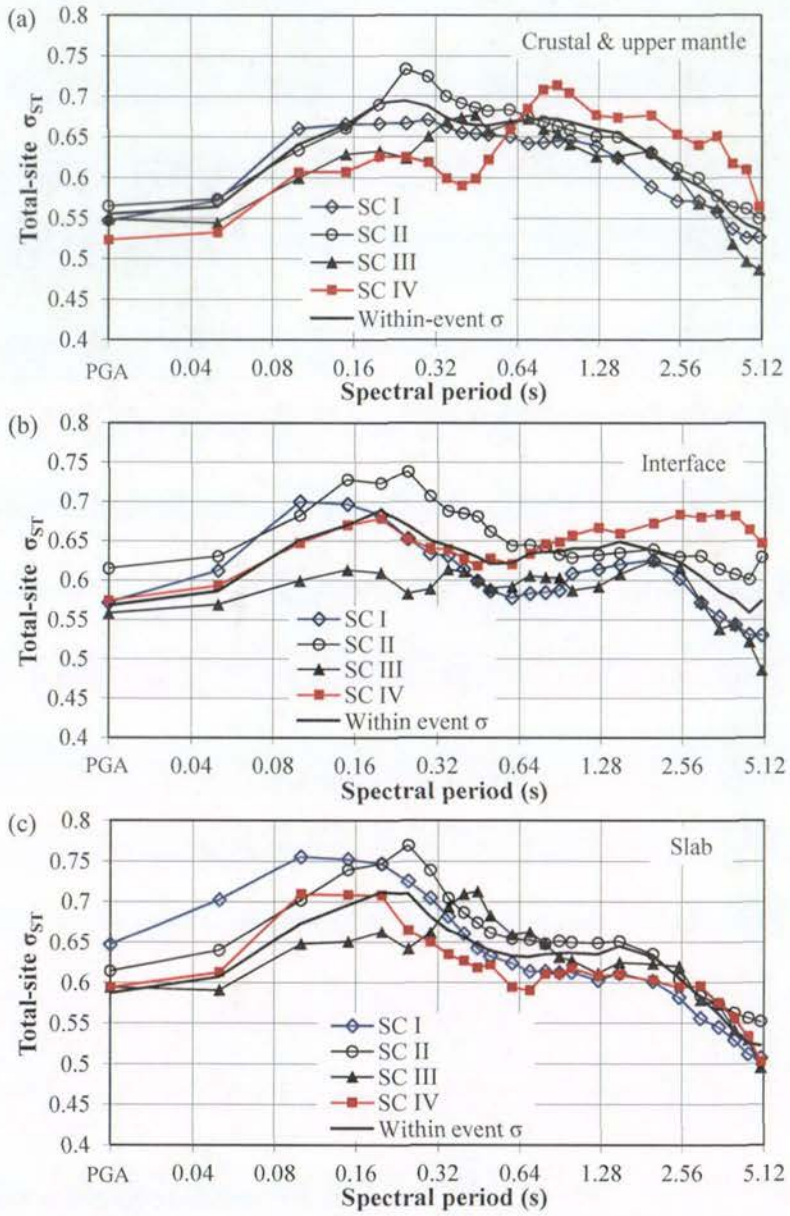

Figure 3.45 Standard deviations estimated for (a) between-site residuals, and (b) within-site residuals for shallow crustal and upper mental earthquake records.

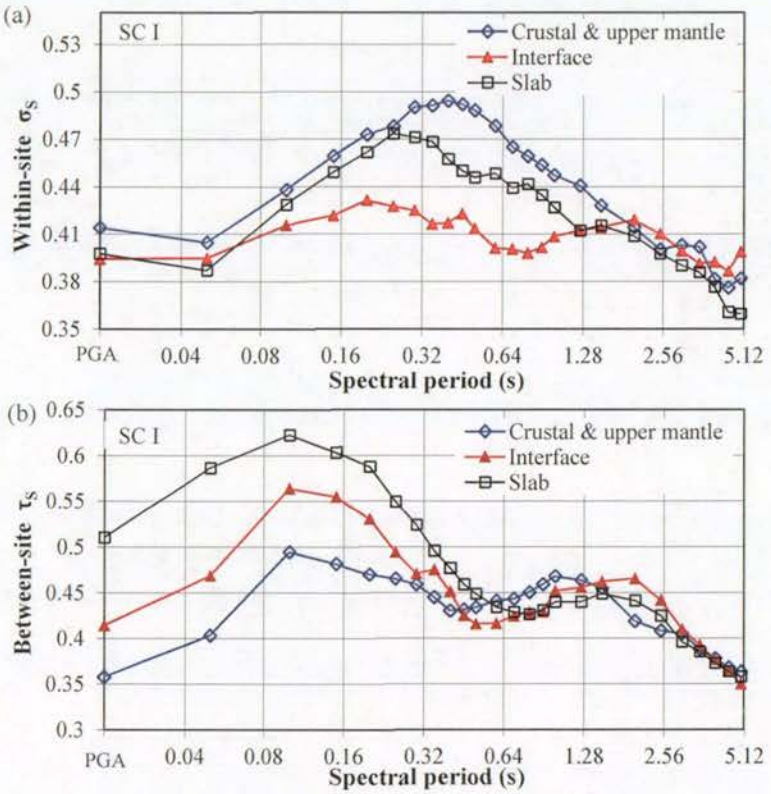

Figure 3.46 Standard deviations estimated for (a) between-site residuals, and (b) within-site residuals for SC I sites.

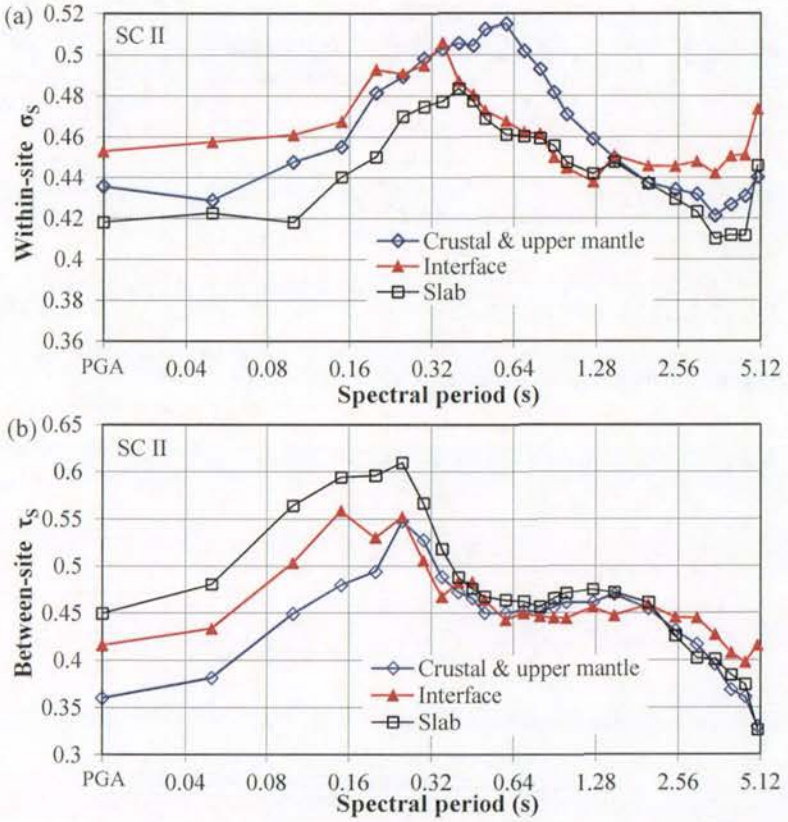

Figure 3.47 Standard deviations estimated for (a) between-site residuals, and (b) within-site residuals for SC II sites.

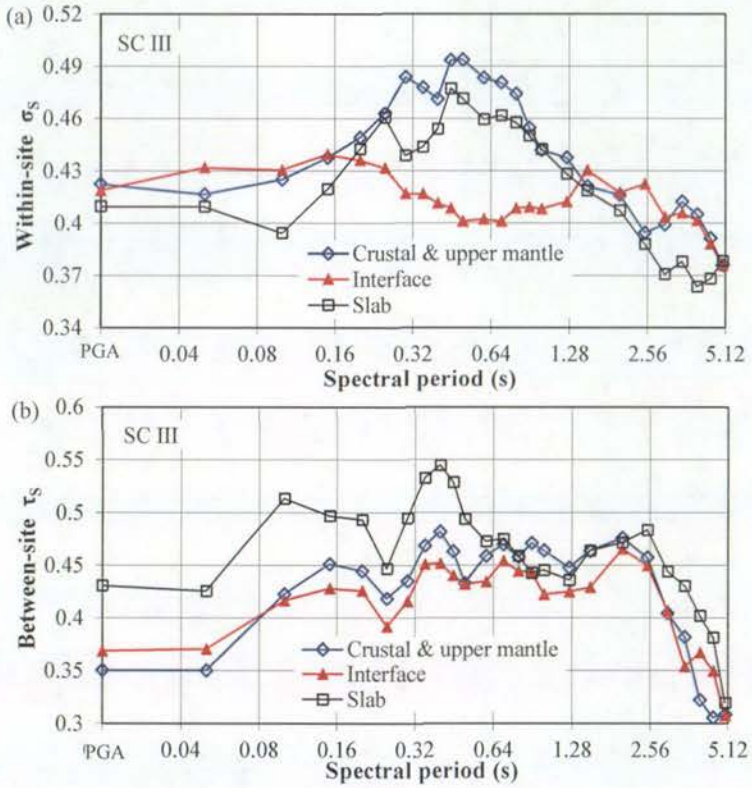

Figure 3.48 Standard deviations estimated for (a) between-site residuals, and (b) within-site residuals for SC III sites.

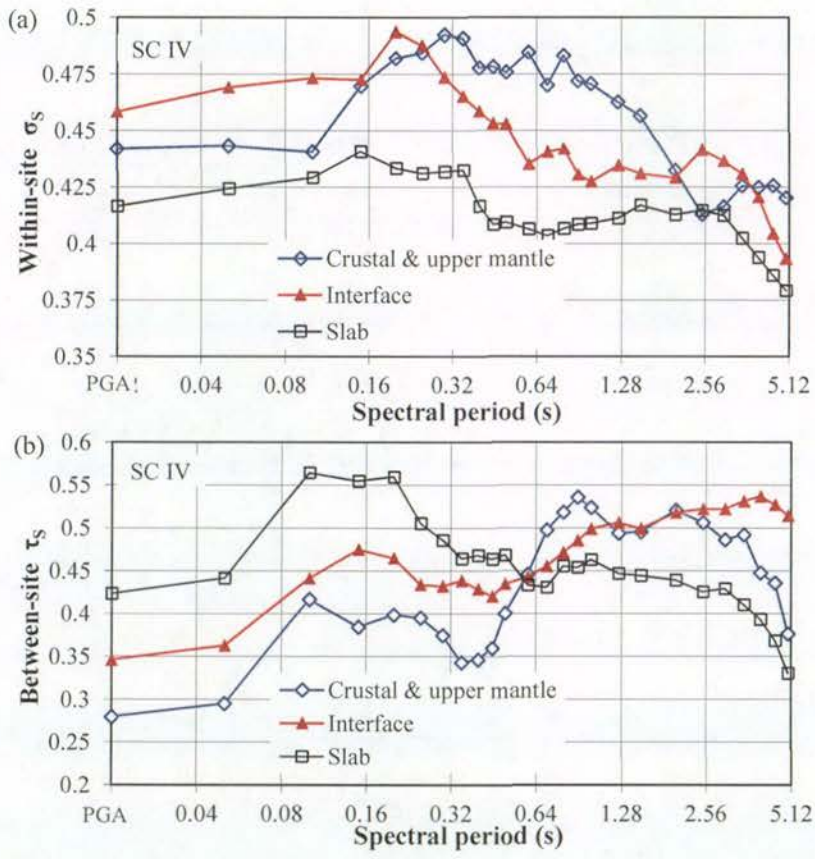

Figure 3.49 Standard deviations estimated for (a) between-site residuals, and (b) within-site residuals for SC IV sites.

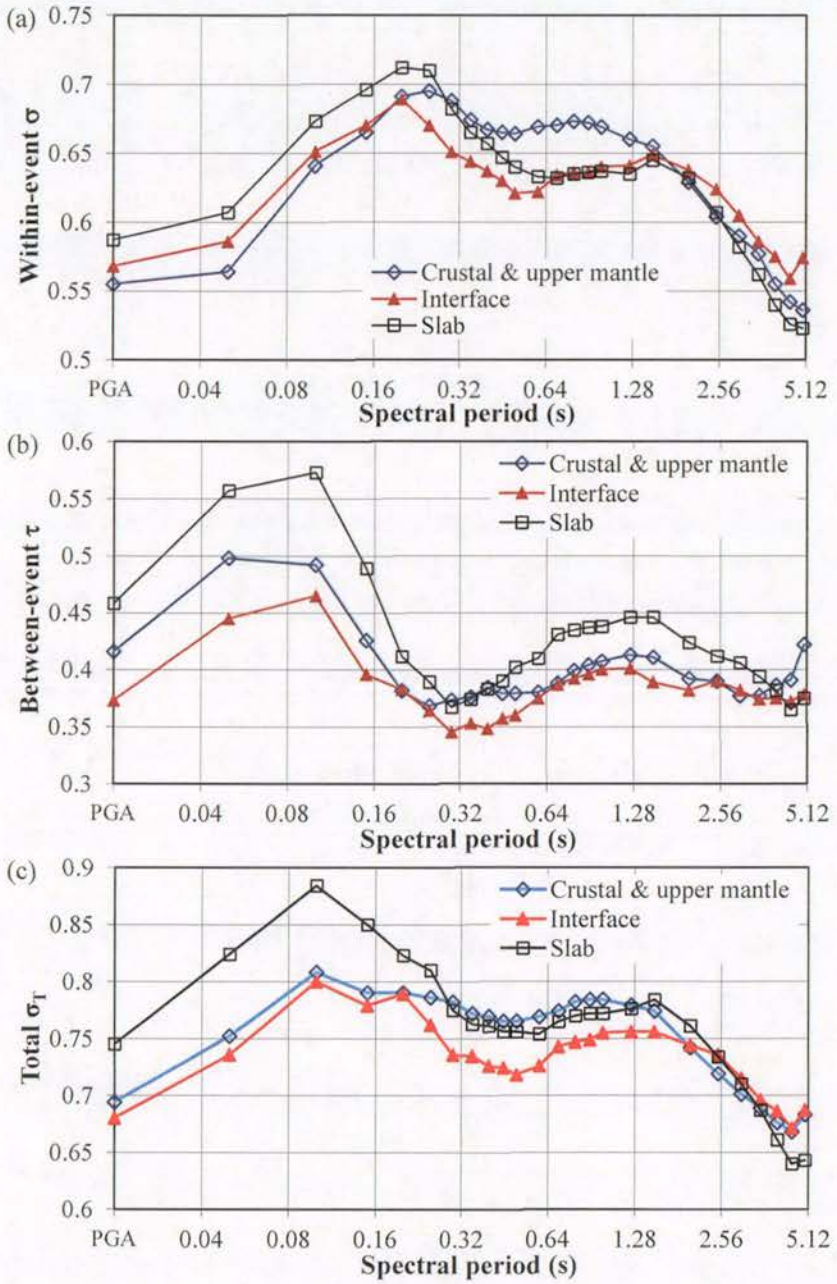

Figure 3.50 Comparison of standard deviations for (a) within-event residuals, (b) between-event residuals and (c) total residuals from the models for shallow crustal and upper mantle earthquakes, subduction interface events and subduction slab events.

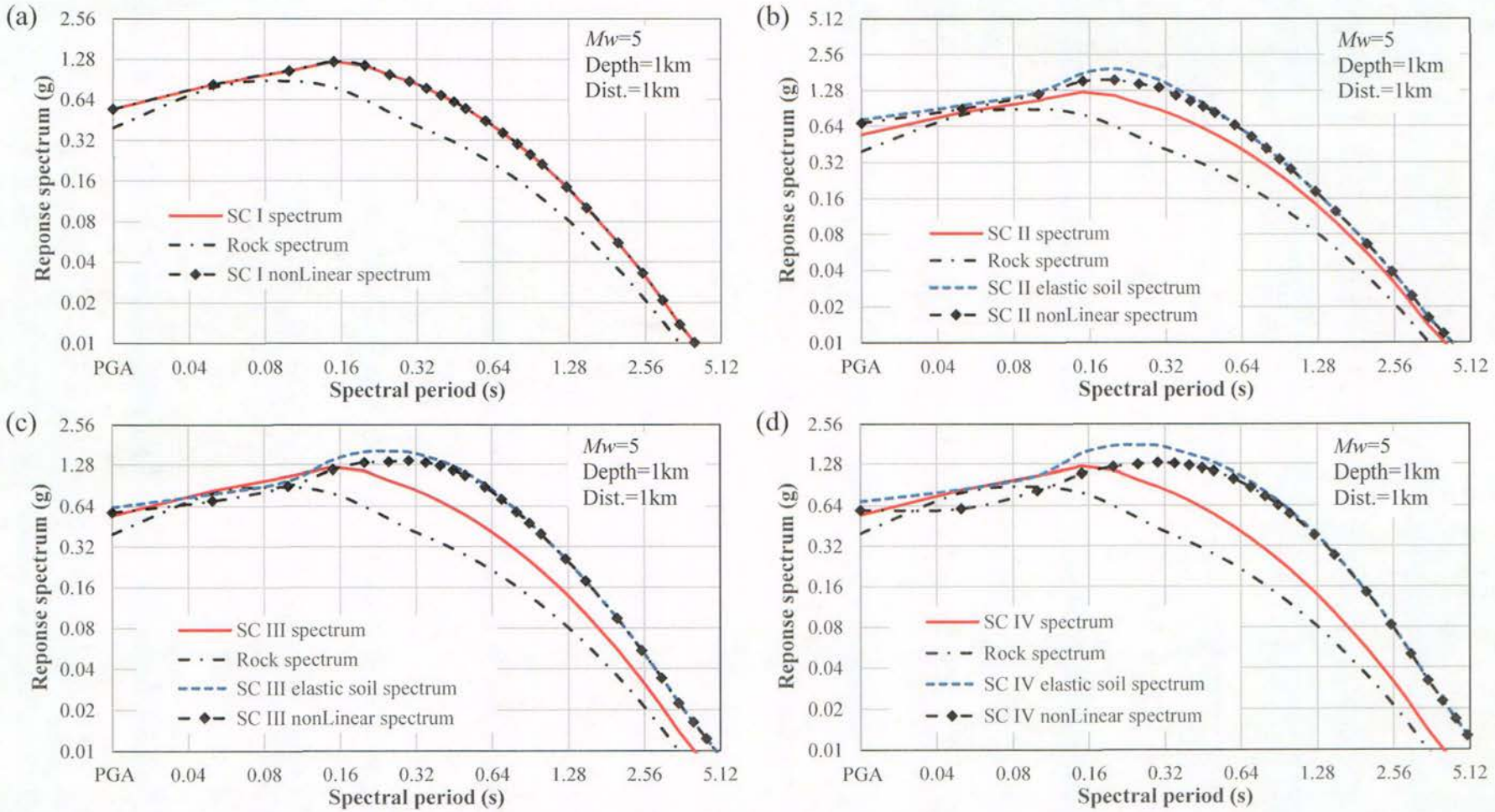

Figure 3.51 Predicted response spectra for an MW=5 shallow crustal event with a fault-top depth of 1km, a reverse or strike-slip faulting mechanism, and at a distance of 1km for SC I sites in (a), SC II site in (b), SC III sites in (c) and SC IV sites in (d), together with rock spectrum, elastic soil spectrum and nonlinear soil spectrum.

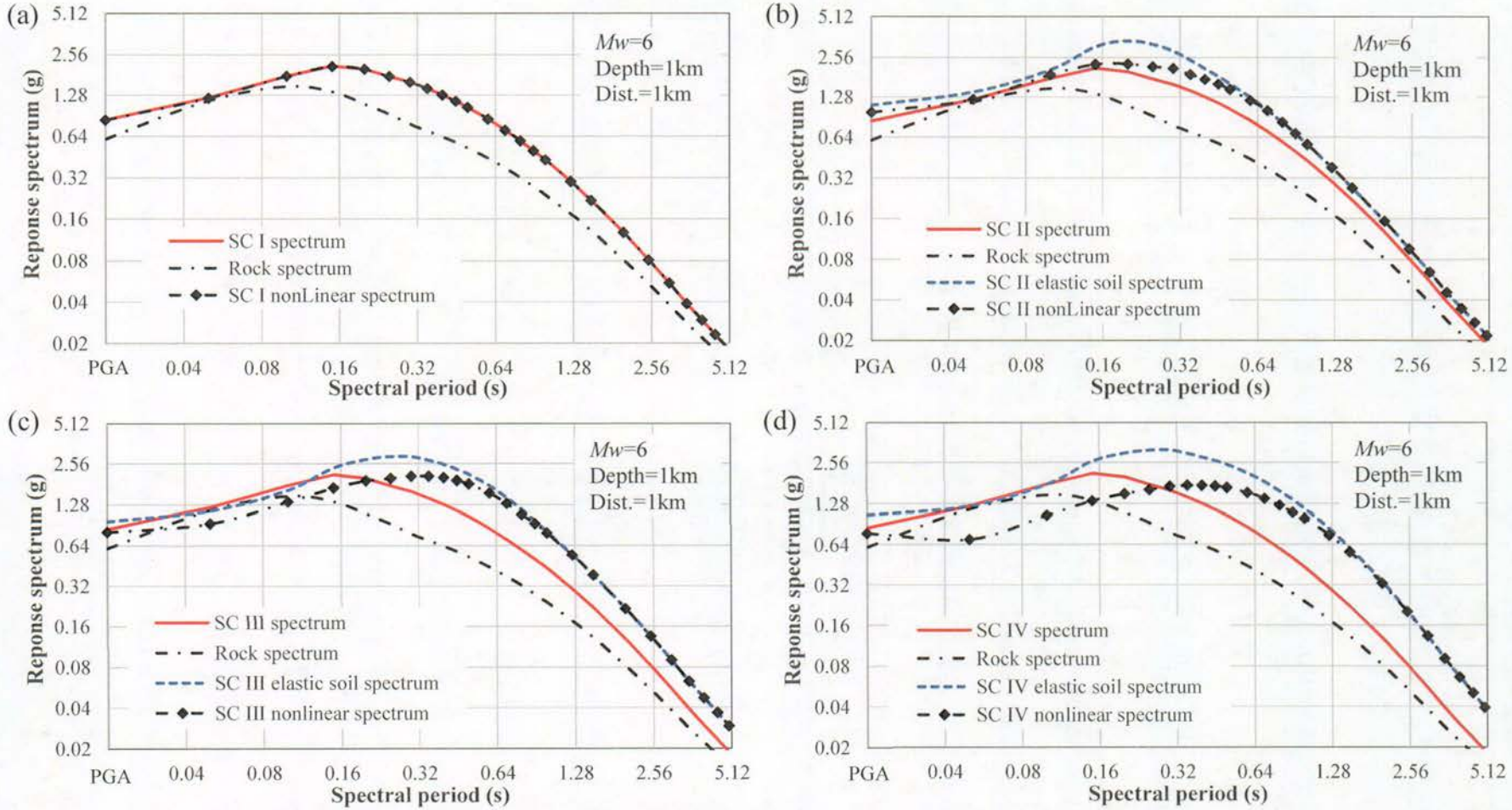

Figure 3.52 Predicted response spectra for an M_W =6 shallow crustal event with a fault-top depth of 1km, a reverse or strike-slip faulting mechanism, and at a distance of 1km for SC I sites in (a), SC II site in (b), SC III sites in (c) and SC IV sites in (d), together with rock spectrum, elastic soil spectrum and nonlinear soil spectrum.

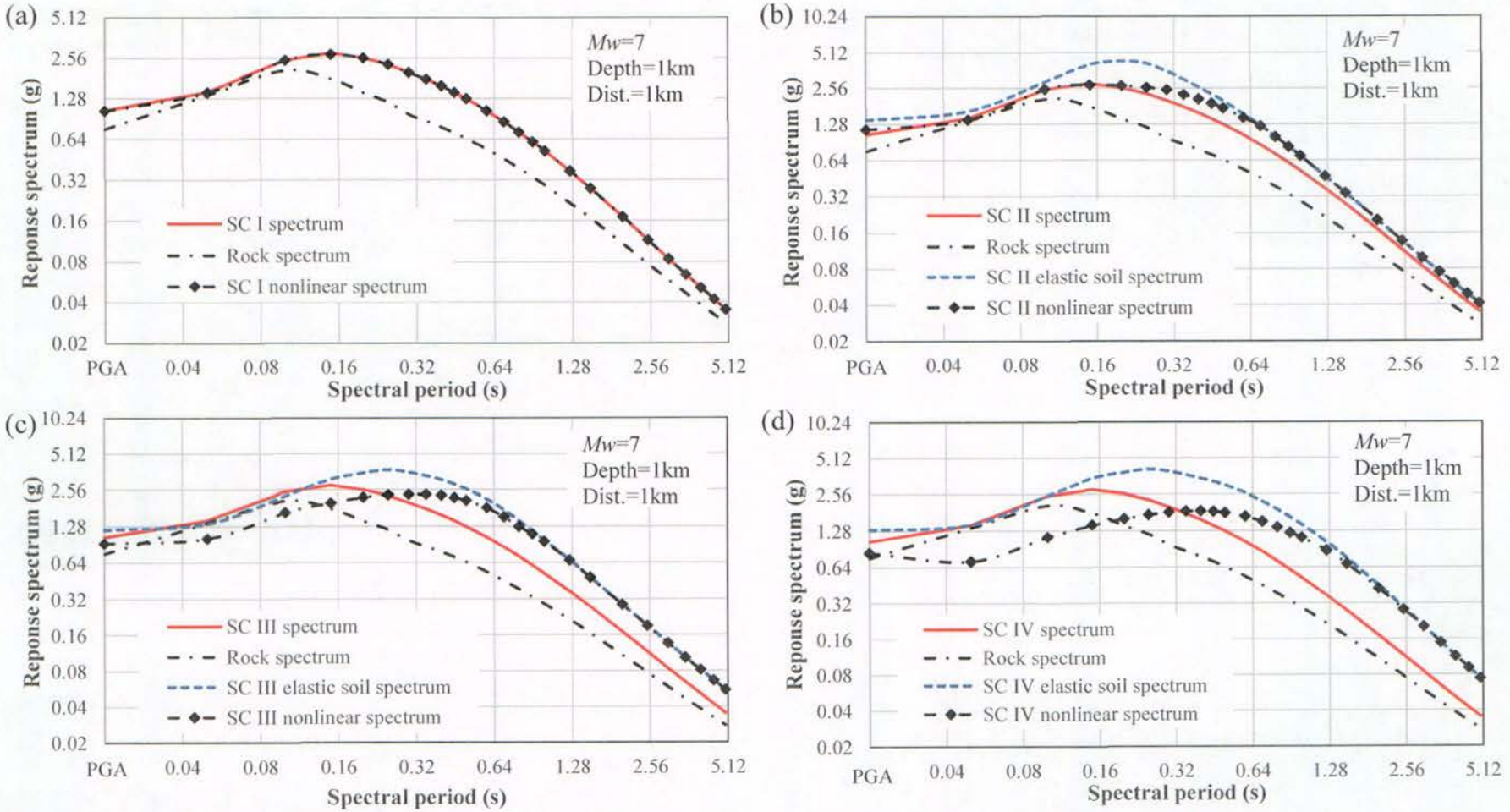

Figure 3.53 Predicted response spectra for an M_W =7 shallow crustal event with a fault-top depth of 1km, a reverse or strike-slip faulting mechanism, and at a distance of 1km for SC I sites in (a), SC II site in (b), SC III sites in (c) and SC IV sites in (d), together with rock spectrum, elastic soil spectrum and nonlinear soil spectrum.

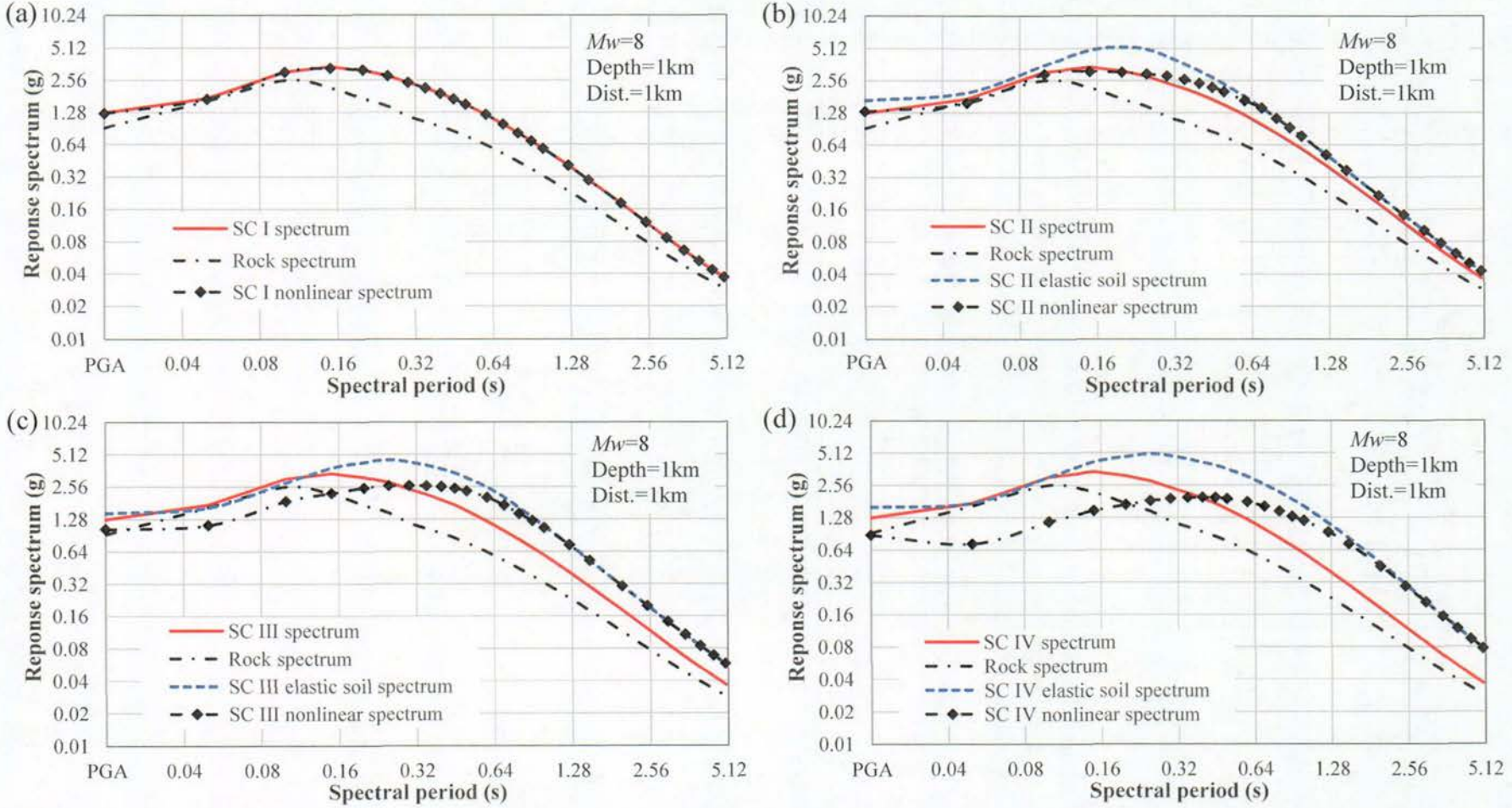

Figure 3.54 Predicted response spectra for an M_W =8 shallow crustal event with a fault-top depth of 1km, a reverse or strike-slip faulting mechanism, and at a distance of 1km for SC I sites in (a), SC II site in (b), SC III sites in (c) and SC IV sites in (d), together with rock spectrum, elastic soil spectrum and nonlinear soil spectrum.

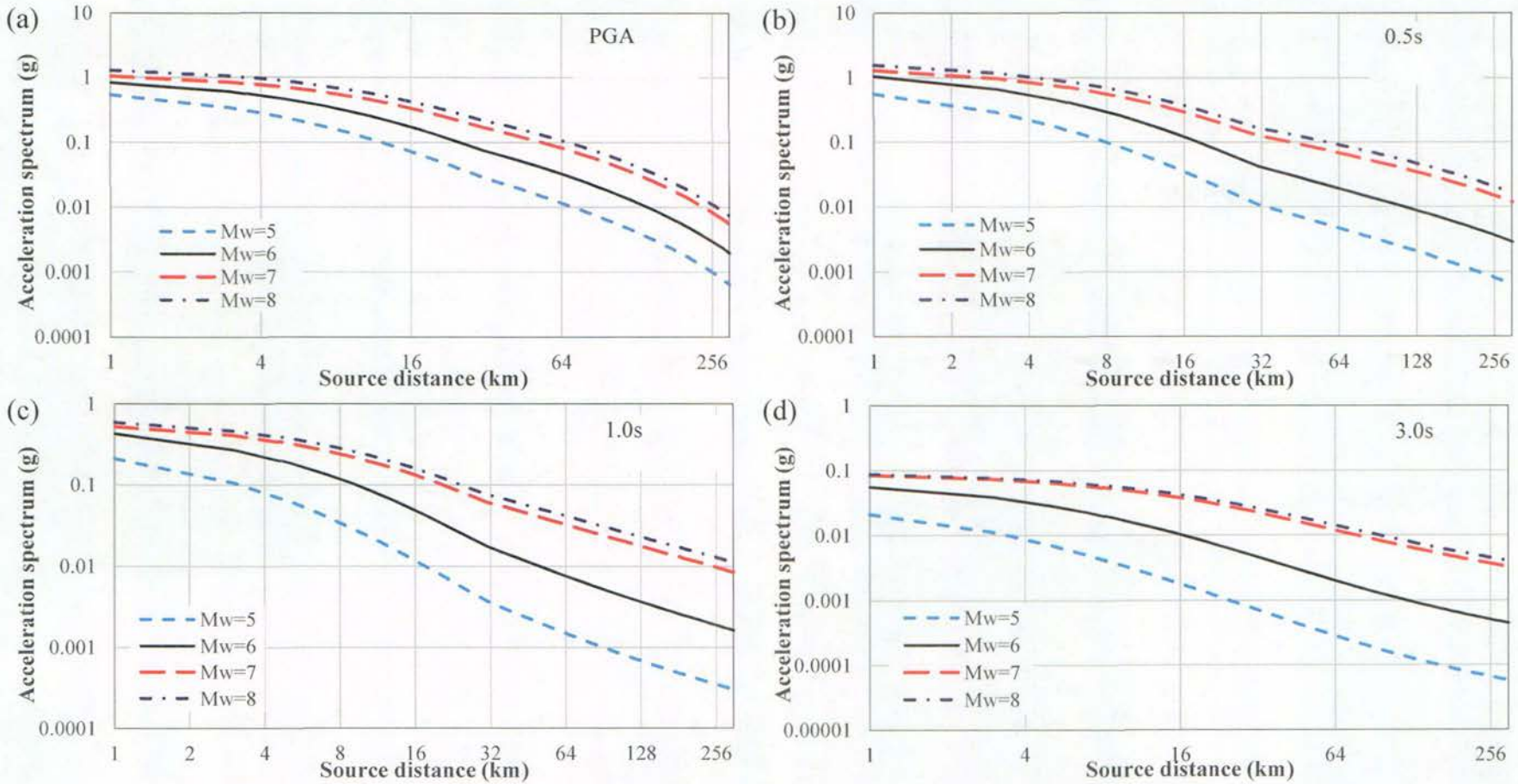

Figure 3.55 Attenuation for predicted response spectra for 4 magnitude units, a fault-top depth of 1km, crustal events and SC I sites for PGA in (a), 0.5s in (b), 1.0s in (c) and 3.0s in (d).

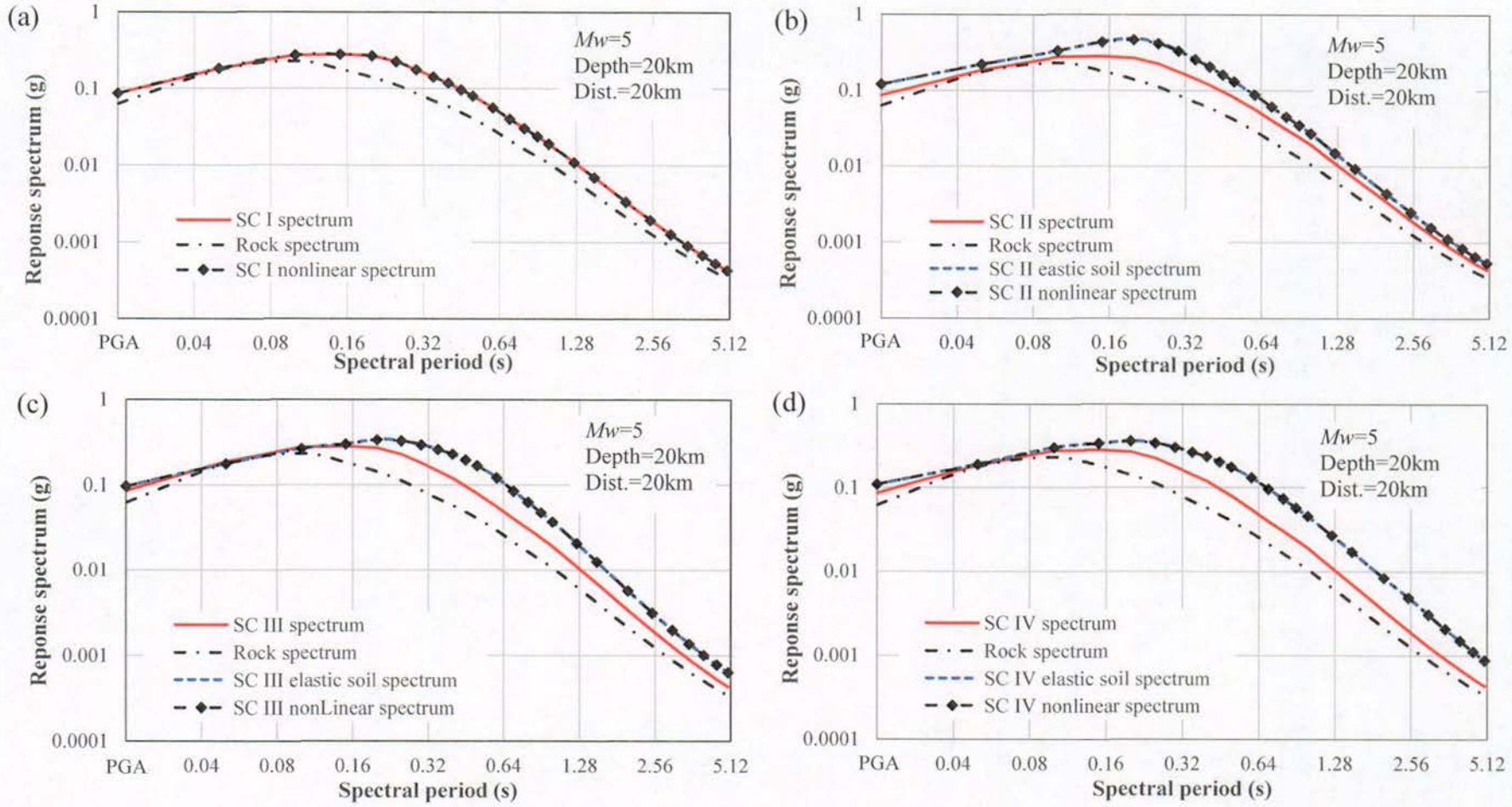

Figure 3.56 Predicted response spectra for an M_W =5 shallow interface event with a fault-top depth of 20km, and at a distance of 20km for SC I sites in (a), SC II site in (b), SC III sites in (c) and SC IV sites in (d), together with rock spectrum, elastic soil spectrum and nonlinear soil spectrum.

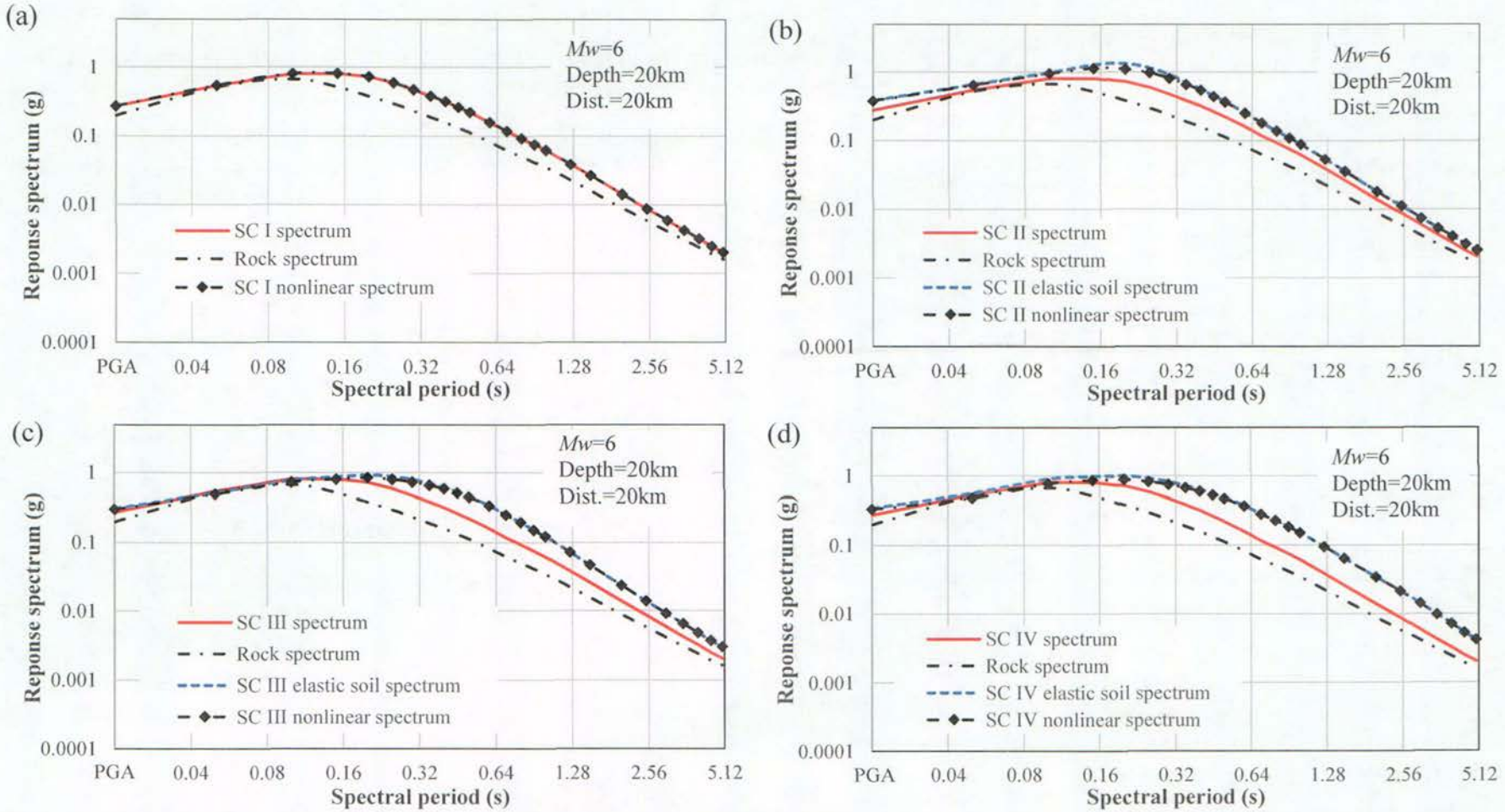

Figure 3.57 Predicted response spectra for an M_W =6 shallow interface event with a fault-top depth of 20km, and at a distance of 20km for SC I sites in (a), SC II site in (b), SC III sites in (c) and SC IV sites in (d), together with rock spectrum, elastic soil spectrum and nonlinear soil spectrum.

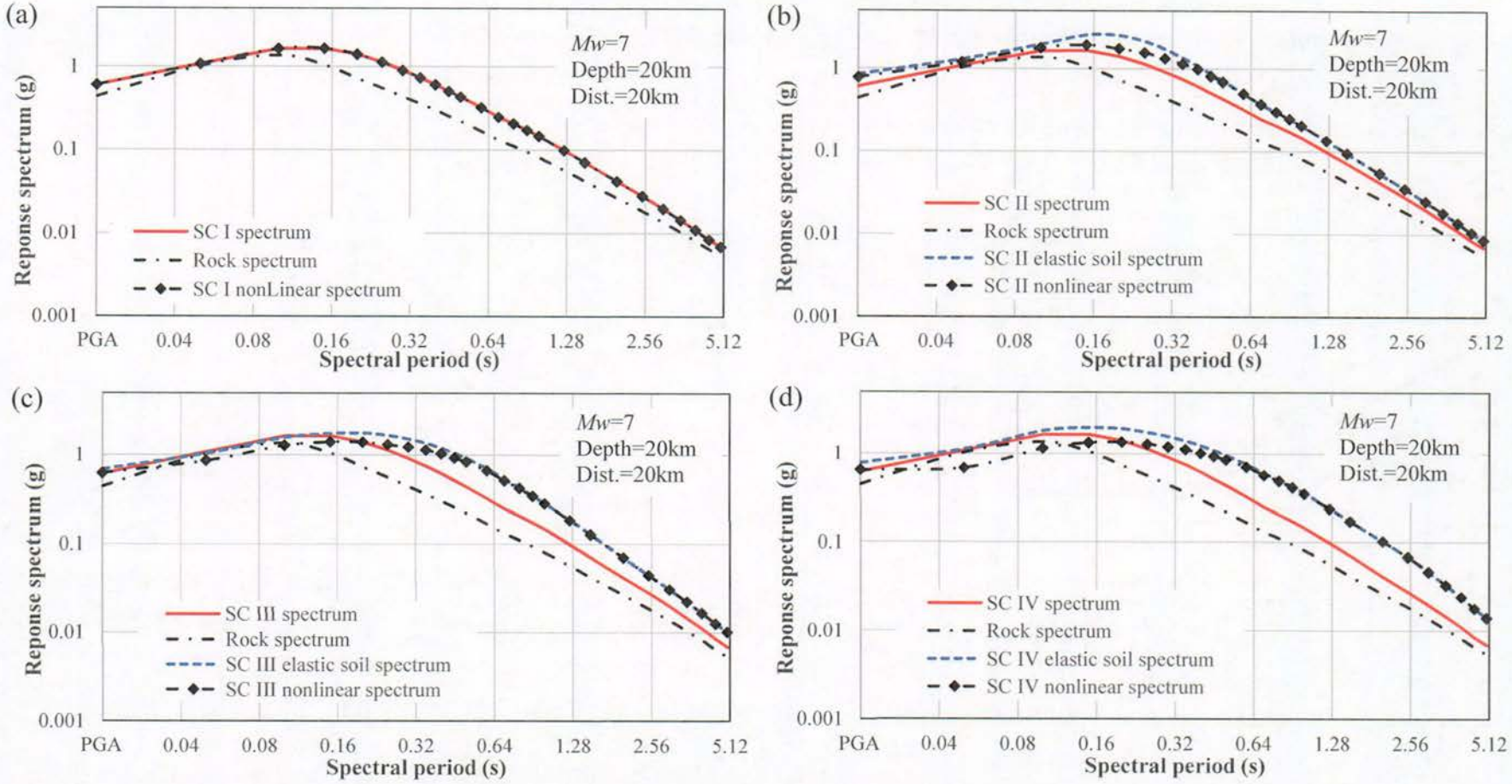

Figure 3.58 Predicted response spectra for an M_W =7 shallow interface event with a fault-top depth of 20km, and at a distance of 20km for SC I sites in (a), SC II site in (b), SC III sites in (c) and SC IV sites in (d), together with rock spectrum, elastic soil spectrum and nonlinear soil spectrum.

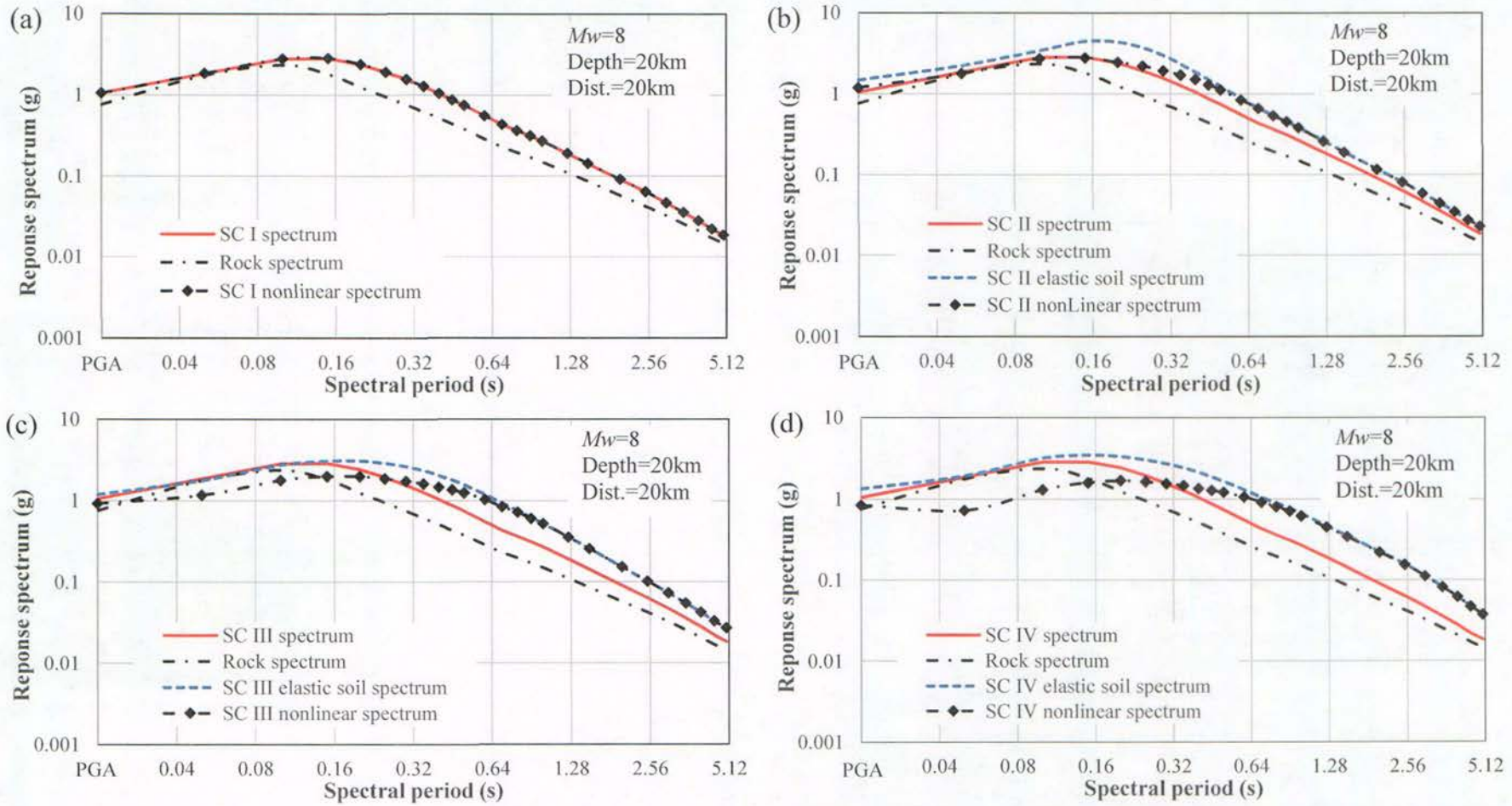

Figure 3.59 Predicted response spectra for an M_W =8 shallow interface event with a fault-top depth of 20km, and at a distance of 20km for SC I sites in (a), SC II site in (b), SC III sites in (c) and SC IV sites in (d), together with rock spectrum, elastic soil spectrum and nonlinear soil spectrum.

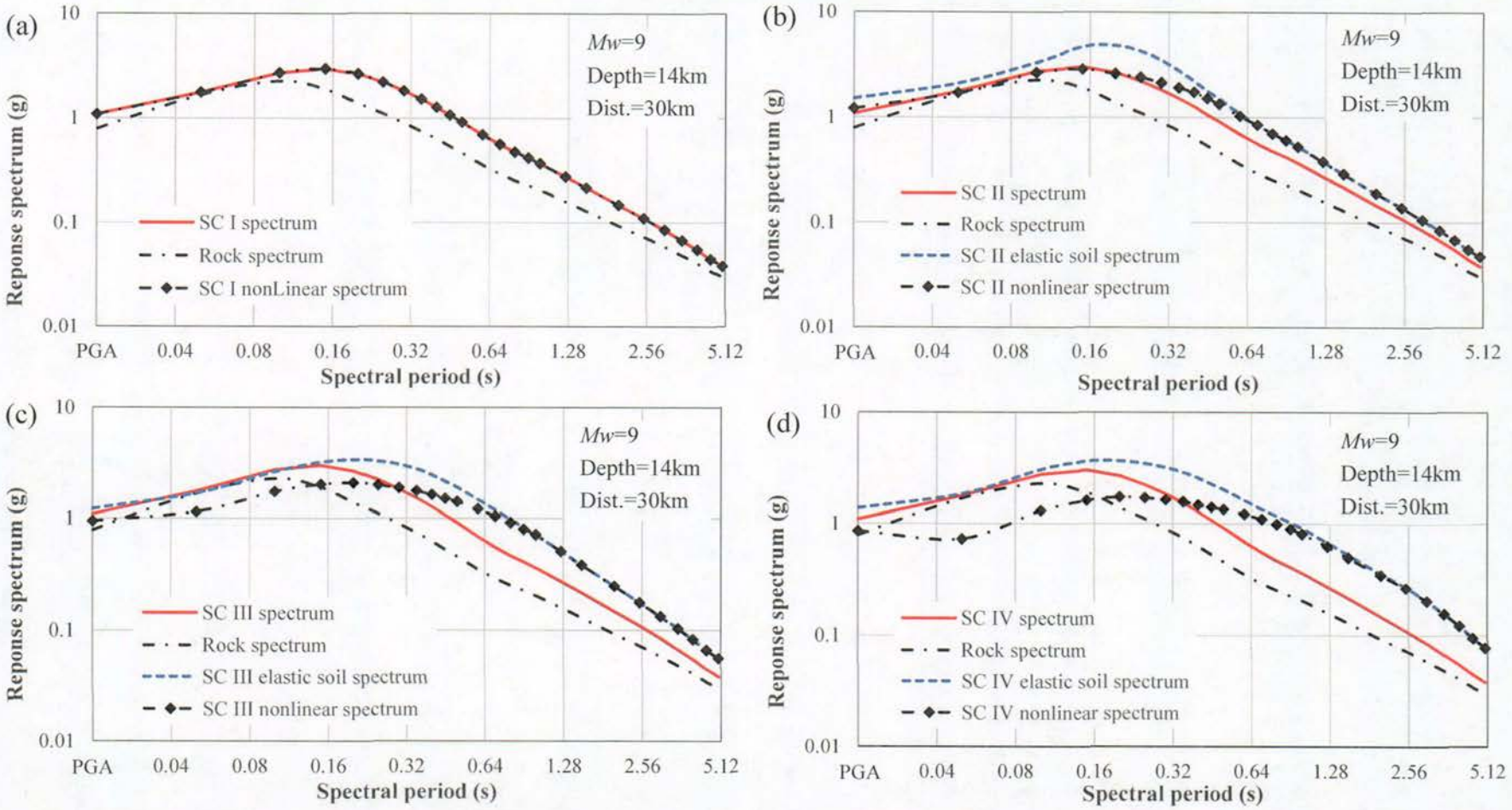

Figure 3.60 Predicted response spectra for an M_W =9 shallow interface event with a fault-top depth of 14km, and at a distance of 30km for SC I sites in (a), SC II site in (b), SC III sites in (c) and SC IV sites in (d), together with rock spectrum, elastic soil spectrum and nonlinear soil spectrum. The distance from the closest station to the fault plane for the 2011 Tohoku earthquake is just over 30km.

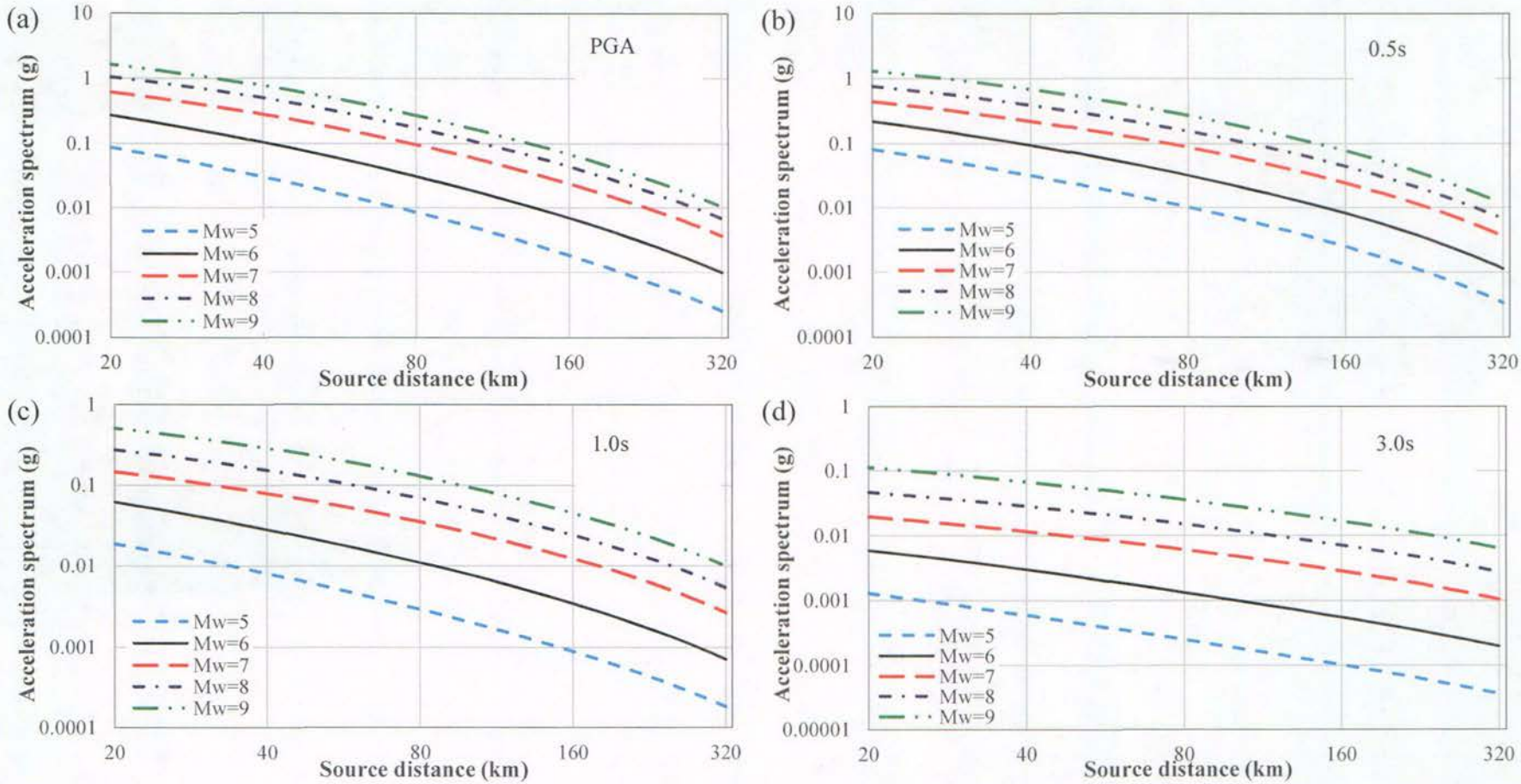

Figure 3.61 Attenuation for predicted response spectra for 5 magnitude units, a fault-top depth of 20km, subduction interface events and SC I sites for PGA in (a), 0.5s in (b), 1.0s in (c) and 3.0s in (d). The fault depth for the M_W=9 event is 14km, the same as the 2011 Tohoku earthquake.

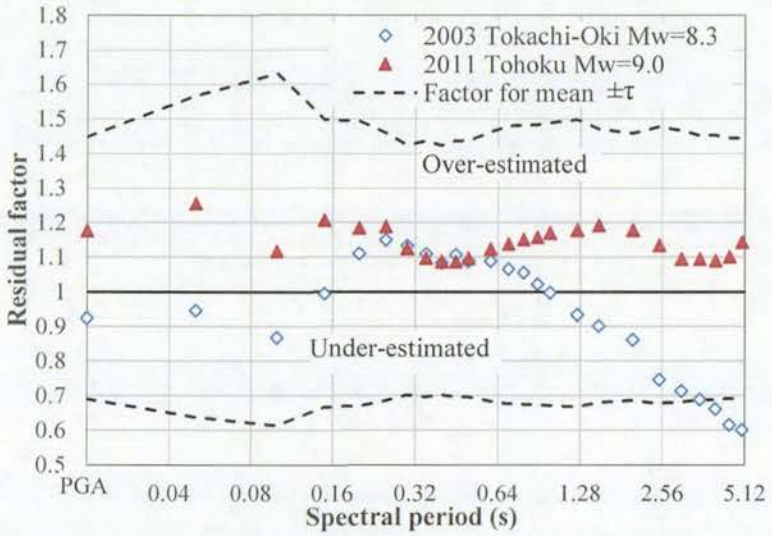

Figure 3.62 Residual factors, the exponential of the negative between-event residual, for the two largest subduction interface events together with the factors for mean ± τ. When the residual factor is large than 1.0, the spectrum is over-estimated and when the residual factor is less than 1.0 the spectrum is under-estimated, on average.

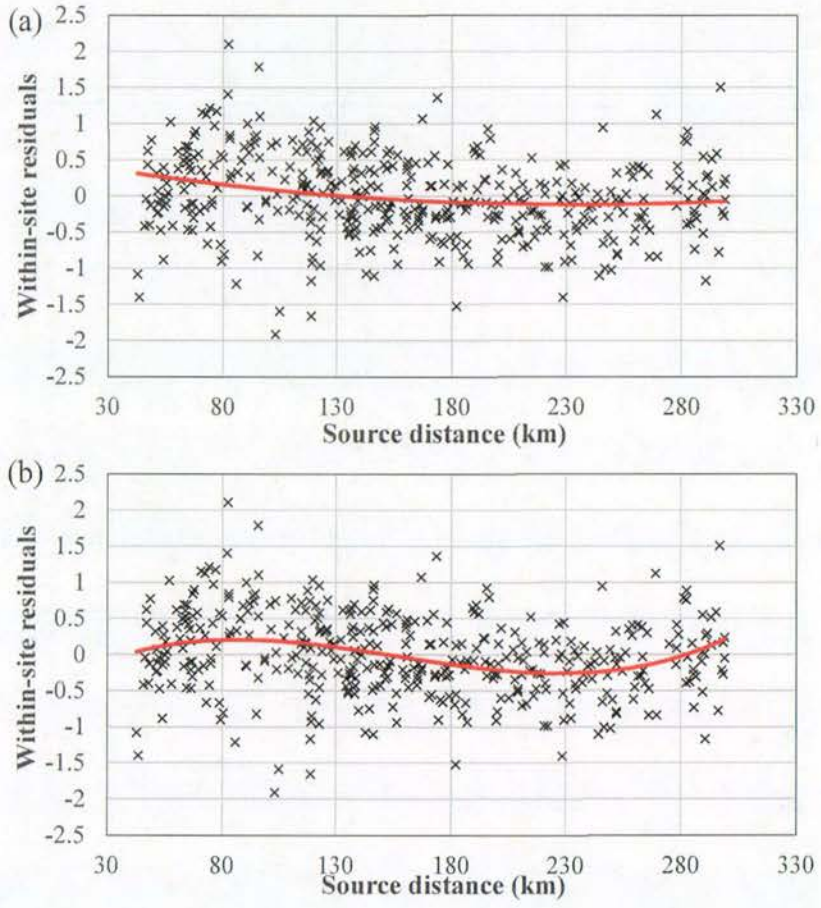

Figure 3.63 Distribution of PGA residuals with respect to source distance with a trend line of a second order polynomial of source distance in (a) and with a trend line of third order polynomial in (b).

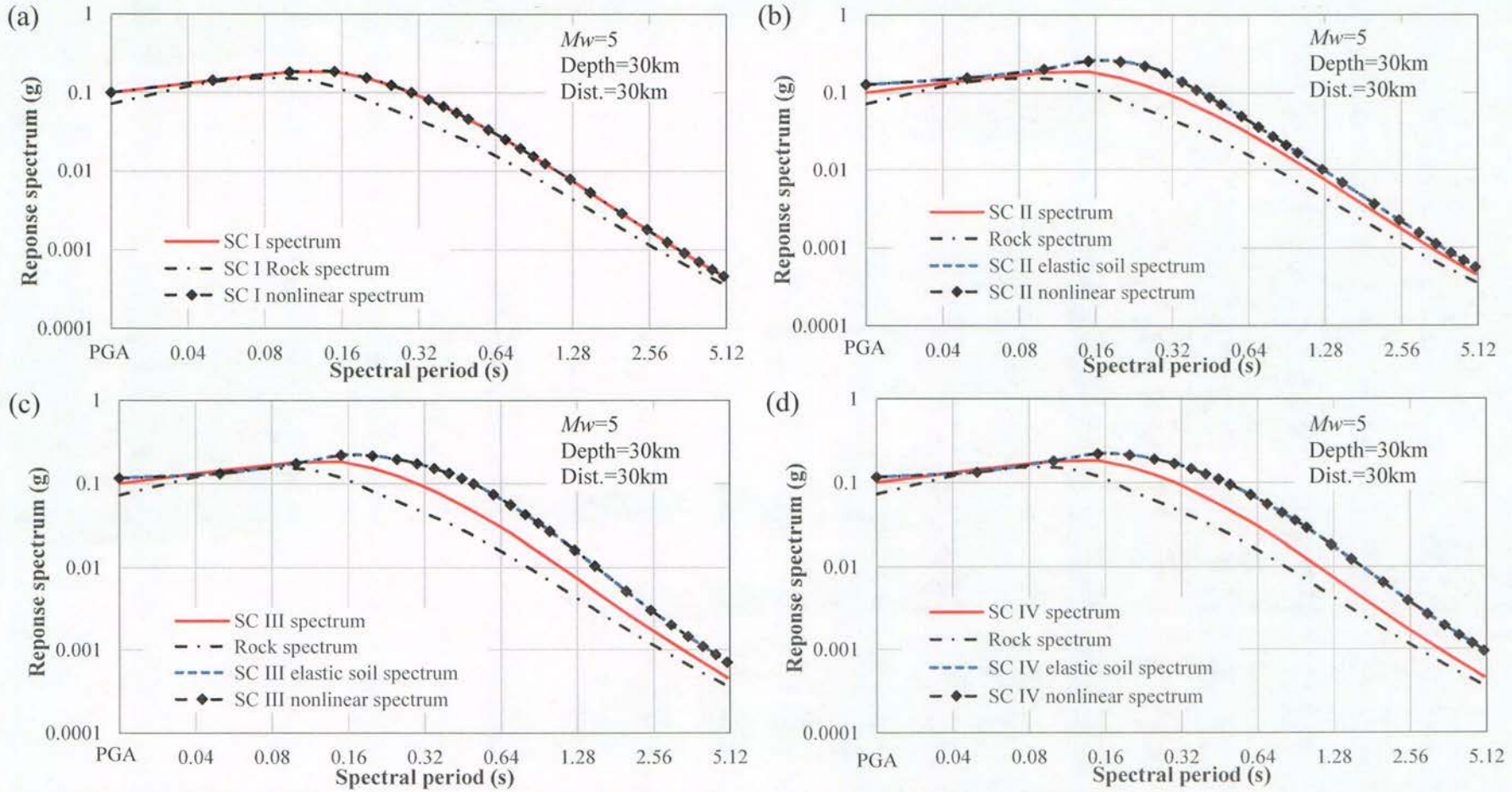

Figure 3.64 Predicted response spectra for an M_W =5 slab event with a fault-top depth of 30km, and at a distance of 30km for SC I sites in (a), SC II site in (b), SC III sites in (c) and SC IV sites in (d), together with rock spectrum, elastic soil spectrum and nonlinear soil spectrum.

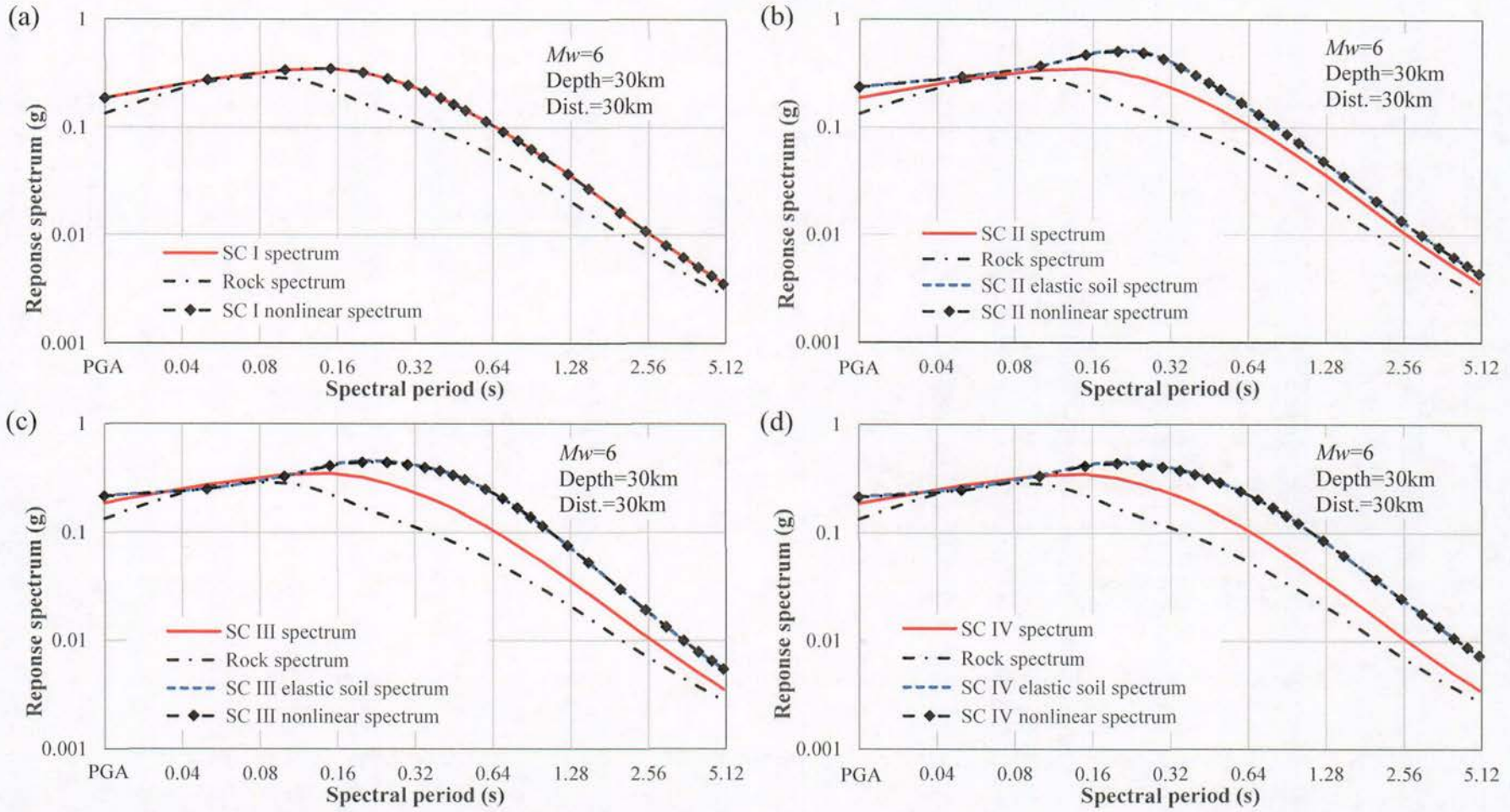

Figure 3.65 Predicted response spectra for an M_W =6 slab event with a fault-top depth of 30km, and at a distance of 30km for SC I sites in (a), SC II site in (b), SC III sites in (c) and SC IV sites in (d), together with rock spectrum, elastic soil spectrum and nonlinear soil spectrum.

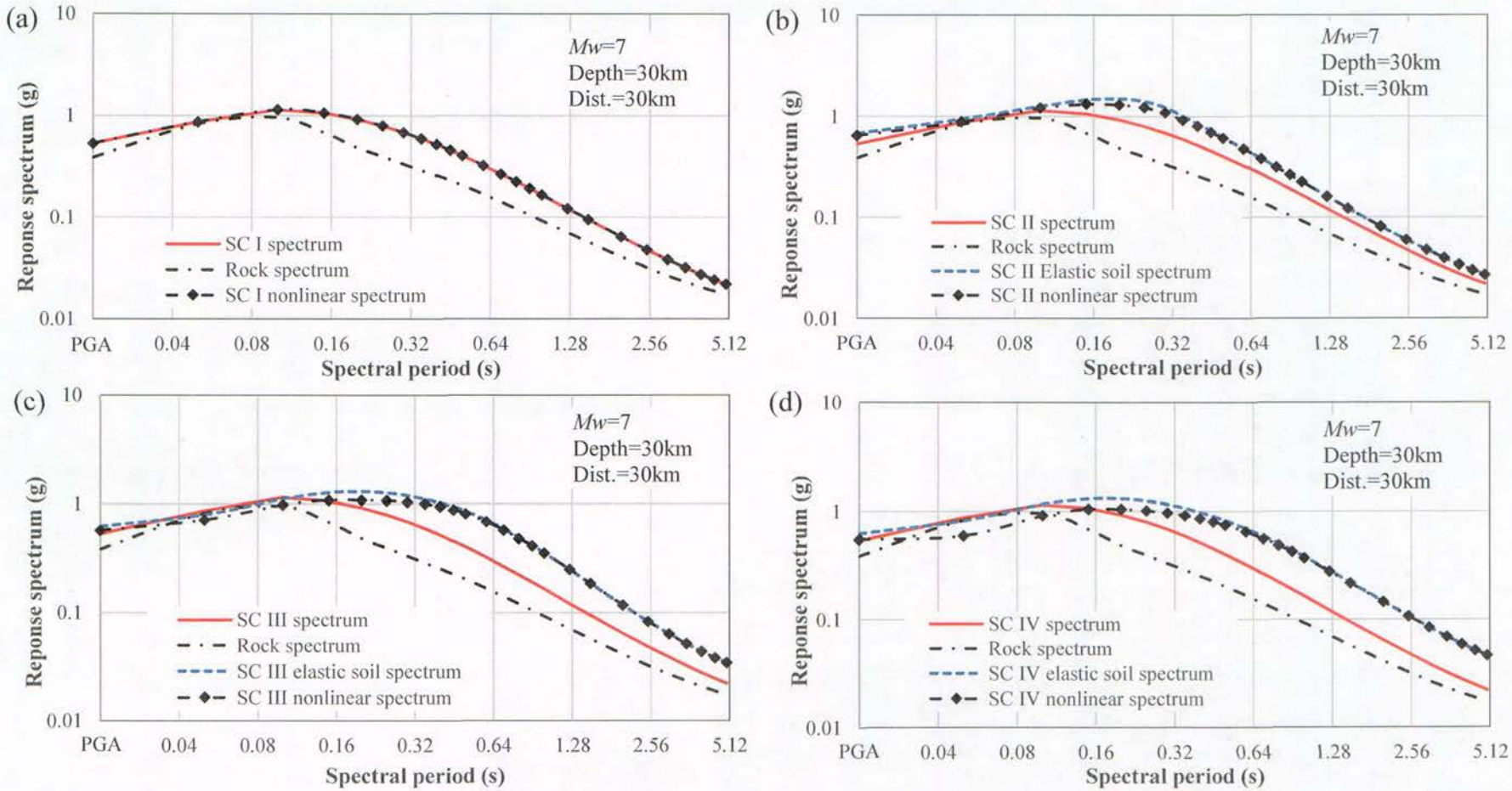

Figure 3.66 Predicted response spectra for an M_W =7 slab event with a fault-top depth of 30km, and at a distance of 30km for SC I sites in (a), SC II site in (b), SC III sites in (c) and SC IV sites in (d), together with rock spectrum, elastic soil spectrum and nonlinear soil spectrum.

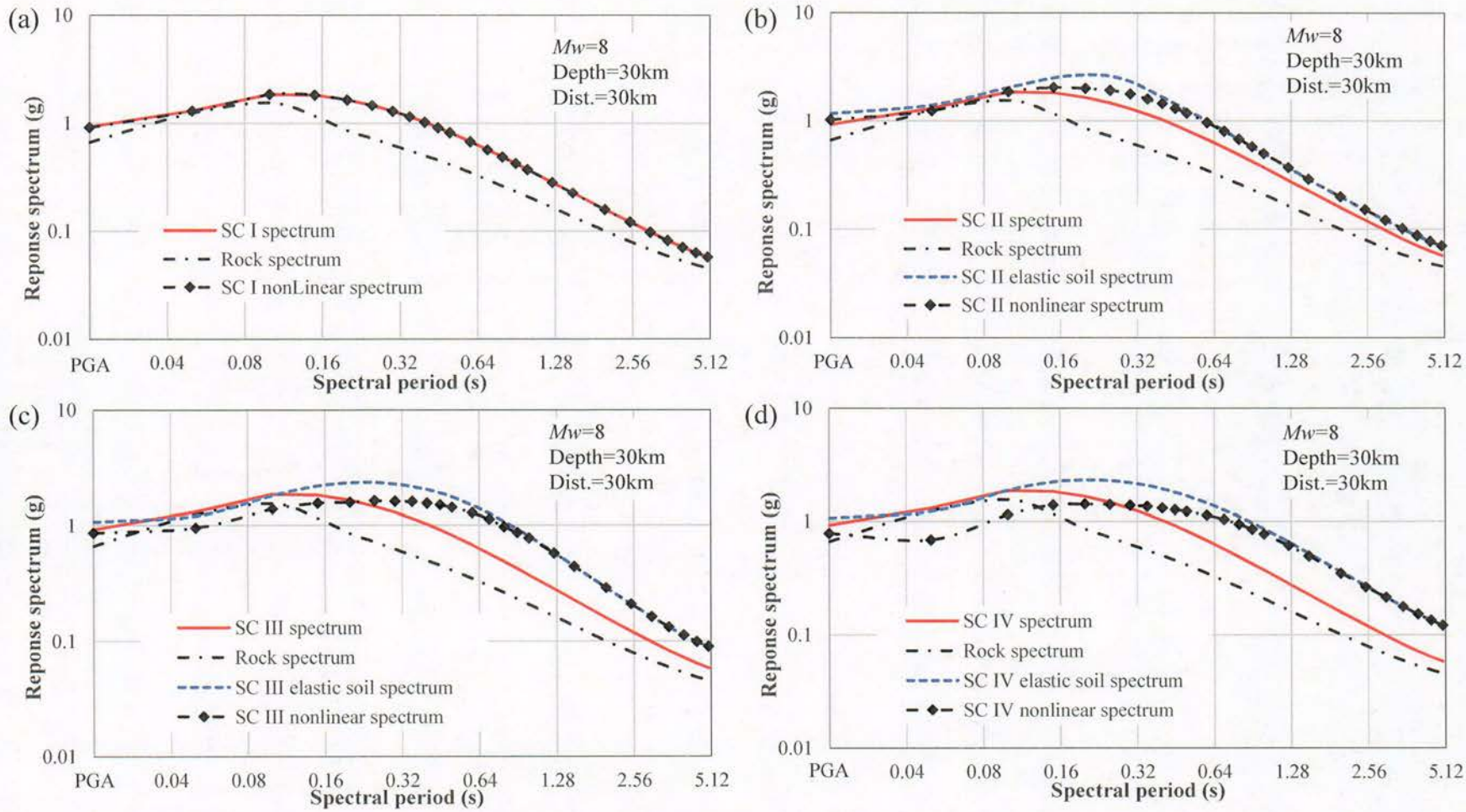

Figure 3.67 Predicted response spectra for an M_W =8 slab event with a fault-top depth of 30km, and at a distance of 30km for SC I sites in (a), SC II site in (b), SC III sites in (c) and SC IV sites in (d), together with rock spectrum, elastic soil spectrum and nonlinear soil spectrum.

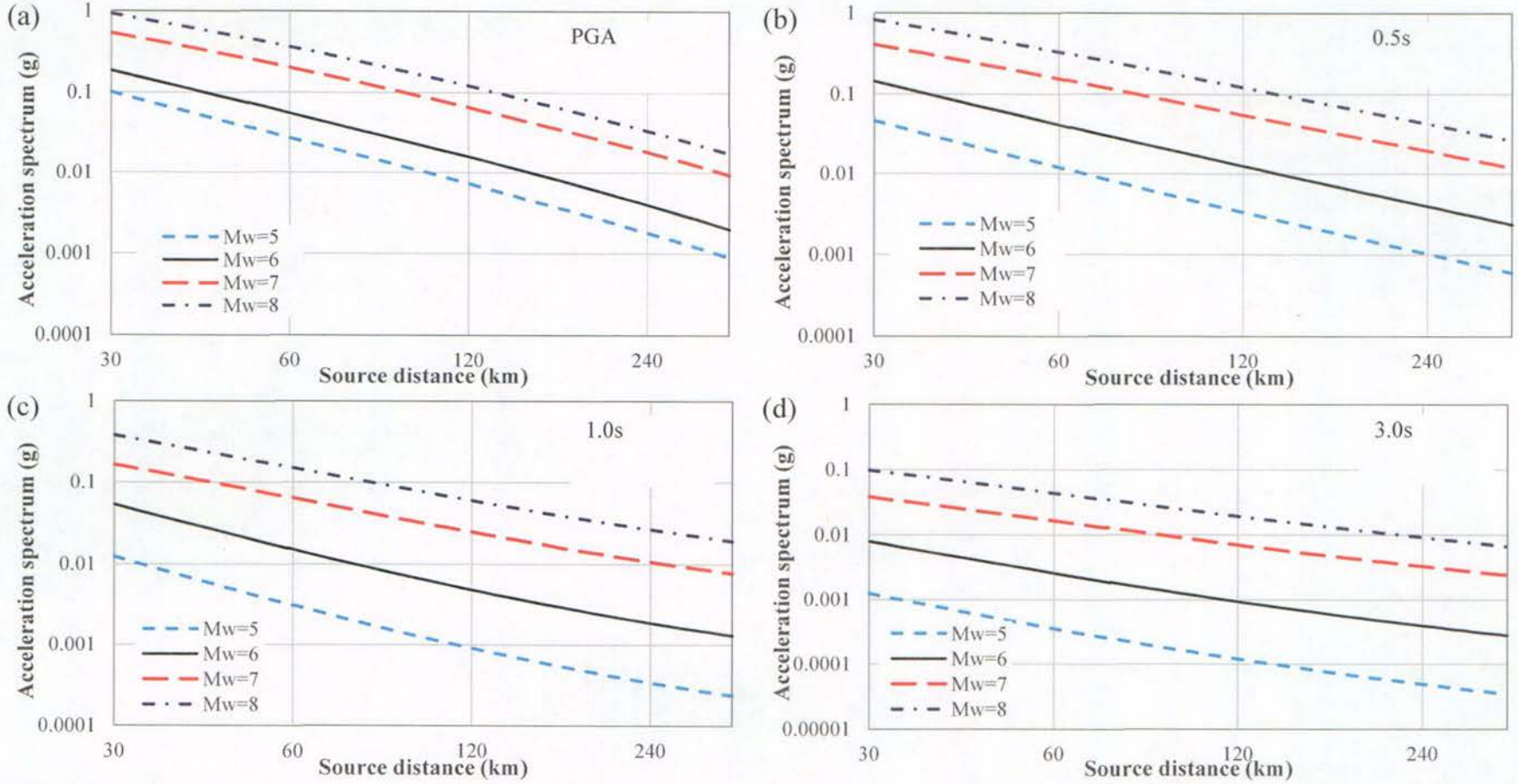

Figure 3.68 Attenuation of predicted response spectra for 4 magnitude units, a fault-top depth of 20km, subduction slab events and SC I sites for PGA in (a), 0.5s in (b), 1.0s in (c) and 3.0s in (d).

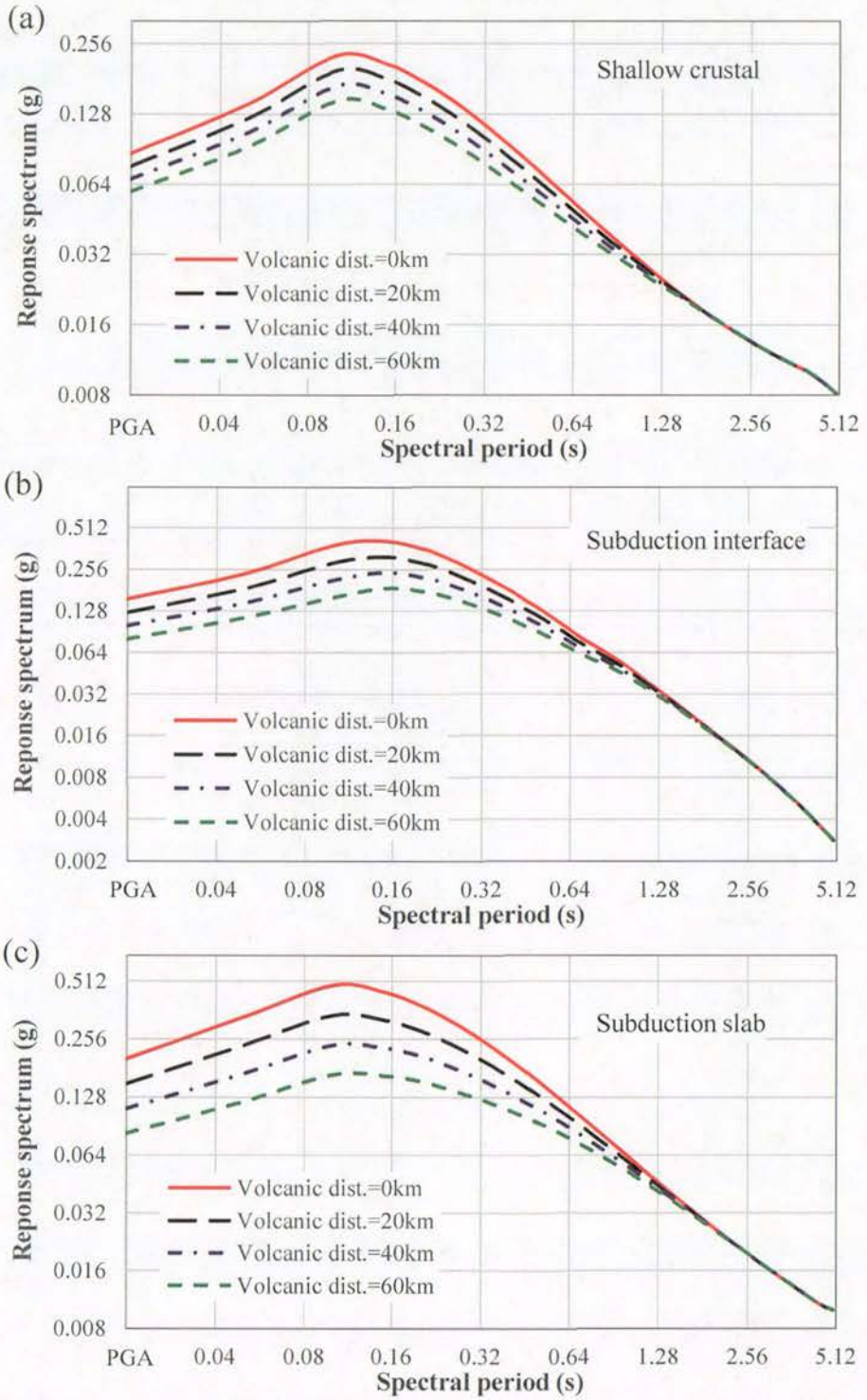

Figure 3.69 Predicted response spectra from an M_W =7.0, at a source distance of 60km with the travel path within a volcanic zone for 0, 20, 30, 40 and 60km, (a) for a shallow crustal event with a fault depth of 1km, (b) for a subduction interface event with a fault-top depth of 20km, and (c) for a subduction slab event with a depth of 40km.

4.0 ACKNOWLEDGEMENTS

The work reported here is partially supported by New Zealand Earthquake Commission 2010 Biennial Research Grant, by research grants from the National Science Foundation of China (51278432) and the Southwest Jiaotong University (SWJTU12ZT04). At the early stage (2011) support was received from the New Zealand Foundation for Research Science and Technology, New Zealand Hazards Platform contract C05X0907. The authors would like to thank Dr. Jim Cousins and Chris Van Houtte of the GNS Science and Professor Jian Zhang for their review of this report. This project was not possible without the contribution from the post-graduates working with the leading author in the Southwest Jiaotong University in China: Shuanglin ZHOU, Fei JIANG, Pingjun GAO, Junsheng HU, Hao XING, Pencheng YU, Tao LONG, Chen ZHAO, Jun ZHOU, Xiaofu HUANG, Zeshi ZHU and Jinmei WANG. We would like to thank Dr. Kimiyuki Asano from the DPRI of Kyoto University for supplying the fault model parameters for a number of earthquakes, Dr. Changjiang Wu from Japan for assistance with the JMA catalogue. Dr. Hong Kie Thio from URS Corporation for assistance in the earthquake classification. We would like to thank the National Institute of Earth Science and Disaster Prevention for supplying the strong-motion records from the K-net and Kik-net.

5.0 REFERENCES

Abrahamson, N. A., and W. J. Silva (2008). Summary of the Abrahamson & Silva NGA Ground-Motion Relations, *Earthquake Spectra*, **24,** no. 1, 67–97.

Abrahamson, N. A., and R. R. Youngs (1992). A stable algorithm for regression analysis using the random effect model, *Bulletin of the Seismological Society of America*, **82,** no. 1, 505–510.

Akaike, H. (1974). A new look at the statistical model identification, *IEEE Trans. Auto. Control, AC.*, **19,** no. 6, 716–723.

Atkinson (2006). Single-Station Sigma, *Bulletin of the Seismological Society of America*, **96,** no. 2, 446–455.

Atkinson, G. M., and D. M. Boore (2003). Empirical Ground-Motion Relations for Subduction-Zone Earthquakes and Their Application to Cascadia and Other Regions, *Bulletin of the Seismological Society of America*, **93,** no. 4, 1703–1729.

Bonilla, L. F., K. Tsuda, N. Pulido, J. R´egnier, and A. Laurendeau (2011). Nonlinear site response evidence of K-NET and KiK-net records from the 2011 off the Pacific coast of Tohoku Earthquake, *Earth Planets Space*, **63,** 785–789.

Boore, D. M., and G. M. Atkinson (2008). Ground-Motion Prediction Equations for the Average Horizontal Component of PGA, PGV, and 5%-Damped PSA at Spectral Periods between 0.01 s and 10.0 s, *Earthquake Spectra*, **24,** no.1, 99–138.

Boore, D. M., A. A. Skarlatoudis, B. N. Margaris, C. B. Papazachos, and C. Ventouzi (2009). Along-Arc and Back-Arc Attenuation, Site Response, and Source Spectrum for the Intermediate-Depth 8 January 2006 M 6.7 Kythera, Greece, Earthquake, *Bulletin of the Seismological Society of America*, **99,** no. 4, 2410–2434.

Building Seismic Safety Council (BSSC) (2000). The 2000 NEHRP Recommended Provisions for New Buildings and Other Structures, Part I (Provisions) and Part II (Commentary), FEMA 368/369, Washington DC.

Campbell, K. W., and Y. Bozorgnia (2008). NGA Ground Motion Model for the Geometric Mean Horizontal Component of PGA, PGV, PGD and 5% Damped Linear Elastic Response Spectra for Periods Ranging from 0.01 to 10s, *Earthquake Spectra*, **24,** no. 1, 139–171.

Chiou, B. S.-J., and R. R. Youngs (2008), An NGA model for the average of horizontal component of peak ground motion and response spectra, *Earthquake Spectra,* **24,** no. 1, 173–216.

Choi, Y., and J. P. Stewart (2005). Nonlinear site amplification as function of 30 m shear wave velocity, *Earthquake Spectra*, **21,** 1–30.

Cousins, J., and G.H. McVerry (2010). Overview of strong motion data from the Darfield earthquake, *Bulletin of the New Zealand Society for Earthquake Engineering*, **43**, no. 4, 222–227.

Dowrick, D. J., and D. A. Rhoades (2004). Rhoades Relations between Earthquake Magnitude and Fault Rupture Dimensions: How Regionally Variable Are They? *Bulletin of the Seismological Society of America*, **94,** no.3, 776–788.

Eberhart-Phillips, D, and G. H. McVerry (2003). Estimating Slab Earthquake Response Spectra from a 3D Q Model, *Bulletin of the Seismological Society of America*, **93,** no.6, 2649–2663.

Gamage, S. S. N., N. Umino, A. Hasegawa1, and S. H. Kirby (2009). Offshore double-planed shallow seismic zone in the NE Japan forearc region revealed by sP depth phases recorded by regional networks, *Geophys. J. Int.*, **178,** 195–214.

Ghofrani, H., and G. M. Atkinson (2014). Ground-Motion Prediction Equations for Interface Earthquakes of M7 to M9 Based on Empirical Data from Japan, *Bulletin of Earthquake Engineering*, **12,** no.2, 549–571.

Graves, R. W., and A. Pitarka (2010). Broadband Ground-Motion Simulation Using a Hybrid Approach, *Bulletin of the Seismological Society of America*, **100,** no.5A, 2095–2123.

Hayes, G. P., D. J. Wald, and R. L. Johnson (2012). Slab1.0: A three-dimensional model of global subduction zone geometries, *J. Geophys. Res.*, **117,** B01302.

Iwasaki, T., F. Tatsuoka, and Y. Takaki (1978). Shear modulus of sands under torsional shear loadings, *Soils and Foundations, JSSMFE.*, **18,** no. 1, 39–56.

Kanno, T., A. Narita, N. Morikawa, H. Fujiwara, and Y. Fukushima (2006). A new attenuation relation for strong ground motion in Japan based on recorded data, *Bulletin of the Seismological Society of America,* **96,** no. 3, 879–897.

Kobayashi, S., T. Takahashi., S. Matsuzaki, M. Mori, Y. Fukushima, J. X. Zhao, and P. G. Somerville (2000). A spectral attenuation model for Japan using digital strong motion records of JMA87 type. In: 12WCEE 2000. Proceedings of the World Conference on Earthquake Engineering.

Lu, M., X. J. Li, X. W. An, and J. X. Zhao (2010). A comparison of recorded response spectra from the great 2008 Wenchuan, China, earthquake with modern ground-motion prediction models, *Bulletin of the Seismological Society of America*, **100,** no. 5B, 2357–2380.

McBean, K. M., J.G. Anderson, and H. Kawase (2014). Event Terms for the Shallow 2011 Normal Faulting Earthquakes in the Ibaraki Fukushima Prefectural Border Region, Japan, *2014 Annual Meeting of Seismological Society of America*, held during 30 April–2 May 2014 in Anchorage, Alaska, USA, Abstract number 230.

McVerry, G. H., J. X. Zhao, N. A. Abrahamson, and P.G. Somerville (2006). Crustal and Subduction zone attenuation relations for New Zealand earthquakes, *Bulletin of the New Zealand Society for Earthquake Eng.*, **39,** no. 1, 1–58.

Régnier, Julie, H. Cadet, L. F. Bonilla, E. Bertrand, and J.-F. Semblat (2013). Assessing Nonlinear Behavior of Soils in Seismic Site Response: Statistical Analysis on KiK-net Strong-Motion Data, *Bulletin of the Seismological Society of America*, **103,** no. 3, 1750–1770.

Safak, E. (1997). Models and methods to characterize site amplification ratios from a pair of records. *Earthquake Spectra*, **13,** no.1, 97–129.

Sandıkkaya, M. A., S. Akkar and P.-Y. Bard (2013). A Nonlinear Site-Amplification Model for the Next Pan-European Ground-Motion Prediction Equations, *Bulletin of the Seismological Society of America*, **103,** no. 1, 19–32.

Schnabel, P. B., J. Lysmer and H. B. Seed (1972). SHAKE, a computer program for earthquake response analysis of horizontal layered sites. Report No. EERC72-12, December.

Seed, H., R. Wong, I. Idriss and K. Tokimatu (1986). Moduli and damping factors for dynamic analyses of cohesionless soils, *Journal of the Geotechnical Engineering Division, ASCE*, **112,** no. GT11, 1016–1032.

Somerville, P., K. Irikura, R. Graves, S. Sawada, D. Wald, N. Abrahamson, Y. Iwasaki, T. Kagawa, N. Smith, and A. Kowada (1998). Characterizing earthquake slip models for the prediction of strong ground motion, *Seism. Res. Lett.*, **70,** 59–80.

Somerville, P. G., and J. Yoshimura (1990). The influence of critical Moho reflections on strong ground motions recorded in San Francisco and Oakland and during the 1989 Loma Prieta earthquake. *Geophysical Research Letters*, **17,** no. 8, 1203–1206.

Standards New Zealand 2004. Structural Design Actions– Part 5 Earthquake Actions – New Zealand. New Zealand Standard NZS 1170.5:2004.

Vucetic, M. and R. Dobry, (1991). Effect of soil plasticity on cyclic response. *Journal of Geotechnical Engineering, ASCE*, **117,** no. GT1, 89–107.

Walling, M., W. Silva, and N. Abrahamson (2008). Nonlinear Site Amplification Factors for Constraining the NGA Models. *Earthquake Spectra,* **24,** no. 1, 243–255.

Youngs, R. R., S.-J Chiou, W. J. Silva, and J. R. Humphrey (1997). Strong ground motion attenuation relationships for subduction zone earthquakes, *Seismological Research Letters*, **68,** no.1, 58–73.

Zhao, J. X. (2014) Magnitude Scaling Rates for Large Earthquakes in Ground Motion Prediction Equations for Japan *2014 Annual Meeting of Seismological Society of America*, held during 30 April–2 May 2014 in Anchorage, Alaska, USA.

Zhang, J., and J. X. Zhao (2009). Response spectral amplification ratios from 1- and 2-dimensional nonlinear soil site models, *Soil Dynamics and Earthquake Engineering*, **29,** 563–573.

Zhao, J. X., J. Zhang, A. Asano, Y. Ohno, T. Oouchi, T. Takahashi, H. Ogawa, K. Irikura, H. K. Thio, P. G. Somerville, Yasu. Fukushima and Yoshimitsu Fukushima (2006a). Attenuation relations of strong ground motion in Japan using site classification based on predominant period, *Bulletin of the Seismological Society of America*, **96,** no.3, 898–913.

Zhao, J. X., K. Irikura, J. Zhang , Y. Fukushima, P. G. Somerville, A. Asano, Y. Ohno, T. Oouchi, T. Takahashi, and H. Ogawa (2006b). An Empirical Site-Classification Method for Strong-Motion Stations in Japan Using H/V Response Spectral Ratio. *Bulletin of the Seismological Society of America*, **96,** no.3, 914–925.

Zhao, J. X. (2010). Geometric spreading functions and modelling of volcanic zones for strong-motion attenuation models derived from records in Japan, *Bulletin of the Seismological Society of America*, **100,** no.2, 712–732.

Zhao, J. X. and H. Xu (2013). A comparison of V_{S30} and site period as site effect parameters in response spectral ground-motion prediction equations, *Bulletin of the Seismological Society of America*, **103,** no.1, 1–18.

Zhao, J. X., and H. Xu (2012). Magnitude-scaling rate in ground-motion prediction equations for response spectra from large subduction interface earthquakes in Japan, *Bulletin of the Seismological Society of America*, **102,** no.1, 222–235.

Zhao, J. X., and M. Lu (2011). Magnitude-scaling rate in ground-motion prediction equations for response spectra from large shallow crustal earthquakes, *Bulletin of the Seismological Society of America*, **101,** no. 6, 2643–2661.

Zhao, J. X., and J. Zhang (2010). Side-effect of using response spectral amplification ratios for soft soil sites: earthquake source-type dependent amplification ratios. *Soil dynamics and earthquake engineering*, **30,** no.4, 258–269.

Zhao, J. X., J. Zhang, and K. Irikura (2009). Side effect of using response spectral amplification ratios for soil sites: variability and earthquake-magnitude and source-distance dependent amplification ratios for soil sites, *Soil dynamics and earthquake engineering*, **29,** no. 9, 1262–1273.

Zhao, J. X., S. L. Zhou and F. Jiang, P. J. Gao, and D. A. Rhoades (2014). Magnitude scaling rates for large and great earthquakes for ground-motion prediction equations for Japan using depth-scaled geometric attenuations, in preparation.

6.0 REFERENCES FOR FAULT MODELS

Aoi, S., B. Enescu, W. Suzuki, Y. Asano, K. Obara, T. Kunugi, and K. Shiomi (2012). Stress transfer in the Tokai subduction zone from the 2009 Suruga Bay earthquake in Japan, nature geoscience, 20 June 2010.

Asano, K., and T. Iwata (2006). Source process and near-source ground motions of the 2005 West Off Fukuoka Prefecture earthquake, *Earth Planets Space*, **58**, 93–98.

Asano, K., and T. Iwata (2009). Source Rupture Process of the 2004 Chuetsu, Mid-Niigata Prefecture, Japan, Earthquake Inferred from Waveform Inversion with Dense Strong-Motion Data, *Bulletin of the Seismological Society of America*, **99**, no. 1, 123–140.

Asano, K., and T. Iwata (2009). Source Rupture Process of the 2004 Chuetsu, Mid-Niigata Prefecture, Japan, Earthquake Inferred from Waveform Inversion with Dense Strong-Motion Data, *Bulletin of the Seismological Society of America*, **99**, no. 1, 123–140.

Asano, K., and T. Iwata (2009). Source Rupture Process of the 2004 Chuetsu, Mid-Niigata Prefecture, Japan, Earthquake Inferred from Waveform Inversion with Dense Strong-Motion Data, *Bulletin of the Seismological Society of America*, **99**, no. 1, 123–140.

Asano, K., and T. Iwata (2011). Source-Rupture Process of the 2007 Noto Hanto, Japan, Earthquake Estimated by the Joint Inversion of Strong Motion and GPSData, *Bulletin of the Seismological Society of America*, **101**, no. 5, 2S467–2480.

Asano, K., and T. Iwata (2011). Source-Rupture Process of the 2007 Noto Hanto, Japan, Earthquake Estimated by the Joint Inversion of Strong Motion and GPS Data, *Bulletin of the Seismological Society of America*, **101**, no. 5, 2467–2480.

Fukushima, Y., Y. Takada, and M. Hashimoto (2013). Complex Ruptures of the 11 April 2011Mw6.6 Iwaki Earthquake Triggered by the 11 March 2011Mw9.0 Tohoku Earthquake, Japan, *Bulletin of the Seismological Society of America*, **103**, no. 2B, 1572–1583.

Hikima, K., and K. Koketsu (2005). Rupture processes of the 2004 Chuetsu (mid-Niigata prefecture) earthquake, Japan: A series of events in a complex fault system, *Geophysical Research Letters*, **32**.

Hiramatsu, Y., K. Moriya, T. Kamiya, M., and T. Nishimura (2008). Fault model of the 2007 Noto Hanto earthquake estimated from coseismic deformation obtained by the distribution of littoral organisms and GPS: Implication for neotectonics in the northwestern Noto Peninsula, *Earth Planets Space*, **xx**, 1–12.

Kobayashi, T., M. Tobita, M. Koarai, T. Okatani, A. Suzuki,Y. Noguchi, M. Yamanaka, and B. Miyahara (2012). InSAR-derived crustal deformation and fault models of normal faulting earthquake (Mj in the Fukushima-Hamadori area, *Earth Planets Space*, **64**, 1209–1221.

Koketsu, K., Y. Yokota, N. Nishimura, Y. Yagi, S. Miyazaki, K. Satake, Y. Fujii, H. Miyake, S. Sakai, Y. Yamanaka, and T. Okada (2011). A unified source model for the 2011 Tohoku earthquake, *Earth and Planetary Science Letters*, **310**, 480–487.

Koketsua, K., Y. Yokotaa, N. Nishimura, Y. Yagi, S. Miyazaki, K. Satakea, Y. Fujii, H. Miyake, S. Sakai, Y. Yamanaka, T. Okada, (2011). A unified source model for the 2011 Tohoku earthquake, *Earth and Planetary Science Letters*, **310**, 480-487.

Kubo, H., and Y. Kakehi (2013). Source Process of the 2011 Tohoku Earthquake Estimated from the Joint Inversion of Teleseismic Body Waves and Geodetic Data Including Seafloor Observation Data: Source Model with Enhanced Reliability by Using Objectively Determined Inversion Settings, *Bulletin of the Seismological Society of America*, **103**, no. 2B, 1195–1220.

Kubo, H., K. Asano, and T. Iwata (2013). Source-rupture process of the 2011 Ibaraki-oki, Japan, earthquake (Mw7.9) estimated from the joint inversion of strong-motion and GPS Data: Relationship with seamount and Philippine Sea Plate, *Geophysical Research Letters*, **40**, 3003–3007.

Miyatake, T.; Y. Yagi; T. Yashuda (2004). The dynamic rupture process of the 2001 Geiyo, Japan, earthquake, *Geophys. Res. Lett.*, **31**, no. 12, 10.1029/2004GL019721.

Ohta, Y., S. Miura, M. Ohzono, S. Kita, T. Iinuma, T. Demachi, K. Tachibana, T.Nakayama, S. Hirahara, S. Suzuki, T. Sato, N. Uchida, A. Hasegawa, and N. Umino (2011). Large intraslab earthquake (2011 April 7, M 7.1) after the 2011 off the Pacific coast of Tohoku Earthquake (M 9.0): Coseismic fault model based on the dense GPS network data, *Earth Planets Space*, **63**, 1207–1211.

Rodriguez-Lozoya, H. E., L. Quintanar, R. Ortega, C. J. Rebollar, and Y. Yagi (2008). Rupture process of four medium-sized earthquakes that occurred in the Gulf of California, *J. Geophys Res.*, **113**, B10301, doi:10.1029/2007JB005323.

Sekiguchi H., S. Aoi, R. Honda, N. Morikawa, T. Kunugi, and H. Fujiwara (2006). Rupture process of the 2005West Off Fukuoka Prefecture earthquake obtained from strong motion data of K-NET and KiK-net, *Earth Planets Space*, **58**, 37–43.

Suzuki, W., S. Aoi, and H. Sekiguchi (2009). Rupture Process of the 2008 Northern Iwate Intraslab Earthquake Derived from Strong-Motion Records, *Bulletin of the Seismological Society of America*, **99**, no. 5, pp. 2825–2835.

Suzuki, W., S. Aoi, and H. Sekiguchi (2010). Rupture Process of the 2008 Iwate–Miyagi Nairiku, Japan, Earthquake Derived from Near-Source Strong-Motion Records, *Bulletin of the Seismological Society of America*, **100**, no. 1, 256–266.

Takada, Y., T. Kobayashi, M. Furuya, and M. Murakami (2009). Coseismic displacement due to the 2008 Iwate-Miyagi Nairiku earthquake detected by ALOS/PALSAR: preliminary results, *Earth Planets Space*, **61**, e9–e12.

Tanioka, Y., and K. Katsumata (2007). Tsunami generated by the 2004 Kushiro-oki earthquake, *Earth Planets Space*, **59**, e1–e3.

Yagi, Y. (2004). Source rupture process of the 2003 Tokachi-oki earthquake determined by joint inversion of teleseismic body wave and strong ground motion data, *Earth Planet and Space*, **56**, 311–316.

Yagi, Y., A. Nakao, and A. Kasahara (2012). Smooth and rapid slip near the Japan Trench during the 2011 Tohoku-oki earthquake revealed by a hybrid back-projection method, *Earth Planet. Sci. Lett.*, **355-356**, 94-101, doi: 10.1016/j.epsl.2012.08.018.

Yagi, Y., and Y. Fukahata (2011). Rupture process of the 2011 Tohoku-oki earthquake and absolute elastic strain release, *Geophys. Res. Lett*, **38**, L19307, doi:10.1029/2011GL048701.

Yagi, Y., N. Naoki, and Kasahara, A. (2012). Source process of the 12 May 2008 Wenchuan, China, earthquake determined by waveform inversion of teleseismic body waves with a data covariance matrix, *Earth, Planets and Space*, **64**, e13-e16 doi: 10.5047/eps.2012.05.006.

Yamanaka, Y., and M. Kikuchi (2003). Source process of the recurrent Tokachi-oki earthquake on September 26, 2003, inferred from teleseismic body waves, *Earth Planets Space*, **55**, e21-e24.

Yue , H., and T. Lay (2013). Source Rupture Models for theMw9.0 2011 Tohoku Earthquake from Joint Inversions of High-Rate Geodetic and Seismic Data, *Bulletin of the Seismological Society of America*, **103**, no. 2B, 1242–1255.

APPENDIX

Bulletin of the Seismological Society of America, Vol. 102, No. 1, pp. 222–235, February 2012, doi: 10.1785/0120110154

Magnitude-Scaling Rate in Ground-Motion Prediction Equations for Response Spectra from Large Subduction Interface Earthquakes in Japan

by John X. Zhao* and H. Xu

Abstract Magnitude-scaling rates (MSRs; the rates of increase in predicted response spectra with increasing moment magnitude) are evaluated for three ground-motion prediction equations for response spectra from subduction interface earthquakes, including two empirical models developed for data from Japan and a model based on synthetic records generated by using a stochastic finite-fault model. MSRs vary significantly among the three models, and the difference between the two empirical models is unacceptably large. A set of 2100 strong-motion records from subduction interface events with a magnitude of 6.5 or larger from Japan, including the 11 March 2011 magnitude 9 earthquake, were compiled. The earthquakes were grouped according to magnitude, so that the magnitude spread in each group is less than 0.2 magnitude units. Each earthquake group was treated as a single event with magnitude equal to the average magnitude for the group. A simple attenuation model was fitted to the normalized and grouped data. The model has a constant term for each earthquake group to represent the effect of magnitude. Three separate functions of magnitude (a linear model for events with a magnitude greater than 7, a bilinear model, and a curved model) were then fitted to the constants, and MSRs were derived from these functions. At short periods, the derived MSRs are only a fraction of those from two of the three attenuation models. At spectral periods greater than 0.5 s, the derived MSRs are between about 1/3 and 1/2 of those of the two empirical models but are closer to those based on a set of synthetic records.

Introduction

Zhao and Lu (2011) evaluated the magnitude-scaling rate (MSR) for five modern ground-motion prediction equations for shallow large crustal earthquakes. They found that the MSRs of the four Next Generation Attenuation models (Abrahamson and Silva 2008; Boore and Atkinson 2008; Campbell and Bozorgnia 2008; Chiou and Youngs 2008) varied significantly. Zhao and Lu (2011) also showed that a model without a magnitude term fits the response spectra from 12 of the 13 large crustal earthquakes with moment magnitude $M_w > 7$ very well, suggesting zero magnitude scaling. They attributed zero magnitude scaling to the rapid increase in fault length and duration of strong shaking with increasing magnitude and to the reduced energy ratio (the energy contributed to the response spectra over the total energy of a strong-motion record) for records from large earthquakes. For large subduction interface earthquakes with $M_w > 7$, the increase in magnitude may similarly lead to an increase in duration but may not necessarily lead to a significant increase in ground-motion amplitude. The present study will investigate this aspect.

The recent M_w 9 earthquake (11 March 2011, Japan Time) caused a devastating tsunami and human casualties. However, a large set of strong-motion records was obtained from this event: 230 records within a source distance (the closest distance to the fault rupture) of 300 km and the largest horizontal peak ground acceleration (PGA) of $2.75g$ from a rock/stiff shallow soil site at a source distance of 70 km. The PGAs from five records exceed $1g$ at a source distance over 59 km. Figure 1a compares the normalized PGA with the prediction from the Zhao, Zhang, *et al.* (2006) model, hereafter referred to as the Z2006 model. The normalized PGA was corrected to the site class (SC) II conditions defined in Zhao, Irikura, *et al.*, 2006, using the site terms from Z2006 model. Figure 1a also shows the median $-\sigma$ of the Z2006 model and the prediction from the Kanno *et al.* (2006) (or K2006) model with $V_{S30} = 400$ m/s. Figure 1b compares the spectral accelerations at 3-s spectral periods with the same models. The Z2006 model overpredicted the recorded ground motion

*Also at GNS Science, 1 Fairway Dr., Avalon, Lower Hutt, New Zealand.

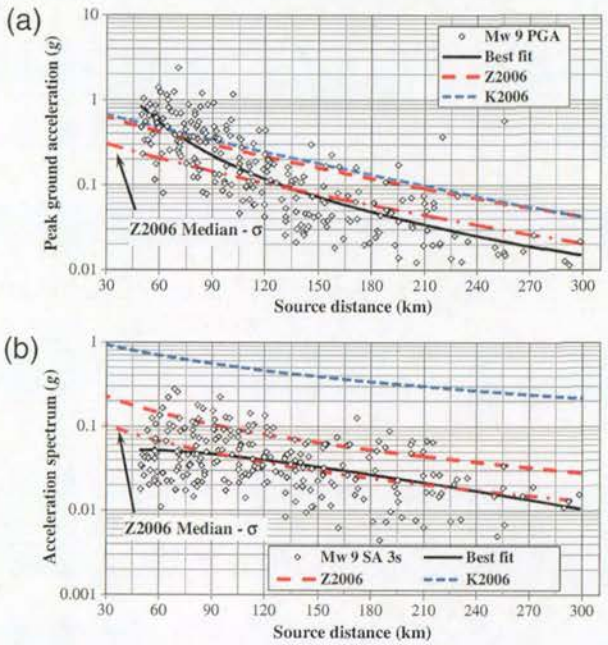

Figure 1. Comparison between the recorded spectra, the prediction by the Zhao, Zhang, *et al.* (2006) model (Z2006), median $-\sigma$ of the Z2006 model, Kanno *et al.* 2006 model (K2006), and the best model fitted to the data using the form of the Z2006 model: (a) peak ground acceleration, and (b) spectral acceleration at 3-s spectral period. The PGA and spectrum were normalized to site class II; that is, they were multiplied by $\exp(S_k - S_2)$ where S_k and S_2 are the site terms of the Z2006 model for the k-th class and the second class, respectively. The color version of this figure is available only in the electronic edition.

by a very large factor compared with the best fit using the similar functional form to that of the Z2006. The best fit for the dataset is very close to the median $-\sigma$ of the Z2006 model for both PGA and the spectrum at 3-s periods at most distances. The K2006 model predicts similar PGA to those yielded by the Z2006 model (Fig. 1a) and predicts much higher spectral accelerations at 3-s spectral periods than does the Z2006 model (Fig. 1b). The median -2σ from the K2006 model is still larger than the median values from the Z2006 model, which is most likely caused by the lack of a magnitude-squared term in the K2006 model. The preliminary comparison with the other attenuation models shows that the Atkinson and Boore (2003) and the Gregor *et al.* (2002; referred to as G2002) models have very similar extent of overprediction (D. Boore, personal comm., 2011).

The overprediction may be caused largely by magnitude scaling, as none of the datasets used in these models contains any event larger than 8.3. For these models that used the data from the 26 September 2003 M_w 8.3 earthquake in Japan, the magnitude scaling is still not well constrained. Many models have a magnitude-squared term or magnitude-cubed term with a negative coefficient that enhances the magnitude scaling for earthquakes with M_w <~6.5 and reduces the magnitude scaling for large earthquakes. Zhao *et al.* (2009) and Zhao, Zhang, *et al.* (2006) interpreted the enhanced magnitude scaling for small events at long periods as a result of the calculation of response spectra when energy associated with short-period ground motions contributes to the response spectra at long spectral periods. However, the coefficient for the magnitude-squared term is usually unnecessary for short spectral periods. The magnitude-squared term is largely controlled by the small events, which outnumber the large events by many times. In the present study, the subduction interface events with $M_w \geq 6.5$, including the recent M_w 9 event, will be used to assess the MSR for large earthquakes without being constrained by small earthquakes.

The Z2006 and K2006 models both were based on data from Japan, including the September 2003 M_w 8.3 earthquake. The K2006 model used a much larger dataset than did the Z2006 model, with many events that do not have source types (tectonic locations, such as shallow crustal, subduction interface, and subduction slab). The K2006 model does not have a magnitude-squared term, and the standard deviation for the model is much larger than that from the Z2006 model. Any differences in magnitude scaling for the two models may be a result of the functional form used in these two models.

The G2002 model was developed using the results from numerical simulation based on a stochastic finite-fault model developed by Silva *et al.* (1990) and calibrated by the 19 September 1985 M_w 8.0 Michoacan, Mexico, earthquake and the 3 March 1985 M_w 8.0 Valparaiso, Chile, earthquake. The magnitude scaling from this model will also be investigated. If appropriate MSRs can be derived from numerical simulation, such numerical modelling can be used to constrain the model predictions for large earthquakes or to fill in the magnitude gap among real events.

Magnitude-Scaling Rates of Three Recent Ground-Motion Prediction Equations

For all models, we used linear and squared or cubed magnitude terms and magnitude-dependent geometric terms to compute response spectra. The computed spectra were then normalized with respect to the spectrum computed for M_w 6.5 at source distances of 30, 60, 120, 180, and 240 km, and the effects of focal depth and site terms were cancelled by the normalization. Note that all distances are the closest distance to the fault rupture plane. The MSR is defined as the average slope of a curve in a 2D plot for the normalized spectra in logarithmic scale with respect to moment magnitude in linear scale. The effect of magnitude-dependent geometric attenuation is included.

Figure 2 shows the normalized spectra for the Z2006 model. Figure 2a shows that, at a 30-km distance, the PGA for an M_w 9 event is about 4.7 times that of an M_w 6.5 event, and this ratio increases with increasing source distance. At a source distance of 240 km, the PGA from an M_w 9 event is about 11.7 times that from an M_w 6.5 event. The MSRs generally decrease with increasing magnitude. This model

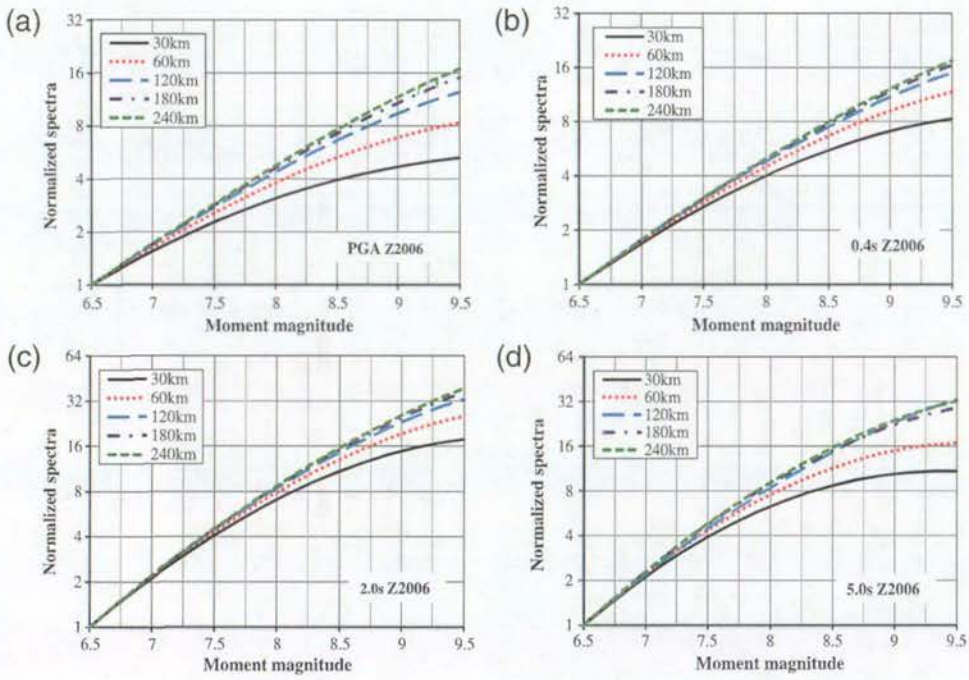

Figure 2. Normalized spectra predicted by the Z2006 model for (a) PGA and for spectral periods of (b) 0.4 s, (c) 2.0 s, and (d) 5.0 s. The spectra for a given magnitude was divided by the spectrum from an M_w 6.5 event. The color version of this figure is available only in the electronic edition.

does not have a magnitude-squared term for PGA, and the reduced MSR at large magnitude is the effect of an added magnitude-dependent geometric attenuation term. At large distances, the MSR is essentially constant. Figure 2b shows the normalized spectra at 0.4 s. At large distances, the normalized spectra at all magnitudes are similar to the normalized PGA. At a distance of 30 km, the normalized spectra are similar to the normalized PGA at a distance of 60 km. The normalized spectra at 0.4 s and a distance of 60 km are generally similar to those of the normalized PGA at a distance of 120 km.

Figure 2c shows the normalized spectra at 2.0 s spectral period from the Z2006 model. The variation of MSRs is twice those at the 0.4-s period at all distances. Figure 2d shows that, at 5.0 s, the normalized spectra at distances larger than 120 km are similar to those at the 2.0-s period at the same distance, while the normalized spectra at a source distance of 80 km or less are considerably smaller than those at a 2.0-s period at the same distance. The MSRs at the 5.0-s period at magnitudes close to 9 and at a source distance of less than 80 km (the result from 80 km is not shown) are insignificant.

The linear magnitude term in the Z2006 model varies between just over 1.0 for PGA to just below 2.0 at long periods, as suggested by the slope of the normalized spectra at magnitudes between 6.5 and 7.0.

Figure 3 shows the normalized spectra from the G2002 model for the same spectral periods and source distance as used in the Z2006 model. The G2002 model used a linear magnitude-dependent geometric attenuation term and has a constant added distance term to provide finite prediction at zero distance. A magnitude-cubed term was used to provide variable MSR with magnitude, but the coefficient varies between negative and positive. The positive values produce an MSR that increased with increasing magnitude, which is not consistent with the models for crustal earthquakes reviewed by Zhao and Lu (2011) or with the two other models reviewed in the present study. Figure 3a shows that the normalized PGA is essentially a linear function of magnitude and the MSR increases with increasing source distance, an effect of the linear magnitude-dependent geometric attenuation function. The MSRs for PGA at all distances are much smaller than those of the Z2006 model. For example, at M_w 9, the normalized PGA at a source distance of 30 km is only 1.5 times that from an M_w 6.5 event, while the same ratio from the Z2006 model is 4.7. The normalized PGAs for an M_w 9 event are 1.9, 3, 3.9, and 4.9 at source distances of 60, 120, 180, and 240 km, respectively, while the normalized spectra from the Z2006 model are 6.8, 10, 11, and 11.7 at the same distance, varying between 2.4 and 11.7 times those of the G2002 model.

Figure 3b shows the normalized spectra at a 0.4-s spectral period for the G2002 model. The curvature of the normalized spectra is positive, in contrast to the other spectral periods and those of the Z2006 model. The increase in MSR with increasing magnitude is caused by the positive values for the magnitude-cubed term. The average MSRs are much

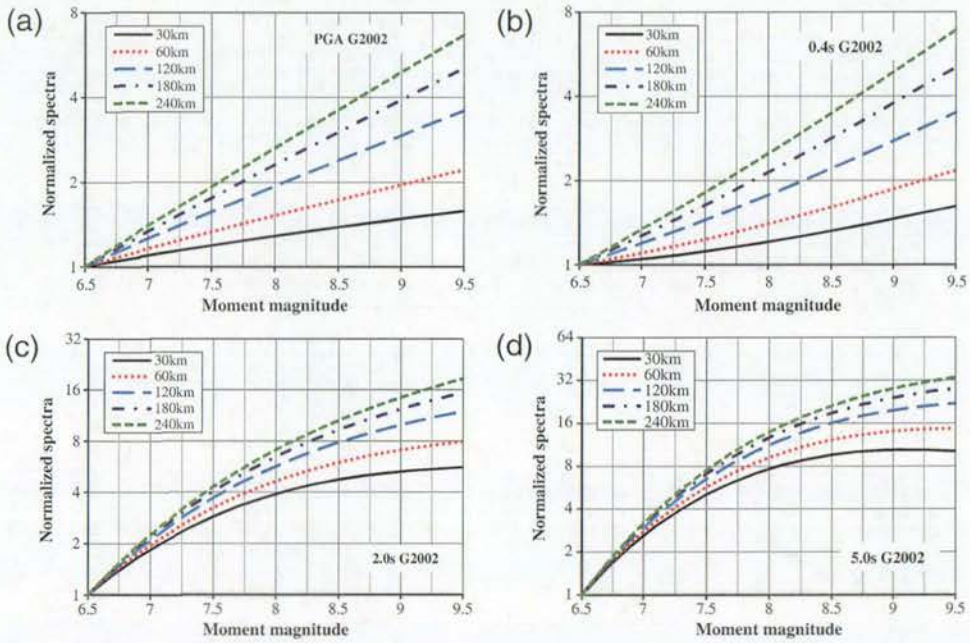

Figure 3. Normalized spectra predicted by the Gregor *et al.* (2002) model for (a) PGA and for spectral periods of (b) 0.4 s, (c) 2.0 s, and (d) 5.0 s. The color version of this figure is available only in the electronic edition.

less than those of the Z2006 model. At M_w 9.0, the normalized spectra vary between 1.5 and 5.2 in a distance range of 30–240 km, while the normalized spectra of the Z2006 model vary between 7.2 and 13. At a 2.0-s spectral period, the normalized spectra of the G2002 model in Figure 3c are still significantly lower than those of the Z2006 model shown in Figure 2c. The normalized spectra from the G2002 model at 5.0 s (Fig. 3d) are very close to those of the Z2006 model shown in Figure 2d.

Figure 4 shows the normalized spectra from the K2006 model. This model has very similar normalized PGA to that of the Z2006 model and only moderately larger than that of

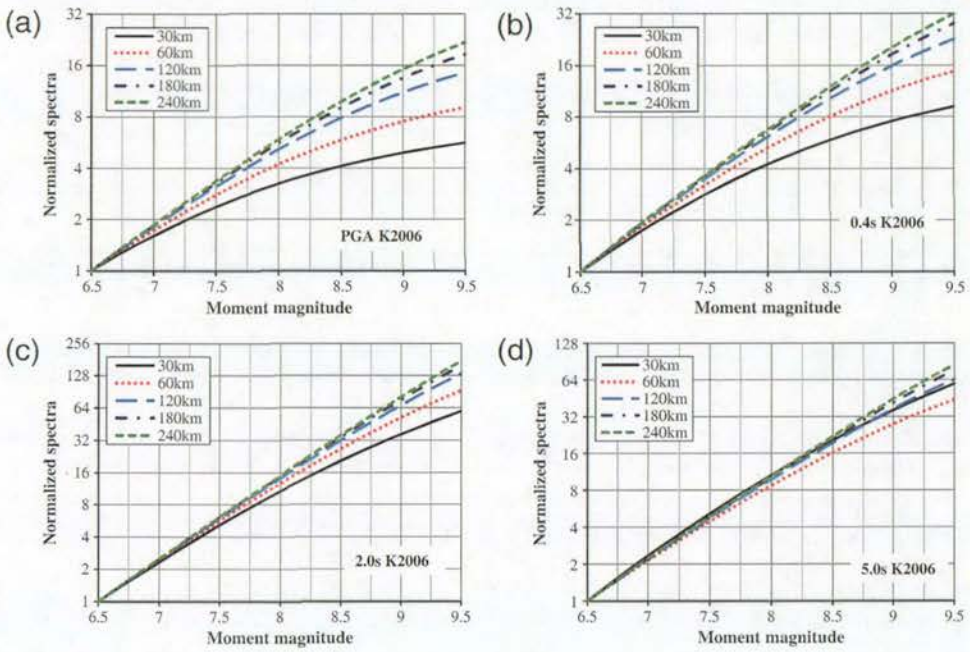

Figure 4. Normalized spectra predicted by the Kanno *et al.* 2006 model for (a) PGA and for spectral periods of (b) 0.4 s, (c) 2.0 s, and (d) 5.0 s. The color version of this figure is available only in the electronic edition.

the Z2006 model at a source distance of 180 km or larger, as shown in Figure 4a. Figure 4b shows the normalized spectra at 0.4 s. They are similar to or slightly higher than those of the Z2006 model at distances equal to or less than 60 km. At a large distance, the normalized spectra are about 1.5–1.8 times those of the Z2006 model at M_w 9.0. At long periods, compared with the results in Figure 2c,d, the normalized spectra are much larger than those of the Z2006 model by a factor of up to 3, as shown in Figure 4c,d. The normalized spectra increase almost linearly with increasing magnitude because the K2006 model does not have a magnitude-squared term at long periods. The slight nonlinear increase with increasing magnitude is caused by the added magnitude-dependent distance in the geometric attenuation term.

The analyses presented here show a very large variation in the MSRs among the three models, and the differences are extremely large between the Z2006 and the K2006 models for moderate and long spectral periods, even though they were both derived from the Japanese data. The G2002 model has the lowest MSRs, but the curvature of the normalized spectrum is positive for some spectral periods, suggesting that the normalized spectrum increases faster than does the linear function of magnitude. That is not consistent with all other models evaluated here and in the study by Zhao and Lu (2011) and may not be physically plausible either. However, the small MSRs of the G2002 model at short distance appear to lead to better prediction of the data from the 11 March 2011 (M_w 9) Japan earthquake than do the other models compared by D. Boore (personal comm., 2011).

Strong-Motion Dataset

A total of 2100 strong-motion records from 30 subduction interface earthquakes in Japan, recorded by K-NET, KiK-net, and strong-motion networks operated by Port and Harbour Research Institute and Japan Meteorological Agency, with a magnitude of 6.5 or larger were compiled, including 230 records from the recent 11 March 2011 M_w 9.0 earthquake (Off the Pacific Coast of Tohoku earthquake; National Research Institute for Earth Science and Disaster Prevention (NIED), 2011). The dataset has 256 records from the 26 September 2003 M_w 8.3 event (Tokachi-Oki earthquake), 222 records from the 26 September 2003 M_w 7.4 event (an aftershock of the Tokachi-Oki earthquake), 256 records from the 16 August 2005 M_w 7.2 event (Miyagi-ken Oki earthquake), and 153 records from the 9 March 2011 M_w 7.5 event (a foreshock of the Tohoku earthquake). The dataset also includes records from other large subduction interface events used in the Z2006 model. Figure 5a shows the earthquake distribution with respect to magnitude and focal depth, and Figure 5b shows the number of records for each event and its magnitude. Half of the events have 10 records or fewer, and four events have only one record. Figure 6a–d show the data distribution with respect to source distance and magnitude from SC I, SC II, SC III, and SC IV sites, respectively. The site classes were from Zhao, Irikura, *et al.* (2006) and were broadly similar to those of the National Earthquake Hazard Reduction Program (NEHRP) site classes (Building Seismic Safety Council, 2000); see table 1 in Zhao (2010). Fault rupture models are available for 20 of the 30 earthquakes, and the hypocentral distances were used for the events without a fault rupture model. The fault mode for the M_w 9.0 2011 Tohoku earthquake is from NIED (2011). The fault model for the second largest earthquake, the M_w 8.3 2003 Tokachi-Oki earthquake, is from Yagi (2004); it has an optimal focal depth of 17 km. The use of shallow depth in the model by Yagi (2004) leads to a distance of 28.3 km for the closest strong-motion station. If the focal depth of 27 km from the U.S. Geological Survey is adopted, the closest station to the fault plane would be about 35 km. This level of difference in distance is not expected to significantly affect the results presented in the present study.

Figure 7 shows the attenuation of the normalized PGA and response spectra at 3-s spectral periods from three recent large subduction interface events: the 9 March 2011 M_w 7.5 event, the 26 September 2003 M_w 8.3 event, and the 11 March 2011 M_w 9.0 earthquake. A few features can be

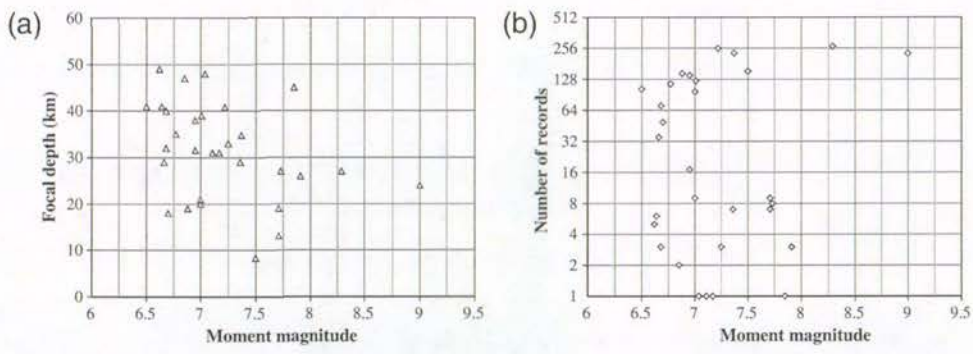

Figure 5. (a) The distribution of strong-motion records from large subduction interface earthquakes from Japan, with respect to magnitude and focal depth. (b) The number of records for each of the 30 earthquakes with a magnitude of 6.5 or larger, including 230 records from the 11 March 2011 earthquake with M_w 9.0.

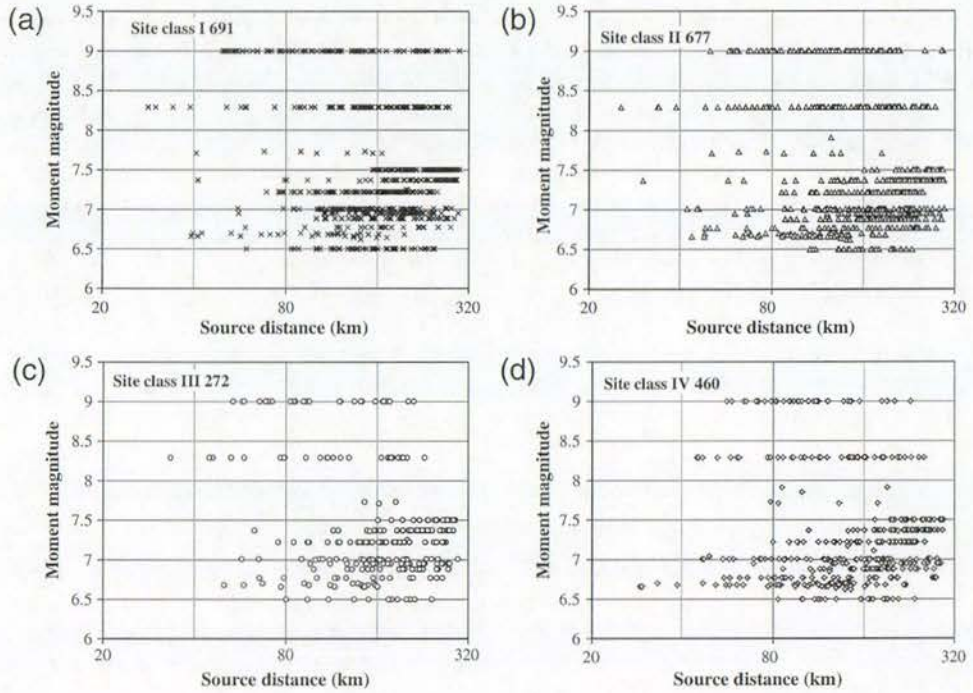

Figure 6. Distribution of strong-motion records with respect to distance and magnitude: (a) 691 records for site class I, (b) 677 records for site class II, (c) 272 records for site class III, and (d) 460 records for site class IV.

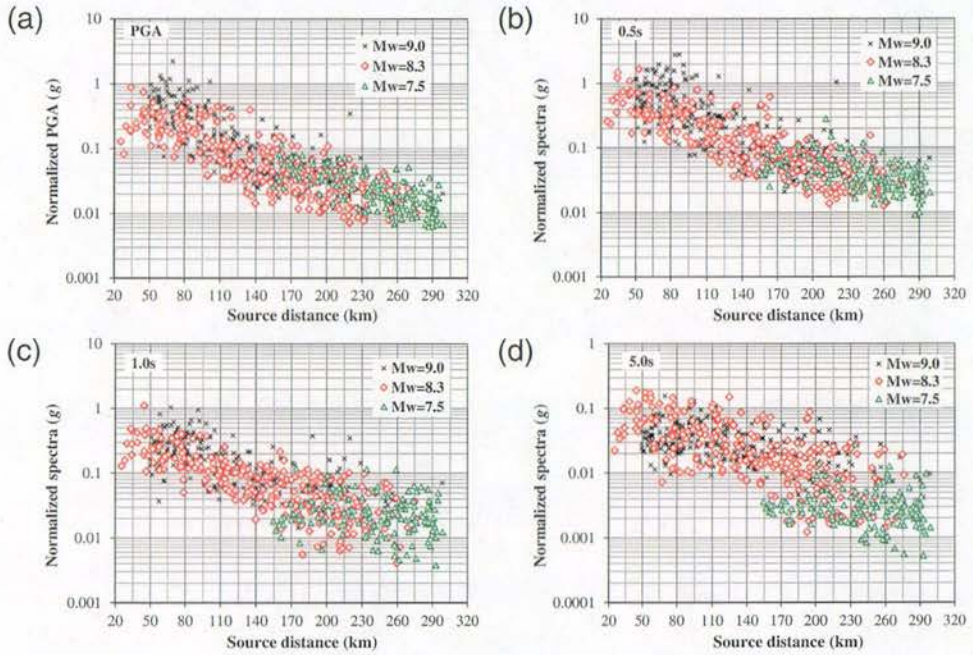

Figure 7. The attenuation of normalized spectra with respect to source distance (the closest distance to the fault rupture plane) for the two large events and hypocentral distance for the other earthquake: (a) PGA and spectra at (b) 0.5 s, (c) at 1.0 s, and (d) at 5.0 s. The PGA and spectrum were normalized to site class II; that is, they were multiplied by $\exp(S_k - S_2)$, where S_k and S_2 are the site terms of the Z2006 model for the k-th class and the second class, respectively. The color version of this figure is available only in the electronic edition.

observed. The PGA and acceleration spectra were normalized to the site class II condition, at a focal depth of 20 km using the site and the depth terms from the Z2006 model. Visual inspection suggests that the data from the M_w 9 and M_w 8.3 events are similar at distances over 150 km. The PGA and spectral accelerations at 0.5 s and 1.0 s from the M_w 9 event are, on average, moderately larger than those from the M_w 8.3 and M_w 7.5 events at distances within 150 km. The PGA and spectral accelerations at 0.5 s and 1.0 s from the M_w 7.5 and 8.3 events can be fitted very well with an attenuation function without a magnitude term. At 5.0 s, Figure 7d shows that the spectra from the two larger events are comparable, while the spectra from the M_w 7.5 event are evidently smaller than those from the other two events.

Method of Analyses

The objective of the present study is to assess the MSRs for large subduction interface earthquakes. Zhao and Lu (2011) suggested that the use of a random effects model makes the analyses complicated, with interpretation required for both the magnitude term and the interevent residuals. Among the events used in the present study, four events have one record, one event has two records and three events have three records, as shown in Figure 5b. When a magnitude term and the interevent residuals are used, misfit of these records propagates into interevent and intraevent errors, and these records do not contribute significantly to the determination of path and source effects. This means that the statistical power of the events that have only a few records can be reduced significantly. To accommodate those events with a small number of records, the earthquakes are divided into eight groups according to their magnitudes. The magnitude spread in each group is less than 0.2 magnitude units. The total number of records for PGA in each group varies between 28 and 536 so that each group of earthquakes has a reasonable number of records for statistical analyses. Each group of events can then be treated as an earthquake with a magnitude equal to the average magnitude of all events in this group.

In the present study, all data are from Japan. The model parameters such as site class terms, depth terms, and the terms that control the near-source model prediction from a previous study (Zhao 2010) can be used, to avoid any effect from the reduced number of records compiled in the present study. The Zhao (2010) study accommodated the variation of geometric attenuation rates for both shallow crustal and subduction slab events and depth-dependent anelastic attenuation rates for subduction interface events. The model parameters for site class and depth and the near-source terms from Zhao (2010) are used. The justifications for using site class, depth, and near-source terms from the Zhao (2010) study are as follows:

1. The site amplification ratios derived from site class terms (reflecting the relative differences between the site terms for a soil class and the SC I site class) of the Zhao (2010) and Zhao, Zhang, *et al.* (2006) studies are virtually identical, though the two models used very different geometric attenuation functions. This result suggests that the dataset is large enough and the distributions of the records with depth, magnitude, distance, and site classes are good enough to diminish the trade-offs between the estimates for the source, path, and site effect terms. Note that the proposed way of using the site terms from the Zhao (2010) model in the following section excludes the effect of absolute values of the site terms.
2. The Zhao (2010) study used separate depth terms for crustal, subduction interface, and subduction slab earthquakes and a depth-dependent anelastic attenuation term for subduction interface events. These new features lead to a much smaller depth term for the subduction interface events than that of the Zhao, Zhang, *et al.* (2006) study. Any differences between the estimates for the depth term in the Zhao (2010) study and the model proposed in the present study can be caused by the change of datasets, but the effect from different values for the depth term should be small.
3. The near-source terms in the Zhao (2010) study were constrained by the near-field records from Californian earthquakes, and they cannot be reliably estimated by the present dataset without the overseas near-source records. The best approach would be the use of the near-source terms from the Zhao (2010) study, with adjustment that can be derived for large earthquakes as suggested in the subsequent section, A Simple Attenuation Model for Assessing Magnitude Scaling.

With the earthquakes grouped together according to their magnitude, and adopting the site class terms, depth terms, and the near-source terms, a very simple model can be used to assess the magnitude scaling for large subduction interface earthquakes from Japan.

A Simple Attenuation Model for Assessing Magnitude Scaling

For subduction interface earthquakes, the anelastic attenuation rate for shallow events differs from that of deep events, as shown by Zhao (2010). First, the acceleration spectra were normalized to site class II and a focal depth of 20 km using the results from the Zhao (2010) study. The normalization effectively deleted these parameters from the attenuation model. A simple model is proposed in the present study:

$$\log_e(y_{i,j}) = \alpha[\log_e(r_{i,j}) + \beta \log_e(r_{i,j} + r_a)] + b_{SH} x_{i,j} \delta_{SH} + b_{DEEP} x_{i,j} \delta_{DEEP} + f + \lambda_i, \quad (1)$$

$$\delta_{SH} = \begin{cases} 1 & \text{if depth} \le 25 \text{ km} \\ 0 & \text{if depth} > 25 \text{ km} \end{cases}, \quad (2)$$

$$\delta_{\mathrm{DEEP}} = \begin{cases} 1 & \text{if depth} > 25 \text{ km} \\ 0 & \text{if depth} \le 25 \text{ km} \end{cases}, \tag{3}$$

$$r_{i,j} = x_{i,j} + \exp(c + d\psi_i), \tag{4}$$

and

$$\psi_i = \begin{cases} M_i & \text{if } M_i \le C_{\max} \\ C_{\max} & \text{if } M_i > C_{\max} \end{cases}, \tag{5}$$

where x_i is the shortest distance between a recording station and the fault plane; coefficient α is the geometric attenuation rate; b_{SH} is the anelastic attenuation rate for earthquakes with a focal depth of 25 km or less; b_{DEEP} is the anelastic attenuation rate for earthquakes with a focal depth over 25 km; f is a constant; and λ_i is a constant for the i-th group events. For the group of events with an average magnitude of 6.5, $\lambda_i = 0.0$ is enforced. Parameter β is the added geometric attenuation rate primarily for records with a source distance larger than r_a, as used by Chiou and Youngs (2008) and Zhao and Lu (2011) to accommodate the reduced attenuation rate at large distances as shown in Figure 7. Subscript i denotes the i-th earthquake group, and j denotes the j-th record in the i-th earthquake group. The terms c and d control the near-source prediction, and the values from the Zhao (2010) model were adopted, as these terms cannot be determined reliably from the present dataset. For large and great earthquakes, $C_{\max}$ is used to adjust the model prediction within about 50 km. The main interest in the present study is to determine the constant λ_i for each earthquake group, and the MSR can then be assessed by the variation of λ_i with the average magnitude for each earthquake group. Note that the geometric attenuation function form in equation (1) differs from that in Zhao (2010), which means that the site class and depth terms derived by using equation (1) may differ from those in Zhao (2010). However, the differences between these terms from the Zhao (2010) and Zhao and Zhang *et al.* (2006) are reasonably small even though the geometric attenuation functions in these two studies are very different. This provides some confidence in that the use of site class and depth terms from the Zhao (2010) study would not lead to any serious and systematic bias in the estimate of magnitude scaling.

The terms adopted from the Zhao (2010) study are c and d, which cannot be determined reliably from the dataset used in the present study. Geometric attenuation terms α and β, anelastic attenuation rates b_{SH} for shallow subduction interface events and b_{DEEP} for deep subduction interface events, near-source term $C_{\max}$, and λ_i for seven groups of earthquakes, are to be determined by a regression analysis. The total number of terms to be determined in equation (1) is 16, which is moderately large, and some may not be statistically significant. As the total number of records and the number of records in each earthquake group are reasonably large, it is possible to rely on statistical properties of each term to determine which parameter is statistically necessary, especially the constants for each group of the earthquakes. The approach was to perform a regression analysis assuming all the terms in equation (1) were nonzero, and the t-test was carried out for each term to verify that the estimate for each term was statistically significant at a 5% significance level. Ratios of the median estimates for each term over their standard deviations were computed, and the term with the smallest ratio and that was not statistically significant was deleted. This process was repeated until the estimates for all terms in the final model were statistically significant. Parameter β was obtained by minimizing model prediction error subjected to obtaining negative or zero values for all anelastic attenuation terms.

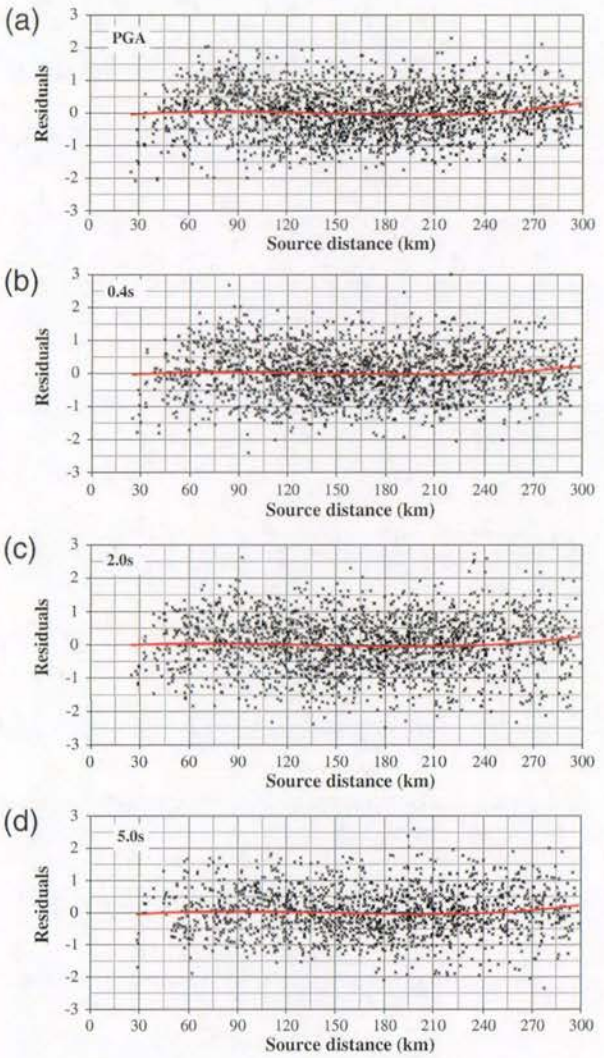

Figure 8. Distribution of residuals with respect to source distance for the simple model derived in the present study for (a) PGA and spectral periods of (b) 0.4 s, (c) 2.0 s and (d) 5.0 s. The color version of this figure is available only in the electronic edition.

Figure 8 shows the distribution of residuals with respect to source distance, for PGA, and acceleration spectra at 0.4-s, 2.0-s, and 5.0-s spectral periods. Trendlines as a polynomial of third order of source distance are also presented. The residuals were defined such that a positive residual means an underprediction by a factor of the exponential of the residual value, and a negative residual means an overprediction. If the value for the trend line is zero at all distances, the overall fit to the source distance is unbiased. Apart from the data at large distances over 250 km, Figure 8 shows that the model in equation (1) with the terms that passed the statistical tests have unbiased residual distributions with respect to source distance for all periods. The slight underprediction at large distances can be eliminated if more complex geometric attenuation functions, similar to those for the subduction slab earthquakes from the Zhao (2010) model, are adopted. This aspect of the subduction interface earthquakes will not be pursued further in the present study.

Figure 9a shows the variation of geometric attenuation rate with spectral period. The largest absolute value of the geometric attenuation rate is at 0.6 s, beyond which the rate decreases rapidly with increasing spectral period. Figure 9b shows the absolute values in percentage for the anelastic attenuation rates for the events with a focal depth of 25 km or less (shallow) and those for deep events with a focal depth between 25 and 50 km. The anelastic attenuation rates for shallow earthquakes are much larger than those for the deep earthquakes, consistent with the results from Zhao (2010).

Figure 10 shows the variation of parameter β and $C_{\max}$ with spectral period, and they have been smoothed across the periods. Figure 10a shows that, over a 2-s spectral period, the absolute value of β decreases quickly with increasing period, because the decrease in attenuation rate with increasing distance becomes less prominent at long period as shown in Figure 7d. Figure 10b shows the variation of parameter $C_{\max}$ with spectral period. Parameter d was fixed as 1.15 (corresponding to 0.5 in $\log_{10}$ scale) and the added distance $\exp(c + d\psi_i)$ is a fraction of fault length that reduces the geometric attenuation rate at short distance to a much lower value. This term can also be interpreted as the portion of the fault that makes a significant contribution to the response spectra in the near-source region. The seismic waves from the portion of the fault further away from a near-source recording station may contribute little to the response spectra at this particular station because of the geometric and anelastic attenuation and the incoherence of short seismic waves that do not lead to constructive interference. Figure 10b suggests that, for PGA and the spectrum at a 0.05-s period and for earthquakes with a magnitude larger than 6, the portion of the fault that contributes significantly to the response spectra at a near-source station is the same as for an M_w 6 event. As the period increases, the effects of incoherence, geometric attenuation rate, and anelastic attenuation rate decrease with increasing period. Therefore, the portion of the fault [represented by $\exp(c + dC_{\max})$] that significantly contributes to the response spectra at a near-source station also increases with increasing magnitude, leading to the increase in $C_{\max}$ with increasing periods as shown in Figure 10b. However, the capped magnitude $C_{\max}$ is still much less than the magnitude of the largest event in the present dataset at a 5.0-s spectral period.

Magnitude Scaling

The constants for each group of earthquakes in equation (1) are presented next. These constants represent the effect of earthquake magnitude for each group of events rather than each event. However, the difference in magnitude over the events in one group is less than 0.2 magnitude unit, and each magnitude group can be taken as one event. A function of magnitude that can be fitted to these constants very well can be taken as the magnitude-scaling part in an attenuation model. Thus, the MSR is the slope of a curve in the 2D plot of the constants in equation 1 versus the average magnitude. Because the interest of the present study is to assess the magnitude scaling for large subduction interface earthquakes, normalization can be used to present the possible magnitude scaling so as to eliminate the effect of the absolute values. Figures 11–13 present the constant λ_i in equation (1) (with $\lambda_i = 0.0$ for the event group with an average magnitude of 6.5). Parameter λ_i is labeled as normalized magnitude scaling in a natural logarithm scale, and this function of the

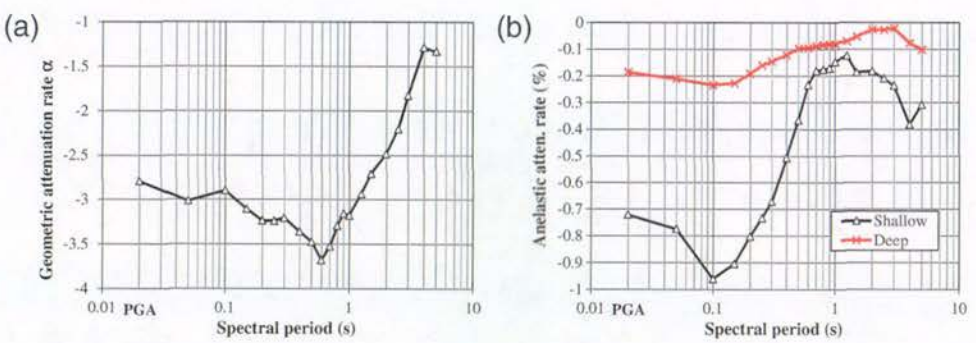

Figure 9. Variation of (a) geometric attenuation rate and (b) anelastic attenuation rates. Absolute values multiplied by 100 are used for the anelastic attenuation rate. The color version of this figure is available only in the electronic edition.

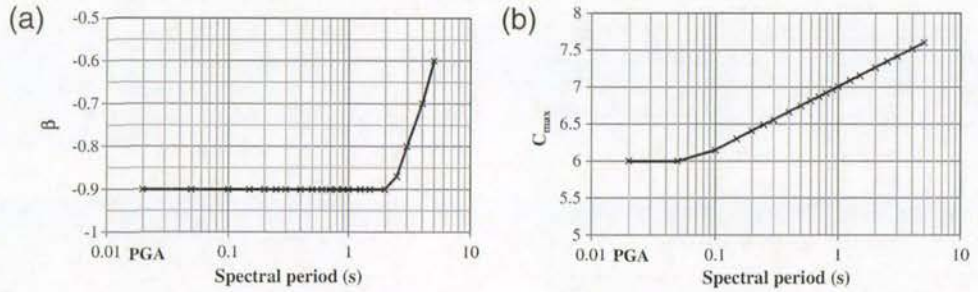

Figure 10. Variation of model parameters, (a) additional geometric attenuation rate β and (b) the near-source term C_{max}.

magnitude may be used in an attenuation model. For the models used by Youngs *et al.* (1997) (referred to as Y1997), and the Z2006, K2006, and Zhao (2010) studies, the exponential of the magnitude scaling presented in Figures 11–13 represents the normalized spectrum at a very large distance because the effect of the near-source terms on the magnitude scaling is represented separately by ψ_i in equation (5). When the distance is large, the effect of added magnitude-dependent distance in the geometric attenuation term (as used by Zhao 2010 and Kano *et al.* 2006) is negligible, and therefore the normalized spectra in Figures 11 and 13 are equivalent to the normalized spectra for a large distance as shown in Figures 2 and 4.

A number of functions can be fitted to the normalized spectrum. The data suggest that the simplest one would be to fit a straight line to the data for magnitude over 7 and the slope of the straight line would be the magnitude term that can be used in an attenuation model for the earthquakes over magnitude 7. The slopes are labeled as M_{SR} in Figures 11–13. Another possibility is to fit a bilinear model with two segments, and the slope of the second segment (for magnitude larger than the corner magnitude) can be used as the magnitude term in an attenuation model for large earthquakes. The slope for the first segment would be the magnitude term for events with a magnitude between 6.5 and the corner magnitude. The distribution of the constants with respect to magnitude shown in Figures 11–13 strongly supports a bilinear model for all periods. The third possible option is to fit a smoothed curve to the data. The functions used in Figures 11–13 have the form

$$F(M_w) = (M_w - 6.5)\exp[\mu \log_e(M_w - 6.5 + \rho) + \varphi], \tag{6}$$

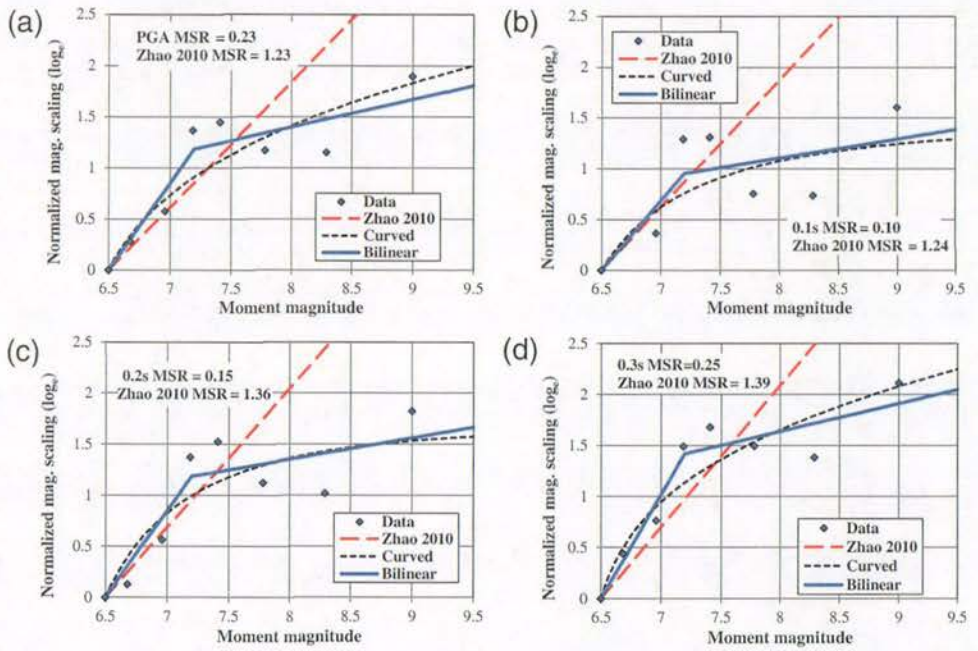

Figure 11. Normalized magnitude scaling in natural logarithm scale λ_i as a function of moment magnitude, a possible magnitude-scaling rate (MSR; the slope of the fitted straight line function of magnitude for earthquakes with a magnitude 7 or larger), a bilinear model and a curved model fitted to the data, for (a) 0 s (PGA) and spectral periods of (b) 0.1 s, (c) 0.2 s, and (d) 0.3 s spectral periods. The curved model is given in equation (6). The color version of this figure is available only in the electronic edition.

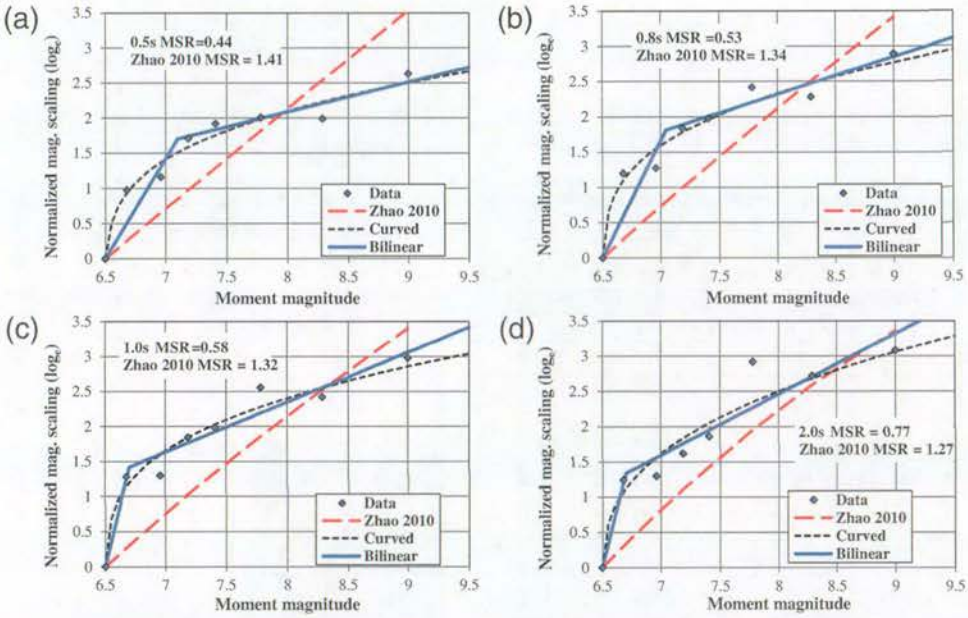

Figure 12. Normalized spectra in natural logarithm scale λ_i as a function of moment magnitude, a possible MSR, for spectral periods of (a) 0.5 s, (b) 0.8 s, (c) 1.0 s, and (d) 2.0 s. The curved model is given in equation (6). The color version of this figure is available only in the electronic edition.

where μ, φ, and ρ are constants to be determined by a regression analysis. Equation (6) is not overly complex to use for an attenuation model. The curved magnitude scaling fits the data even better than does a bilinear model, but the number of data points is very limited.

Figure 11 shows the normalized magnitude scaling λ_i for PGA and spectra at 0.1-, 0.2-, and 0.3-s spectral periods, together with those derived from Zhao (2010) (broken line), the bilinear model, the curved model in equation (6), and the MSR derived from a straight line fitted to the data from earthquakes over M_w 7. The scatter is large but generally smaller than or similar to the interevent standard deviation for large events in the Zhao (2010) model. The MSRs from the bilinear model and the linear model for $M_w > 7$ events are generally similar, but they are much smaller than those of all attenuation models for the subduction interface events examined in the present study. For example, for PGA, the MSR is 1.23 in the Zhao (2010) model. The linear model gives an MSR varying between 0.10 at 0.1 s and 0.25 at 0.3 s, while the MSRs for the Zhao (2010) model vary between 1.23 and 1.39. The corner magnitudes that separate two linear segments of the bilinear models are 7.2 for the data in Figure 11. The curved models provide better fitting to the data.

Figure 12 presents the normalized magnitude scaling λ_i for spectra at 0.5 s, 0.8 s, 1 s, and 2 s. The MSRs derived from the linear model increase with increasing spectral period, from 0.44 at 0.5 s to 0.77 at 2 s. Again the MSRs derived from the linear model are generally similar to the slope of the second segment for events larger than 7. The MSRs for the Zhao (2010) model derived from the broken lines in Figure 12 are 1.41 at 0.5 s, 1.34 at 0.8 s, 1.32 at 1 s, and 1.27 at 2 s, about 2.5 times those for the linear models. Note

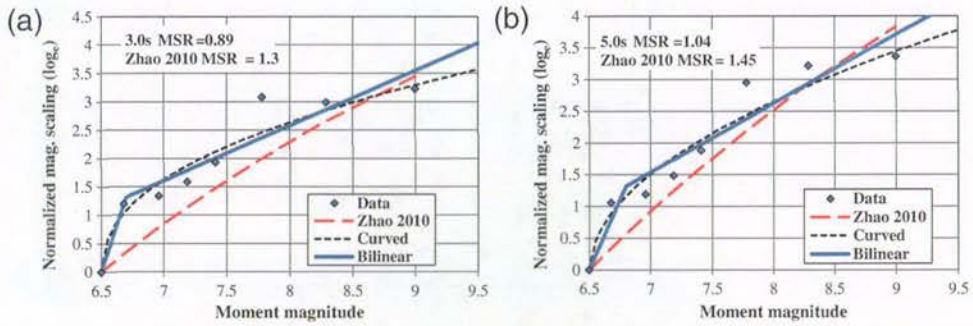

Figure 13. Normalized spectra in natural logarithm scale λ_i as a function of moment magnitude, a possible MSR, for spectral periods of (a) 3.0 s and (b) 5.00 s. The curved model is given in equation (6). The color version of this figure is available only in the electronic edition.

that the magnitude-squared term is less than zero at spectral periods over 0.15 s, and the absolute values increase from 0 at 0.1 s to 0.16 at 5 s. When the magnitude-squared term is not zero, the MSR is the first derivative of the magnitude function (from the linear magnitude term plus the magnitude-squared term) with respect to magnitude and is computed for M_w 8.

Figure 13 shows the normalized magnitude scaling λ_i for 3-s and 4-s spectral periods. The MSR from a linear model is 0.89 for 3 s and 1.04 for 5 s, while the Zhao (2010) model has an MSR of 1.3 at 3 s period and 1.45 at 5 s. The MSRs of the bilinear model for large events are similar at both spectral periods.

Figure 14a compares the MSRs of the present study with those of various models. Note that the G2002 model has a magnitude-dependent geometric spreading term and the MSRs depend on source distance. Figure 14a presents the MSRs computed for 100- and 200-km source distances for the G2002 model, while the MSRs for all other models are for large distances where the magnitude-dependent added distance has little effect. The Y1997, Z2006, and Zhao (2010) models all have magnitude-squared or cubed terms, and the MSRs were computed at M_w 8. The MSRs from the G2002 model for rock sites at a source distance of 100 km are very close to those of the present study. However, at source distance of 30 km, the MSRs of the G2002 model are less than those from the present study. The MSRs from the Z2006, Zhao 2010, and Y1997 models vary between 1.0 and 1.5 at all periods. The magnitude-scaling rates of the K2006 model are similar to those of the Z2006 model at periods up to 0.8 s and then increase quickly with increasing period, with the largest value being just over 2.

Figure 14b compares the model standard deviation from the present study with those of the Z2006, K2006, and Y1997 models. The standard deviation from the present study was computed approximately from

$$\sigma_T = \sqrt{\sigma^2 + \tau^2}, \tag{7}$$

where σ is the standard deviation in the regression analysis for equation (1) and τ is the standard deviation in the regression for equation (6). The analysis procedure used in the present study is similar to the two-step analyses of Joyner and Boore (1981), but the use of magnitude group can still underestimate the true standard deviation derived from the two-step method without magnitude grouping.

The standard deviation from equation (7) varies between that of the Y1997 model for rock and that of the K2006 model. The standard deviation from the present study is generally higher than that of the Z2006 model at most spectral periods, probably caused by the restriction imposed on the terms for near-source model prediction, site effect, and the effect of focal depth. With these restrictions, the standard deviations of the present study are still less (by a large margin at some periods) than those of the K2006 model.

Zhao and Lu (2011) suggested that the reduced magnitude-scaling rate for large earthquakes was a result of a reduced energy ratio (the ratio of energy contributed to the response spectrum at a given spectral period over the total energy) for large earthquakes. Figure 15 shows the energy ratios for a set of strong-strong-motion records from New Zealand and those from the two large subduction earthquakes (M_w 7.5 on 9 March 2011 and M_w 9 on 11 March 2011). Figure 15 shows clearly that the average energy ratio for the M_w 9 event is considerably smaller than those for the earthquakes with a magnitude of 7–7.5.

Discussion and Conclusions

Using a similar method to a previous study by Zhao and Lu (2011), the present study investigates magnitude scaling for large subduction interface earthquakes from the Zhao, Zhang, *et al.* (2006) (Z2006) model, Kanno *et al.* (2006) (K2006) model, and Gregor *et al.* (2002) (G2002) model. Similar to the models for large shallow crustal earthquakes, the MSRs from the models for subduction interface earthquakes vary significantly among different models. The difference between the Z2006 and K2006 models at periods

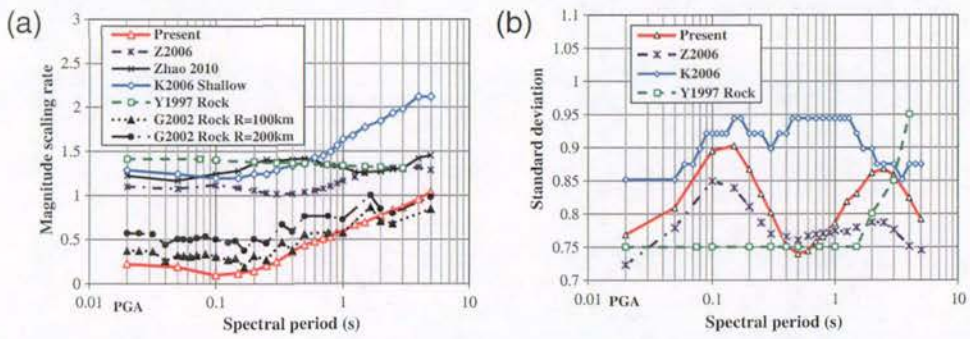

Figure 14. (a) Comparison of the MSRs at large distance derived from the present study and MSRs from the Z2006 and Zhao (2010) models, the K2006 model for shallow earthquakes, the Youngs *et al.* (1997) model (Y1997 model) for rock sites, and the G2002 model for rock sites. (b) Comparison of the standard deviation for the model derived in the present study with those from the Z2006 model, the K2006 model for shallow earthquakes, and the Y1997 model for rock sites. The color version of this figure is available only in the electronic edition.

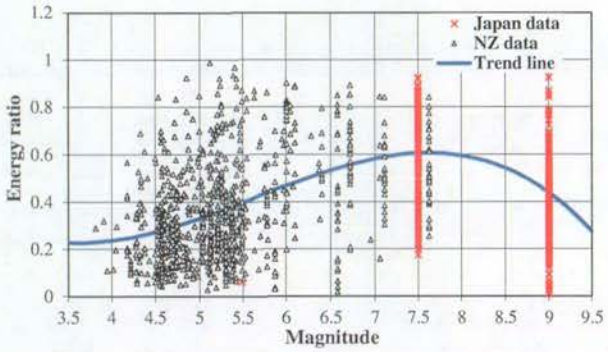

Figure 15. Energy ratios calculated according to Zhao and Lu (2011) for a 5-s spectral period for the data from New Zealand (NZ) and two recent large earthquakes from Japan. The color version of this figure is available only in the electronic edition.

over 1 s is alarmingly large, as the two models were both derived from the Japanese data.

A total of 2100 strong-motion records from 30 large subduction interface earthquakes in Japan with a moment magnitude of 6.5 or larger were compiled, including the 11 March 2011 M_w 9 event. These earthquakes were grouped according to their magnitude. An attenuation model with geometric and anelastic attenuation rates and a constant term for each earthquake group was fitted to the normalized spectra. The simple model without a magnitude term allows a constant term for each earthquake group to account for the magnitude effect. Three possible models were used to derive the magnitude-scaling rates: a simple linear model for those events with a magnitude over 7 supported by the data, a bilinear model with a corner magnitude to separate the magnitude-scaling function into two linear segments, and a simple curved model as functions of magnitude. The slopes of these straight lines would be the simple magnitude terms for a new model for a full dataset, while the interest of the present study is primarily to assess the magnitude-scaling rate—the slope of magnitude-scaling curves for large earthquakes.

The results show that MSRs derived from large subduction interface earthquakes are significantly smaller than those of the empirical prediction equations derived from real earthquake records. At short periods, the MSRs derived in the present study are only a fraction of those from the three empirical attenuation models derived from primarily the Japanese data. At spectral periods over 0.5 s, the MSRs derived in the present study are between about 1/3 and 1/2 of those from the existing empirical models.

The MSRs of the G2002 model, derived from synthetic data using a stochastic finite-fault model are surprisingly close to the values derived from the data in the present study, especially at short distances. However, at a distance of 50 km the MSRs of the G2002 model are less than the values from the present study.

The results of the present study, however, differ from those of the Zhao and Lu (2011) study for shallow crustal earthquakes. Zhao and Lu (2011) showed that a zero magnitude-scaling model worked well for the data from 13 large crustal earthquakes with M_w over 7 for spectral periods between 0.6 and 5 s, while the present study shows that the MSR increases with increasing spectral period. While no theoretical justification can be provided to explain the difference, the anelastic attenuation rates for a deep subduction interface event are considerably smaller than those from shallow subduction interface events and shallow crustal events. This means that the seismic waves from a distant part of the fault for a deep subduction interface earthquake are attenuated much less rapidly than for those from a crustal event, allowing a large part of the ground-motion generation area to produce the seismic waves that contribute significantly to the response spectrum at a recording station. This leads to a larger magnitude beyond which ground-motion amplitude would be saturated in the period range for engineering applications. Twenty of the 30 events used in the present study have a focal depth larger than 25 km, the boundary between shallow and deep subduction interface earthquakes assigned in the Zhao (2010) study.

Another feature of the subduction interface earthquake is that its fault area can have a width that can be very close to its length. This may allow a larger ground-motion generation area on a fault to produce ground motions that contribute to the response spectra at a station for a given distance, compared with a relative narrow and long fault for a crustal earthquake.

It is encouraging to find that numerical simulations used by Gregor *et al.* (2002) produced very similar magnitude scaling to those derived from the present study. Such a close match may allow researchers to apply this method to fill in the data gap and/or to constrain the model prediction for large damaging subduction earthquakes. The recent study by Atkinson and Goda (2010) shows that the synthetic strong-motion records generated by a stochastic finite-fault model developed by Motazedian and Atkinson (2005) produced very similar inelastic response spectra to those of real strong-motion records with minor modification or amplitude scaling. These results provide confidence in using synthetic strong-motion records for engineering applications.

Data Resources

The strong-motion records are from K-NET and KiK-net, administered by the National Research Institute for Earth Science and Disaster Prevention of Japan. A small number of records are from the Port and Airport (Port and Harbour) Research Institute and the Japan Meteorological Agency.

Acknowledgments

The authors would like to thank David Rhoades for his review of this manuscript, Jane Forsyth for her editorial comments and B. Edwards for his detailed review and comments. This project is partially supported by New Zealand Foundation for Research Science and Technology, New Zealand Hazards Platform contract C05X0907.

References

Abrahamson, N. A., and W. J. Silva (2008). Summary of the Abrahamson & Silva NGA ground-motion relations, *Earthq. Spectra* **24,** no. 1, 67–97.

Atkinson, G. M., and D. M. Boore (2003). Empirical ground-motion relations for subduction-zone earthquakes and their application to Cascadia and other regions, *Bull. Seismol. Soc. Am.* **93,** 1703–1729.

Atkinson, G. M., and K. Goda (2010). Inelastic seismic demand of real versus simulated ground-motion records for Cascadia subduction earthquakes, *Bull. Seismol. Soc. Am.* **100,** 102–115.

Boore, D. M., and G. M. Atkinson (2008). Ground-motion prediction equations for the average horizontal component of PGA, PGV, and 5%-damped PSA at spectral periods between 0.01 s and 10.0 s, *Earthq. Spectra* **24,** no. 1, 99–138.

Building Seismic Safety Council (2000). The 2000 NEHRP Recommended Provisions for New Buildings and Other Structures, Part I (Provisions) and Part II (Commentary), *FEMA 368/369*, Washington, D.C., 374 pp.

Campbell, K. W., and Y. Bozorgnia (2008). NGA ground motion model for the geometric mean horizontal component of PGA, PGV, PGD and 5% damped linear elastic response spectra for periods ranging from 0.01 to 10 s, *Earthq. Spectra* **24,** no. 1, 139–171.

Chiou, B. S.-J., and R. R. Youngs (2008). An NGA model for the average of horizontal component of peak ground motion and response spectra, *Earthq. Spectra* **24,** no. 1, 173–216.

Gregor, N. J., W. J. Silva, I. G. Wong, and R. R. Youngs (2002). Ground-motion attenuation relationships for Cascadia subduction zone megathrust earthquakes based on a stochastic finite-fault model, *Bull. Seismol. Soc. Am.* **92,** 1923–1932.

Joyner, W. B., and D. M. Boore (1981). Peak horizontal acceleration and velocity from strong-motion records including records from the 1979 Imperial Valley, California, earthquake, *Bull. Seismol. Soc. Am.* **71,** 2011–2038.

Kanno, T., A. Narita, N. Morikawa, H. Fujiwara, and Y. Fukushima (2006). A new attenuation relation for strong ground motion in Japan based on recorded data, *Bull. Seismol. Soc. Am.* **96,** 879–897.

Motazedian, D., and G. M. Atkinson (2005). Stochastic finite-fault modelling based on a dynamic corner frequency, *Bull. Seismol. Soc. Am.* **95,** 995–1010.

National Research Institute for Earth Science and Disaster Prevention (NIED; 2011). Source process of the 2011 Off the Pacific Coast of Tohoku earthquake based on strong ground motions (preliminary), http://www.k-net.bosai.go.jp/k-net/topics/TohokuTaiheiyo_20110311/nied_kyoshin2e.pdf (last accessed September 2011).

Silva, W., R. Darragh, C. Stark, I. Wong, J. Stepp, J. Schneider, and S. Chiou (1990). A methodology to estimate design response spectra in the near-source region of large earthquakes using the band-limited-white-noise ground motion model, in *Proc. U.S. Fourth National Conference on Earthquake Engineering*, Palm Springs, California, 20–24 May 1990, Vol. **1**, 487–494.

Yagi, Y. (2004). Source rupture process of the 2003 Tokachi-Oki earthquake determined by joint inversion of teleseismic body wave and strong ground motion data, *Earth Planets Space* **56,** 311–316.

Youngs, R. R., S. J. Chiou, W. J. Silva, and J. R. Humphrey (1997). Strong ground motion attenuation relationships for subduction zone earthquakes, *Seismol. Res. Lett.* **68,** 58–73.

Zhao, J. X. (2010). Geometric spreading functions and modelling of volcanic zones for strong-motion attenuation models derived from records in Japan, *Bull. Seismol. Soc. Am.* **100,** 712–732.

Zhao, J. X., and M. Lu (2011). Magnitude-scaling rate in ground-motion prediction equations for response spectra from large, shallow crustal earthquakes, *Bull. Seismol. Soc. Am.* **101,** no. 6, 2643–2661.

Zhao, J. X., K. Irikura, J. Zhang, Y. Fukushima, P. G. Somerville, A. Asano, Y. Ohno, T. Oouchi, T. Takahashi, and H. Ogawa (2006). An empirical site classification method for strong motion stations in Japan using H/V response spectrum ratio, *Bull. Seismol. Soc. Am.* **96,** 914–925.

Zhao, J. X., J. Zhang, A. Asano, Y. Ohno, T. Oouchi, T. Takahashi, H. Ogawa, K. Irikura, H. K. Thio, P. G. Somerville, Yasuhiro Fukushima, and Fukushima Yoshimitsu (2006). Attenuation relations of strong ground motion in Japan using site classification based on predominant period, *Bull. Seismol. Soc. Am.* **96,** 898–913.

Zhao, J. X., J. Zhang, and K. Irikura (2009). Side effect of using response spectral amplification ratios for soil sites: Variability and earthquake-magnitude and source-distance dependent amplification ratios for soil sites, *Soil Dynam. Earthq. Eng.* **29,** no. 9, 1262–1273.

Southwest Jiaotong University
111, 1st Section
Northern 2nd Ring Road
Chendu, Sichuan
China

Manuscript received 19 May 2011

Bulletin of the Seismological Society of America, Vol. 103, No. 1, pp. 1–18, February 2013, doi: 10.1785/0120110251

A Comparison of V_{S30} and Site Period as Site-Effect Parameters in Response Spectral Ground-Motion Prediction Equations

by John X. Zhao* and Hua Xu

Abstract V_{S30}, the shear-wave travel time averaged soil shear-wave velocity of the top 30 m, has been used to represent site effects in many recent ground-motion prediction equations (GMPEs). However, while V_{S30} has been found to be a reasonable parameter to represent site effects in some studies, other studies provide contradictory evidence. In the present study, a systematic comparison between the predictive capabilities of these two site-effect parameters is carried out using a large ground-motion dataset from Japan. The basis of the adopted approach is to compare the standard deviations and amplitudes of amplification ratios in empirically modeling site effects by using either site period (T_S, four times the shear-wave travel time from the bedrock to the ground surface) or V_{S30}. The site effects modeled specifically include site amplification ratios between surface and borehole records from KiK-net, in addition to the site-effect terms from a GMPE. For KiK-net data, T_S is determined to be a better predictive parameter than V_{S30} for soil sites with $T_S > 0.6$ s, while the two parameters lead to a similar variability in amplification ratios for sites with $T_S < 0.6$ s. For site effects obtained from the GMPE, V_{S30} and T_S are statistically equal for all site classes at most periods, while V_{S30} leads to smaller variability than T_S at some spectral periods. The conflict between the KiK-net surface–borehole records, and the results from the GMPE is likely to be a result of large variability in the GMPE, containing source-, path-, and site-variability, as compared with the reduced variability in the surface–borehole KiK-net data pairs. Although V_{S30} and T_S lead to statistically similar standard deviations for the data from a GMPE, T_S still leads to better median amplification ratios than V_{S30}.

Introduction

Near-surface site conditions are one of the most influential factors affecting ground-motion parameters for engineering design. In ground-motion prediction equations (GMPEs) for peak ground acceleration (PGA) and 5% damped spectral accelerations, site effects are often characterized by a set of simplified parameters that seek to characterize the salient features of the near-surface soils when subjected to ground-motion shaking. Common site parameters include the site period (T_S, four times the shear-wave travel time from the bedrock to the ground surface in the vertical direction) and the time-averaged shear-wave velocity over the top 30 m of the soil deposit, V_{S30}. Zhao, Zhang, *et al.* (2006) and Zhao, Irikura, *et al.* (2006), for example, used site classes based on T_S, while McVerry *et al.* (2006) used site classes based on geological and geotechnical descriptions of soil layers and T_S. Conversely, V_{S30} is the most commonly used site parameter in modern GMPEs, including Next Generation of Attenuation (NGA) models (Abrahamson and Silva, 2008; Boore and Atkinson, 2008; Campbell and Bozorgnia, 2008; Chiou and Youngs, 2008). However, there are ample research articles that demonstrate the limitations of V_{S30}, as reviewed by Castellaro *et al.* (2008). McVerry (2011) showed the improvement in the prediction of response spectra by using T_S as the site parameter in a GMPE and the inappropriateness of V_{S30} as a site parameter for New Zealand strong-motion recording stations. In this study, we discuss appropriate site parameters for GMPEs only.

Some authors have considered T_S to be a better site parameter from both theoretical and practical perspectives (Zhao, Irikura, *et al.*, 2006; Zhao, Zhang, *et al.*, 2006; Castellaro *et al.*, 2008; Luzi *et al.*, 2011; McVerry, 2011). Luzi *et al.* (2011) also proposed the combination of V_{S30} and site fundamental frequency using Italian records. The depth used to calculate T_S depends on the shear-wave velocity of engineering bedrock, which is defined as having a shear-wave velocity equal to or greater than 700 m/s by Zhao, Zhang, *et al.* (2006), and adopted herein, while 1100 m/s was used

*Also at GNS Science, 1 Fairway Drive, Avalon, Lower Hutt 5010, New Zealand.

by Walling *et al.* (2008). T_S is considered to be zero when engineering bedrock outcrops are found at the surface. For a higher bedrock shear-wave velocity, the depth of bedrock is also usually greater. Therefore, very high shear-wave velocity values are not usually used in a GMPE because they are not generally available for engineering applications or there is a high cost to measure the shear-wave velocity for a large depth.

The use of V_{S30} as the only site parameter for shallow soil layers in some GMPEs, such as those of Boore and Atkinson (2008) and Campbell and Bozorgnia (2008), is controversial as it is considered a theoretically incomplete parameter. The reliability of V_{S30} was debated during the Symposium on Effects of Surface Geology on Seismic Motion held in the University of California at Santa Barbara (2011). Abrahamson (2011) suggested that V_{S30} was a suitable site parameter in a GMPE and worked well for providing a smoothed transition for response spectrum from rock to soil sites. Castellaro (2011) suggested that V_{S30} alone should not be a proxy for site effect at all. Zhao (2011) investigated the modeling of site effects by using T_S and V_{S30}. This article expands on the results of Zhao (2011).

We used two large sets of strong-motion records from Japan, and the large number of records allows for very detailed assessment of the appropriateness of T_S and V_{S30} as site parameters. Surface–borehole, strong-motion record pairs from KiK-net sites were also used because the amplification ratios between the surface and borehole records are less affected by the variability associated with source and path effects than GMPEs. This study may provide some plausible insights to the debate about the suitability of V_{S30} as the proxy for site effects, and why many GMPE developers have used V_{S30}, although many agree that V_{S30} cannot account for many other aspects of site response. We also propose and evaluate the T_S as a possible alternative to V_{S30} for a GMPE. To assess the appropriateness of T_S and V_{S30} as site parameters, it is important to examine the correlation between them for a large number of strong-motion recording stations. If these two site parameters are highly correlated, either can be used as a site parameter. To make a simple comparison, a pseudo site period is defined:

$$T_{V_{S30}} = \frac{120 \text{ m}}{V_{S30}}, \tag{1}$$

in which the unit for V_{S30} is m/s. For a site where bedrock is reached at a depth of 30 m, $T_{V_{S30}}$ equals the T_S based on an assumption of a 1D model (4 × depth = 120 m). Figure 1 shows the correlation of these two site parameters, with the solid line being a function of T_S for calculating $T_{V_{S30}}$. Figure 1a shows all stations in this study, and Figure 1b shows the KiK-net stations only. The correlation is excellent for $T_S \leq 0.4$ s for both sets of stations. The standard deviation is 0.266 on a natural logarithm scale for all sites, and 0.173 for sites with $T_S = 0.4$ s or less for all stations used in the present study, much less than the model prediction standard deviation of most GMPEs. The correlation between T_S and $T_{V_{S30}}$ for KiK-net stations is better than for all stations, with a standard deviation of 0.213 with respect to the correlation curve. For sites with $T_S < 0.04$ s (in the case where a very thin layer of soil lies on an engineering bedrock), on average both $T_{V_{S30}}$ and the amplification ratio (KiK-net surface and borehole) are essentially constant. Therefore, T_S fixed at 0.04 s if it is less than 0.04 s. The good correlation for short-period sites (up to 0.4 s) suggests that T_S and V_{S30} can be equally good site parameters. The scatter for sites with $T_S > 0.5$ s is considerable and may lead to different model predictions between the two site parameters. The important point is whether the large scatter in Figure 1 for moderate and long-period (more than 0.5 s) sites can lead to statistically significant, and practically different, site amplification ratios and associated variability in a GMPE. The small standard deviation in the correlation between the two site parameters means that any difference in the site effect between them can be obscured by the large model prediction

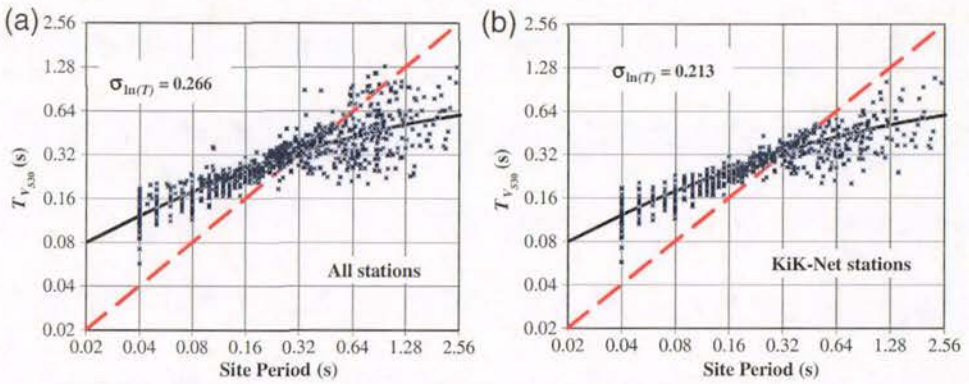

Figure 1. Correlation between T_S and $T_{V_{S30}}$ for strong-motion recording stations in Japan, (a) all stations used in the present study and (b) KiK-net stations only. The site period for KiK-net sites is computed to the bedrock depth, four times the shear-wave travel time to the bedrock depth. For those sites with $T_S < 0.04$ s, T_S was set as 0.04 s. The KiK-net stations have a better correlation between site period and $T_{V_{S30}}$. The color version of this figure is available only in the electronic edition.

variability, typically 0.6–0.8 on a natural logarithm scale, of a GMPE.

Methodology

The best way to empirically assess the suitability of a site parameter, such as V_{S30} or T_S, to represent site effects in a GMPE, is to use a large strong-motion dataset suitable for developing GMPE. In such an empirical assessment, all necessary earthquake parameters are needed, including the shear-wave velocity profiles of the recording stations, preferably measured values down to the depth of engineering bedrock. Therefore, we have assembled records from the strong-motion networks of KiK-net and K-NET, operated by the Institute of Earth Science and Disaster Prevention in Japan, and the network operated by the Port and Airport Research Institute (PARI) with the necessary shear-wave velocity profile. All KiK-net stations have three-component accelerometers both at the surface and at the bottom of a borehole, and many boreholes reach engineering bedrock. Among 134 K-NET stations, 102 stations have engineering bedrock depths of less than 20 m. Among 37 PARI stations, 15 stations have measured shear-wave velocity profiles down to engineering bedrock. For the remaining 32 K-NET stations and 22 PARI stations, site periods, which were all from site classification (SC) IV, were estimated by horizontal-to-vertical (H/V) ratios with reasonable confidence by the method of Zhao, Irikura, *et al.* (2006). However, a note of caution in using H/V ratio is that the peak period in the H/V ratio does not necessarily correspond to the peak period in the surface–borehole amplification ratios. The two peak periods may coincide only if the borehole censor is located at the soil–rock interface as suggested by Safak (1997) and the results from the analyses of downhole records by Parolai *et al.* (2009). This inconsistency is likely to contribute to overall uncertainty in the analyses presented in this study.

Site classes are used for presenting spectral amplification ratios only and are defined by T_S, not $T_{V_{S30}}$.

Spectral Amplifications from Surface–Borehole Record Pairs

These surface–borehole amplification ratios differ from the response spectral amplification ratios between the ground surface record at a soil site and a nearby rock site surface record (Safak 1997). From equation (4) of Zhao (1996), for example, the ratio between soil surface displacement and that at the bottom of the soil layer is independent of material properties of the bedrock and the impedance ratio. Surface–borehole amplification ratios exclude the effect of radiation damping (the effect from the portion of downgoing waves that is leaked back to the half-space). Equation (4) of Zhao (1996) shows that from a modeling point of view, compared with surface–borehole spectral ratios, the Fourier spectral ratio between the soil surface and bedrock outcrop is a function of impedance ratio and therefore radiation damping is accounted for in the amplification ratios between a surface soil and a nearby surface rock site (or bedrock outcrop) as implied in a GMPE. The suitability of a site parameter can be checked by

$$A_{\text{pseudo-site}}(T_{\text{site}}, T_{\text{SP}}) = \frac{A_{\text{SB}}(T_{\text{site}}, T_{\text{SP}})}{A_{\text{SB}}(T_{\text{rock}}, T_{\text{SP}})}, \qquad (2)$$

in which $A_{\text{pseudo-site}}$ is the pseudoamplification ratio for a soil site over a rock site at a spectral period of T_{SP}, in which an amplification ratio that may be similar to that of a GMPE. A_{SB} is the average amplification ratio between the surface and borehole response spectra, T_{site} is a site parameter, and T_{rock} is the site parameter for rock site. Both T_{site} and T_{rock} can be either T_S or $T_{V_{S30}}$, used in a GMPE. We refer to the amplification ratio in equation (2) as a pseudoamplification ratio to differentiate it from the amplification ratio of a surface soil site over a surface rock site in a GMPE. Although radiation damping is not included in equation (2), $A_{\text{pseudo-site}}$ will be similar to surface soil–surface rock ratios in two cases: (1) when the bedrock is rigid, or (2) when the radiation damping effects on $A_{\text{SB}}(T_{\text{soil}}, T_{\text{SP}})$, for soil sites, and $A_{\text{SB}}(T_{\text{rock}}, T_{\text{SP}})$, for rock sites, are identical. In the latter case, the effect of radiation damping is cancelled out, although this assumption is likely to be applicable for sites only with short to moderate spectral periods. Zhao (1996) showed that the radiation damping ratio is proportional to the period and, therefore, its effect is less at short periods than at long periods. The small effect of radiation damping leads to similar values for $A_{\text{pseudo-site}}$ to the spectral amplification ratios of surface soil–surface rock sites for spectral periods up to about 1.5 s (within 20% for short-period sites; the results are not presented in this paper because of length constraints). Because the wave path of the surface and borehole records is identical from the earthquake source to the base of the borehole, $A_{\text{pseudo-site}}$ will not be affected by the variability associated with earthquake source and wave propagation path for that particular event, and hence the reason why KiK-net surface–borehole record pairs were used. It is possible that, if a site parameter can be used to accurately model the surface–borehole spectral ratio, it can be used to model the amplification ratios of surface soil–surface rock records because of the similarity between the two types of amplification ratios.

The variability of the response spectral ratios from a site with a borehole record is arguably too large to assess the suitability of a site parameter by comparing the spectral amplification ratios with theoretical results from simple models. Instead, an empirical method is used herein. The average amplification ratio is calculated for each site, and regression is used to examine its dependence on T_S or $T_{V_{S30}}$. The residuals between the average amplification ratio of a site and the median value from the regression equation are referred to as intersite (or between sites) residuals. In a similar way to the random-effects model used by Abrahamson and Youngs (1992), the residuals between the amplification ratio of each

record and the average amplification ratio from all records at this particular site are referred to as intrasite (or within sites) residuals, the definition of which is not strictly consistent with random effects methodology. A rigorous separation of residuals into the inter and intrasite parts requires a random-effects model to be fitted to the amplification ratios, and the inter and intrasite errors can then be estimated simultaneously. However, a rigorous model is not necessary for a preliminary study to assess the suitability of a site parameter because our main objective is to derive the standard deviations for the two site parameters. However, the approximate separation may lead to the intra and intersite residuals for sites with few records being biased.

The standard deviation of the intersite residuals is used to gauge the suitability of the site parameter. The conclusion may be reached by performing an F-test between the two sets of intersite residuals obtained using T_S or $T_{V_{S30}}$ with the hypothesis that the standard deviations of the two sets of residuals are statistically similar. If the hypothesis is rejected at a significantly low probability, such as $p = 0.05$ or 0.1, the site parameter that leads to the smaller standard deviation may be considered to show significantly better predictions. Such comparisons and statistical tests are performed for all data, including those grouped according to the site classes (Table 1). Such site-class grouped testing is important because a site parameter that appears to be better for all sites in one group may not be the better parameter for all site classes.

Note that the shear-wave velocities at the borehole location for two sites with the same site period, or the depth of the borehole sensors at two sites with identical shear-wave velocity profiles, are unlikely to be equal. These differences will bring variability to the surface–borehole amplification ratios as shown by Safak (1997). However, for KiK-net stations, borehole sensors are usually located in the engineering bedrock. Therefore, minor differences in borehole depth may not have a significant effect.

Spectral Amplifications from Ground-Motion Prediction Equations (GMPEs)

The second approach for examining the difference between T_S and V_{S30} as a measure of site effects is to use the results from a GMPE. For example, Zhao (2010) used a random-effects model (Abrahamson and Youngs, 1992) to investigate the options for geometric attenuation functions; Zhao and Xu (2012) used a model that is largely equivalent to the random-effects model to investigate the magnitude scaling for large subduction-interface earthquakes in Japan. The random-effects model by Abrahamson and Youngs (1992) separates the residuals into two parts, interevent (between earthquakes as termed by Atik *et al.*, 2010) and intraevent (within earthquakes as termed by Atik *et al.*, 2010) residuals. Theoretically, the interevent residuals are associated with earthquake source parameters only for a large dataset with ideal distribution with respect to magnitude, source distance and site classes. Interevent residuals will not be used in this study even though the data distribution is not ideal because we consider the possible effect of imperfect data distribution is likely to be secondary. In order to describe site effects by a continuous site parameter, such as T_S or $T_{V_{S30}}$, from a GMPE based on site classes, we need to recover the portion of site effect that can be described by a continuous site parameter but has been forced into intraevent residuals by the use of site classes. The site term plus the intraevent residuals contain random intraevent errors, random errors associated with the site effect, and the underlying portion of the site effect that can be described by a function of a continuous site parameter in an empirical model. Theoretically speaking, fitting a function of site parameters, either T_S or $T_{V_{S30}}$, to the site term plus the intraevent errors by a least squares method can obtain estimates of the appropriate function for site effects, as random errors associated with intraevent variability and site effects can be averaged out. The standard deviation of the intersite residuals can then be used to gauge the suitability of the site parameter. The results from this approach are directly applicable to GMPEs, and we also expect that the intersite variability from this dataset is larger than that from the first approach. The results from this approach may address the reason why most GMPE developers use V_{S30}, although many GMPE developers agree that V_{S30} alone is not a theoretically sound parameter to represent site effects. It is perhaps the case that the large variability hides the theoretical inappropriateness of the controversial site parameter V_{S30} used as the proxy for site effects.

Strong-Motion Dataset

We used two datasets. The first dataset has 3018 surface-borehole pairs of strong-motion records, obtained by the KiK-net stations from earthquakes for which moment magnitude,

Table 1
Site-Class Definitions Used in the Present Study and the Approximately Corresponding NEHRP Site Classes (Building Seismic Safety Council [BSSC], 2000)

Site Class	Description	Natural Period	V_{S30} Calculated from T_S	NEHRP Site Classes
SC I	Rock	$T < 0.2$ s	$V_{S30} > 600$	A+B+C
SC II	Hard soil	$0.2 \le T < 0.4$ s	$300 < V_{S30} \le 600$	C
SC III	Medium soil	$0.4 \le T < 0.6$ s	$200 < V_{S30} \le 300$	D
SC IV	Soft soil	$T \ge 0.6$ s	$V_{S30} \le 200$	E+F

reliable focal depth, and tectonic source types are available. The earthquakes have a moment-magnitude range of 4.9–9.0 and a focal depth up to 130 km. The records are from 10 shallow-crustal, 31 subduction-interface, and 54 subduction-slab events, as shown in Table 2 and Figure 2. The source distance (the closest distance to the fault rupture model for large earthquakes with computed finite fault and hypocentral distance for the remaining others) is up to 300 km and a magnitude-dependent cutoff distance is used to avoid the effect of untriggered stations. Nine hundred fifty-nine pairs of records are from SC I, 678 from SC II, 399 from SC III, and 982 from SC IV sites, as shown in Table 3 and Figure 3. These records will be used for the analysis of the response spectral amplification ratios between the surface and the borehole accelerograms.

The second dataset consists of records from 39 shallow-crustal, 64 subduction-interface, and 37 subduction-slab earthquakes as shown in Table 4 and Figure 4. There are a total of 2014 ground-motion records from these 140 earthquake events, many from the first dataset, including 669 records from SC I, 467 from SC II, 200 from SC III, and 678 from SC IV sites as shown in Table 5 and Figure 5. The earthquakes have similar magnitude and focal depth range to those of the first dataset. All records are from ground surface stations and have previously been used by Zhao (2010) and Zhao and Xu (2012) for assessing GMPE parameters. The remainder of those records used by Zhao (2010) and Zhao and Xu (2012) are not used in the present study because T_S of the recording stations are not available. In particular, the strong-motion records from the 2011 M_w 9 Off the Pacific coast of Tohoku earthquake were used in both datasets. For stations where shear-wave velocity is only available down to a depth of 20 m, as for K-NET stations and some PARI stations, the shear-wave velocity for the last layer was used for the soil between depths of 20 and 30 m to compute V_{S30}. Boore *et al.* (2011) and Kanno *et al.* (2006) developed correlation equations between average shear-wave velocity of top 20 m (V_{S20}) and V_{S30} for a large range of V_{S20}, and our simple extension appears to work satisfactorily for SC IV sites as calibrated by using KiK-net stations. However, to simply extend the shear-wave velocity of the last layer down to 30 m would not lead to a reasonable estimate for T_S.

These two datasets utilized in this study have a low level of overlapping ground motions. The first dataset contains

Table 2
First Dataset: Number of Earthquakes in Each Site Class and Earthquake Source Type

	Focal Mechanism			Total in Each Source Type
	Reverse	Strike-Slip	Normal	
Shallow crustal	6	4		10
Subduction interface	31			31
Subduction slab	35	8	11	54
Total in each focal mechanism group	72	12	11	Grand total 95

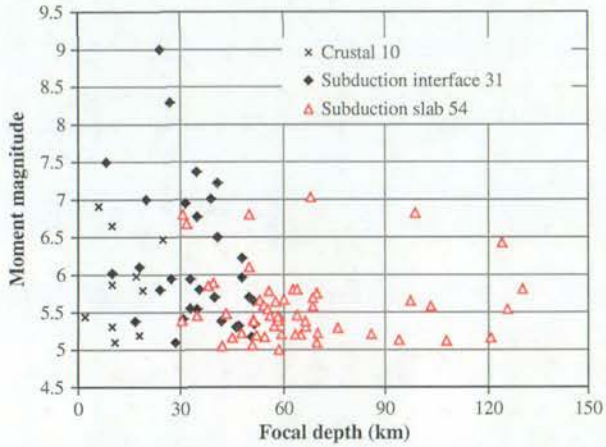

Figure 2. First dataset: distribution of earthquakes with respect to focal depth and magnitude for KiK-net data. The number of events is given in the legend. The color version of this figure is available only in the electronic edition.

448 records from the second dataset while the second dataset contains 743 records from the first dataset. This relatively low level of data overlap makes it impossible to use the analysis on the site terms plus intraevent residuals, which represent variations within a given earthquake (Abrahamson and Youngs, 1992), for the first dataset. This is because the intraevent residuals for the KiK-net surface records that are not in the second dataset are not available, unless a new GMPE is developed based on all strong-motion records in both datasets. In this study, approximate intraevent residuals for the KiK-net surface records in the first dataset are computed with respect to a GMPE developed by Zhao (2010). The results from the KiK-net surface records will be used as confirmation for the results from the analyses of the second dataset.

Significant nonlinear soil response is likely to develop when a surface soil site PGA is more than $0.2g$ for SC III and IV sites. In the first dataset, a very small portion—49 of 1381 records—from SC III and IV sites have a geometric mean PGA more than $0.2g$. In the second dataset, only 77 records from SC III and IV sites have a geometric mean PGA more than $0.2g$. We do not expect that the effect of nonlinear soil

Table 3
First Dataset: Number of KiK-net Records in Each Site Class and Earthquake Source Type

	Site Class				Total in Each EQ Type
	SC I	SC II	SC III	SC IV	
Shallow crustal	155	105	58	104	422
Subduction interface	339	232	145	379	1095
Subduction slab	465	341	196	499	1501
Total in each site class	959	678	399	982	Grand total 3018

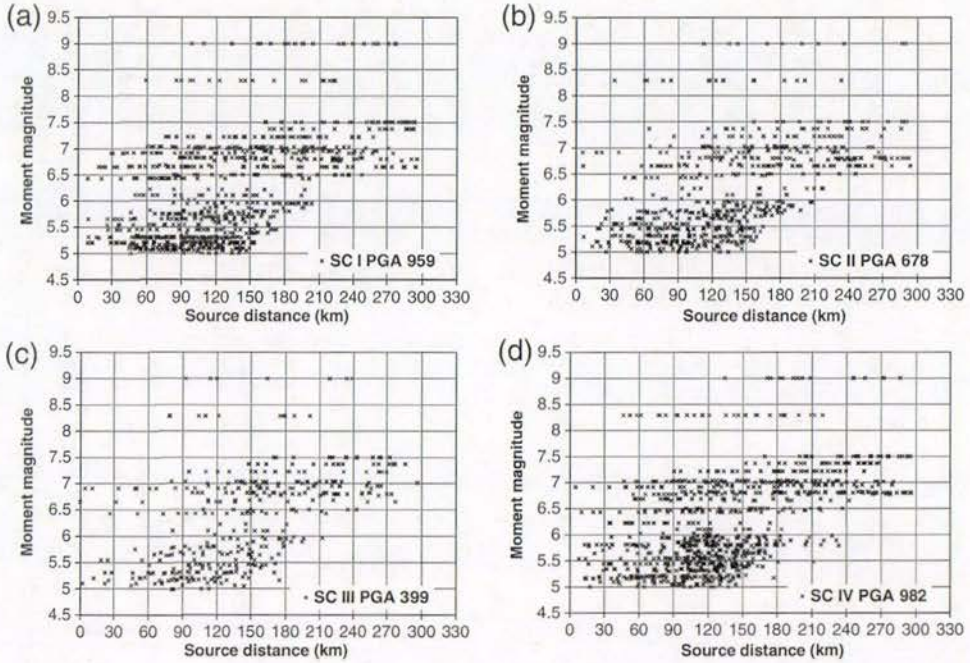

Figure 3. First dataset: distribution of strong-motion records from KiK-net stations used in the present study for peak ground acceleration (PGA). A magnitude-dependent cut-off distance is used to avoid the effect of untriggered instruments. Site classes were defined by site period.

response from such a small portion of stations would have any significant impact on the results reported in the present study. Note that nonlinear models for some GMPEs (Abrahamson and Silva, 2008; Campbell and Bozorgnia, 2008; Chiou and Youngs, 2008), were derived from numerical modeling (Walling *et al.* 2008), suggesting that it is not possible to derive reliable GMPE terms accounting for nonlinear soil response from strong-motion records only. The results present in this study are applicable only to the linear site term (independent of rock site PGA or spectra) in a GMPE.

Analyses of KiK-net Response Spectral Amplification Ratios from the First Dataset

The average spectral amplification ratios are computed for each site first. For those sites that have a large number of records, the effect of magnitude and source distance can be minimized by taking the average amplification ratio for all records in each site. A small number of stations have only one record, and the amplification ratio for this record was taken as the average ratio while in a random-effects model the residual for a single record can be partitioned into inter and intrasite residuals. Based on visual inspection on the variation of surface–borehole amplification ratios with T_S (or $T_{V_{S30}}$), a number of possible functions were used to describe the average amplification ratios. The function with the fewest terms that are statistically significant and the smallest standard deviation was selected. Based on this selection procedure, the following simple function of site parameter T was fitted to the site amplification ratios between the surface and borehole response spectra,

$$\ln[A_{SB}(T, T_{SP})] = a_{SB}(T_{SP})T + b_{SB}(T_{SP})\ln(T) + c_{SB}(T_{SP})[\ln(T)]^2 + d_{SB}(T_{SP}). \quad (3)$$

Table 4
Second Dataset: Number of Earthquakes in Each Site Class and Earthquake Source Type

	Focal Mechanism				Total in Each Source Type
	Unknown	Reverse	Strike-Slip	Normal	
Shallow crustal		11	26	2	39
Subduction interface		62	2		64
Subduction slab	1	18	9	9	37
Total in each focal mechanism group	1	91	37	11	Grand total 140

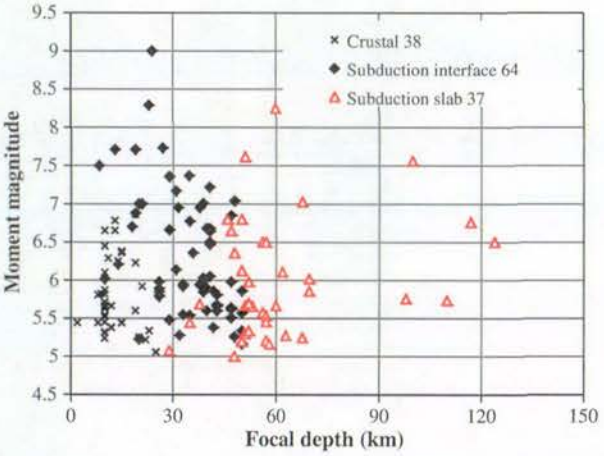

Figure 4. Second dataset: distribution of earthquakes with respect to focal depth and magnitude from the Zhao (2010, 2011) studies. The color version of this figure is available only in the electronic edition.

in which T is either T_S or $T_{V_{S30}}$, and $a_{SB}(T_{SP})$, $b_{SB}(T_{SP})$, $c_{SB}(T_{SP})$, and $d_{SB}(T_{SP})$ are regression coefficients for a given value of T_{SP}. Even for equation (3), not all terms are statistically significant for some spectral periods and only the terms with statistically significant estimates were used. The impedance ratio is not used as a site parameter in equation (3) because our initial study suggests that the terms to represent this parameter are not statistically significant. This aspect may be investigated further in a future study.

The differences between the natural logarithm of the amplification ratios and those calculated from equation (3) are referred to as intersite residuals for the simple model. Their standard deviation is referred to as intersite variability (τ_s). Note that τ_s is the prime parameter for this study, and it was determined that τ_s is not overly sensitive to the specific functional form of equation (3). Figure 6 shows the amplification ratios for spectral periods of 0.5 (top row) and 1.0 s (bottom row). The corresponding curves characterized by T_S are in the left panel and $T_{V_{S30}}$ are in the right panel. For the 0.5 s spectral period, the intersite standard deviation for the fitted equation is 0.45 when T_S is used and 0.43 when $T_{V_{S30}}$ is used, suggesting that both parameters can be used to characterize the site effect equally well. For the 1.0 s spectral period, the standard deviation for the fitted equation is 0.32 for T_S and 0.37 for $T_{V_{S30}}$, suggesting that T_S is slightly better than $T_{V_{S30}}$, although a confirmation by statistical tests is necessary. Figure 7 shows amplification ratios for spectral periods of 2.0 (top row) and 4.0 s (bottom row); the corresponding curves characterized by T_S are in the left panel and those by $T_{V_{S30}}$ in the right. The scatter in the right panel of Figure 7 is clearly larger than that in the left. For both spectral periods, the standard deviation for the fitted equation of T_S is less than that for $T_{V_{S30}}$, tentatively suggesting that T_S is a better site parameter.

Table 5
Second Dataset: Number of Records in Each Site Class and Earthquake Source Type

	Site Class				Total in Each EQ Type
	SC I	SC II	SC III	SC IV	
Shallow crustal	122	84	12	79	297
Subduction interface	344	254	139	469	1206
Subduction slab	203	129	49	130	511
Total in each site class	669	467	200	678	Grand total 2014

The residuals are grouped together according to their site class defined in Table 1 using T_S, and the standard deviation of the intersite residuals is then computed for each site class. Figure 8 compares the intersite standard deviation (labeled as intersite variability for convenient presentation in all relevant figures) derived from equation (3) using both $T_{V_{S30}}$ and T_S for four site classes. For three site classes, SC I (rock), II (hard soil), and III (intermediate soil), the standard deviations derived by using either T_S or $T_{V_{S30}}$ are nearly identical for all spectral periods. At some spectral periods, 0.2–0.7 s for SC I and III sites, and up to 0.5 s for SC IV sites, the intersite standard deviation based on using $T_{V_{S30}}$ is slightly smaller than that derived using T_S. For SC IV sites, the intersite standard deviation using T_S is much smaller for spectral periods of more than 1 s, as shown in Figure 8d. Figure 9a shows the intersite standard deviation for all data as one group. The standard deviation obtained using T_S is similar to that using $T_{V_{S30}}$ at short spectral periods and moderately smaller for spectral periods in the range of 1–4.5 s. The probability of an F-test on the hypothesis that the standard deviation by using T_S is similar to that using $T_{V_{S30}}$ is less than 5% in a spectral period range of 0.9–4.5 s, as shown in Figure 9a, suggesting that T_S results in a statistically smaller uncertainty than $T_{V_{S30}}$ in this period range. However, Figure 9b shows that the probability for the same hypothesis is less than 5% only for SC IV sites in the spectral period range of 1.25–5 s and is less than 10% for spectral periods of 1 s or longer. These results illustrate that T_S is a better site parameter than $T_{V_{S30}}$ for predicting amplification of spectral acceleration on soft soil sites within a spectral period range of 1–5 s. For other site classes and spectral period bands, $T_{V_{S30}}$ and T_S work equally well.

When site classes are used, alternative intrasite-class residuals can be defined as the differences between those of each record and the average amplification ratios in each site class (assuming constant amplification ratios within each site class). Figure 10a shows the standard deviation of intrasite-class residuals for these discrete site classes. For the first three site classes—SC I, II, and III—the intrasite-class standard deviations for all spectral periods tend to increase with increasing T_S, increasing site class from I to III. For SC IV sites, the intrasite-class standard deviations at short periods are smaller than those for the other three site classes but become much larger at long spectral periods. The standard deviations for the intrasite residuals in Figure 10b are

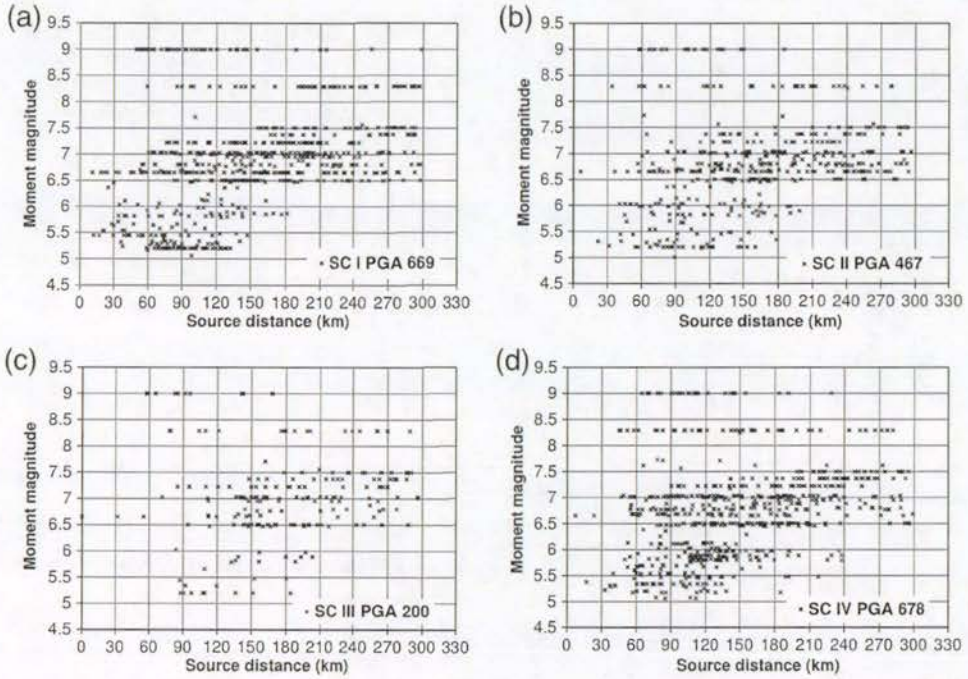

Figure 5. Second dataset: distribution of strong-motion records used in the present study for PGA. Site classes were defined by site period.

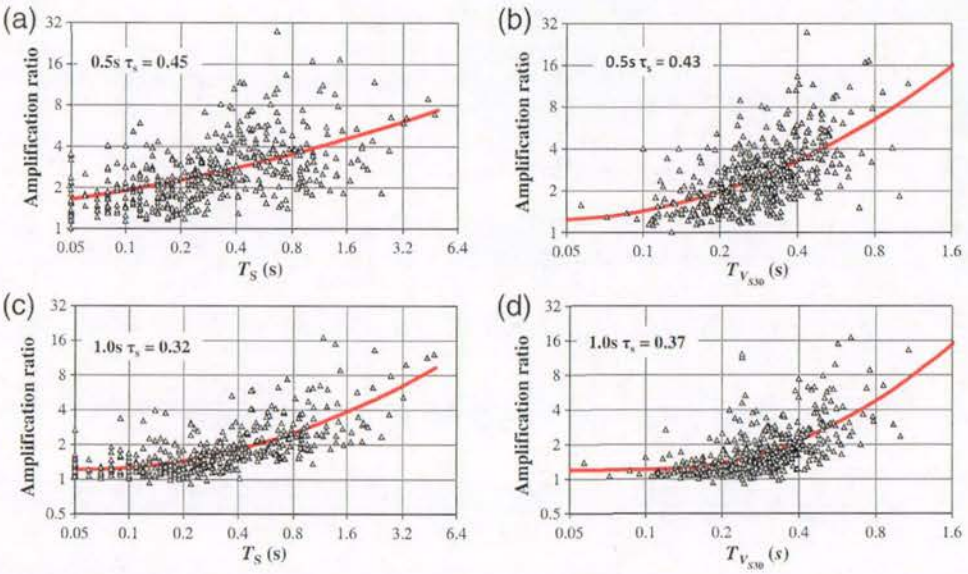

Figure 6. Amplification ratios between the KiK-net site surface and borehole records for 0.5 s spectral period (top row) and 1.0 s (bottom row). The left plots use T_S as the site parameter, and the right plots use $T_{V_{S30}}$. The color version of this figure is available only in the electronic edition.

generally much smaller than those of the intersite residuals at short periods (in Fig. 10a) but they are similar at long periods for rock and stiff-soil class sites (SC I and II). The intrasite residuals exclude the single-record sites for which the approximate intrasite residuals are zero. For soft-soil sites (SC IV) the standard deviation for intrasite residuals is much less than that for intersite residuals at all spectral periods. The small intrasite standard deviation derived from this study is probably one of the reasons why the standard deviation from the strong-motion records obtained at a particular

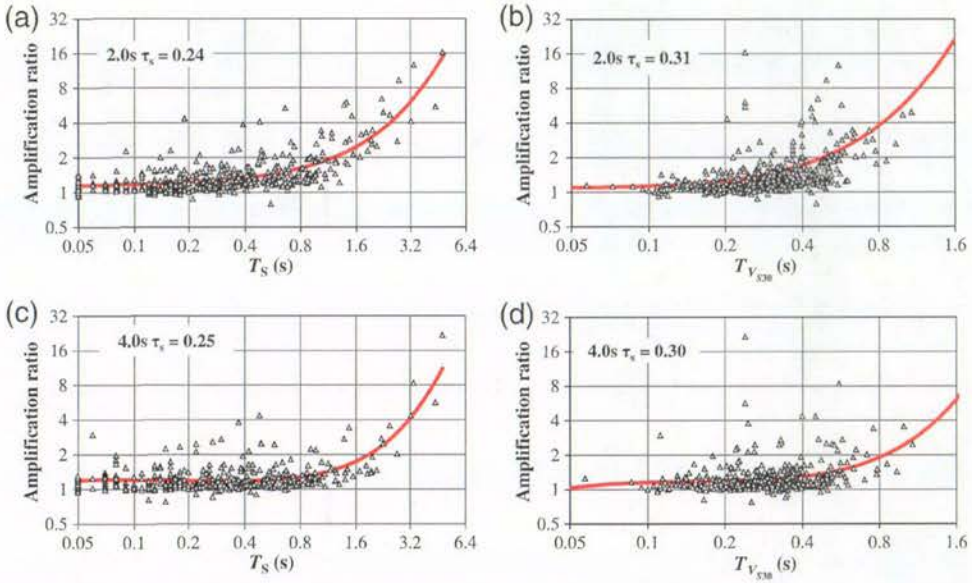

Figure 7. Amplification ratios between the KiK-net site surface and borehole records for 2.0 s spectral period (top row) and 4.0 s (bottom row). The left panel uses T_S as the site parameter, and the right panel uses $T_{V_{S30}}$. The color version of this figure is available only in the electronic edition.

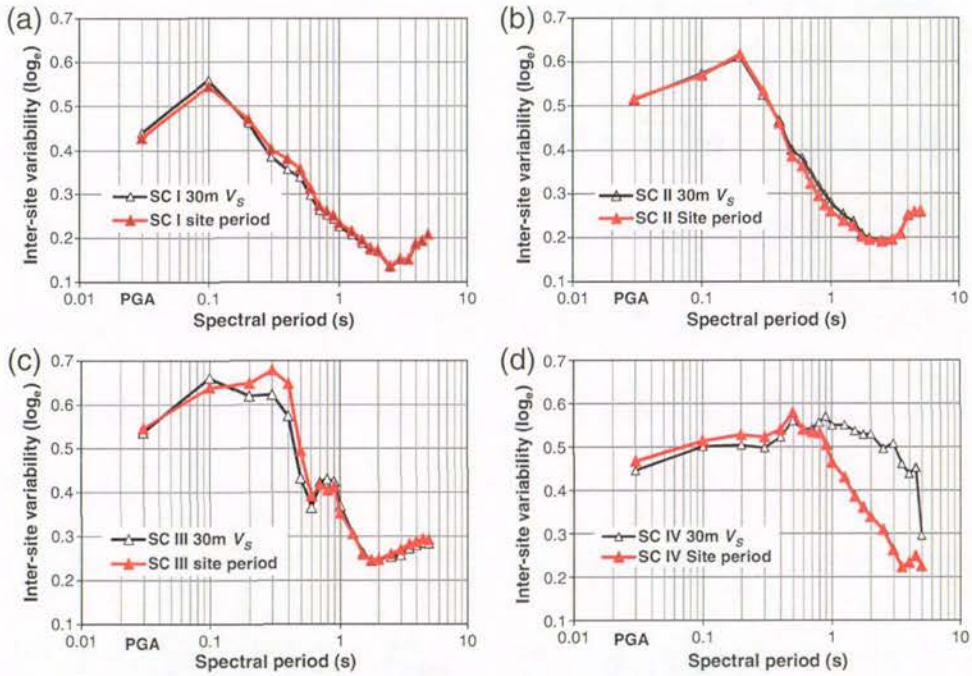

Figure 8. Comparison of intersite standard deviations (labeled as intersite variability for convenient presentation) derived by using T_S and $T_{V_{S30}}$ for site classification (SC) I in (a), SC II in (b), SC III in (c), and SC IV in (d), for the KiK-net site surface and borehole records. Values for peak ground acceleration (PGA) are plotted at 0.03 s spectral periods for a convenient presentation in logarithm scales. The color version of this figure is available only in the electronic edition.

site would be smaller than that in the regional GMPE, as reported by Atkinson (2006). The intrasite standard deviation being smaller than the intersite standard deviation suggests that the probability of similar amplification ratios at a given site from different earthquakes is higher than the probability of similar amplification ratios between two sites with

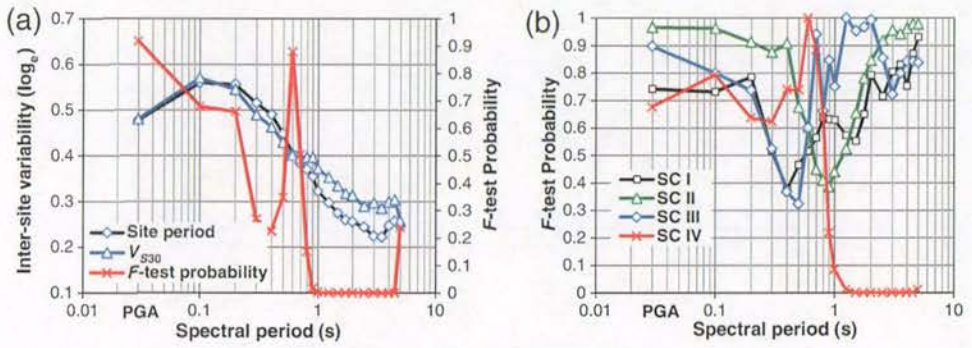

Figure 9. Intersite standard deviations and probability from F-test for the intersite residuals by using T_S and $T_{V_{S30}}$, (a) all data and (b) each site class for the KiK-net site surface and borehole records. Values for peak ground acceleration (PGA) are plotted at 0.03 s spectral periods for a convenient presentation in logarithm scales. The color version of this figure is available only in the electronic edition.

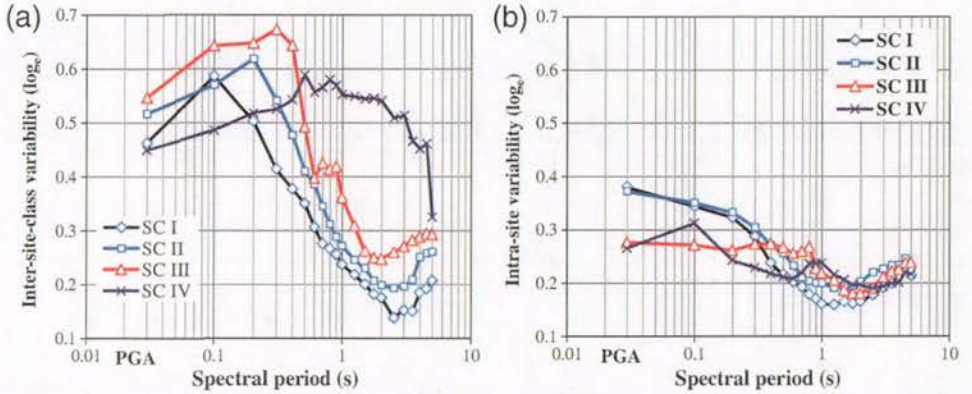

Figure 10. Intrasite-class standard deviations in (a) and intrasite standard deviations in (b) for response spectral amplification ratios, assuming constant amplification ratios in each site class for the KiK-net site surface and borehole records. Values for peak ground acceleration (PGA) are plotted at 0.03 s spectral periods for a convenient presentation in logarithm scales. The color version of this figure is available only in the electronic edition.

identical site classes or T_S. The small intrasite variability compared with intersite standard deviation also suggests that appropriate site modeling can reduce the variability of predicted site amplification ratio, as, in theory, intersite standard deviation can be excluded in the probabilistic seismic-hazard analysis for this particular site. However, the uncertainty in the selection of theoretical site response models will be an equivalent to intersite variability in this case.

Figure 10b also shows that, at short periods up to 0.4 s, the intrasite standard deviations for SC I and II sites are larger than those for sites III and IV. A possible reason is that the variability tends to be relatively large at spectral periods close to T_S, although this is obscured by the general reduction in the intrasite standard deviation with increasing spectral period up to 1.5 s. If this linear reduction is removed, the intrasite variability tends to have a peak at the average T_S for each site class. The T_S range for SC I and II sites has T_S less than 0.4 s, and this may be the reason for the relatively large intrasite standard deviations at short periods.

Analysis of Residuals from GMPEs for Records from the Second Dataset

Similar to the previous analysis of KiK-net ground-motion data, the average value of the site class terms plus intraevent residuals for each site is used so as to minimize the variability associated with path effect. The exponential of the site class term plus intraevent residuals is referred to as the site-effect factor B_{site}. Based on the same selection procedure as for equation (3), the following simple function of either T_S or $T_{V_{S30}}$ was fitted to the average values

$$\ln[B_{\text{site}}(T, T_{\text{SP}})] = a_{\text{site}}(T_{\text{SP}})T + b_{\text{site}}(T_{\text{SP}})\ln(T) + c_{\text{site}}(T_{\text{SP}})[\ln(T)]^2 + d_{\text{site}}(T_{\text{SP}}), \quad (4)$$

in which a_{site}, b_{site}, c_{site}, and d_{site} are regression coefficients for a given spectral period T_{SP}. A t-test was performed to examine the statistical significance of each coefficient in equation (4) and only those that are statistically significant

(when the absolute value is greater than zero) at a 5% significance level were retained. As previously noted, the variability associated with the fitted empirical site model is referred to as the intersite variability, and the standard deviation from equation (4) will be the principal indicator used for quantifying site response in this study.

Figure 11 shows the average values for the site-effect factor from the Zhao (2010) and Zhao and Xu (2012) studies in each site and values computed from equation (4) for PGA and spectral accelerations at 0.5 s. Because of the small number of long-period sites, the decrease in the site-effect factor with increasing site period in the left panel of Figure 11 at long site periods is poorly constrained and more sites are required to obtain reliable estimates. It is also possible that equation (4) is not the best empirical model to describe the site effect. However, the prime purpose of this study is the selection of site parameters by evaluating intersite standard deviation, which is not very sensitive to the detailed variation of the average site-effect factor within the site parameter. For example, if a more complex model than equation (4) is used to achieve a constant average site-effect factor at a long site period, the intersite standard deviation, τ_s, is largely unchanged. Figure 12 shows the results for spectral periods of 1.0 and 2 s. The standard deviations for the empirical models described by equation (4) using T_S or $T_{V_{S30}}$ are very similar, with $T_{V_{S30}}$ producing a slightly smaller standard deviation for PGA and 0.5 s period. The standard deviations for 1.0 and 2.0 s spectral periods are very similar between the two site parameters.

Figure 13 compares the intersite standard deviations (τ_s) derived from using T_S or $T_{V_{S30}}$ in the place of T in equation (4). For SC I sites, the standard deviations from using T_S and $T_{V_{S30}}$ are very similar for all spectral periods, although $T_{V_{S30}}$ leads to a slightly smaller standard deviation than T_S as shown in Figure 13a. Figure 13b shows that, for SC II sites, using T_S leads to a smaller standard deviation in a spectral period range 0.8–3 s than using $T_{V_{S30}}$ for SC II sites. Both site parameters lead to very similar standard deviations for other spectral periods. For SC III sites, Figure 13c shows that, at periods up to 0.6 s, using T_S leads to a slightly larger standard deviation than using $T_{V_{S30}}$. The use of T_S leads to smaller standard deviations at most spectral periods of more than 0.6 s. However, for SC IV sites, using T_S actually leads to a sizable increase in the intersite standard deviations between spectral periods 0.3 and 1.0 s compared with those using $T_{V_{S30}}$, while using T_S leads to smaller standard deviations at spectral periods of more than 1.2 s, as shown in Figure 13d.

Figure 14a shows that the F-test probability for the hypothesis that the intersite residuals from two site parameters have statistically similar standard deviations is less than 10% in a period range of 0.6–0.9 s for SC IV sites, in which T_S actually performs worse than $T_{V_{S30}}$ does. The F-test probability for all other three site classes is more than 25%. Figure 14b shows the intraevent/site standard deviation, $\sigma_{\text{event/site}}$, the standard deviation for the residuals between the intraevent residuals for each record and the average intraevent residuals for a given site. The results from

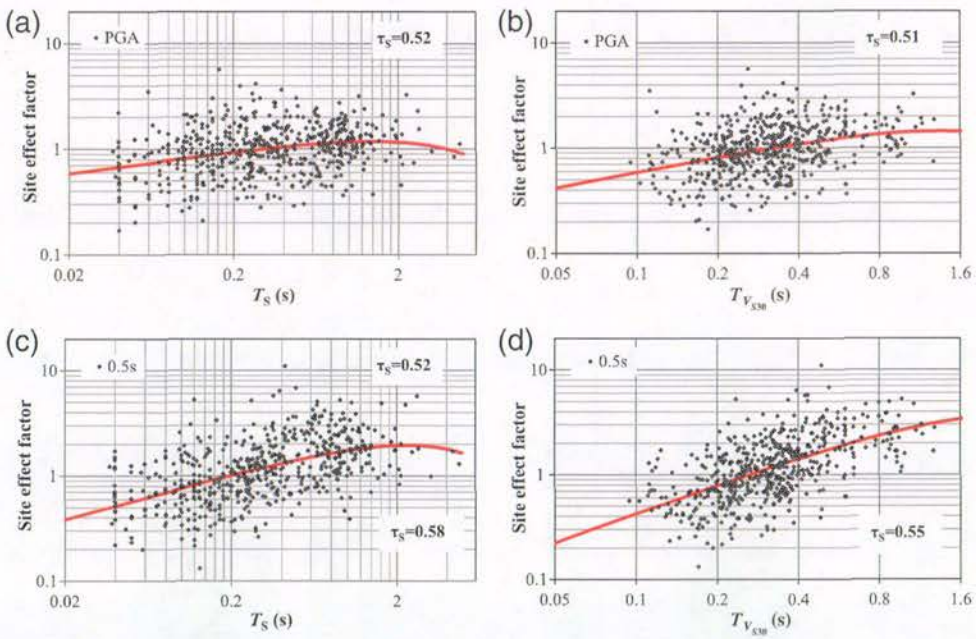

Figure 11. Site-effect factor for each site and the simple functions fitted to the site-effect factor, using T_S as the site parameter in the left panel and $T_{V_{S30}}$ in the right panel. The top row is for peak ground acceleration (PGA), and the bottom is for the 0.5 s spectral period. The color version of this figure is available only in the electronic edition.

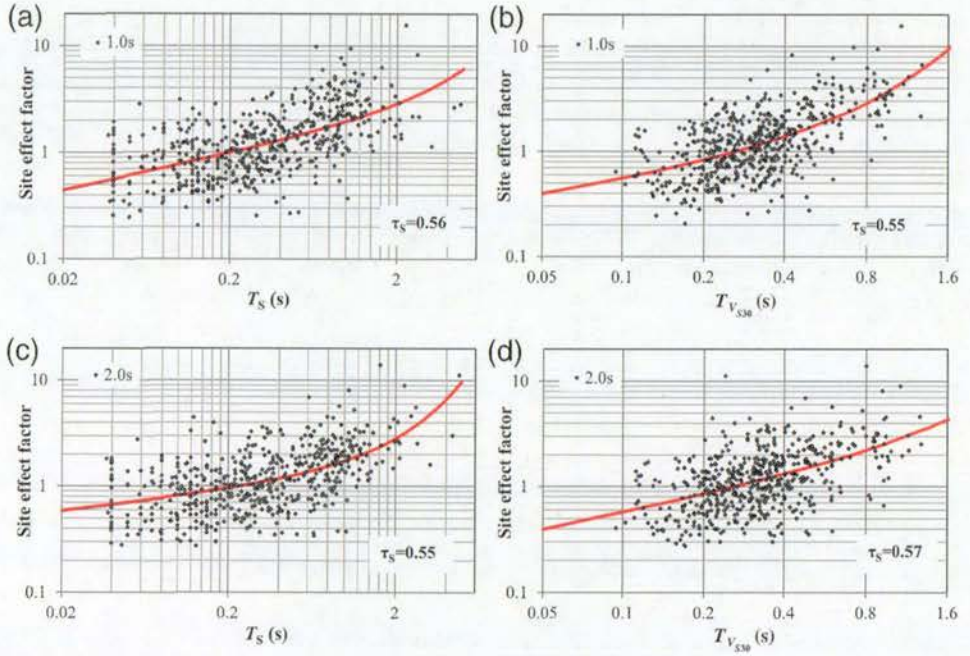

Figure 12. Site-effect factor for each site and the simple functions fitted to the site-effect factor, using T_S as the site parameter in the left panel and $T_{V_{S30}}$ in the right panel. The top row is for 1.0 s, and the bottom is for the 2.0 s spectral period. The color version of this figure is available only in the electronic edition.

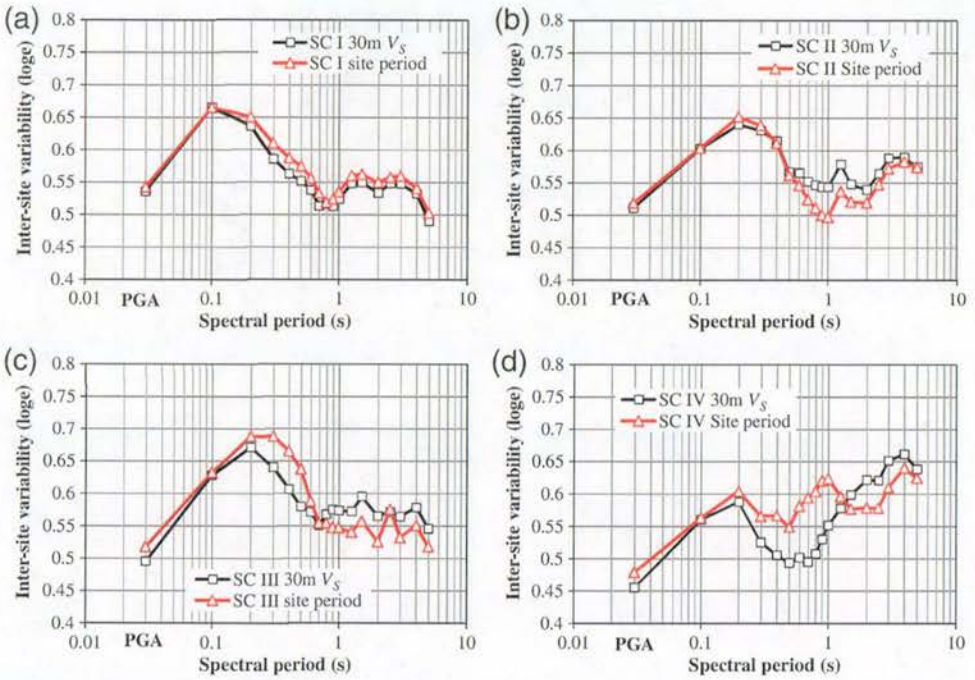

Figure 13. Comparison between the intersite standard deviations (labeled as intersite variability for convenient presentation) modeled by using $T_{V_{S30}}$ and T_S as site parameters: (a) for site classification (SC) I, (b) SC II, (c) SC III, and (d) SC IV recording stations. Values for peak ground acceleration (PGA) are plotted at 0.03 s spectral periods for a convenient presentation in logarithm scales. The color version of this figure is available only in the electronic edition.

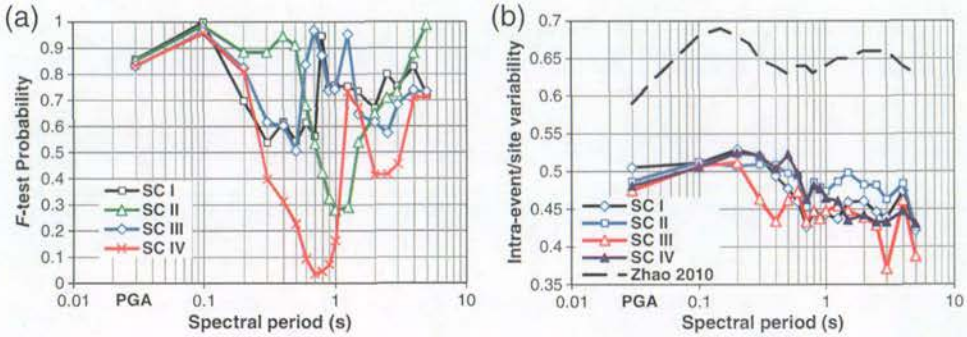

Figure 14. Probability of F-test in (a) and intraevent–site standard deviations in (b) for four site classes. Values for peak ground acceleration (PGA) are plotted at 0.03 s spectral periods for a convenient presentation in logarithm scales. The color version of this figure is available only in the electronic edition.

single-record stations were excluded from the calculation of the intraevent–site standard deviation. Figure 14b also shows the intraevent standard deviations from the Zhao (2010) model, which is much larger than the intraevent–site standard deviations from the present study. For PGA, the intersite and the intraevent–site standard deviations are similar. For all other spectral periods, the intraevent–site standard deviations are either similar to, or smaller than, the intersite standard deviations presented in Figure 13. For SC IV sites, the intraevent–site standard deviation is considerably smaller than the intersite standard deviation at other spectral periods. The total intraevent standard deviation $\sigma_{\text{intra-event}}$ from the present study can be calculated by

$$\sigma_{\text{intra-event}} = \sqrt{\sigma^2_{\text{event/site}} + \tau^2_{\text{s}}}. \tag{5}$$

The total intraevent standard deviation, $\sigma_{\text{intra-event}}$, is almost identical to the intraevent standard deviations from the Zhao (2010) study. The single site standard deviation, $\sigma_{\text{s-site}}$, defined by

$$\sigma_{\text{s-site}} = \sqrt{\sigma^2_{\text{event/site}} + \tau^2_{\text{inter-event}}}, \tag{6}$$

in which $\tau_{\text{inter-event}}$ is the interevent standard deviation from a GMPE. Clearly $\sigma_{\text{s-site}}$ is likely to be smaller than the total regional standard deviation from a GMPE because of the exclusion of τ_s, as shown by Atkinson (2006).

A possible cause for the discrepancies between the results presented in Figures 9b and 14a may be the introduction of K-NET and PARI stations in the second dataset, as all K-NET stations and some PARI stations have a shear-wave velocity to a depth of only 20 m. One way to evaluate this possibility is to compare the mean intersite residuals and the standard deviations for the KiK-net data and the data from the rest of the stations in the second dataset. The results show that the standard deviations between these two groups of data within the second dataset are statistically similar, with an F-test probability over 30% for the residuals from using T_S or $T_{V_{S30}}$. For the data using $T_{V_{S30}}$, a t-test at 5% significance level shows that the mean intersite residuals from the KiK-net data are also statistically similar to the rest of the data in the second dataset. Another t-test shows that the mean intersite residuals from the KiK-net data differ statistically from the data of the other stations in the second dataset at some periods, but the difference is practically insignificant, only about 10% or less. It can be shown that this level of difference between the mean intersite residuals from two groups of data within the dataset will lead to a negligible increase in the standard deviation for the entirety of the second dataset. These results suggest that the conflicting conclusions derived from the first and second datasets are unlikely to be caused by any inconsistency in the site periods between the two groups of stations in the second dataset.

In theory, if the dataset used by a GMPE is large and evenly distributed between earthquake events and ground-motion stations (in which the total number of records is large and the number of records from each station is equally large), the random errors from source and path effects can be eliminated by averaging the site terms in addition to intraevent residuals for a particular site. For such a perfect dataset, intra- and interevent errors can be completely separated. However, the dataset used in the GMPE of Zhao (2010) and Zhao and Xu (2012) is far from ideal, especially for the partial dataset used in the present study. Most of the stations have a relatively small number of records, and as well as many of the earthquakes. Consequently, some of the interevent random errors and the intraevent errors may have propagated into the intersite variability. The error propagated into intersite residuals may be larger at spectral periods close to T_S than at other spectral periods because amplification ratios tend to be large at spectral periods close to T_S. Also, as the number of records with useable response spectral periods greater than 1.5 s reduces quickly with increasing spectral period, the effect of improper data distribution may increase with increasing period. Therefore, the discrepancies between the results in Figures 9b and 14a at site periods, as well as at long periods, may be caused by the larger variability in the second dataset as shown clearly in Figure 15. At long spectral periods, the standard deviations from the first dataset are much

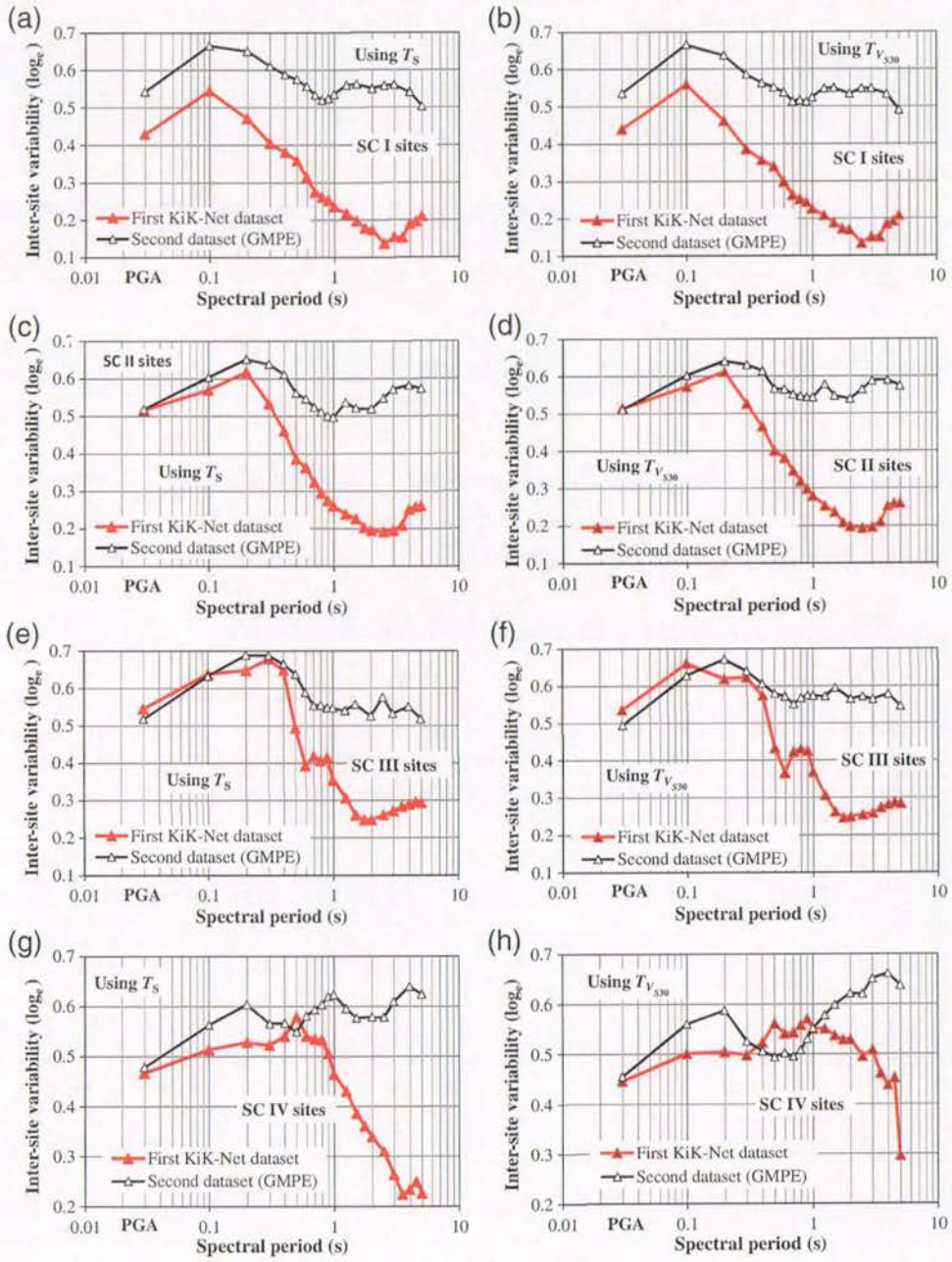

Figure 15. Comparison of intersite standard deviations between the first dataset (KiK-net surface–borehole spectral ratios) and the second dataset from a ground-motion prediction equation (GMPE). The left panel shows the result of using T_S as a site parameter, and the right panel shows the result of using $T_{V_{S30}}$. The top row is for site classification (SC) I sites, the second for SC II, the third for SC III, and the fourth for SC IV. Values for peak ground acceleration (PGA) are plotted at 0.03 s spectral periods for a convenient presentation in logarithm scales. The color version of this figure is available only in the electronic edition.

smaller than those from the second dataset, and the differences rise with increasing spectral period. The large differences at long periods may be a result of error propagation exacerbated by the reduced number of records with increasing spectral periods. For SC I sites at short periods, Figure 15a,b shows that the standard deviations of the first dataset are smaller than those of the second dataset by a large factor for all spectral periods. The large differences at PGA and short periods for SC I sites may be caused by the short-site period (0–0.2 s) for SC I sites, in which the variability tends to be larger at spectral periods close to T_S. At short periods and for SC II, III, and IV sites as shown

in Figure 15c–h, the standard deviations from the two datasets at spectral periods shorter than site periods are generally similar.

Analysis of Residuals from GMPEs for Records from the First Dataset

The results from the analyses of the first dataset using surface and borehole spectral amplification ratios appear to be inconsistent with those from the analyses of the second dataset used in GMPE studies by Zhao (2010) and Zhao and Xu (2012). There is a possibility that the second dataset contains some recording stations that do not have a measured shear-wave velocity to the bedrock. To clarify this aspect, we present the results from the analyses of site class term plus the intraevent residuals for surface records in the first dataset. However, 1796 surface records in the first dataset were not used in the GMPE studies of Zhao (2010) and Zhao and Xu (2012), and, therefore, intraevent residuals are not readily available. We used an approximate method to calculate the intraevent residuals for these records.

We calculated the total residuals for the 1796 surface records in the first dataset with respect to the GMPE of Zhao (2010) and then calculated the average total residuals for each earthquake. The average total residual for each earthquake event is then taken as the approximate interevent residual, and the difference between the total and the approximate interevent residual is taken as the approximate intraevent residual. The approximate intraevent residuals were then combined with the intraevent residuals for the records that were included in the Zhao (2010) and Zhao and Xu (2012) studies. The same procedure used in the analyses for the second dataset was applied to the site term plus the approximate intraevent residuals together with data for the remaining records in the first dataset from the GMPE studies by Zhao (2010) and Zhao and Xu (2012). Note that their model parameters were not published.

Figure 16 shows the intersite variability and the F-test probability for all data as one group. For spectral periods up to 0.5 s and spectral periods of 2 s or longer, the interevent standard deviations derived by using T_S and $T_{V_{S30}}$ are very similar. The standard deviations using T_S are smaller than those from using $T_{V_{S30}}$ by 0.05 at the other spectral periods. The probability of accepting equal standard deviations from the two site parameters is less than 10% in a spectral period range of 0.6–1.2 s and less than 5% in a spectral period range of 0.7–1 s. The use of T_S for amplification ratios in a period range of 0.7–1.0 s leads to statistically significant reduction in the intersite standard deviation.

Figure 17 shows the intersite residuals and F-test probability for the data in four site classes. Figure 17a shows that the intersite standard deviations for SC I sites from using T_S and $T_{V_{S30}}$ are nearly identical and the probability of accepting statistically similar standard deviations are more than 60%. For SC II sites in Figure 17b, the standard deviations from the two site parameters are also nearly identical

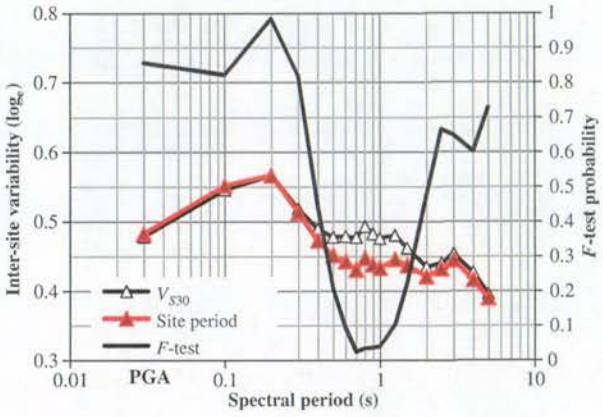

Figure 16. Comparison between the intersite standard deviations modeled by using $T_{V_{S30}}$ and T_S as site parameters for the KiK-net surface records with respect to ground-motion prediction equations (GMPEs) for the first dataset as one group. Values for peak ground acceleration (PGA) are plotted at 0.03 s spectral periods for a convenient presentation in logarithm scales. The color version of this figure is available only in the electronic edition.

and the F-test probability is more than 90%. For SC III sites, Figure 17c shows that the intersite standard deviations from the two site parameters are nearly identical for spectral periods up to 0.5 s. The standard deviations from using T_S are less than those from using $T_{V_{S30}}$ at other spectral periods by 0.05. The F-test probability is more than 45% for all spectral periods. Figure 17d shows that the standard deviations using T_S are very similar to those using $T_{V_{S30}}$ at spectral periods up to 0.3 s and spectral period of 1.5 s or longer. The standard deviations from using T_S are less than those from using $T_{V_{S30}}$ by about 0.05 in a spectral period range of 0.4–1.25 s. The F-test probability for accepting equal intersite standard deviations from two site parameters is more than 20% for all spectral periods. These results suggest that the differences in the standard deviations from the two site parameters are statistically similar for all spectral periods in all site classes. However, the lower standard deviations from using T_S than using $T_{V_{S30}}$ in a spectral period range of 0.7–1.0 s for SC III and IV sites lead to statistically lower standard deviations for all sites as one group by using T_S than that from using $T_{V_{S30}}$.

Comparison of Amplification Ratios Predicted by Using $T_{V_{S30}}$ and T_S

It is well known that using appropriate site modeling parameters in GMPEs does not usually lead to significant reduction in the model standard deviations. However, the appropriate site modeling can lead to appropriate spectral shapes that are consistent with the definition of site classes. Zhao, Irikura, *et al.* (2006) showed that the spectral amplification ratios for the spectra from SC II, III, and IV over SC I class, derived from GMPEs using site class based on T_S, leads to much more consistent amplification ratios than using the site classes based on geological and geotechnical description.

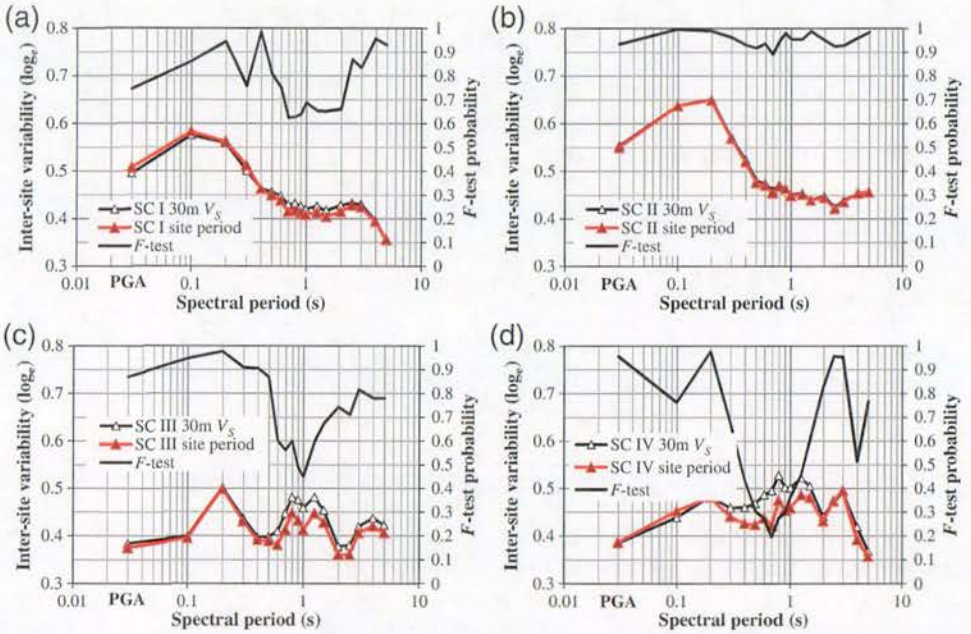

Figure 17. Comparison between the intersite standard deviations modeled by using $T_{V_{S30}}$ and T_S as site parameters for the KiK-net surface records with respect to ground-motion prediction equations (GMPEs): (a) for SC I, (b) SC II, (c) SC III, and (d) SC IV recording stations. Values for peak ground acceleration (PGA) are plotted at 0.03 s spectral periods for a convenient presentation in logarithm scales. The color version of this figure is available only in the electronic edition.

Fukushima *et al.* (2003) found that using site classes based on T_S for the European data led to little reduction in regression standard deviation but produced better spectral shape. A recent study (Di Alessandro *et al.*, 2012) also found similar results. These results mean that achieving consistent median amplification ratios is also an important indication of using appropriate site parameters. Consistent median amplification ratios means that:

(a) the peak amplification ratios tend to rise with increasing T_S; and
(b) the peak amplification periods tend to exist at a spectral period close to T_S at least for SC I, II, and III, and some SC IV sites.

Figure 18 presents the response spectral amplification ratios A_{site} calculated by

$$A_{\text{site}}(T_{\text{site}}, T_{\text{SP}}) = \frac{B_{\text{site}}(T_{\text{site}}, T_{\text{SP}})}{B_{\text{site}}(T_{\text{rock}}, T_{\text{SP}})}. \quad (7)$$

The rock-site period $T_{\text{rock}} = 0.1$ was selected. The variation of amplification ratios with T_S is not smooth for some site periods and is possibly caused by the use of a partial dataset. For all sites shown in Figure 18, the amplification ratios derived by using T_S are very similar to those using $T_{V_{S30}}$ for spectral periods up to 0.4 s. The good agreement demonstrated is a result of good correlation between T_S and $T_{V_{S30}}$ at short periods, as shown in Figure 1. At spectral periods of more than 0.4 s, the peak amplification ratios computed by using $T_{V_{S30}}$ are generally less than those computed by using T_S, and the differences rise quickly with increasing T_S. Using $T_{V_{S30}}$, the long-period amplification ratios are severely underestimated compared with those using T_S because of the saturation of $T_{V_{S30}}$, with respect to T_S as shown in Figure 1.

Conclusions

The following conclusions can be reached in this study:

(1) The correlation between site period (T_S, four times the travel time of shear-wave velocity in the soil layers) and $T_{V_{S30}}$, 120 m/V_{S30} (the average shear-wave velocity to a depth of 30 m with a unit of m/s), is excellent for sites with $T_S < 0.4$ s. This means that for short-period sites, both V_{S30} and T_S can be used as the site parameter to model the response spectral amplification ratios with equivalent predictive capabilities. For periods greater than ~0.5 s, the variability in correlation between $T_{V_{S30}}$ and T_S is considerable.
(2) For the KiK-net records, standard deviations for intersite errors, the difference between average residuals for each site and the empirical model used to estimate response spectral amplification ratios, are in a range of 0.18–0.6 in the natural logarithm scale. The larger value is associated with short spectral periods and the smaller value with long spectral periods.
(3) For the KiK-net records, the standard deviation of the intrasite errors that represents the variation of amplification ratios from different records in each station is much smaller

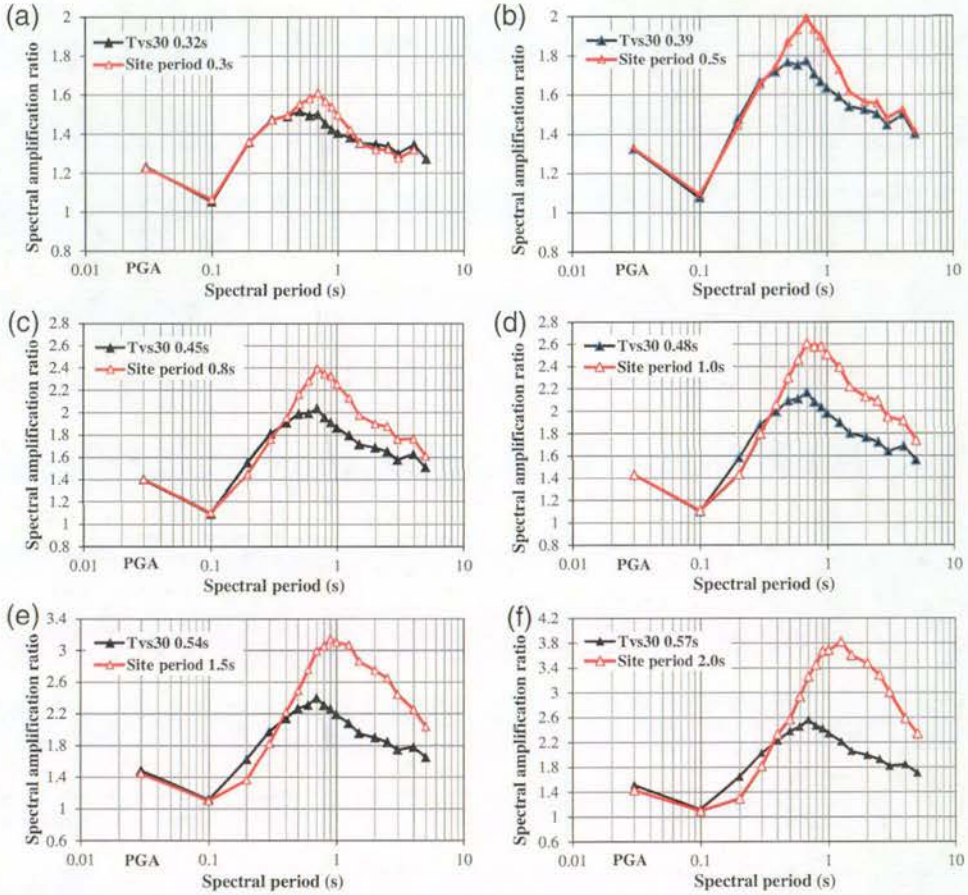

Figure 18. Comparison between spectral amplification ratios for soil sites with respect to rock sites with a site period of 0.1 s, derived by using T_S and by $T_{V_{S30}}$, for site periods (a) 0.3 s, (b) 0.5 s, (c) 0.8 s, (d) 1.0 s, (e) 1.5 s, and (f) 2.0 s. Values for peak ground acceleration (PGA) are plotted at 0.03 s spectral periods for a convenient presentation in logarithm scales. The color version of this figure is available only in the electronic edition.

than the standard deviation of intersite residuals at short spectral periods but similar at long periods.

(4) For the KiK-net data, in terms of standard deviation for intersite errors, T_S is a better site parameter for modeling amplification ratios than V_{S30} for sites with $T_S > 0.6$ s. The variability of amplification ratios derived using T_S or V_{S30} are statistically similar for sites with short and medium periods.

(5) Using T_S or V_{S30} to model site class terms, plus intraevent residuals from Zhao (2010) and Zhao and Xu (2012), leads to statistically similar intersite standard deviations for three site classes (rock, hard soil, and medium soil) and for most spectral periods in the soft-soil site class. At a few spectral periods around 0.8 s, V_{S30} leads to statistically smaller standard deviations than T_S.

(6) The relatively small intrasite standard deviations for the site amplification ratio may be a possible cause for the smaller single-site standard deviation than the regional GMPE standard deviation.

(7) The modeling of approximate intraevent residuals from the KiK-net surface records in the first dataset with respect to the GMPE of Zhao (2010) and Zhao and Xu (2012) shows that T_S and V_{S30} lead to similar intersite standard deviations for all spectral periods for each site class. Site periods lead to statistically similar intersite standard deviations for all records as one group at most spectral periods.

(8) Even though the intersite variability calculated by using T_S is statistically similar to that using V_{S30} for the second dataset, T_S is still arguably a better site parameter for a GMPE. This is because using T_S leads to more reasonable median amplification ratios, especially for soft-soil sites at long spectral periods, than V_{S30}.

Data and Resources

The strong-motion records used in the present study are from K-NET and KiK-net operated by the National Institute of Earth Science and Disaster Prevention, and the network operated by the Port and Airport Research Institute (PARI) in Japan.

Acknowledgments

The authors wish to thank Brendon Bradley for his review of the manuscript and Jane Forsyth for her editorial comments. Comments from two anonymous reviewers were constructive and invaluable. Encouragement, detailed comments, and suggestions from Associate Editor Stefano Parolai are greatly appreciated. The work reported here is partially supported by research grants from the National Science Foundation of China (51278432), the Southwest Jiaotong University (SWJTU12ZT04), New Zealand Earthquake Commission 2010 Biennial Research Grant, and by New Zealand Foundation for Research Science and Technology, New Zealand Hazards Platform contract C05X0907.

References

Abrahamson, N. A. (2011). Is V_{S30} an effective parameter for site characterization?, in *Fourth IASPEI/IAEE International Symposium: Effects of Surface Geology on Seismic Motion*, University of California, Santa Barbara, 23–26 August 2011, http://esg4.eri.ucsb.edu/sites/esg4.eri.ucsb.edu/files/Abrahamson%20ESG4%20Vs30.pdf (last accessed November 2012).

Abrahamson, N. A., and W. J. Silva (2008). Summary of the Abrahamson & Silva NGA ground-motion relations, *Earthq. Spectra* **24,** no. 1, 67–97.

Abrahamson, N. A., and R. R. Youngs (1992). A stable algorithm for regression analysis using the random effect model, *Bull. Seismol. Soc. Am.* **82,** no. 1, 505–510.

Atik, L. A., A. Abrahamson, J. J. Bommer, F. Scherbaum, F. Cotton, and N. Kuehn (2010). The variability of ground-motion prediction models and its components, *Seismol. Res. Lett.* **81,** no. 5, 794–801.

Atkinson, G. M. (2006). Single station sigma, *Bull. Seismol. Soc. Am.* **96,** no. 2, 446–455.

Boore, D. M., and G. M. Atkinson (2008). Ground-motion prediction equations for the average horizontal component of PGA, PGV, and 5%-damped PSA at spectral periods between 0.01 s and 10.0 s, *Earthq. Spectra* **24,** no. 1, 99–138.

Boore, D. M., E. M. Thompson, and H. Cadet (2011). Regional correlations of V_{S30} and velocities averaged over depths less than and greater than 30 m, *Bull. Seismol. Soc. Am.* **101,** no. 6, 3046–3059.

Building Seismic Safety Council (BSSC) (2000). The 2000 NEHRP Recommended Provisions for New Buildings and Other Structures, *Part I (Provisions) and Part II (Commentary)*, FEMA 368/369, Washington, D.C..

Campbell, K. W., and Y. Bozorgnia (2008). NGA ground motion model for the geometric mean horizontal component of PGA, PGV, PGD and 5% damped linear elastic response spectra for periods ranging from 0.01 to 10 s, *Earthq. Spectra* **24,** no. 1, 139–171.

Castellaro, S. (2011). The VFZ matrix: Simplified seismic soil classification from a different perspective, in *Fourth IASPEI/IAEE International Symposium: Effects of Surface Geology on Seismic Motion*, University of California, Santa Barbara, 23–26 August 2011, http://esg4.eri.ucsb.edu/sites/esg4.eri.ucsb.edu/files/Castellaro%20ESG4%20Vs30.pdf (last accessed November 2012).

Castellaro, S., F. Mulargia, and P. L. Rossi (2008). V_{S30}: Proxy for seismic amplification? *Seismol. Res. Lett.* **79,** no. 4, 540–543.

Chiou, B. S.-J., and R. R. Youngs (2008). An NGA model for the average of horizontal component of peak ground motion and response spectra, *Earthq. Spectra* **24,** no. 1, 173–216.

Di Alessandro, C., L. F. Bonilla, D. M. Boore, A. Rovelli, and O. Scotti (2012). Predominant-period site classification for response spectra prediction equations in Italy, *Bull. Seismol. Soc. Am.* **102,** no. 2, 680–695.

Fukushima, Y., C. Berge-Thierry, P. Volant, D. A. Griot-Pommera, and F. Cotton (2003). Attenuation relation for west Eurasia determined with recent near-fault records from California, Japan and Turkey, *J. Earthq. Eng* **7,** no. 1, 1–26.

Kanno, T., A. Narita, N. Morikawa, H. Fujiwara, and Y. Fukushima (2006). A new attenuation relation for strong ground motion in Japan based on recorded data, *Bull. Seismol. Soc. Am.* **96,** 879–897.

Luzi, L., R. Puglia, F. Paco, M. R. Gallipoli, D. Bindi, and M. Mucciarelli (2011). Proposal for a soil classification based on parameters alternative or complementary to V_{S30}, *Bull. Earthq. Eng.* **9,** 1877–1898.

McVerry, G. H. (2011). Site-effect terms as continuous functions of site period and V_{S30}, in *Pacific Conference on Earthquake Engineering (9PCEE): Building an Earthquake Resilient Society*, Paper 010, University of Auckland, Auckland, New Zealand, 14–16 April 2011.

McVerry, G. H., J. X. Zhao, N. A. Abrahamson, and G. H. Somerville (2006). Crustal and subduction zone attenuation relations for New Zealand earthquakes, *Bull. N. Z. Soc. Earthq. Eng.* **39,** no. 1, 1–58.

Parolai, S., A. Ansal, A. Kurtulus, A. Strollo, R. Wang, and J. Zschau (2009). The Ataköy vertical array (Turkey): Insights into seismic wave propagation in the shallow-most crustal layers by waveform deconvolution, *Geophys. J. Int.* **178,** no. 3, 1649–1662.

Safak, E. (1997). Models and methods to characterize site amplification ratios from a pair of records, *Earthq. Spectra* **13,** no. 1, 97–129.

Walling, M., W. Silva, and N. Abrahamson (2008). Nonlinear site amplification factors for constraining the NGA models, *Earthq. Spectra* **24,** no. 1, 243–255.

Zhao, J. X. (1996). Estimating modal parameters for a simple soft-soil site having a linear distribution of shear wave velocity with depth, *Earthq. Eng. Struct. Dyn.* **25,** no. 2, 163–178.

Zhao, J. X. (2010). Geometric spreading functions and modeling of volcanic zones for strong-motion attenuation models derived from records in Japan, *Bull. Seismol. Soc. Am.* **100,** no. 2, 712–732.

Zhao, J. X. (2011). Comparison between V_{S30} and site period as site parameters in ground-motion prediction equations for response spectra, in *Fourth IASPEI/IAEE International Symposium: Effects of Surface Geology on Seismic Motion*, University of California, Santa Barbara, Paper 6.9, 23–26 August 2011, http://esg4.eri.ucsb.edu/sites/esg4.eri.ucsb.edu/files/6.9%20Zhao.pdf (last accessed November 2012).

Zhao, J. X., and H. Xu (2012). Magnitude-scaling rate in ground-motion prediction equations for response spectra from large subduction interface earthquakes in Japan, *Bull. Seismol. Soc. Am.* **102,** no. 1, 222–235.

Zhao, J. X., K. Irikura, J. Zhang, Y. Fukushima, P. G. Somerville, A. Asano, Y. Ohno, T. Oouchi, T. Takahashi, and H. Ogawa (2006). An empirical site classification method for strong motion stations in Japan using H/V response spectrum ratio, *Bull. Seismol. Soc. Am.* **96,** no. 3, 914–925.

Zhao, J. X., J. Zhang, A. Asano, Y. Ohno, T. Oouchi, T. Takahashi, H. Ogawa, K. Irikura, H. K. Thio, P. G. Somerville, Y. Fukushima, and Y. Fukushima (2006). Attenuation relations of strong ground motion in Japan using site classification based on predominant period, *Bull. Seismol. Soc. Am.* **96,** no. 3, 898–913.

Southwest Jiaotong University
No.111, 1st North Section 2nd Ring Road
Chengdu 610031, Sichuan
China

Manuscript received 8 September 2011

www.gns.cri.nz

Principal Location

1 Fairway Drive
Avalon
Lower Hutt 5010
PO Box 30368
Lower Hutt 5040
New Zealand
T +64-4-570 1444
F +64-4-570 4600

Other Locations

Dunedin Research Centre
764 Cumberland Street
Dunedin 9016
Private Bag 1930
Dunedin 9054
New Zealand
T +64-3-477 4050
F +64-3-477 5232

Wairakei Research Centre
114 Karetoto Road, RD4
Taupo 3384
Private Bag 2000
Taupo 3352
New Zealand
T +64-7-374 8211
F +64-7-374 8199

National Isotope Centre
30 Gracefield Road, Gracefield
Lower Hutt 5010
PO Box 31312
Lower Hutt 5040
New Zealand
T +64-4-570 1444
F +64-4-570 4600